Nonlinear equilibration of baroclinic eddies: the role of boundary layer processes and seasonal forcing

by

Yang Zhang

Submitted to the Department of Earth, Atmospheric and Planetary Sciences
in partial fulfillment of the requirements for the degree of

Doctor of Philosophy

at the

MASSACHUSETTS INSTITUTE OF TECHNOLOGY

September 2009

Author .....
Department of Earth, Atmospheric and Planetary Sciences
August 21, 2009

Certified by .....
Peter H. Stone
Professor of Climate Dynamics
Thesis Supervisor

Accepted by .....
Maria Zuber
Head, Department of Earth, Atmospheric and Planetary Sciences

Nonlinear equilibration of baroclinic eddies:

the role of boundary layer processes and seasonal forcing

by

Yang Zhang

Submitted to the Department of Earth, Atmospheric and Planetary Sciences
on August 21, 2009, in partial fulfillment of the
requirements for the degree of
Doctor of Philosophy

Abstract

In this thesis, the influence of boundary layer processes and seasonal forcing on baroclinic eddy equilibration is studied to understand how the baroclinic adjustment is modified when taking into account these two factors.

A modified β plane multilevel quasi-geostrophic (QG) model with an interactive stratification and a simplified parameterization of atmospheric boundary layer physics is used as the atmospheric model in this study. Comparisons between experiments with the modified QG model and the traditional QG model with fixed stratification show that it is necessary to include the interaction between vertical eddy heat flux and stratification to obtain a realistic equilibrated state, i.e. robust isentropic slope. A slab surface model is also coupled with the atmospheric model to provide an interactive surface temperature distribution in some experiments in this study.

The effect of boundary layer processes is first studied under the situation with fixed underlying surface temperature. The boundary layer vertical thermal diffusion, along with the surface heat exchange, is found primarily responsible for the limitation of the PV homogenization in the boundary layer. The boundary layer processes can influence the eddy activity in at least two competing ways. First, in the eddy energy budget, all the boundary layer processes act to damp the eddy energy directly. On the other hand, the boundary layer processes also influence the mean flow, which can further influence the eddy behavior. For the boundary layer thermal damping, the indirect effect on the eddy activity becomes dominant. Stronger boundary layer thermal forcing results in stronger meridional temperature gradients and eddy heat fluxes. For the frictional dissipation, the resulting changes in the zonal wind and in the location of the critical latitude lead to a meridional variation of the eddy forcing, which can further result in a non-monotonic response of the mean flow.

The role of the boundary layer processes in the baroclinic eddy equilibration is further studied using a simple air-sea thermally coupled model. Although in the coupled system, each boundary layer process has more and different ways to influence the equilibrium state, their effect on the lower level PV homogenization is very robust. Surface friction and surface

heat flux all act to damp the lower level PV mixing and stronger surface damping prevents the PV homogenization more strongly, but the way in which each boundary layer process affects the PV homogenization is very different.

Baroclinic eddy equilibration under seasonal forcing is studied in both the atmospheric model and the coupled model. In the situation with specified seasonal variation of the underlying surface temperature, a Northern-Hemisphere like seasonal variation of the surface temperature is used to act on the atmospheric flow through the boundary layer processes and the radiative-convective heating. Under slowly varying seasonal forcing, the eddy and the mean flow behavior is characterized by four clearly divided time intervals: an eddy inactive time interval in the summer, a mainly dynamically determined eddy spinup time interval starting from mid-fall and lasting less than one month, a quasi-equilibrium time interval for the zonal mean flow available potential energy from late fall to late spring and a mainly external forcing determined eddy spindown time interval from late winter to late spring. In spite of the strong seasonality of the eddy activity, a robust PV structure is still observed through all the seasons. It is found that besides baroclinic eddies, the boundary layer thermal forcing as well as the moist convection all can help maintain the lower level PV structure. The sensitivity study of the eddy equilibration to the time scale of the external forcing also indicates that the time scale separation between the baroclinic adjustment and the external forcing in midlatitudes is only visible for external forcing cycle one year and longer. The seasonality study with the coupled model confirms the conclusions obtained in the uncoupled model.

Thesis Supervisor: Peter H. Stone
Title: Professor of Climate Dynamics

Acknowledgments

First and foremost, I owe my deepest gratitude to my advisor, Peter Stone. This thesis would not be possible without his patient guidance, constant support and many valuable ideas and suggestions he offered. I appreciate the great freedom Peter gave me in every aspect of my research and his intention to encourage me think and find each solution by myself, which trained me to carry out my research more and more independently. I am also very grateful to his numerous help in my scientific writing and the experience he shared with me on scientific presentation. Peter's deep and comprehensive understanding on climate dynamics, his enthusiasm for research and his truly scientific spirit will always be an inspiration for me.

I gratefully thank my committee members for their invaluable advices and many constructive suggestions on improving the early draft of my thesis. To Richard Lindzen, for his insight on this research subject and the 'critical thinking' he taught me; To Raffaele Ferrari and Alan Plumb, for being generous with their time, knowledge, and scientific wisdom in many individual discussions with me.

I also would like to show my gratitude to Kerry Emanuel and Paul O'Gorman, for their thoughtful comments on my thesis work. To John Marshall, for all his suggestions when I met difficulties in model modification. To Glenn Flierl and Lodovica Illari, for the beneficial and joyful time I had in their classes. To Joe Pedlosky and Carl Wunsch, for the knowledgeable classes they offered. And my special gratitude to Amy Solomon, who gave me her multilayer QG model, read and commented on several drafts of my first research paper.

My thanks also go to my wonderful friends at MIT. To my student mentor and groupmate Masahiro Sugiyama, my officemate Roberto Rondanelli, and Vikram Khade, for many talks and discussions we had which led me to a better understanding of my journey as a Ph.D. student. To Gang Chen, Jeff Scott and Yong-Sang Choi, for helping me prepare the presentation, giving me suggestions on my research and sharing their research experience with me. To Mary Elliff, for her constant help and every good-luck gift she gave me before the important days. To my other two officemates, Nikki Privé and Daniela Domeisen, for making the office such a delightful place to work in. To my classmates Yu Zhang, Shaoyu

Yuan, Cegeon Chan, Stephanie Waterman, Daniel Enderton, Bhaskar Gunturu, Ian Fenty and Tatiana Rykova, for each busy and fruitful day we shared in our first two years. To Kelly Klima, Brian Tang and Angela Zalucha for each lunch and chat we had together. I am also grateful to the warm and friendly administrative stuff in our department, Carol Sprague, Linda Meinke, Roberta Allard and Jacqueline Taylor. Thank you all for making my life as an MIT student as easy as possible.

Finally, I cannot thank my family enough for their unflagging love and support. To my parents, Mr and Mrs Zhang, for their unconditional care and consideration. And deep gratitude to my husband, Yitong, who is always there supporting me, encouraging me and has made my days as a Ph.D. student so colorful. This thesis is dedicated to them.

Contents

List of Figures

List of Tables

Chapter 1

Introduction

Baroclinic eddies, as shown in many observational and modeling studies (i.e. Oort and Peixoto (1983); Peixoto and Oort (1992); Philips (1956); Gall (1976); Simmons and Hoskins (1978); Edmon et al. (1980); Stone and Miller (1980) and so on), play an important role in determining the midlatitude climate. They are the dominant components in extratropic heat and momentum transports. They also influence the mean state and the atmospheric general circulation by wave-mean flow interaction.

One basic issue in the baroclinic eddy study is to understand and quantify the relation between the eddy fluxes and the mean flow. For this purpose, several theories have been proposed, with most attention being focused on two groups of theoretical assumptions. One is the baroclinic adjustment theory, which proposes that, like in convective adjustment, baroclinic eddies always try to adjust the mean flow to a neutral state. Another is the diffusive theory, which proposes the tendency of baroclinic eddies to reduce the potential vorticity (PV) gradient of the mean flow and quantifies the eddy fluxes from the mean flow through a diffusive approach.

Baroclinic adjustment and the diffusive theories propose seemingly different relations between the eddy activity and the mean flow. The baroclinic adjustment theory, especially the proposed 'neutral state', is inspired by the linear baroclinic instability theory. It proposes a preferred equilibrium state and a very strong feedback between the eddy heat fluxes and

the temperature structure, which has applications to the general circulation and the climate sensitivity. In the baroclinic adjustment scenario, the eddy fluxes are sensitive to the variation of the external forcing (i.e. seasonal forcing and climate change), but leave the structure of the mean state almost unchanged or slightly changed. However, in the diffusive theory, which will be further discussed in Chapter 3, the eddy fluxes are predicted by the mean flow. The relation between these two theories is further discussed in Zurita-Gotor (2007).

In this study, we will mainly focus on the baroclinic adjustment theory, and discuss to what extent the baroclinic adjustment theory can be applied to interpret the midlatitude climate. More specifically we will investigate the effect of the boundary layer processes and the seasonal forcing on the eddy-mean flow interaction, and how they can modify the baroclinic adjustment.

1.1 Review of baroclinic adjustment theories

The concept of baroclinic adjustment was first clearly proposed by Stone (1978), who found that, through all the seasons, the 600 mb zonal mean meridional temperature gradients in the extratropical atmosphere never appreciably exceed the critical temperature gradient for the two-level model (Philips, 1954). He suggested that this is due to the strong feedback between baroclinic eddies and the mean state. His suggestion was supported by the later observational study of Stone and Miller (1980), in which they found a strong negative correlation between the meridional eddy sensible heat flux and the mean temperature gradient in the extratropics.

The effect of eddies on modifying the vertical thermal structure of the mean flow was investigated by Gutowski (1985). Based on the neutral state derived from the Charney-Stern theorem (Charney and Stern, 1962), Gutowski suggested another way for baroclinic eddies to equilibrate. In the continuous model, the zonal mean meridional PV gradient is defined as

$$\frac{\partial [q]}{\partial y} = \beta - \frac{\partial^2 [u]}{\partial y^2} - \frac{1}{\rho}\frac{\partial}{\partial z}(\rho \frac{f_o^2}{N^2}\frac{\partial [u]}{\partial z}) - \frac{f_o^2}{N^2}\frac{\partial [u]}{\partial z}\delta(z - z_b), \tag{1.1}$$

where the detailed definition of each variable can be found in Chapter 2 and z_b is the level

of the boundary. Gutowski found that with fixed vertical wind shear, the negative surface PV gradient can also be eliminated by increasing the lower level static stability. In his later study on the eddy life cycle (Gutowski et al., 1989), he found that baroclinic eddies adjust the mean flow by both reducing the meridional temperature gradient and increasing the mean flow static stability.

The idea of PV mixing appears in the study of Lindzen and Farrell (1980), in which they calculated the height to which the surface delta function PV gradient has to be smoothed to eliminate the negative PV gradient. Then they estimated the heat flux as well as the temperature gradient needed to achieve this. The adjusted state with homogenized PV was proposed by Lindzen (1993). He noted that, like the Eady problem, the observed interior PV gradient is much smaller than the PV gradients at the surface and the tropopause. Combined with the fact that short waves are stable in the Eady model, he suggested that eddies can equilibrate by transmitting the surface PV upward, mixing the interior PV gradient and raising the tropopause. As a result, the adjusted mean state is stable for the longest wave in the real atmosphere. He also argued that the scale of the longest waves is constrained by the width of the jet.

As mentioned above, since the concept of baroclinic adjustment was proposed, there are studies that suggest different scenarios on how the baroclinic eddies can 'neutralize' the mean flow. Stone and Nemet (1996) compared the theories of Stone (1978), Gutowski (1985) and Lindzen (1993) with observations (comparison between the isentropic slopes) and found that these baroclinic adjustment theories work well only around the level of 400-800 hpa in midlatitudes, but is less consistent with observations in the boundary layer. A similar comparison was also made by Kirk-Davidoff and Lindzen (2000), who calculated the Ertel's PV gradient. They found that the structure of the PV gradient varies little in the extratropical region through all the seasons, but the zero PV gradient appears only around a narrow level, 600-800 hpa, which challenges the assumption that PV can be efficiently mixed during the eddy equilibration. A numerical study with a two-layer model by Stone and Branscome (1992) confirmed a preferred equilibrium state when the forcing is varied, but

the equilibrium state is supercritical compared with linear instability theories. The authors suggested a weaker form of the baroclinic adjustment, in which the equilibrium state is proportional to the critical shear.

There is no clear interpretation of why these theories fail to work near the boundary layer and what determines the extent of supercriticality of the equilibrium state. One factor that can cause this disagreement is the boundary layer dissipation as suggested in Gutowski (1985), Branscome et al. (1989) and Zurita-Gotor and Lindzen (2007). In this thesis, we study which boundary layer processes are most responsible for the incomplete adjustment near the surface, and to what extent they can influence the eddy equilibration.

In addition to the boundary layer processes, there are two other factors that may also challenge the application of the baroclinic adjustment theories to interpreting the midlatitude climate. One is the role of the nonlinear interaction in the eddy equilibration. As discussed above, the baroclinic adjustment theories are all based on the linear instability theory. The real atmosphere, however, is nonlinear in essence. How the nonlinear dynamics can modify the linear instability theory becomes an important question to evaluate the validity of the baroclinic adjustment.

A nonlinear baroclinic adjustment scenario was proposed by Cehelsky and Tung (1991), in which the difference between the 'linearly most unstable wave' and the 'most efficient heat transporting wave' was emphasized. The authors proposed that the adjustment process is still quasi-linear as suggested by Stone (1978), however, when under high enough external forcing, it is the interaction between the mean flow and the 'efficient wave', instead of the 'linearly most unstable wave', that determines the equilibrated state. The saturation of the most unstable wave and the dominance of the larger scale waves are the results of nonlinear dynamics. Welch and Tung (1998a,b) using a two layer QG model further studied these nonlinear dynamics and investigated the nonlinear dominant-wave selection mechanism. The threshold of the eddy heat transport at each wave scale and an equilibrium spectrum of the transient waves in this scenario were discussed .

The study of Schneider and Walker (2006) provides an explanation for the quasi-linear

or the weakly nonlinear behavior of the baroclinic eddies. Using an idealized GCM, the authors show that baroclinic eddies by reducing the surface temperature and stabilizing the thermal stratification can maintain a dynamic constraint similar to that of Stone (1978), so that the scale of the energy-dominant eddies is not far from the most unstable waves and the nonlinear wave-wave interactions are suppressed. Both the studies of Cehelsky and Tung (1991) and Schneider and Walker (2006) indicate that, though inspired from the linear baroclinic instability theory, the baroclinic adjustment constraints should play an important role in quantifying the eddy activities in spite of the atmospheric macroturbulence being strongly nonlinear.

Another difficulty in applying the baroclinic adjustment theory to the real atmosphere in the midlatitudes is that the atmospheric flow is not only baroclinic as in Charney (1947) or Eady (1949), but also has a prominent barotropic component, whose meridional structure as well as the eddy momentum flux have a strong influence on both the baroclinic instability and the baroclinic eddy equilibration as shown in many studies. For the linear instability theory, the 'barotropic governor' was proposed by James (1987), which showed that the linear baroclinic instability is suppressed when a barotropic shear of the zonal mean wind is included. The life cycle studies by Simmons and Hoskins (1978, 1980), displayed the importance of the barotropic decay in the later stage of the eddy life cycle. Eddy heat and momentum fluxes can also be modified when the initial zonal flow has a different barotropic component. The baroclinic-barotropic adjustment was further studied by Nakamura (1999). He suggested that, in addition to the destruction of the vertical shear as proposed in the baroclinic adjustment, baroclinic eddies also rearrange the PV structure meridionally, which results in a well-defined barotropic jet that is neutral for all the waves allowed for the geometry of the domain. This mechanism is analogous to that of Lindzen (1993), but instead of mixing the PV vertically and adjusting the height of the tropopause, the author suggested the baroclinic eddies can mix the PV and separate the large PV gradient meridionally. However, this study is based on the two-layer model framework, which as discussed later has a model-dependent short-wave cutoff. How this mechanism works in the real atmosphere

still needs further study.

How the nonlinear interaction process and the barotropic component can modify the baroclinic adjustment may depend on the boundary layer processes as well, especially the surface friction. As suggested by Held (1999) and Thompson and Young (2007), surface friction can stop the inverse energy cascade, which can determine the scale of the energy containing eddies. Surface friction also can directly affect the barotropic component of the zonal winds. As suggested by Robinson (2000), in the equilibrium state, the meridional shear of the lower flow is very sensitive to the surface friction, which can modify the equilibration of the baroclinic eddies. All of these studies suggest the importance of the boundary layer processes and indicate that they can affect the baroclinic eddy equilibration through different mechanisms.

1.2 Review of modeling studies

The tendency of baroclinic eddies to neutralize the mean flow was noted in many life cycle studies (Simmons and Hoskins, 1978; Gutowski et al., 1989; Thorncroft et al., 1993). These studies investigate how initial small perturbations develop into certain finite amplitude eddies, as well as the evolution of the mean flow under eddy-mean flow interaction, which is insightful on our understanding of the baroclinic eddy equilibration. However, the life cycle study is not equivalent to the study of baroclinic equilibration. This is not only because the baroclinic eddies usually take a longer time to equilibrate than a single life cycle, but also because the equilibrated state is directly related to the climate, a state averaged over a long period, and the equilibration study focuses on the maintenance of this state.

Since proposed by Philips (1954), the two-layer quasi-geostrophic (QG) model, as an insightful tool and the simplest model that can capture some essential features of the mid-latitude dynamics, has been widely used to investigate the saturation of baroclinic eddies (Stone and Branscome, 1992; Cehelsky and Tung, 1991; Held and Larichev, 1996; Welch and Tung, 1998a; Zurita-Gotor, 2007, and so on). To what extent can the two-layer model simulate the eddy equilibration? Or equivalently, what is the main limitation of the two-layer

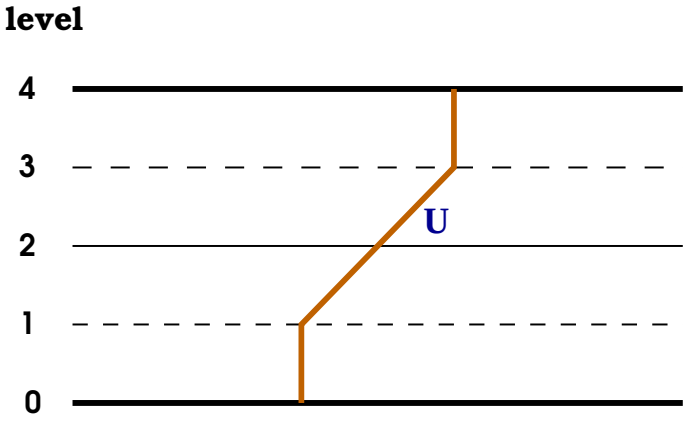

Figure 1-1: Vertical profile of the zonal mean zonal wind in the two-layer model.

model? There are at least two factors that challenge the reality of the two-layer model to the midlatitude atmosphere: one is the coarse vertical resolution and the consequent vertical structure as well as the dynamic feedback it could lose; the other is the limitation for all the traditional QG models, which is the fixed static stability and the consequent omitted feedback between the vertical eddy heat flux and the thermal stratification.

The first limitation of the two-layer model due to the coarse vertical resolution, as discussed in Zurita-Gotor and Lindzen (2007), is the 'artificial' critical shear for the baroclinic instability. Due to the poor vertical resolution, in the two-layer model, the PV gradient defined in Eq.1.1 in pressure coordinates is phrased as

$$\frac{\partial [q_1]}{\partial y} = \beta - \frac{\partial^2 [u_1]}{\partial y^2} - F([u_3] - [u_1]) \tag{1.2}$$

$$\frac{\partial [q_3]}{\partial y} = \beta - \frac{\partial^2 [u_3]}{\partial y^2} + F([u_3] - [u_1]) \tag{1.3}$$

where, as shown in Figure 1-1, subscript 1 indicates variables defined on the lower layer, 3 indicates variables defined on the upper layer, and $F = \frac{f_o^2}{s\Delta p} = \frac{1}{{L_d}^2}$ (see Chapter 2 for the detailed definition), and L_d is the Rossby deformation radius. The δ function negative PV gradient defined in Eq.1.1 is smoothed over the whole lower level, whose equivalent vertical wind shear distribution is shown in Fig.1-1. Then the critical shear derived from the Charney-Stern theorem to maintain a non-negative PV gradient is mainly due to the coarse vertical

resolution, and should not exist in the continuous model. This questions the interpretation of the robust 'critical shear' observed in the real atmosphere. Is it a coincidence or it does indicate some dynamic constraints, i.e. baroclinic adjustment? More specially, what is the relation and difference between the two layer model and the continuous model as well as the real midlatitude atmosphere? There are still no clear answers to these questions.

The limitations of the coarse vertical resolution were further discussed in Held and O'Brien (1992), Pavan (1996), and Solomon and Lindzen (2000). Held and O'Brien (1992) using a three layer QG model showed that, when a Newtonian Cooling form diabatic forcing is applied to the flow, the eddy activity depends on the vertical distribution of the radiative-equilibrium (RE) state meridional temperature gradients. Eddy PV flux is more sensitive to the lower troposphere RE state meridional temperature gradient than the upper troposphere. Pavan (1996) using a multi-layer QG model confirmed the result of Held and O'Brien (1992) and interpreted it as a consequence of the importance of shallow eddies. He further showed that to better simulate the eddy dynamics, it is necessary to use a sufficiently high resolution. A vertical resolution between 10 to 20 layers was suggested. Solomon and Lindzen (2000) studied the impact of the resolution on the numerical simulation of the barotropic point jet. Due to the similarity between the barotropic and baroclinic instability, their results suggest that neither the linear growth rate nor the equilibrium state eddy fluxes can be adequately resolved under coarse resolution. Observed midlatitude eddy activities also demonstrate obvious vertical structure of baroclinic eddies: eddy kinetic energy and eddy momentum flux all have peaks near the tropopause; eddy sensible heat flux has a first peak around 850 hpa and a secondary peak in the upper troposphere. All of these facts indicate the low vertical revolution of the two-layer model is problematic in simulating the baroclinic eddies appropriately.

Another problem in the classic QG model lies in the assumption of fixed static stability. The relation between static stability and eddy activities has been investigated in many studies. In the study of Stone (1972), a simplified radiative-dynamical model was proposed to study the static stability in a rotating atmosphere, in which the role of the vertical eddy heat

flux in determining the thermal stratification was emphasized. Lindzen and Farrell (1980) found that for the midlatitude atmosphere with larger static stability, i.e. over ice-covered land, eddy heat transport can be largely suppressed and, subsequently, the elimination of meridional temperature gradients is inhibited. Gutowski (1985) also advanced the idea that the adjustment of static stability by the vertical eddy heat flux is an important process during the eddy equilibration. This effect has recently been studied by Schneider (2004) with an ideal GCM with a radiative forcing acting to relax the temperature towards a radiative equilibrium state. Although the temperature profile in radiative equilibrium is statically unstable in the extratropics, Schneider found like Stone (1972) that baroclinic eddies can transport heat upward efficiently enough to maintain a statically stable troposphere at midlatitudes. Those studies reveal the importance of the feedback between eddy vertical heat flux and the static stability. Without this process, we cannot simulate the eddy equilibration reasonably.

The effect of the boundary layer on the eddy equilibration is another component that is not treated carefully in the conventional modeling studies. As will be discussed in the next section, previous studies suggested that both the boundary layer momentum dissipation (i.e. surface friction and the boundary layer vertical momentum dissipation) and the boundary layer thermal damping (i.e. surface heat exchange and the boundary layer vertical thermal diffusion) could influence the eddy equilibration. Especially the effects of the surface heat flux and the boundary layer vertical thermal diffusion have been traditionally neglected in formal studies on baroclinic eddies, in which an Ekman boundary layer is used and only the momentum dissipation is considered. The boundary layer may have a more important influence on the eddy activity given the fact that the critical layer, which plays an important role in baroclinic instability, also lies in the boundary layer or at the top of the boundary layer (Randel and Held, 1991). Studies (Lindzen et al., 1980; Boyd, 1983; Lindzen and Barker, 1985; Lindzen, 1988) have shown that baroclinic instability, in some sense, can be understood as a critical layer behavior. It is near the critical layer that eddy heat and PV fluxes are strongest with the strongest wave-mean flow interaction. It is also near the critical

layer that PV is supposed to be homogenized and the meridional temperature gradient is reduced most from the gradient in radiative equilibrium. The fact that this critical layer lies in the boundary layer indicates the influence of the boundary layer cannot be simply neglected.

To summarize this section, the previous numerical studies on the baroclinic eddy equilibration suggest that to better simulate the eddy dynamics, an atmospheric model with interactive stratification, relatively high vertical resolution and better boundary layer physics is needed.

1.3 Motivation

1.3.1 Boundary layer processes

It is known from observational studies that the planetary boundary layer is characterized by turbulent momentum and heat transports, and strong surface friction as well as heat exchange with the underlying surface. However, with the existence of large scale baroclinic eddies in the extratropics, it is still an open question as to what determines the boundary layer thermal structure and how these boundary layer processes influence the eddy equilibration.

As discussed in the review section, although several theories have been proposed to understand the role of baroclinic eddies in atmospheric circulation, these theories either fail to work in the boundary layer or simply neglect the influence of boundary layer processes. The baroclinic adjustment theory works only in the free troposphere and fails to work near the lower boundary in the extratropics. The observed strong meridional temperature gradients near the surface challenge the validity of this theory. Under the assumption that eddies mix potential vorticity and surface temperature diffusively and that the horizontal eddy diffusivity is essentially vertically uniform, Schneider (2004) obtained a relation between surface temperature gradient and the thermal stratification in the extratropics. However, as Schneider mentions in his paper, this relation is derived from an idealized model in which the

boundary layer processes, especially the vertical thermal diffusion and surface heat exchange, are not considered. The influence of boundary layer processes on his result is neglected.

Stone and Nemet (1996), and Zurita-Gotor and Lindzen (2007) attribute the lack of surface thermal homogenization to boundary layer processes. However, the mechanism by which the boundary layer limits the baroclinic adjustment is still not clear. Swanson and Pierrehumbert (1997), through an observational study of the lower troposphere heat flux, find that surface heat flux and vertical thermal diffusion in the boundary layer damp temperature fluctuations in very short time scales, and suggest that these boundary layer processes may prevent the surface temperature mixing by baroclinic eddies. Zurita and Lindzen (2001) noted that in the Charney model, the PV homogenization at the steering level is a necessary condition for neutralizing the flow (Bretherton, 1966). Given the fact that the baroclinic instability can be understood as the critical layer instability (Lindzen et al., 1980; Boyd, 1983; Lindzen and Barker, 1985; Pedlosky, 1987), instead of homogenizing the PV gradient through the whole free troposphere, the authors proposed that, short Charney waves can equilibrate by homogenizing the PV gradient only around the steering level. Thus, Zurita-Gotor and Lindzen (2004) suggest a mechanism for short Charney waves through which surface friction can limit their homogenization of the surface temperature gradient. They propose that surface friction, by reducing surface westerlies, can stop the critical level dropping to the surface and the temperature gradient near the surface cannot be efficiently mixed. James (1987) and James and Gray (1986) imply another possible mechanism by which surface friction influences the boundary layer PV structure. They found that under weak surface friction, the strong barotropic shear of the zonal mean flow can reduce the growth rate of baroclinic eddies and suppress the eddy activity. This 'barotropic governor' effect, as indicated in Robinson (1997) and Chen et al. (2007), may also play an important role during eddy equilibration. When including all these boundary layer processes, how these mechanisms work together to influence the lower troposphere thermal structure and which is the dominant mechanism that causes the failure of baroclinic adjustment theory in the boundary layer are the questions that we try to answer in this study.

In this study, we also discuss the equilibrium response of eddy activity to different boundary layer processes. For each individual boundary layer process, regardless of the change of the underlying surface, there exist at least two different ways that they can influence the eddy behavior. First, in terms of the eddy energy budget, the direct effect of boundary layer processes is a damping of eddy energies (Peixoto and Oort, 1992). This is consistent with some studies on linear baroclinic instability and eddy life cycle. Card and Barcilon (1982) and Valdes and Hoskins (1988), by including the effects of surface friction as modeled by an Ekman layer, showed that the boundary layer leads to a reduction in instability. The eddy life cycle study of Branscome et al. (1989), comparing the maximum eddy heat flux reached during the life cycle in viscous and inviscid cases, also illustrated that the boundary layer acts as a damping for the eddy fluxes. On the other hand, during eddy equilibration, boundary layer processes also influence the mean flow thermal structure and modify the mean flow available potential energy (hereafter MPE), which can further affect the eddy energy and eddy heat fluxes. For each boundary layer process, how these two effects compete is another focus of this study.

When taking into account the influence of the boundary layer processes on the surface temperature, the role of the boundary layer processes in the eddy equilibration in the air-sea coupled system is more complicated, because the surface temperature can strongly influence the lower level baroclinicity which can further act on the baroclinic eddy activity. Thus, in this thesis, we start our study on the role of the boundary layer processes from a simpler case, in which the underlying surface temperature is fixed during the eddy equilibration. Then we continue our study in an air-sea thermally coupled model, in which the underlying surface temperature can be modified during the eddy equilibration.

1.3.2 Seasonal forcing

Though the concept of baroclinic adjustment was partly inspired by the observed extratropical robust isentropic slope and PV structure through all the seasons, baroclinic eddy equilibration under seasonal forcing is barely studied. As summarized in the previous section,

although many equilibrium studies have been done to investigate the baroclinic adjustment, in these studies the external forcing is always specified and kept fixed during the eddy equilibration. How can these results be applied to interpret the observed midlatitude climate? The answer is based on the validity of one commonly used assumption on the baroclinic eddy equilibration time scale (baroclinic adjustment time scale), in which the mean flow adjustment by the baroclinic eddies is always assumed much faster than the variation of the external forcing. If this assumption is appropriate, the conclusions from the equilibrium studies can be used to interpret and predict the midlatitude climate by assuming that in spite of the variation of the external forcing, the baroclinic eddies can always quickly respond to the variation and adjust the mean flow to an equilibrium state. This time scale assumption is a precondition that the baroclinic adjustment theories work well in the real atmosphere.

However, an estimate of the baroclinic adjustment time scale is not easy, and the time scale separation between the dynamics and the forcing is not clear in midlatitudes. If the eddy growth rate predicted by the baroclinic instability is relevant to estimate the adjustment time scale, baroclinic eddies have a life cycle time scale of a few days, which is also the life cycle time scale of synoptic eddies in midlatitudes. However, the eddy-mean flow interaction usually takes a longer time. Many numerical studies also suggest that the equilibration of the baroclinic eddies is much longer than a single life cycle, and can be as long as one hundred days (Solomon and Stone, 2001a; Chen et al., 2007). In addition, the boundary layer forcing, as suggested by Swanson and Pierrehumbert (1997), acts on the surface air in less than one day, which is a faster process than the baroclinic eddies. Above the boundary layer, the radiative forcing time scale, which is around tens of days, is slower than the baroclinic eddies, but the moist convection and release of latent heating can be a fast process, if considering them also playing an important role in midlatitudes (Emanuel, 1988; Gutowski et al., 1992; Juckes, 2000; Korty and Schneider, 2007). The time scale of the baroclinic adjustment was explicitly addressed by Barry et al. (2000). In the spindown experiment using a general circulation model, by turning off the radiation and other physical processes, a 15-20 days adjustment time scale for the temperature and a roughly 30 days adjustment time scale

for the stratification were suggested, which is comparable with the radiative time scale and questions the validity of the baroclinic adjustment.

In this study, we want to test the quick baroclinic eddy adjustment assumption by studying the baroclinic eddy equilibration under a time varying external forcing and the example of the time varying forcing we choose is the Northern Hemisphere-like seasonal forcing. We hope our study can help understand to what extent the quick adjustment time scale can be a good assumption when applied to the real atmosphere and to what extent the baroclinic adjustment theory can be applied to interpret the robust thermal structure in the Northern Hemisphere midlatitude.

1.4 Outline

In Chapter 2, the models used in this study are introduced. As discussed in the previous review sections, to study the role of the boundary layer processes and the seasonal forcing, a β-plane quasi-geostrophic channel model with higher vertical resolution, interactive static stability and carefully treated boundary layer is used as the atmospheric model in this study. In addition, a slab surface model is also coupled with the atmospheric model in some experiments to provide an interactive underlying surface temperature.

The role of the interactive stratification is investigated in Chapter 3 by comparing the baroclinic eddy equilibration in the traditional and our modified (with interactive stratification) multi-layer QG models. We will show that when varying the radiative-convective equilibrium state (RCE) baroclinicity, the robustness of the isentropic slope can be obtained only when the stratification is allowed to be modified by the eddy vertical heat flux. Some closure theories are also compared between the two models.

In Chapter 4, groups of sensitivity studies are carried out using the atmospheric model with fixed underlying surface temperature, in which the different roles of each boundary layer process in the baroclinic eddy equilibration are studied. The mechanisms through which each boundary layer process can prevent the PV homogenization and modify the baroclinic adjustment theory near the boundary layer are discussed. The content of this

chapter appears in Zhang et al. (2009).

In Chapter 5, the parameters used in the surface model are specified. The spin-up runs with the atmosphere-surface coupled model are investigated, from which we will show how including the baroclinic eddies can enhance the sensible heat exchange between the surface and the atmosphere, and how this modifies the meridional temperature gradient in the equilibrium state.

In Chapter 6, the experiments in Ch.4 are carried out but with the coupled model. We will show how the different boundary layer processes can influence the underlying surface energy budget and surface temperature differently. With the interactive surface temperature, compared with the experiments in Ch.4, we will show how they can further affect the eddy activity, damp the PV homogenization and modify the thermal structure of the coupled system through more complicated mechanisms.

Eddy equilibration under seasonal forcing are studied in Chapters 7 and 8. In Ch.7 only the atmospheric model is used. A Northern Hemispheric-like seasonal variation of the underlying surface and the diabatic forcing are specified. Different mechanisms that can act to maintain the robust PV structure and the factors that determine the eddy spin-up, spin-down times scale during their seasonal behavior are discussed. In Ch.8, instead of the surface temperature, the seasonal variation of the solar radiation into the surface is specified. The eddy seasonal behavior in the coupled model is further discussed in this chapter.

A summary and discussion of this thesis work is presented in Chapter 9.

Chapter 2

Model Description

2.1 Introduction

The atmospheric model used in this study is a modified β plane multilevel quasi-geostrophic model with an interactive stratification and a simplified parameterization of atmospheric boundary layer physics, similar to that of Solomon (1997b) and Solomon and Stone (2001a,b). In this model, the potential vorticity equation with diabatic heating and boundary layer dissipation is integrated. All variables are defined in the grid point space. A rigid lid is added at the top as the boundary condition.

The model has a channel length of 21040 km which is comparable with the length of the mid-latitudinal belt, and a channel width of 10000 km. The model has variable horizontal and vertical resolution. In this study, the horizontal resolution of the model is 330 km in both zonal and meridional directions. There are 17 equally spaced pressure levels in the model. As shown by Solomon (1997b) and Solomon and Stone (2001a), such horizontal and vertical resolution is appropriate to simulate the model dynamics. An FFT filter is used on the stream function in this model to remove the smallest scale eddies.

In this study, a slab surface model is used in some chapters to couple with the atmospheric model to provide an interactive surface temperature distribution. The slab surface model has a fixed depth and only allows the heat exchanges with the atmosphere (i.e. surface sensible

and latent heat fluxes, radiative flux) to influence the underlying surface temperature directly. Since in this study, we primarily use the surface model to investigate whether the heat capacity of the underlying surface is big enough to maintain a strong surface temperature gradient in the presence of strong synoptic eddy mixing, as mentioned in Chapter 1, the dynamic heat transport in the surface (i.e. the ocean meridional heat transport) is simply represented in the model by a pre-specified Q-flux, which is not allowed to vary with time. Since this study focuses on mid-latitudes dynamics, sea ice is not included in the model, though snow and ice have a strong influence on the albedo, static stability and poleward heat transport in high latitudes.

In Chapters 3, 4 and 7, the atmospheric model with fixed underlying surface temperature as the lower boundary condition is used. Experiments in Chapters 5, 6 and 8 are carried out with the coupled model.

2.2 Atmosphere

Governing equations

In this model, the potential vorticity equation, including diabatic heating and boundary layer dissipation, is integrated:

$$\frac{\partial PV}{\partial t} = -J(\psi, PV) - f_o \frac{\partial}{\partial p} \frac{QR}{spC_p} + \mathbf{k} \cdot \nabla \times \mathbf{F}, \tag{2.1}$$

where $R = 287\ J\ kg^{-1}\ K^{-1}$ is the ideal gas constant, $C_p = 1004\ J\ kg^{-1}\ K^{-1}$ is the specific heat of the air, and ψ is the geostrophic stream-function. The static stability parameter

$$s = -\frac{1}{\pi} \frac{\partial \bar{\theta}^{xy}}{\partial p},$$

where $^{-xy}$ means averaged horizontally, $\pi = \frac{p}{R}(\frac{p_o}{p})^{R/C_p}$, and p_o is the surface pressure. $\mathbf{F}$ denotes the frictional dissipation and the heating term Q has two contributors: radiative-convective heating Q_r and the thermal diffusion in the boundary layer Q_d.

The potential vorticity is

$$PV = \nabla^2\psi + \beta y + \frac{\partial}{\partial p}\frac{f_o^2}{s}\frac{\partial \psi}{\partial p}, \tag{2.2}$$

where the Coriolis parameter at the center of the channel is $f_o = 1.03 \times 10^{-4}\ s^{-1}$, and the variation of the Coriolis parameter with latitude is $\beta = 1.76 \times 10^{-11}\ m^{-1}s^{-1}$. These are the values at letitude 45^oN. Under the QG assumption, $\theta^\dagger = -\pi f_o \frac{\partial \psi}{\partial p}$, where $\theta^\dagger = \theta - \overline{\theta}^{xy}$ indicates the deviation from the horizontal mean. Thus, Eq.2.1 only predicts the time evolution of $\theta^\dagger$, while $\overline{\theta}^{xy}$ is always specified in the traditional QG model.

One important difference between this model and traditional QG models is that the horizontally averaged potential temperature and static stability, instead of being specified, are allowed to evolve with time according to the the equation (Solomon, 1997b; Solomon and Stone, 2001a,b)

$$\frac{\partial}{\partial t}\overline{\theta}^{xy} = -\frac{\partial}{\partial p}\overline{\omega^*\theta^*}^{xy} + \overline{\frac{Q_r + Q_d}{C_p}}^{xy}(\frac{p_o}{p})^{R/C_p}, \tag{2.3}$$

where the superscript * indicates the eddy component of the variable. In our model, the horizontal mean $\overline{\ }^{xy}$ is averaged over baroclinic zone, which, as described latter, is the central half of the channel. It is the region the eddy activity is confined to. This tendency equation is derived from the horizontally averaged thermodynamic equation and is exact except that the heating associated with the vertical heat flux by the zonal mean flow is neglected. As shown by Gutowski (1983), this is a reasonable approximation in mid-latitudes. Thus, in our model, the thermal stratification is maintained by the vertical eddy heat flux and the radiative-convective heating in the free atmosphere and by the vertical eddy heat flux, diabatic heating and thermal diffusion in the boundary layer. As shown by Gutowski (1985), the interaction between the vertical eddy heat flux and the stratification, which is neglected in conventional QG theory, plays a potentially important role in baroclinic adjustment. Since we still use horizontally uniform stratification, adding Equation 2.3 does not break the QG scaling. In addition, in the quasi-equilibrium state (i.e. the experiments in Chapters 3, 4,

5, 6 and the winter season in the experiments in Chapters 7 and 8), where the stratification has tiny variations with time, the model behavior is similar to the traditional QG model with time-invariant stratification, which has been confirmed by Solomon and Stone (2001a) and by Zurita-Gotor and Vallis (2009).

Since the heat exchange between the atmosphere and the surface is considered in the model, a surface air temperature distribution is needed in the surface heat flux estimation and the surface air temperature may be dependent on the vertical resolution. In our atmospheric model, a surface air temperature is calculated at the mid-level between the surface and the first model level. The surface air tendency equation is derived from the QG thermodynamic equation, which is

$$\frac{\partial \theta^{\dagger}}{\partial t} = -J(\psi, \theta^{\dagger}) - \omega \frac{\partial \overline{\theta}^{xy}}{\partial p} + \frac{Q}{C_p}(\frac{p_o}{p})^{R/C_p}.$$

If we assume that the vertical velocity near the surface is zero, the surface air temperature equation becomes,

$$\frac{\partial T^{\dagger}_{air}}{\partial t} = -J(\psi_{1/2}, T^{\dagger}_{air}) + \frac{Q}{C_p},$$

where $\psi_{1/2} = (\psi_o + \psi_1)/2$, and diabatic heating Q is also estimated at the mid-level between the surface and the first model level.

Radiative-convective heating

Radiative-convective heating in this model is parameterized by the Newtonian cooling form:

$$Q_r = C_p \frac{T_e - T}{\tau_r}, \tag{2.4}$$

where T_e is the atmospheric temperature in radiative-convective equilibrium (RCE) state corresponding to the surface temperature, and $\tau_r = 40$ days, is the relaxation time scale.

In the atmospheric run experiments (Chapters 3, 4, 7), in which the surface temperature is specified at the lower boundary, the meridional variation of the potential temperature of the RCE state in the troposphere is set so that over the central half of the channel, for

$1/4L \leq y \leq 3/4L$,

$$\theta_e{}^{\dagger}(y,p) = -\frac{\Delta_e}{2}\sin\left[\frac{\pi(y-L/2)}{L/2}\right], \tag{2.5}$$

where $\theta_e{}^{\dagger} = \theta_e - \overline{\theta_e}^{xy}$, Δ_e is the temperature difference across the channel, L = 10000 km is the width of the channel, and there is no RCE meridional temperature gradient in the regions $0 \leq y \leq 1/4L$ and $3/4L \leq y \leq L$. In the equilibrium studies with the atmospheric model, the temperature difference over the channel Δ_e is 43K as default (i.e. the standard run in Chs.3 and 4), which approximates the mid-latitude temperature contrast in winter in the Northern Hemisphere. In the stratosphere, the potential temperature gradient of the RCE state is one tenth of that in the troposphere and of opposite sign. The global averaged surface temperature in the model is set to be $280K$. In the atmosphere - surface coupled runs (Chs.5, 6 and 8), the meridional distribution of the potential temperature of the RCE state in the troposphere is set to match the surface temperature T_g by assuming that $\theta_e{}^{\dagger}(y,p) = T_g^{\dagger}(y)$. In the stratosphere, the potential temperature gradient of the RCE state is also one tenth of that in the troposphere and of the opposite sign.

Except in Ch.7, the lapse rate (- $d\overline{T_e}^{xy}/dz$) of the RCE state is chosen to be $7K/km$ in the troposphere and zero in the stratosphere. In Ch.7, to better understand the role of the stratification in eddy equilibration, we carry out experiments with different lapse rates of the RCE state, which will be further described in Ch.7.

Thermal diffusion in the boundary layer

The surface heat exchange between the atmosphere and the surface is represented by the linearized bulk aerodynamic drag formula:

$$F_{sh} = -C_{dt}C_p\rho_s(\theta_{air} - \theta_g), \tag{2.6}$$

where $C_{dt} = C_{surface}|\mathbf{v_s}|$ is the drag coefficient. In this study, C_{dt} is chosen to be constant, and $0.03m/s$ is taken as its standard value. In Chapters 3, 4 and 7, the surface potential

temperature θ_g is kept fixed, which is the RCE state surface potential temperature. We assume that the first model layer is well mixed so that the surface air potential temperature θ_{air} is equal to the potential temperature at the first level which is 32 hpa above the surface.

Above the surface, the vertical turbulent heat flux in the boundary layer is parameterized in the diffusive form:

$$F_{sh} = \nu_S(p) C_p \rho^2 g \frac{\partial \theta}{\partial p}. \tag{2.7}$$

The vertical distribution of the diffusion coefficient ν_s is

$$\nu_S(p) = \mu_s (\frac{p - p_{bl}}{p_o - p_{bl}})^3 m^2/s, \tag{2.8}$$

for $p \geq p_{bl}$, and $\nu_S(p) = 0$, for $p \leq p_{bl}$, where p_{bl} can be considered as the pressure at the top of the boundary layer and $5m^2/s$ is taken to be the standard value for μ_s. In Ch.4, sensitivity studies are carried out with $p_{bl} = 0$ hpa. Actually, due to the cubic dependence on the pressure, ν_S deceases quickly with the pressure. In Section 4.3, we will show how the setting of p_{bl} can modify the model results. In Ch 3 and Chs.5 to 8, $p_{bl} = 850$ hpa is used in the experiments. As suggested in Stull (1988), many observations show that the turbulent heat and momentum fluxes in the boundary layer are most active below 850 hpa. Heating by thermal diffusion is calculated from the heat flux:

$$Q_d = g (\frac{p}{p_o})^{R/C_p} \frac{\partial F_{sh}}{\partial p}. \tag{2.9}$$

Here we want to point out that because of the vertical turbulent heat transport, the stratification in the boundary layer can be weak. However, this merely means that the vertical temperature advection by the flow is small and the horizontal temperature advection in this case is dominant. Thus, the QG scaling still holds.

Frictional dissipation in the boundary layer

The parameterization of friction is analogous to that for thermal diffusion, $\mathbf{F} = g \frac{\partial \tau_{\mathbf{m}}}{\partial p}$, where $\tau_{\mathbf{m}}$ is the shear stress and is parameterized by a linearized bulk aerodynamic drag at the

surface and vertical diffusion in the boundary layer:

$$\tau_{\mathbf{m}} = -C_{df}\rho_s\mathbf{v} \qquad (surface) \tag{2.10}$$

$$\tau_{\mathbf{m}} = \nu_M(p)\rho^2 g\frac{\partial \mathbf{v}}{\partial p} \qquad (B.L.) \tag{2.11}$$

where $\mathbf{v} = (-\psi_y, \psi_x) = (u_g, v_g)$, and

$$\nu_M(p) = \mu_m(\frac{p - p_{bl}}{p_o - p_{bl}})^3 m^2/s. \tag{2.12}$$

In the standard run, $\mu_m = 5m^2/s$ and C_{df} is still chosen to be $0.03m/s$. In most experiments in this study, only the shear stress by the geostrophic component is considered. We will discuss the influence of the ageostrophic winds in the boundary layer in Sections 4.4 and 6.3.3.

Ageostrophic wind in the boundary layer

In Sections 4.4 and 6.3.3, the effect of ageostrophic winds in the boundary layer is studied. The ageostrophic wind in the model can be estimated from the Ekman momentum approximation by solving the equation :

$$f\mathbf{v_a} = \mathbf{F} = g\frac{\partial \tau_{\mathbf{m}}}{\partial p},$$

where $\tau_{\mathbf{m}}$ is defined in Equation 2.11, except that $\mathbf{v} = \mathbf{v_g} + \mathbf{v_a}$. The frictional dissipation caused by the ageostrophic winds is now included. By solving the differential equation with the boundary condition that at the first level,

$$\nu_M(p)\rho^2 g\frac{\partial(\mathbf{v}_g + \mathbf{v}_a)}{\partial p} = -C_{df}\rho_s(\mathbf{v}_g + \mathbf{v}_a),$$

the ageostrophic winds in the boundary layer can be evaluated.

2.3 Underlying surface

Governing equation

The tendency of the underlying surface temperature, T_g, is calculated from the energy budget equation of the surface layer:

$$\rho_g C_{pg} H_{sur} \frac{\partial T_g}{\partial t} = F_{sur} + Q_{fx}, \tag{2.13}$$

where ρ_g is the density of the surface materials, i.e., soil density or sea water density, and is constant in the model; C_{pg} is its specific heat; H_{sur} is the depth of the surface layer; F_{sur} is the heat flux across the air- surface interface (define the flux from the atmosphere into the surface as positive), Q_{fx} represents the effect of the convergence of the horizontal heat transport and the possible heat flow into the surface layer from deeper layers. In this study, we assume the underlying surface in the standard coupled run is an ocean surface, and $\rho_g C_{pg} \sim 4 \times 10^6\ Jm^{-3}K^{-1}$. Even though the depth of the ocean mixed layer has large spatial and seasonal variation (Levitus, 1994), for simplicity we assume H_{sur} a constant in the model. In the transient response experiments in Section 6.1.2 and 6.3.2, we use a shallower surface layer with $H_{sur} = 5$ m as the default value. In midlatitudes, ocean mixed layer is typically 100 m in the winter and 20 m in the summer. However, we find that even with a shallow ocean mixed layer, the surface response time scale, which is around hundreds of days, is already much longer than the atmospheric response time scales and the mechanism through which the coupled system reaches the equilibrium is the same. To save the computation time, a shallower surface depth is used.

F_{sur} has three components: radiative flux into the surface F_{rad}, sensible heat flux from the surface to the atmosphere F_{sh}, which has the same definition as in Equation 2.6, and latent heat flux from the surface to the atmosphere F_{lh},

$$F_{sur} = F_{rad} - F_{sh} - F_{lh}. \tag{2.14}$$

Our atmospheric model is a dry dynamic model, which does not simulate any moist physics, and the net thermal forcing of radiative and latent heat fluxes is parameterized in a Newtonian cooling form. However, these two forcings are important terms in the surface energy budget. They are estimated explicitly in the surface model.

Latent heat flux

The latent heat flux is estimated using the linear bulk aerodynamic formula:

$$F_{lh} = C_{dl}\rho_s L(q_g - q_{air}), \tag{2.15}$$

where L is the latent heat of evaporation; $C_{dl} = C_{lh}|\mathbf{v_s}|$ is the drag coefficient of latent heat flux, which is chosen to be constant and proportional to the drag coefficient of sensible heat, C_{dt}, in this model. We assume that the mixing ratio of water vapor at the surface q_g is equal to the saturation mixing ratio, q_g^*, at the temperature of the surface. The actual water vapor mixing ratio of the surface air, q_{air}, is expressed in terms of the relative humidity RH. Thus, $q_{air} = RH * q_{air}^*$. In this model, we assume that $RH = 0.8$.

Radiative flux

The net radiative flux F_{rad} has two components: net solar radiation SW and net longwave radiation LW. In our model, SW is specified. In Chapters 5 and 8, the setting of SW in these experiments will be further discussed.

The net longwave radiation $LW = F_{lw}^{\downarrow} - F_{lw}^{\uparrow}$. The upward longwave radiation from the surface into the atmosphere $F_{lw}^{\uparrow} = \epsilon_g \sigma {T_g}^4$, where $\epsilon_g = 0.95$ is the emissivities of the surface, σ is the Stefan-Boltzmann constant. The downward longwave radiation into the surface, $F_{lw}^{\downarrow}$, is estimated from the simplified radiative transfer equation. In a grey atmosphere, the radiative transfer equation is simplified as

$$\mu \frac{dI(\mu,\tau)}{d\tau} = I(\mu,\tau) - B(\tau), \tag{2.16}$$

where $\mu = \cos\Theta$, Θ is the zenith angle, τ is the optical depth, I is the intensity of radiation and $B(\tau) = \sigma T(\tau)^4/\pi$ is the black body function. The optical depth is specified as a function of pressure and in the model only the two most important absorbing gases, water vapor and CO_2 are considered:

$$\tau = \tau_{h_2o}(\frac{p}{p_o})^\alpha + \tau_{co_2}(\frac{p}{p_o}). \tag{2.17}$$

The fist term approximates the structure of water vapor in the atmosphere, and $\alpha = H_p/H_a \approx 7km/2km = 3.5$, where H_a is the scale height of the water vapor and H_p is the scale height of pressure. τ_{h_2o} is specified linearly proportional to the water vapor mixing ratio of the surface air, q_{air}. The second term approximates the contribution from CO2 and we set τ_{co_2} constant in this model.

When $\mu < 0$, $I = I^\downarrow$, is the downward radiative intensity. At the top of the atmosphere where $\tau = 0$, $I^\downarrow = 0$. Using this boundary condition, we have

$$I^\downarrow(\mu, \tau) = -\frac{1}{\mu}\int_0^\tau e^{\frac{\tau'-\tau}{\mu}} B(\tau')d\tau'. \tag{2.18}$$

Then the downward long-wave radiative flux

$$F^\downarrow_{lw}(\tau) = 2\pi\int_{-1}^0 d\mu \int_0^\tau -B(\tau')e^{\frac{\tau'-\tau}{\mu}}d\tau'. \tag{2.19}$$

This equation can be simplified mathematically by the 2-point Gaussian quadrature, where the optimal abscissas chosen from $-1 \le \mu \le 0$ are $\mu_1 = \frac{\sqrt{1/3}-1}{2}$ and $\mu_2 = \frac{-\sqrt{1/3}-1}{2}$. Thus, the simplified downward long-wave radiative flux at the surface, where $\tau = \tau_g = \tau_{h_2o} + \tau co_2$, is

$$F^\downarrow_{lw}(\tau_g) = \int_0^{\tau_g} -\sigma T^4(\tau')(e^{\frac{\tau'-\tau_g}{\mu_1}} + e^{\frac{\tau'-\tau_g}{\mu_2}})d\tau'. \tag{2.20}$$

In our calibration run experiment in Ch.5, we will discuss how the values of the parameters related to the radiative flux are specified and how these parameters can affect the results.

Q-flux

In order to obtain a surface temperature distribution similar to the current climate, a Q-flux is included in the surface model. For the ocean surface, the Q-flux represents the effect of the meridional ocean heat transport and the heat exchange between the mixed layer and the deep ocean. The Q-flux can be pre-calculated from the surface layer energy budget using climatological surface temperatures, an algorithm suggested by Hansen et al. (1983); Russell et al. (1985); Hansen et al. (1988). With the climatological surface temperature as the lower boundary condition, the atmospheric model is integrated until it reaches an equilibrium state. With the equilibrium state atmospheric temperature, from Eqs.2.13 to 2.20, the Q-flux is estimated. More details in the calculation of the Q-flux will be discussed in Ch.5.

Chapter 3

The role of the interactive stratification

Large scale eddies were considered to play an important role in the extratropical thermal stratification as early as in the study of Stone (1972), in which a simplified radiative-dynamical model was proposed to study the static stability in a rotating atmosphere. In the simplified model, given the radiative forcing (i.e. specifying the radiative equilibrium state), and using the linear baroclinic instability theory with a closure assumption for the eddy amplitude, the domain averaged meridional temperature gradient and thermal stratification can be estimated. When applied to Earth, the model predicted the thermal stratification in a realistic regime but only half of the observed value in the real Earth's atmosphere. The author attributed this to the absence of other physical processes, i.e. convection and the hydrological cycle.

The effect of the vertical eddy heat flux on the midlatitude thermal stratification and the subsequent effect in the baroclinic eddy equilibration was studied further by Gutowski (1983, 1985). Gutowski (1983) suggested that baroclinic eddies are the dominant process that determines the midlatitude stratification, and as discussed in Chapter 1, Gutowski (1985) suggested that baroclinic eddies can act to 'neutralize' the mean flow by stabilizing the lower flow stratification.

Even though there are many studies that suggest the importance of the baroclinic eddies as mentioned in Ch.1, the maintenance of the midlatitude thermal stratification and the dynamic constraints on the extratropical tropopause are still not well understood. One of the major reasons is that our previous understanding of midlatitude dynamics is mainly based on the quasi-geostrophic framework and many numerical studies were carried out with the traditional QG model, in which the stratification is an external parameter and not able to interact with the eddy dynamics.

Schneider (2004), instead of using the QG framework but starting from the momentum balance requirement and assuming a vertically uniform eddy diffusivity, developed another dynamic constraint for the height of the extratropical tropopause as well as the slope of the isentropes. With an idealized general circulation model, he showed that baroclinic eddies are able to transport the heating received at the surface upward efficiently enough to balance the destabilization by the radiative forcing and maintain a realistic extratropical tropopause. However, in addition to the uncertainty of the vertically uniform eddy diffusivity, the results of Schneider (2004) also raise another question, that is how to bridge the GCM results with the theories and results obtained under the QG assumption.

As suggested by Schneider (2004, 2007), the main shortcoming of the QG assumption is the specified stratification. In this study, a modified QG model is used, in which a tendency equation for the stratification is coupled with the PV equation, thus the stratification is allowed to evolve with time. The modified QG model will be a useful tool to bridge the traditional QG model and the PE model, especially in investigating the role of the interactive stratification. In this chapter, we will focus on two questions: whether the interactive stratification plays a role in maintaining the robust isentropic slope and whether the interactive stratification has any influence on previous parameterizations obtained under the QG framework. Although the dynamic constraint by Schneider (2004) is derived from the momentum and the PV flux balances, due to the difficulties in relating QGPV to the PV defined on the isentropic surface in Schneider (2004) especially in the lower troposphere, here we will not compare them directly. Instead, we will start comparison from the robustness of

the isentropic slope.

3.1 Robustness of the isentrope slope

In this section, we will study whether the interactive stratification is able to influence the robustness of the isentropic slope by comparing the equilibration of the baroclinic eddies under different strengths of the diabatic heating in our modified model and the traditional QG model. In the group of experiments with our modified model, in addition to the default value of Δ_e in Eq.2.5, which is 43 K, more experiments are carried out by setting $\Delta_e = 15$, 20, 25, 30, 60, 80, 100 K, separately. The target (RCE) state lapse rate is kept the same in these experiments, which is 7 K/km in the troposphere and isothermal in the stratosphere. Thus, as shown in Figure 3-1, the target state isentropic slope is linearly proportional to Δ_e, which is steeper with stronger Δ_e. In another group of experiments with the traditional QG model, we made similar model settings, but with the stratification of the flow fixed and specified to be the target state stratification. These two groups of experiments all started from the zonally symmetric RCE states and small perturbations are added into the flow at the initial moment. The model is integrated over 1000 days, and the statistics are made over the last 600 days.

The vertical distribution of the equilibrium state isentropic slope in the two groups of experiments is displayed in Figure 3-1. The most obvious difference between the two groups of experiments is that with interactive stratification, when the diabatic heating is strong enough, a similar vertical distribution of isentropic slope is observed through most of the free troposphere. In spite of the strong variation of the target state isentropic slope, when the baroclinic eddies are allowed to adjust the thermal stratification, they maintain a relatively robust isentropic slope. Only in the boundary layer where the boundary layer vertical thermal diffusion is strong, is the isentropic slope sensitive to the forcing. However, without an interactive stratification, there is no robust isentropic slope observed, with the equilibrium state isentropic slope being steeper when the target state isentropic slope is stronger. When the diabatic heating is too weak, i.e. $\Delta_e = 15$ or 20 K, the isentropic slope almost retains

the target state value with either the interactive or fixed thermal stratification.

The meridional gradient of the equilibrium state zonal mean potential temperature at the center of the channel and the equilibrium state stratification in the two groups of experiments are also shown in Figures 3-2 and 3-3, respectively. Under weaker diabatic heating, which is $\Delta_e = 15$ and 20 K, the meridional potential temperature gradient is still the target state temperature gradient (which is uniform in the troposphere), with the baroclinic eddies not playing any role in modifying the zonal mean state. As the diabatic heating becomes stronger, the eddies are more active in eliminating the temperature gradient. Near the surface, due to the strong surface damping (which will be further discussed in Ch.4), the temperature gradient is very close to the target state temperature gradient. In the free troposphere, the potential temperature gradient is greatly reduced. Comparing the situations with interactive and specified stratification, we find that with interactive stratification, the temperature gradient is more efficiently reduced especially around 700-900 hpa. With either interactive or specified stratification, the flow equilibrates with a stronger potential temperature gradient under stronger differential heating.

The equilibrium state stratification in the two groups of experiments in Fig.3-3 displays the importance of the vertical eddy heat flux in determining the flow stratification. Since the target state lapse rate is kept the same during these experiments, the difference in the stratification in the interactive stratification runs is entirely due to the baroclinic eddies. Fig.3-3 shows that baroclinic eddies can stabilize the zonal flow by increasing the lower level stratification. Stronger differential heating, which causes stronger eddy activity, results in a more stable lower level stratification. Also as the diabatic heating becomes stronger, the stratification in the upper troposphere even in the lower stratosphere is modified, which indicates that the eddy vertical heat flux in these experiments can penetrate into higher levels. With specified stratification, the equilibrium state stratification is just the target state stratification.

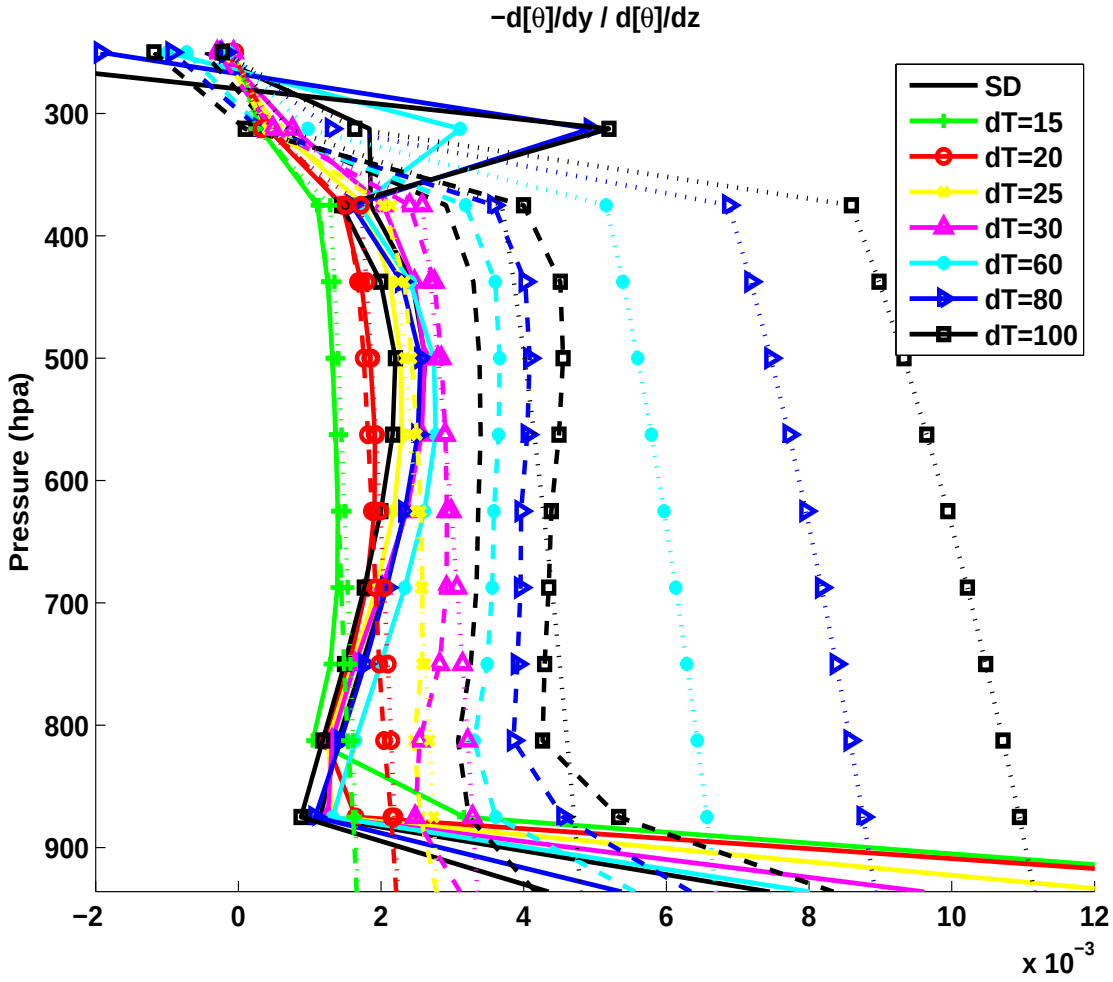

Figure 3-1: Comparison of the equilibrium state isentropic slope $\frac{\partial[\theta]/\partial y}{\partial\overline{\theta}^{xy}/\partial z}$ when Δ_e = 43, 15, 20, 25, 30, 60, 80, 100 K, separately, with interactive stratification (solid curves), specified stratification (dashed curves) and the RCE state isentropic slope in these runs (dotted curves).

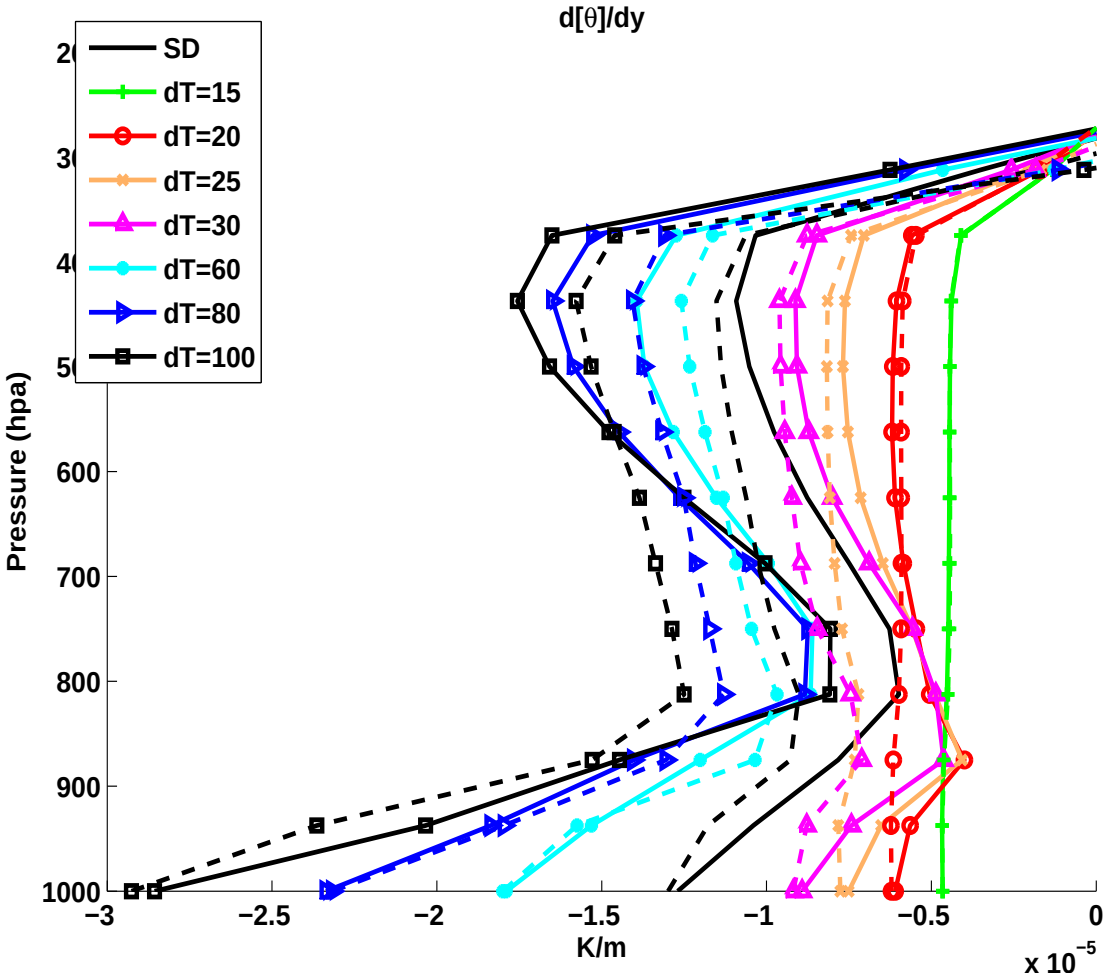

Figure 3-2: Comparison of the equilibrium state meridional gradient of the zonal mean potential temperature at the center of the channel when Δ_e = 43, 15, 20, 25, 30, 60, 80, 100 K, separately, with interactive stratification (solid curves) and specified stratification (dashed curves).

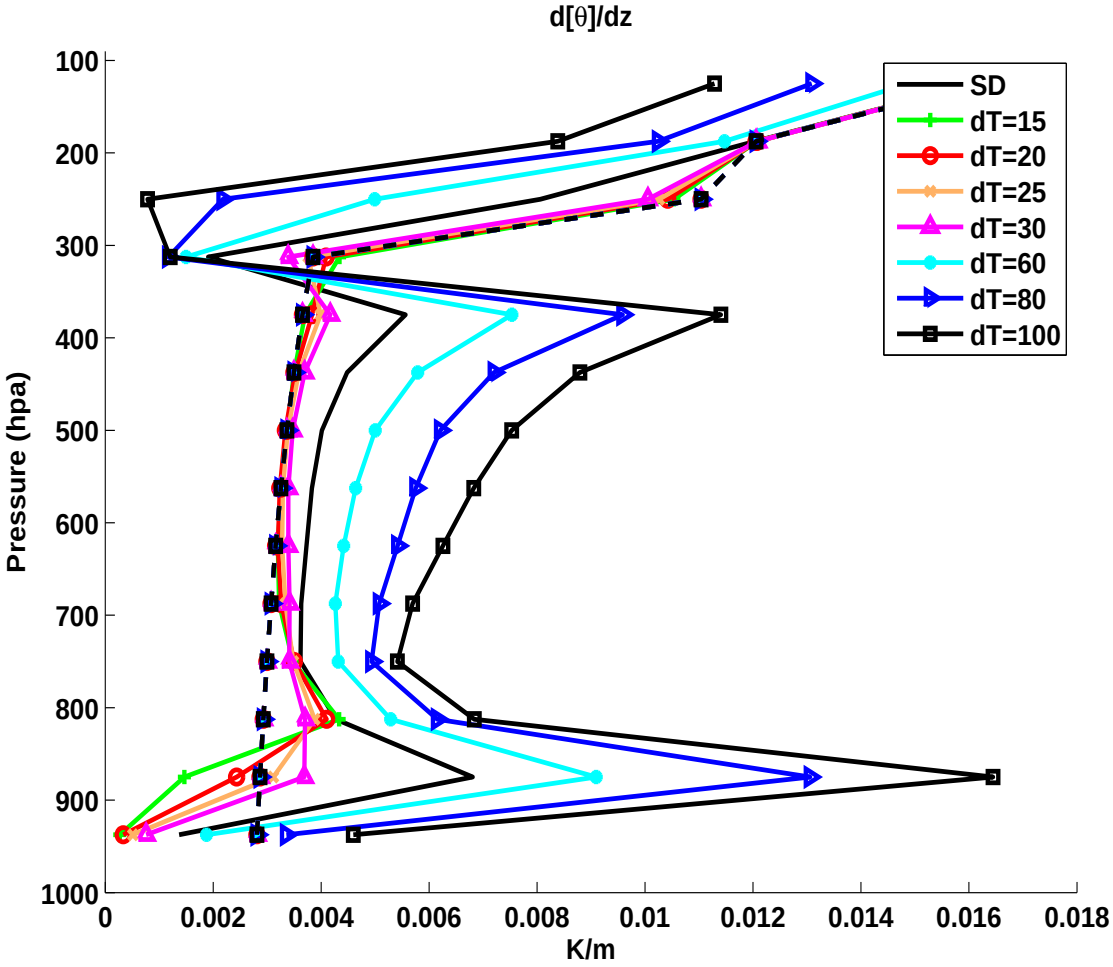

Figure 3-3: Comparison of the equilibrium state stratification when Δ_e = 43, 15, 20, 25, 30, 60, 80, 100 K, separately, with interactive stratification (solid curves) and specified stratification (dashed curves) .

3.2 Eddy heat fluxes

To understand and quantify the relation between the eddy activity and the mean flow, several closure theories have been proposed by means of a diffusive approach. One group of the closure theories (Green, 1970; Stone, 1972; Held, 1978) is based on the assumption that the eddy energies are proportional to the source energy, the mean available potential energy. In these studies, they all assumed that $\theta^* \sim \frac{\partial[\theta]}{\partial y} L_y$, where L_y is the meridional scale, across which the zonal mean available potential energy can be extracted by the baroclinic eddies. Green (1970), Stone (1972), and Held (1978) made different assumptions about this meridional length scale. Green (1970) assumed that L_y was the width of the baroclinic zone, which is determined by the geometry of the background flow. Stone (1972) suggested an isotropy of eddy activities in horizontal and assumed that L_y is comparable with the scale of deformation radius, where he used the form in the Eady model $L \sim \frac{NH_t}{f_o}$, $N = (g\partial ln\theta/\partial z)^{1/2}$ and H_t is the fluid depth, for which the height of the tropopause is a reasonable choice. Held (1978) suggested another option for L_y. On a β-plane, for large β, Charney's model suggests a vertical scale of baroclinic eddies

$$h = \frac{f_o^2 \partial[u]/\partial z}{\beta N^2} = -\frac{f_o}{\beta} \frac{\partial[\theta]/\partial y}{\partial[\theta]/\partial z}. \tag{3.1}$$

Then the characteristic vertical scale of the baroclinic eddies depends on the competition between h and the scale height H. When $h >> H$, H replaces h as the relevant eddy height scale; however, when $H >> h$, h represents the eddy vertical scale and the horizontal length of the most unstable wave is proportional to $L_{eddy} = \frac{Nh}{f_o}$.

Combining the studies of Stone (1972) and Held (1978) by using an effective eddy vertical scale d, Branscome (1983) developed a parametrization of eddy heat fluxes by assuming that the vertical distribution of the heat fluxes follows the most unstable Charney modes. His parametrization of the meridional eddy flux of the potential temperature is

$$[v^*\theta^*] = Const. \frac{gd^2 N_w}{[\theta]_w f_o^2} \left(\frac{\partial[\theta]}{\partial y} \right)_w^2 e^{-z/D}, \tag{3.2}$$

where the subscript w indicates a mass weighted vertical mean; $Const.$ ≈0.6 is suggested by Branscome (1983); the effective eddy vertical scale

$$d = \frac{H}{1 + H/h_w} \; ; \tag{3.3}$$

and the scale depth of the most unstable mode

$$D \approx \frac{H}{1.48H/h_w + 0.48} \tag{3.4}$$

is suggested by Stone and Yao (1990). This parametrization is used in the MIT two-dimensional zonally averaged statistical-dynamical model (Sokolov and Stone, 1998) with a boundary layer modification.

In this section, we will investigate the effect of the interactive stratification on the eddy heat flux parameterization by comparing the model resolved eddy heat flux with the parameterization predicted one. In Stone and Yao (1990), the vertical structure of the eddy heat flux is modified by $[1 - e^{-(z/\Delta z)}]$ to represent the damping of the boundary layer, where Δz is the depth of the boundary layer. In our model, due to the strong boundary layer vertical thermal diffusion, the lowest level lapse rate is close to the dry adiabatic lapse rate and the temperature gradient there is close to the underlying surface temperature gradient, which could result in singularity when calculating h from Equation 3.1. In addition, the lowest level eddy heat flux is always weak due to the strong damping there and does not make important contribution to the vertical average. Thus, the weighted vertical mean in Eqs.3.2 to 3.4 is averaged from the model's second level to the tropopause. The vertical distributions of the model resolved zonal mean poleward eddy heat flux at the center of the channel in the two groups of experiments are displayed in Figure 3-4. Consistent with the zonal mean flow distribution, when Δ_e = 15 and 20 K, eddy activities are weak and do not play any role in the flow. The eddy heat flux gets stronger as the external forcing increases. When comparing the two experiments forced to the same target state but with or without interactive stratification, the magnitudes of the eddy heat flux in the two experiments are

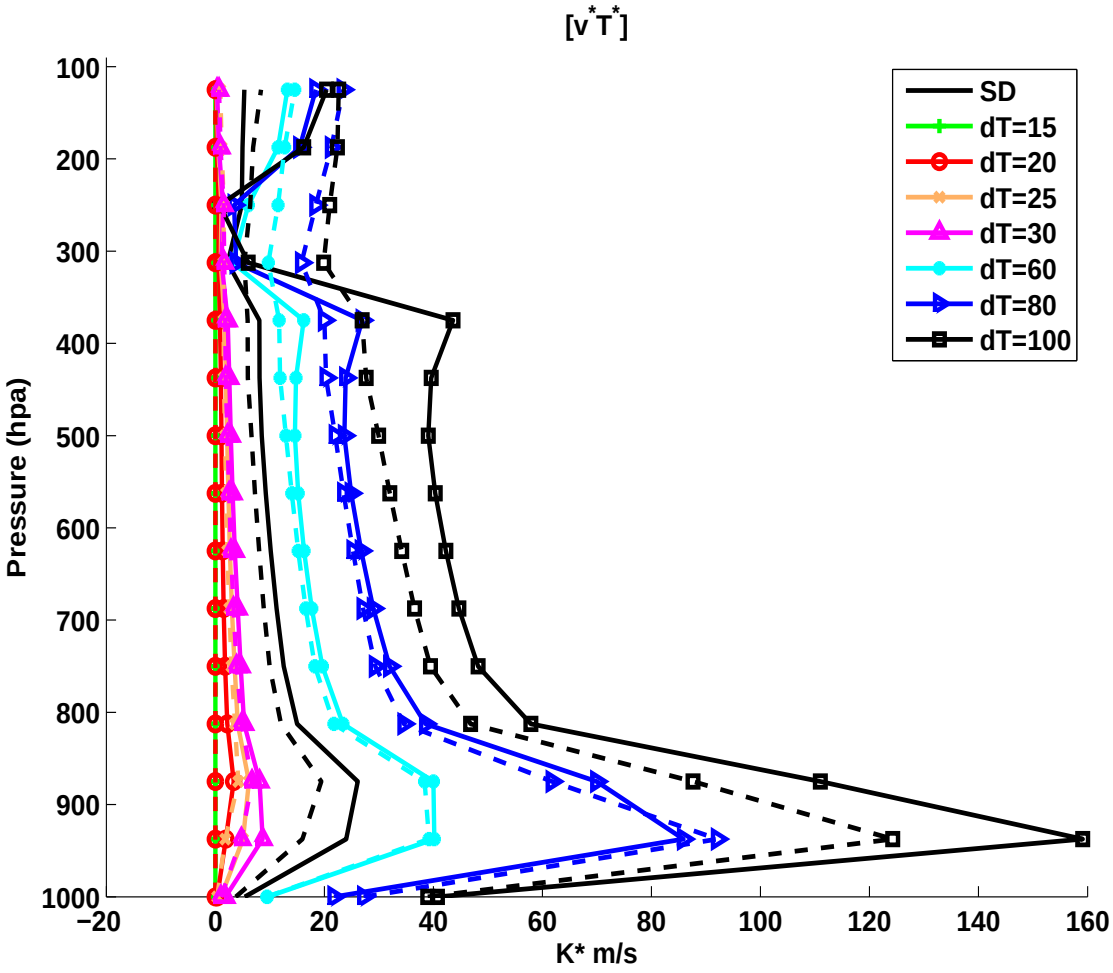

Figure 3-4: Comparison of the equilibrium state poleward eddy heat flux at the center of the channel when $\Delta_e = 43$, 15, 20, 25, 30, 60, 80, 100 K, separately, with interactive stratification (solid curves) and specified stratification (dashed curves).

different. The eddy heat flux in the interactive stratification experiment is always stronger, which is consistent with the fact that the isentropic slope of the zonal flow is more strongly modified when turning on the interactive stratification, but different from the conventional expectation that the strong lower level stratification (i.e. for the experiments under strong diabatic heating and with interactive stratification) always acts to suppress the eddy heat flux. In the experiments with weaker diabatic forcing (i.e. Δ_e less than 43 K), the much less stable stratification in the lower level in the interactive stratification run seems consistent with the stronger eddy heat flux. More discussion on this will be made in later. Under strong differential heating, turning on the interactive stratification also influences the vertical structure of the eddy heat flux, especially near the tropopause.

The estimated poleward eddy flux of the potential temperature from Eq.3.2 is compared with the model resolved vertical averaged eddy heat flux in Figure 3-5. There is a transition in the eddy heat flux as the diabatic forcing increases in both groups of experiments. When the diabatic forcing is weak, as shown in the last section, the zonal mean state is close to the target state and the eddy heat flux remains very weak. In this transition regime, the model resolved eddy heat flux shows much stronger sensitivity than the parameterization predicted, and the parametrization does not work, presumably because, as suggested in Thompson and Young (2007), the boundary layer dissipation, which is neglected in the parameterization, begins to play a role. When the external forcing and the eddy activity are strong enough, with interactive stratification, we find the parametrization is a good approximation for the eddy heat flux. With specified stratification, there is also a regime where the diabatic forcing is weak and the parameterization does not work. However, we find the parameterization is a good approximation only under extremely strong diabatic forcing, i.e. Δ_e is greater that 100 K. In the intermediate regime for Δ_e, the model resolved eddy heat flux still shows more sensitivity than the parametrization estimated, but closer to the parameterization prediction asymptotically as the diabatic forcing gets stronger.

To understand the different behavior of the eddy heat flux between the two groups of experiments, more comparisons are made in Figures 3-6 and 3-7. There are obvious differences

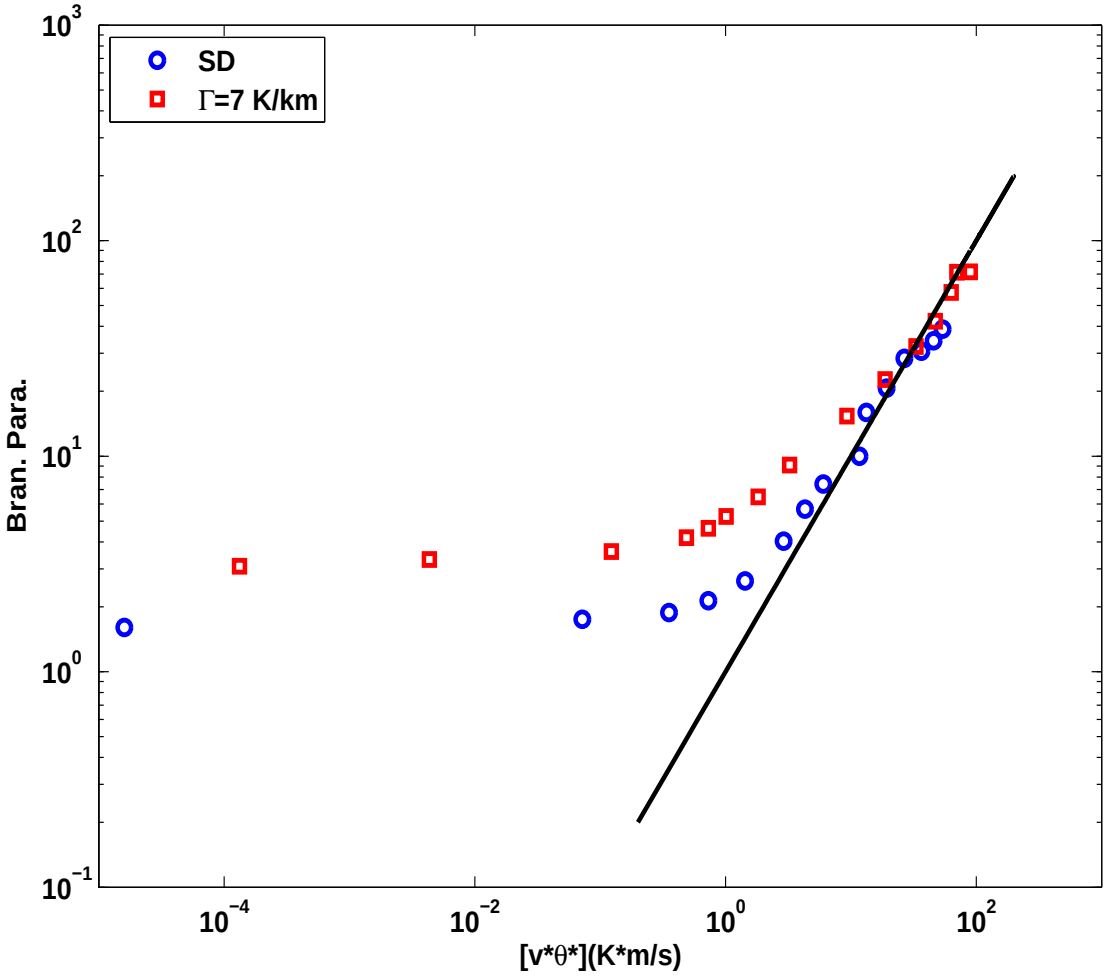

Figure 3-5: Comparison between the predicted poleward eddy heat flux as suggested by Branscome (1983) and the model resolved poleward eddy heat flux under different differential heating with interactive stratification (◯) and specified stratification (□). The solid line indicates the situation where the parametrization is an accurate prediction of the eddy heat flux.

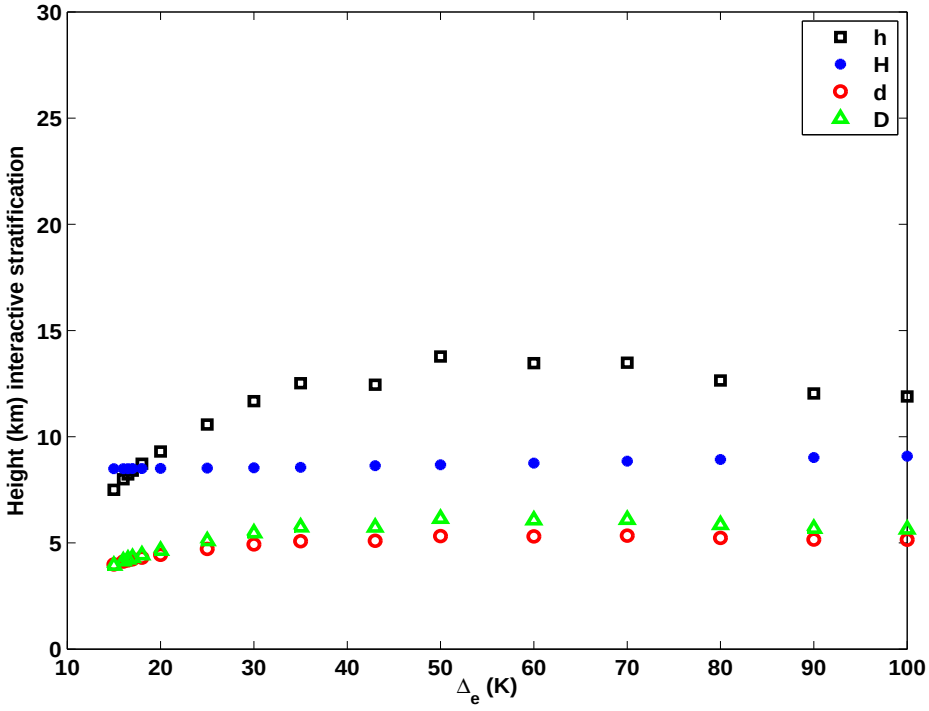

Figure 3-6: Variation of the equilibrium state vertical scale h ($\square$), height of the tropopause H ($*$), effective eddy vertical scale d ($\bigcirc$) and the scale depth of the most unstable mode D ($\triangle$) as a function of the target state temperature difference over the center of the channel in the experiments with interactive stratification.

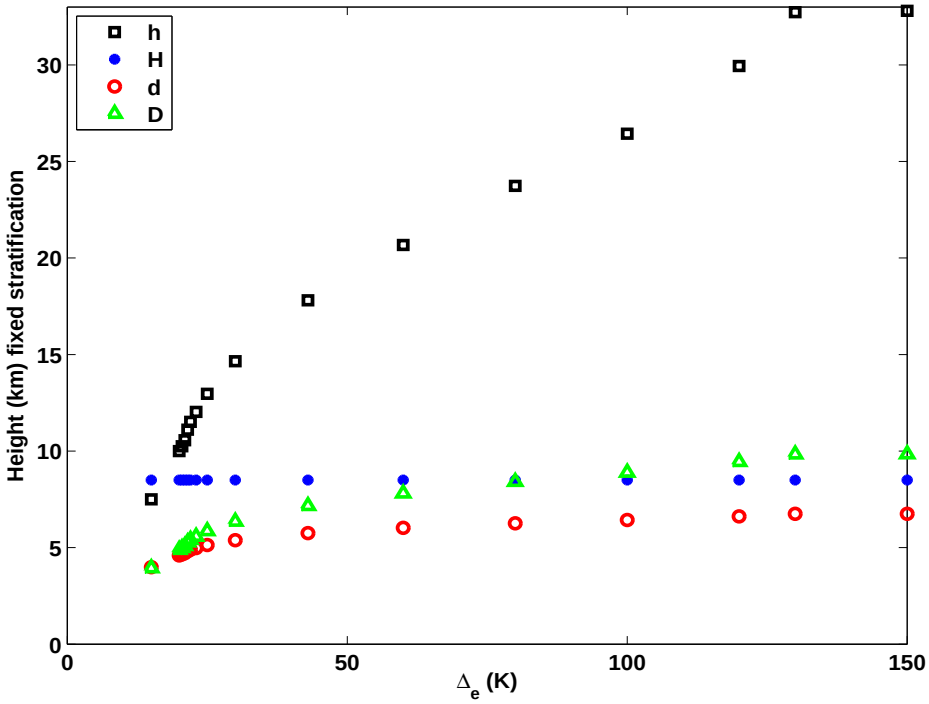

Figure 3-7: Same as Fig.3-6, but for runs with specified stratification.

when turning on the interactive stratification.

- With specified stratification, the scale h, which is linearly proportional to the isentropic slope as defined in Eq.3.1, increases monotonically with Δ_e. However, with interactive stratification, this scale does not show any obvious increase, instead it is not far from the scale height H.

- Another obvious difference between the two groups of experiments is that with interactive stratification, the effective eddy vertical scale d is also the scale depth of the most unstable mode D, which is consistent with the fact that h is comparable with the scale height H. With specified stratification, as h/H gets greater, both d and D are closer to the scale height H, but with D always deeper than d. In this situation, the eddy activity will 'feel' the existence of the tropopause.

In addition, in Fig.3-4, we have shown that the meridional eddy heat flux in the interactive stratification run is always stronger than the one in the corresponding fixed stratification run.

The variation of h/H in the two groups of experiments in Figs. 3-6 and 3-7 indicates that this tendency is consistent with the parameterization in Eq.3.2. With an interactive stratification, the scale h is always close to the scale height H and the effective eddy vertical scale d is almost unchanged as the diabatic forcing increases. Then the eddy heat flux $[v^*\theta^*] \propto N_w \left(\frac{\partial[\theta]}{\partial y}\right)^2$, in which the stronger stratification indicates stronger meridional eddy heat flux. This parameter dependence is the same as the f-plane results suggested by Stone (1972), and consistent with the results in another parameterization comparison in Solomon and Stone (2001b). With a fixed stratification, though the parameterization in Eq.3.2 underestimates the sensitivity of the eddy heat flux to the mean flow, as shown in Fig.3-5, it begins to work well in the regime of very strong diabatic heating. Then as h is much larger than H, the effective eddy vertical scale d shows little variation, so again the eddy heat flux under the fixed stratification $[v^*\theta^*] \propto N_w \left(\frac{\partial[\theta]}{\partial y}\right)^2$. Since in the strong forcing regime, the thermal stratification is more stable than the RCE state, a stronger meridional eddy heat flux can be obtained with the modified QG model.

3.3 Discussion

By comparing the baroclinic eddy equilibration in the modified and traditional multi-layer QG model, we find that only with the interactive stratification, can a robust isentropic slope be obtained in spite of the variation of the forcing. Comparison between the model resolved eddy heat flux with the one predicted by the closure theory of Branscome (1983) shows that the parameterization is a good approximation when the vertical eddy heat flux is allowed to modify the thermal stratification. With fixed stratification, except in the situations with strong diabatic forcing, the eddy heat flux always varies more sensitively to the mean flow than the theory predicted, which confirms the suggestion by Held (2007).

The robustness of the isentropic slope and the fact that, with an interactive stratification, eddy vertical height scale h is always close to the scale height H have further physical meaning. It is the dynamic constraint suggested by the baroclinic adjustment. Further more, as suggested in Schneider and Walker (2006), when the supercriticality does not significantly

exceed one, baroclinic eddies inhibit the nonlinear eddy-eddy interaction as well as the inverse energy cascade from the linearly most unstable mode to larger scales. Schneider and Walker (2006) using an idealized general circulation model showed that baroclinic eddies adjust the mean flow to criticality by reducing the temperature gradient, stabilizing the thermal stratification and modifying the height of the tropopause. In our model, there is a tropopause in the target state exerted on the atmospheric flow, which is fixed around the 300 hpa. Then the height of the tropopause $H_t \sim H$, and the criticality is equivalent to the situation $h \sim H$ in our model. Our simulation suggests that the adjustment of the thermal stratification is more dominant in maintaining a critical state. With an interactive stratification, the flow is weakly nonlinear and the parameterization by Stone (1972), Held (1978), and Branscome (1983) is an appropriate approximation.

There is another group of closure theories (Held and Larichev, 1996; Pavan and Held, 1996; Lapeyre and Held, 2003) based on the presence of an inverse energy cascade and the assumption that the eddy length scale is the scale at which the cascade halts, i.e. the Rhines scale (Rhines, 1975, 1979). Their work was also derived under the traditional QG assumption, in which the modification of the thermal stratification by the baroclinic eddies was not considered. In their theories, the eddy heat flux is more sensitive to the meridional temperature gradient. In our model, with a fixed stratification, h can be far from H and there could be a separation between the dominant eddy scale and the linearly most unstable mode. Then the inverse energy cascade may begin to play an important role. More studies are still needed to test whether this is the situation in our fixed stratification runs and can help explain the stronger sensitivity of the eddy heat flux to the mean flow.

Chapter 4

The role of the boundary layer processes in the atmospheric model

The planetary boundary layer is characterized by turbulent momentum and heat transports, and strong surface friction as well as heat exchange with the underlying surface. What determines the boundary layer thermal structure and how do these boundary layer processes influence the eddy equilibration? These are the questions we will answer in this thesis. In this chapter, using the atmospheric model described in Chapter 2, we start the study on the role of the boundary layer processes from a simpler case, in which the underlying surface temperature is fixed during the eddy equilibration.

Solomon (1997b) used a similar atmospheric model but with a shorter channel length (5260 km) to study the influence of boundary layer processes on eddy equilibration. In her study, surface friction and surface heat flux, as well as vertical thermal and momentum diffusion, share the same parameters. She found that the boundary layer in general damps the mean flow adjustment. However, the mechanism through which different boundary layer processes modify the equilibrated states was not clear. Thus, in this study, we use different parameters for each boundary layer process and vary the value of each parameter to investigate their different roles in eddy equilibration. In addition, even though the dominant transient eddies in mid-latitudes are medium-scale eddies (approximately 4000 - 5000 km as

shown by Randel and Held (1991) and Solomon (1997a)), the short channel length may not be able to provide enough space for wave-wave interactions as well as the variation of eddy length scales. Thus, in this study we use a more realistic channel length (21040 km) for our model.

As discussed in Chapter 1, our study will focus on these questions: which is the dominant mechanism that causes the failure of baroclinic adjustment theory in the boundary layer; how these mechanisms work together to influence the lower troposphere thermal structure; and as discussed, each boundary layer process can influence the eddy activity both directly as an energy damping and indirectly by influencing the zonal mean flow, then how these two effects compete is another focus in this chapter.

4.1 Standard run

Our standard run is the experiment designed to simulate the current winter climate by choosing realistic values for the parameters, similar to the standard run in Solomon and Stone (2001a). The standard run simulates the midlatitude thermal structure reasonably well, with one jet and eddy activities centered at the center of the channel.

Time evolution of the domain averaged zonal/eddy kinetic and available potential energies [1]in the first 1000 days is plotted in Figure 4-1. During the first 7 days, the effects of baroclinic eddies are small and the zonal kinetic energy decays primarily due to boundary layer dissipation. From day 8, the eddy kinetic energy (hereafter, EKE) and eddy available potential energy (hereafter, EPE) begin to grow exponentially and reach their first peak at day 16. Associated with this is a decrease of mean available potential energy (hereafter, MPE) and mean kinetic energy (hereafter, MKE). After day 16, EKE and EPE begin to decay, during which MPE stops decaying and its magnitude increases slightly. Instead of settling down immediately after the first eddy life cycle, second and third life cycles which peak at day 50 and 75 can be clearly observed. Similar to the first life cycle, MPE in

[1]Zonal/eddy kinetic and available potential energies are defined as in Peixoto and Oort (1992), Chapter 14.

these life cycles decreases rapidly as the eddy energy increases but not as steeply as in the first. An FFT analysis of EKE displayed in Figure 4-2 shows that, the first three peaks observed in the figure correspond primarily to the life cycles of wavenumber 6, 5 and 4, respectively. Consistent with Solomon and Stone (2001a), these are also the dominant waves in equilibration. Our quasi-linear run analysis[2] shows that wavenumber 5 and 6 are also the linearly most unstable waves for the initial state. Here, the FFT analysis is only applied on the zonal direction. The meridional structure of the eddy activity in each zonal wavenumber is very similar. They are all centered at the center of the channel and confined to the baroclinic zone, which is the central half of the channel.

After day 300, as shown in Figure 4-1, the system reaches an 'equilibrium state', with the EKE and EPE varying quasi-periodically. Thus, the eddy saturation displays two time scales: the life cycle time scale, which is initially of the order of ten days, and the equilibration time scale, which is more than 300 days in our model.

The evolution of the energy exchange terms [3] and the dissipation terms for EKE and EPE are displayed in Figure 4-3. The dissipation of energy by FFT filter is negligible and not shown in the figure. During the whole process of saturation, the energy cycle is always in the direction that

$$\text{MPE} \rightarrow \text{EPE} \rightarrow \text{EKE} \rightarrow \text{MKE},$$

which is consistent with the previous numerical studies (Philips, 1956) as well as the observed energy cycle in the global atmosphere (Oort and Peixoto, 1983). During the equilibration, frictional dissipation is the largest sink for EKE, which is also the case in the real atmosphere

[2]Similar to Solomon and Stone (2001a), the quasi-linear run is the experiment in which only one wave is included during the evolution. By calculating the growth rate in the growing state of the first life cycle, we find that wavenumber 5 and 6 are the most unstable waves with growth rate $KC_i = 0.48/day$, while wave-number 4 has a growth rate of $0.33/day$. Our quasi-linear run also shows that only including the dominant wave, i.e. wavenumber 6, we can obtain a similar equilibrated mean state to that in the standard run, which indicates the evolution in the standard run is primarily by wave-mean flow interaction.

[3]Terms $P_e \rightarrow K_e$, $P_m \rightarrow P_e$ and $K_e \rightarrow K_m$ are energy fluxes that transfer energy, separately, from EPE to EKE, from MPE to EPE, and from EKE to MKE. They are the QG form energy fluxes that are defined in Peixoto and Oort (1992), Chapter 14, where $P_e \rightarrow K_e$ is proportional to the vertical eddy heat flux, $P_m \rightarrow P_e$ is proportional to the meridional eddy heat flux and $K_e \rightarrow K_m$ is proportional to the meridional eddy momentum flux. The sign of these fluxes is defined positive if the flux acts to transfer energy in the direction shown by the arrow.

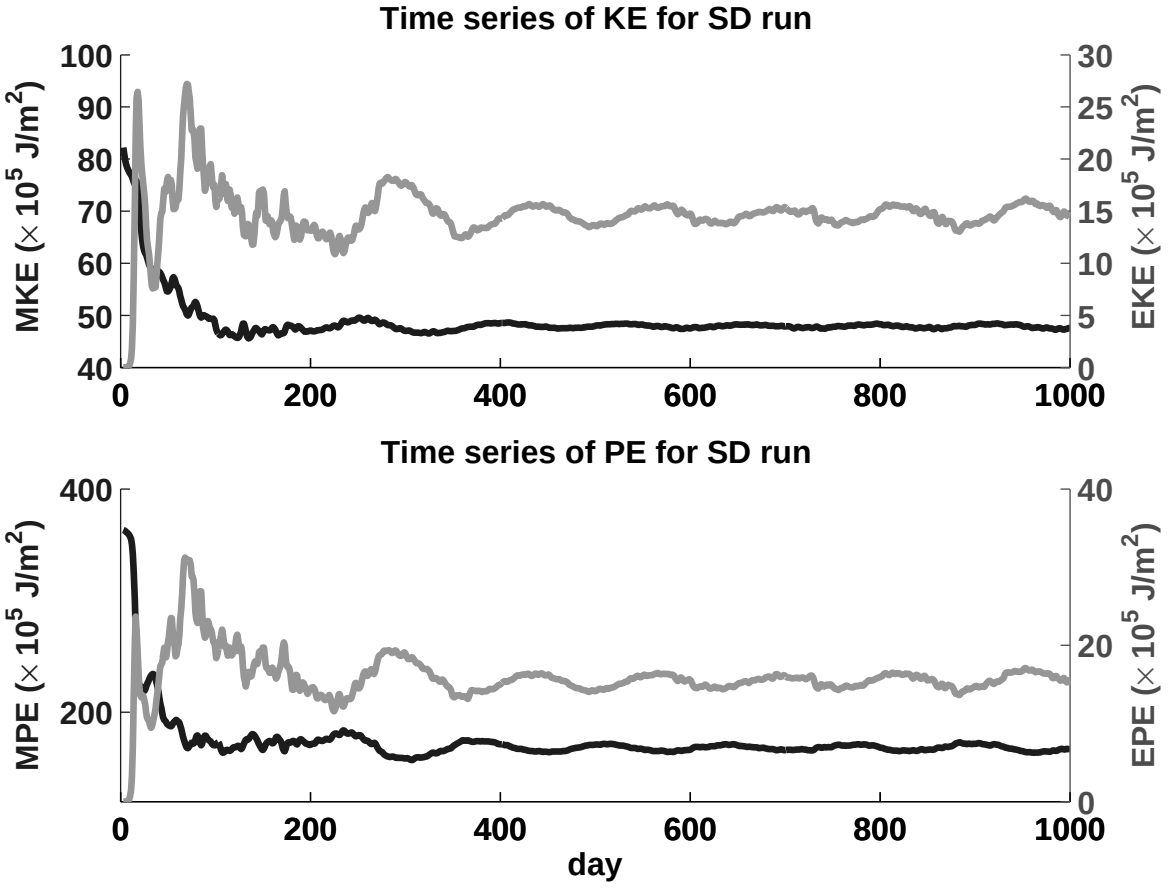

Figure 4-1: Time series of zonal(black), eddy(gray) kinetic energy (upper) and zonal(black), eddy(gray) available potential energy (lower) of the first 1000 days in the standard run. Unit: $10^5 J/m^2$.

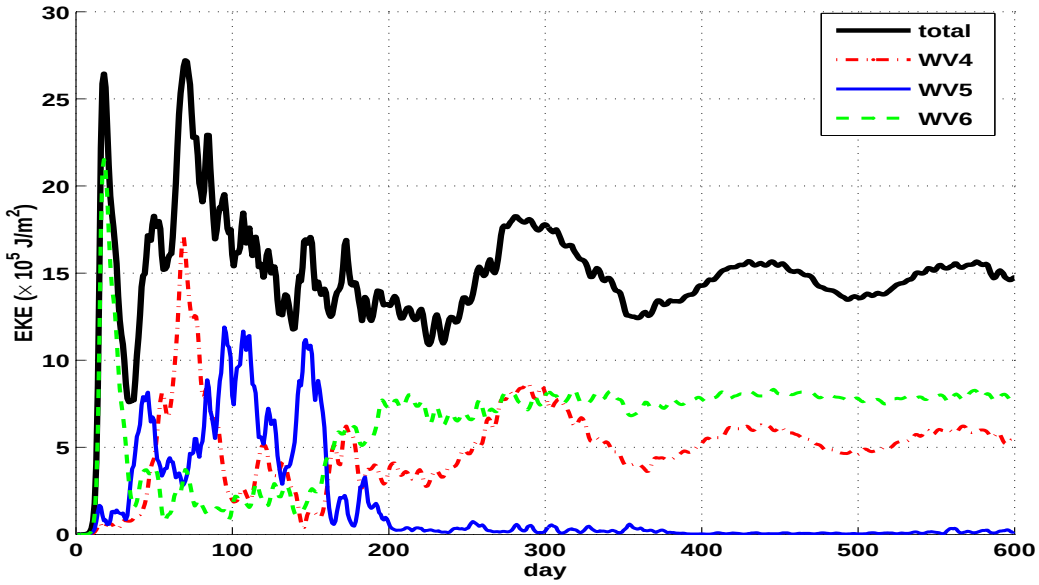

Figure 4-2: Time series of eddy kinetic energy (EKE) carried by wavenumbers 4 (dot-dashed), 5 (solid) and 6 (dashed) in the first 600 days in the standard run. Thick black curve indicates the total EKE.

(Oort and Peixoto, 1983). Boundary layer thermal diffusion, together with diabatic forcing and vertical eddy heat flux, also act to remove EPE during the whole evolution, especially in the equilibrium state, in which the magnitude of the thermal diffusion term is comparable to the $P_e \rightarrow K_e$ term. Thus, the direct effect of the boundary layer is a damping of eddy energies.

4.2 Effect of boundary layer processes

To investigate the influence of each boundary layer process, as will be discussed in Sections 4.2.1 - 4.2.6, four groups of sensitivity studies are carried out to compare with the standard run. In these studies we only vary the value of one coefficient at a time and keep the coefficients representing the other boundary layer processes unchanged. The boundary layer coefficient values used in these experiments are listed in Table 4.1.

Except in Sections 4.2.2 and 4.2.5, in which we discuss the transient response of our

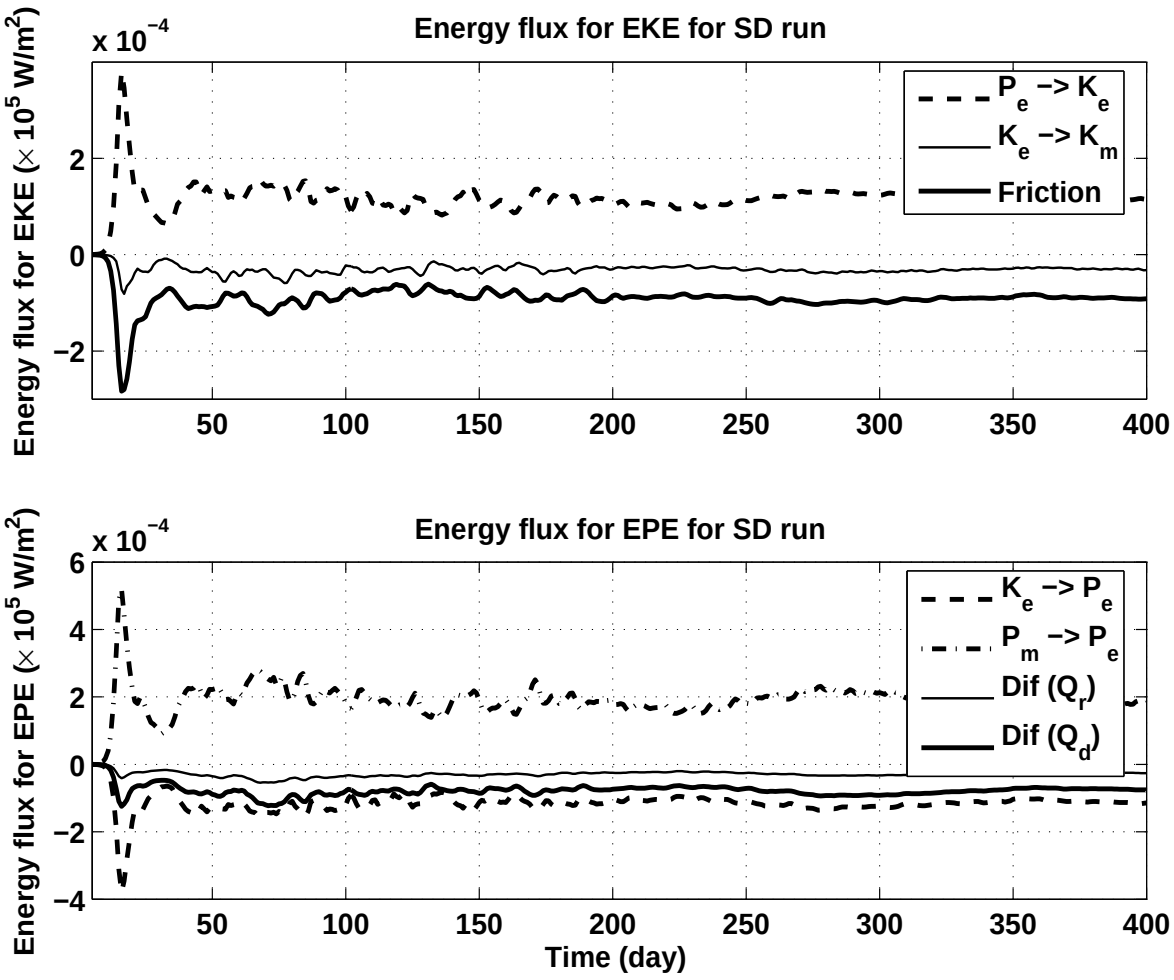

Figure 4-3: Time series of energy flux terms that can cause the variation of EKE(upper) and EPE(lower) in the first 400 days, where $Dif(Q_r)$ in the lower figure is the damping of EPE by the diabatic heating Q_r and $Dif(Q_d)$ is the damping of EPE by the thermal diffusion Q_d. Positive values indicate fluxes enhancing the energies, negative values indicate fluxes reducing the energies. Unit: $10^5 W/m^2$.

model to the sudden variation of vertical thermal diffusion and surface friction, all the experiments discussed in this section start from the axisymmetric RCE state. Small amplitude perturbations in wave-numbers 1 to 9 are added to the mean flow at the initial moment. All the experiments are integrated for 1000 days and the equilibrated states are the states averaged over the last 400 days.

Table 4.1: Values of the coefficients used in the experiments that investigate the model sensitivity to different boundary layer processes, and the eddy characteristics at the center of the channel in the equilibrated states in these experiments.

Run	C_{dt} (m/s)	μ_s (m^2/s)	C_{df} (m/s)	μ_m (m^2/s)	p_{bl} (hpa)	$\overline{[v^*T^*]}max$ $(K*m/s)$	$\overline{[\omega^*T^*]}max$ $(K*Pa/s)$
SD	0.03	5	0.03	5	0	16.8	-0.30
Section 4.2.3							
tcd0	0.00	5	0.03	5	0	10.6	-0.21
tcd1	0.01	5	0.03	5	0	16.4	-0.30
tcd2	0.06	5	0.03	5	0	19.8	-0.38
Section 4.2.1							
snu0	0.03	0	0.03	5	0	7.8	-0.11
snu1	0.03	2	0.03	5	0	16.5	-0.23
snu2	0.03	10	0.03	5	0	22.7	-0.42
Section 4.2.4							
fcd1	0.03	5	0.01	5	0	27.6	-0.30
fcd2	0.03	5	0.06	5	0	15.6	-0.30
Section 4.2.6							
xnu0	0.03	5	0.03	0	0	21.6	-0.32
xnu1	0.03	5	0.03	2	0	20.8	-0.32
xnu2	0.03	5	0.03	10	0	16.3	-0.29

4.2.1 Vertical thermal diffusion

A study of the sensitivity of the equilibrated states to the vertical thermal diffusion was accomplished by varying μ_s in Equation 2.8, which represents the strength of turbulent heat flux in the boundary layer. Figure 4-4 displays how the equilibrium states vary with the values of μ_s.

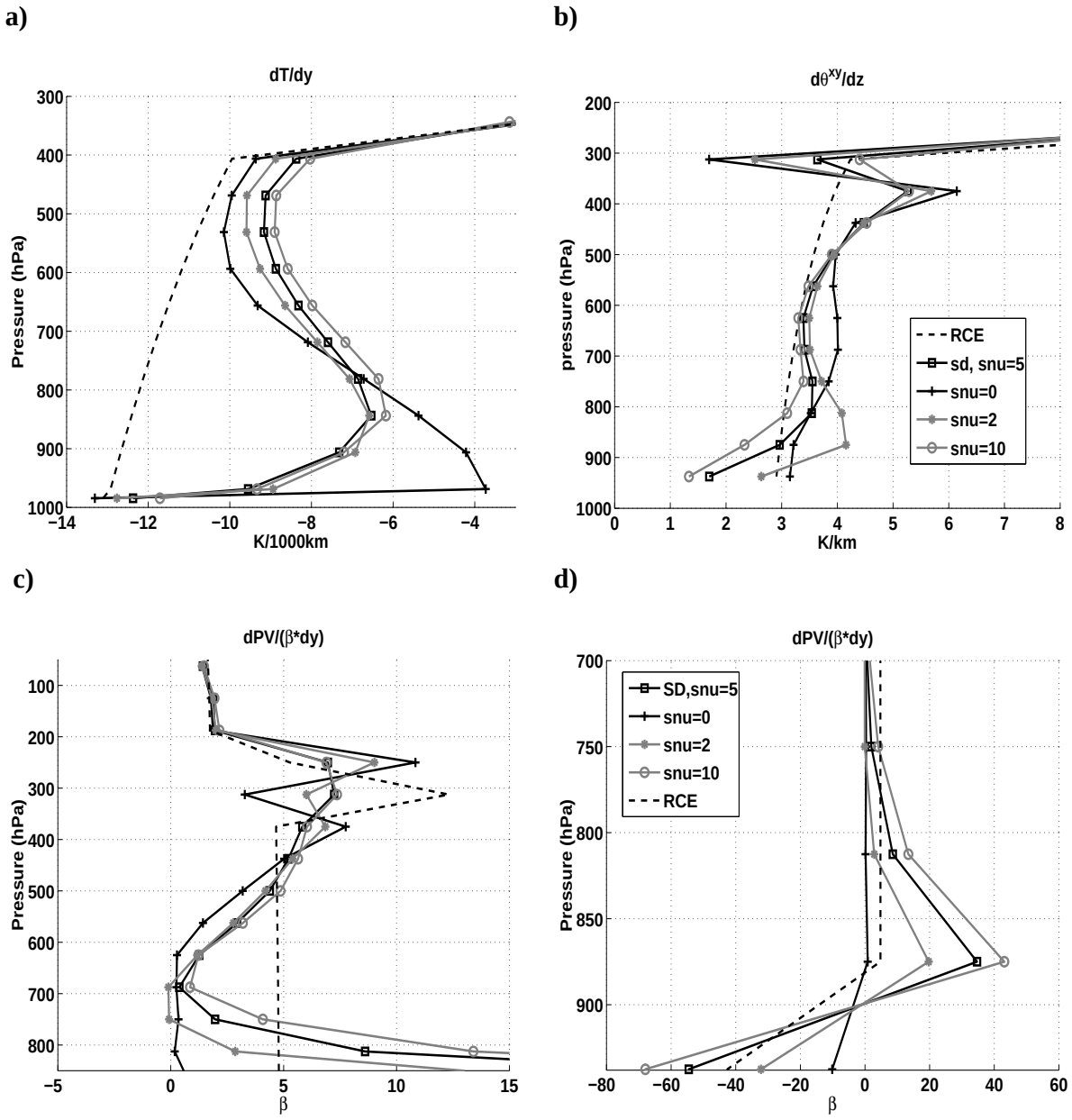

Figure 4-4: Comparison of equilibrated state a) zonal mean dT/dy at the center of the channel, b) $d\overline{\theta}^{xy}/dz$, c) zonal mean $dPV/(\beta dy)$ at the center in the free atmosphere and d) in the boundary layer for standard run (open square), the $\mu_s = 0$ (plus sign), 2 (asterisk), and 10 $m^2 s^{-1}$ (open circle) runs, and the RCE state (black dashed curves).

From Figure 4-4, we find that vertical thermal diffusion can largely suppress the mixing of lower level potential vorticity. As shown in the plot of the PV gradient (Figure 4-4(c)), in the standard run, the PV gradient at the center of the channel, consistent with observations, is less than β only around 700 hpa, with a large PV gradient near the tropopause and the surface. At the surface, there is a strong negative PV gradient, which is the model's version of the surface PV delta-function. If we turn off this vertical thermal diffusion, in the equilibrium states, PV is well homogenized from 600 hpa to 850 hpa, and the surface negative PV gradient is also largely reduced compared with the initial state. The strength of the vertical thermal diffusion also modifies the PV distribution by making it less homogenized under stronger thermal diffusion.

Since in most of our experiments, the baroclinic component dominates the PV gradient, the response of temperature gradients and static stability shows how the vertical thermal diffusion prevents the lower level PV homogenization by influencing the thermal structure. When we turn off the vertical thermal diffusion, the zonal mean temperature distribution we obtain in the lower troposphere is very different from that in the standard run. As illustrated in Figure 4-4(a), the boundary layer temperature gradient is much stronger when vertical thermal diffusion is included. The surface air temperature gradient, due to the strong air-sea surface heat flux, almost keeps its initial value which is also the prescribed temperature gradient of the underlying surface. The atmosphere above, without vertical thermal diffusion, is hardly coupled with the surface air, and its meridional temperature gradient is efficiently reduced primarily due to the mixing of baroclinic eddies. The static stability also behaves differently with and without thermal diffusion. Figure 4-4(b) shows that turning on the vertical thermal diffusion leads to a peak in the static stability near the top of the boundary layer (near 800 hpa), which is consistent with observations (Peixoto and Oort, 1992). However, there is no such feature in the zero thermal diffusion case. This can be explained by looking back to Equation 2.3. Without thermal diffusion, the states of the boundary layer are determined by the balance between diabatic heating and vertical eddy heat flux. However, with the thermal diffusion, the analysis of each term in Equation 2.3 in

the equilibrium state shows that in the lower levels, diabatic heating is much smaller than the thermal diffusion and the eddy transports, and the balance is mainly between the latter two forcings.

Figure 4-4(b) illustrates that the strength of the vertical thermal diffusion can modify the static stability of the equilibrated mean states. Since the thermal diffusion is parameterized as being down the vertical temperature gradient, as shown in Figure 4-4(b), the increase in the thermal diffusion reduces the lower level static stability. This is because the baroclinic eddies transport heat upward to stabilize the flow by cooling the lower troposphere and warming the upper troposphere. A stronger vertical turbulent heat flux in the lower levels can more efficiently compensate for the cooling by baroclinic eddies and prevent the stabilization of the flow.

The response of the eddy heat fluxes to the vertical thermal diffusion is different from what one might expect based on linear theories and life cycle studies. As displayed in Figure 4-5, instead of acting as a damping, stronger vertical thermal diffusion results in enhanced eddy sensible heat fluxes. One phenomenon that helps us understand the response of the eddy heat fluxes and the importance of the vertical thermal diffusion as well as other boundary layer processes, is the location of the critical level which by definition is the level where zonal wind U is equal to the phase speed Cr. Figure 4-6 shows the cross section of the equilibrium state zonal wind and the intrinsic phase speed $(U - Cr)$ of the dominant wave, which is wave-number 6 in these experiments, for the cases without thermal diffusion and with $\mu_s = 10m^2/s$. The phase speeds of the dominant waves are calculated following Gall (1976):

$$C_r = [k(\phi_s^2 + \phi_c^2)]^{-1}\left(\phi_c \frac{\partial \phi_s}{\partial t} - \phi_s \frac{\partial \phi_c}{\partial t}\right), \tag{4.1}$$

where k is the zonal wavenumber, ϕ_s and ϕ_c are the Fourier coefficients of the stream-function. Consistent with the result that a larger temperature gradient is maintained with thermal diffusion, the jet is stronger for the $\mu_s = 10m^2/s$ case. With the much weaker PV gradient for the non thermal diffusion case, the critical level drops to $900hpa$. In the other case, the critical level lies near $800hpa$. If we think that, for the baroclinic eddies generated

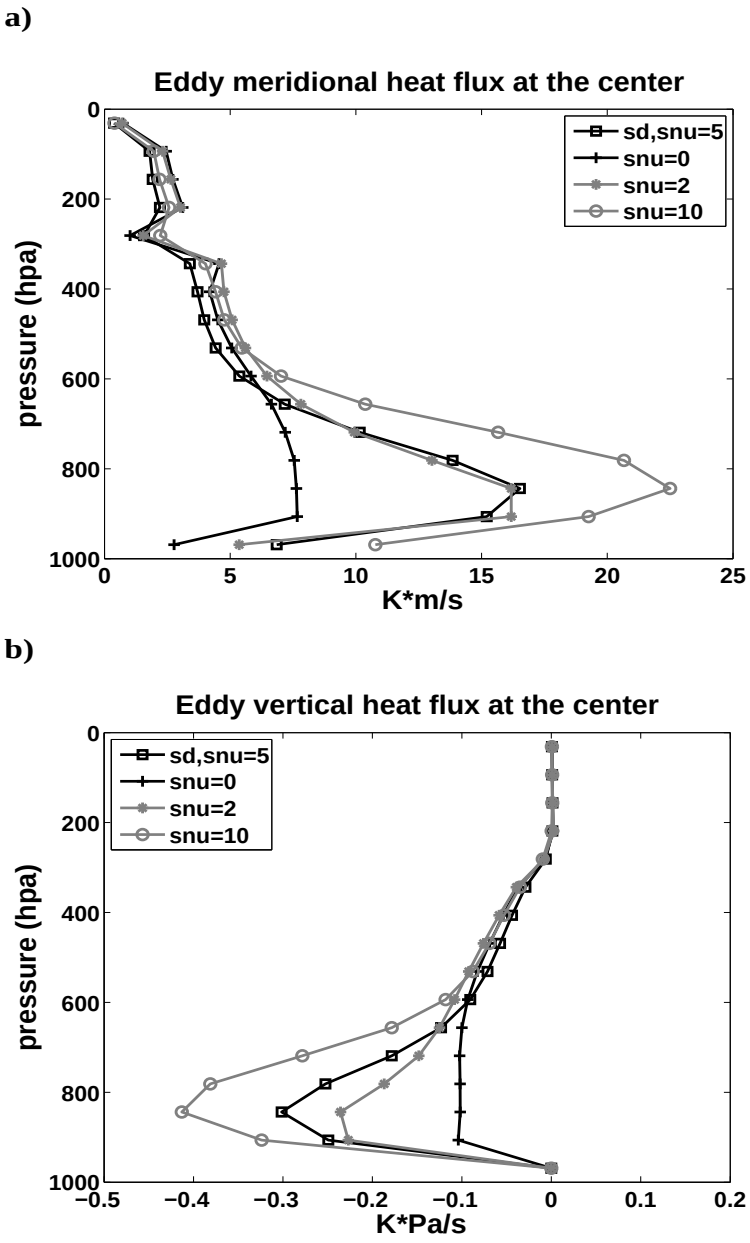

Figure 4-5: Comparison of equilibrated state zonal mean a) eddy meridional heat flux $[v^*T^*]$ and b) eddy vertical heat flux $[\omega^*T^*]$, where [ ] indicates zonal mean, for standard run (open square), and for the $\mu_s = 0$ (plus sign), 2 (asterisk), and 10 m^2/s (open circle) runs.

by instability, the critical level is their source level (Lindzen and Barker, 1985), where the poleward eddy heat flux is largest according to the linear instability theory, then in all of these experiments, the source region of the baroclinic eddies lies just inside the boundary layer or near the top of the boundary layer. The meridional eddy heat flux is colocated with the generation of baroclinic eddies and has a major component there. Thus, the role of the thermal diffusion that always acts to keep the strong baroclinicity of the boundary layer and destabilize the lower level flow, provides an explanation for the enhanced eddy heat fluxes.

4.2.2 Transient response to vertical thermal diffusion

To test the hypothesis we proposed above that explains the larger eddy heat fluxes as we increase the vertical thermal diffusion, a transient response study is carried out, in which the model starts from the equilibrium state of the standard run and a stronger vertical thermal diffusion ($\mu_s = 10m^2/s$) is suddenly introduced. The response of the eddy heat fluxes and eddy energies to the sudden increase in μ_s is plotted in Figure 4-7. We found that the immediate response of EPE and eddy heat fluxes is a decrease in their magnitude, which is consistent with the fact that vertical thermal diffusion is a damping term for EPE. However, the MAPE in the boundary layer increases quickly as we increase the thermal diffusion. Even though the MAPE in the free troposphere is almost unchanged, the total MAPE also increases immediately. Thus, after the initial decrease, EPE as well as the eddy heat fluxes begins to increase. With several days lag, EKE also starts to increase and varies in close correlation with EPE. In the quasi-equilibrium state, MAPE and eddy heat fluxes all reach larger values, EPE and EKE are marginally increased which is primarily due to the compensating effect that stronger thermal diffusion also enhances the damping of eddy energies.

We also investigated the transient response of the flow to a sudden reduction of the vertical thermal diffusion, and we found the eddy behavior is just opposite to what we discussed above. EPE and eddy heat fluxes increase immediately as we reduce the thermal diffusion and then decrease gradually as the MAPE is reduced.

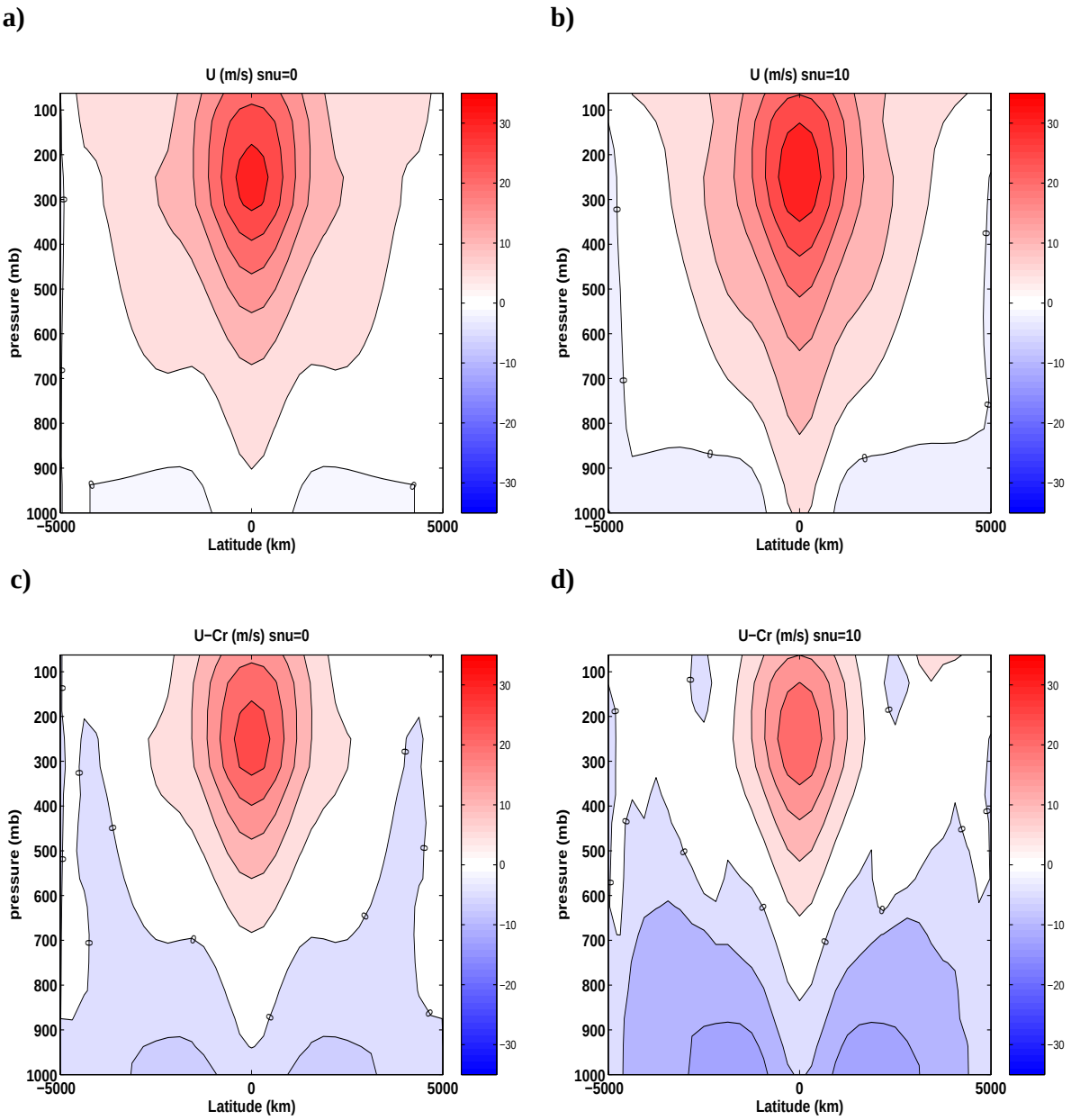

Figure 4-6: Equilibrium state zonal wind for (a) $\mu_s = 0m^2/s$ and (b) $\mu_s = 10m^2/s$, and intrinsic phase speed $U - Cr$ of the dominant wave for (c) $\mu_s = 0m^2/s$ and (d) $\mu_s = 10m^2/s$. Negative value(easterly) appears in the lower levels, contour interval is 5 m/s, zero line is labeled.

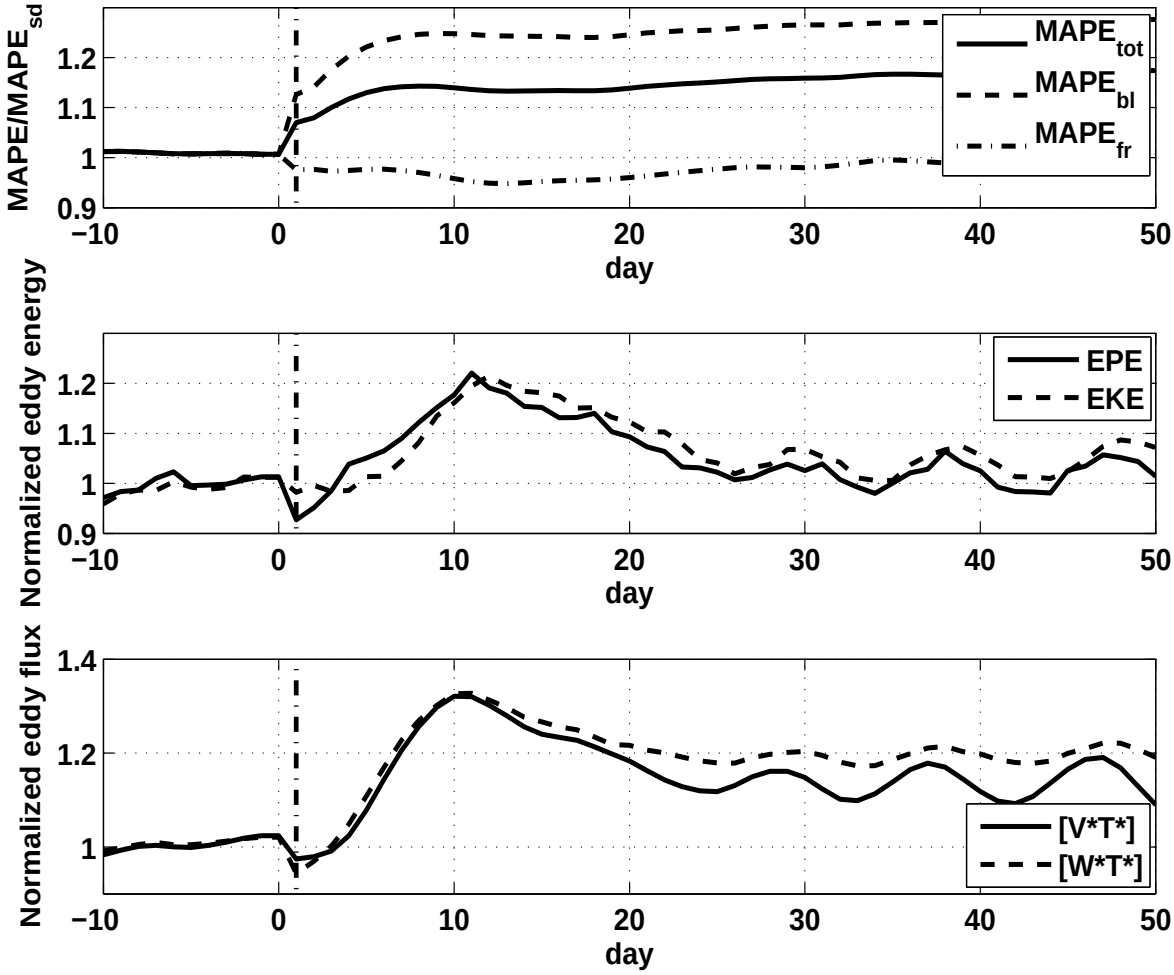

Figure 4-7: Evolution of normalized MAPE averaged globally, averaged over the boundary layer and the free troposphere (upper panel), normalized EKE, EPE (middle panel) and normalized eddy meridional and vertical heat fluxes (lower panel) when the vertical thermal diffusion is suddenly increased at t=0.

4.2.3 Surface heat flux

Since the ocean temperature is fixed in this experiment, the heat exchange between ocean and atmosphere acts to warm the surface air and the ocean surface behaves as an infinite source of heat. To study the influence of this surface heat flux, we vary the value of the heat exchange coefficient C_{dt} in Equation 2.6, and compare it with the standard run.

The equilibrated states for different C_{dt} are displayed in Figure 4-8, from which we find that the surface temperature gradient strongly depends on this surface heat exchange. Without surface heat flux, the surface air temperature gradient is largely reduced. As C_{dt} increases, which indicates stronger heat exchange, the equilibrated surface air temperature gradient is forced to be closer to the temperature gradient of the underlying surface. Associated with this, the meridional eddy heat fluxes, as shown in Table 4.1, are enhanced for stronger surface heat flux.

Combining the results from the previous sensitivity experiments with vertical thermal diffusion, we find that surface air temperatures are mainly determined by the surface heat flux, and with the vertical thermal diffusion in the boundary layer, this surface air temperature gradient can further influence the interior baroclinic equilibration.

If we use the scale estimate,

$$\begin{aligned} \frac{\partial \theta}{\partial t} &\sim \frac{g}{c_p}\frac{\partial F_{sh}}{\partial p} \\ \frac{\theta_{air}-\theta_{sea}}{\tau} &\sim \frac{-gC_{dt}\rho_s(\theta_{air}-\theta_{sea})}{\Delta p} \\ \tau &\sim \frac{\Delta z}{C_{dt}}, \end{aligned}$$

and chose $\Delta z \approx 300m$, and $C_{dt} = 0.03m/s$ as realistic values, then the surface potential temperature relaxation time scale is $10^4 s$, less than one day. This is consistent with the Swanson and Pierrehumbert (1997) study, and confirms our numerical experiment results that the underlying surface temperature, through the surface heat flux, plays an important role in determining the equilibrium states. This time scale is much shorter than the relaxation time scale of the ocean mixed layer, which indicates that fixed ocean surface temperature is

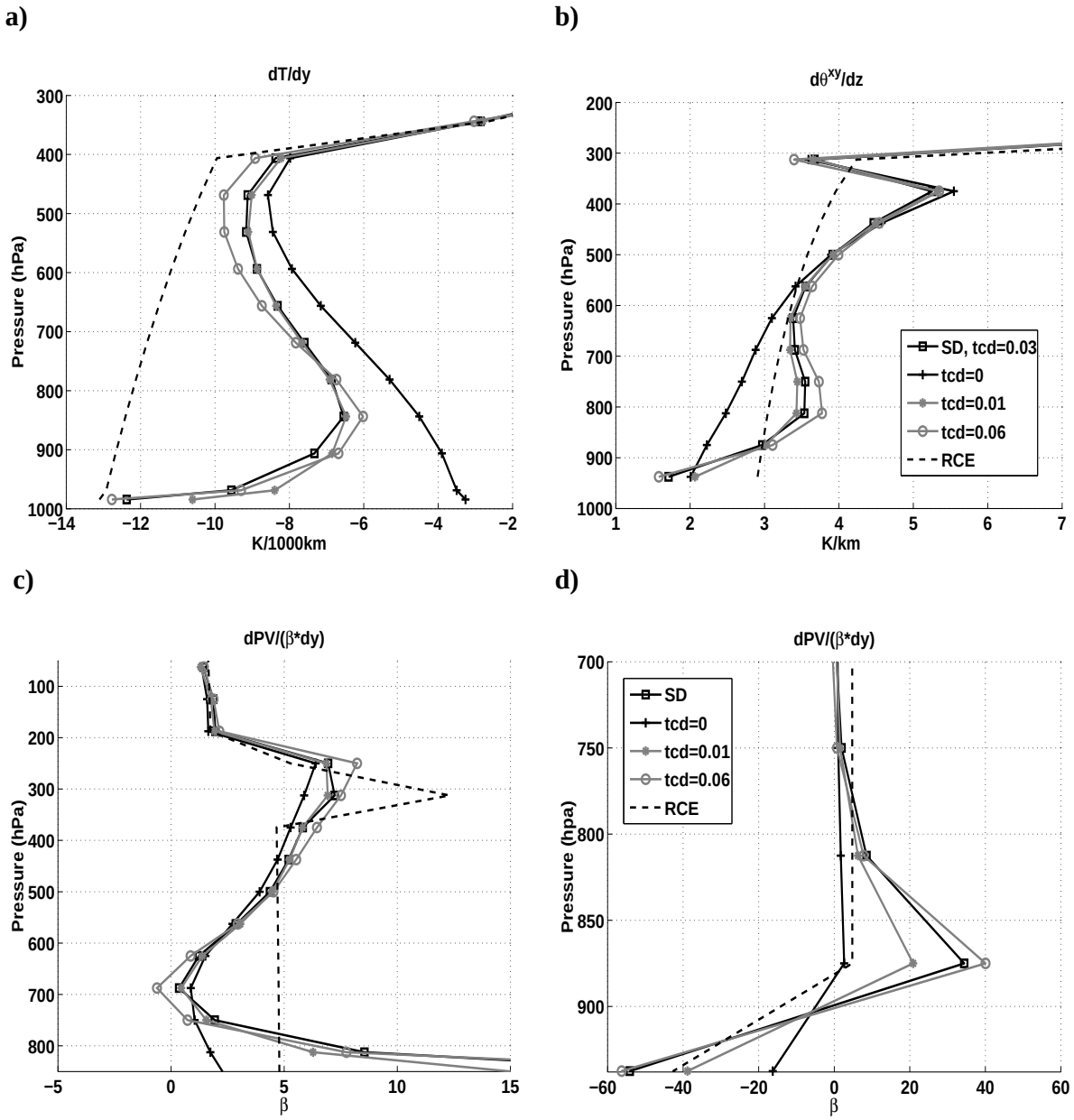

Figure 4-8: Comparison of equilibrated state a) zonal mean dT/dy at the center of the channel, b) $d\overline{\theta}^{xy}/dz$, c) zonal mean $dPV/(\beta dy)$ at the center in the free tropopause and d) in the boundary layer for standard run (open square), the $C_{dt} = 0$ (plus sign), 0.01 (asterisk), and 0.06 m/s (open circle) runs, and the RCE state (black dashed curves).

a reasonable approximation for this study.

4.2.4 Surface friction

Stronger ($C_{df} = 0.06m/s$)[4] and weaker ($C_{df} = 0.01m/s$) surface friction runs are carried out in this section to compare with the standard run. As displayed in Table 4.1, surface friction has a large influence on the meridional eddy heat flux. Weaker surface friction results in stronger meridional eddy heat flux. However, as shown in Figure 4-9, the response of the equilibrated mean fields to the increasing surface friction is not monotonic. In the strong surface friction case, the temperature gradient at the center of the channel is reduced less through the whole troposphere than in the standard run. For weak surface friction, dT/dy is more reduced in the upper troposphere compared to the standard run but not in the lower troposphere. The equilibrium PV gradient is not efficiently eliminated as we reduce the surface friction. Strong boundary layer PV gradients are observed in all the three runs. The PV gradient also displays a non-monotonic tendency when reducing surface friction. Under weak surface friction, it is even stronger near $750hpa$ than in the other two cases.

The spectral distribution of eddy kinetic energy (Figure 4-10(a), (b), (c)) shows that enhancing the surface friction also affects the dominant wave length in the equilibrium state. The dominant wave-number (which is wave 6 in the standard run) shifts to wave-number 4 for $C_{df} = 0.01m/s$, and wave-number 5 for $C_{df} = 0.06m/s$ run. Such an effect is not found when varying the parameters representing the other boundary processes. Besides the dominant eddy scale, surface friction also affects the smaller scale eddy spectral distribution, which implies that the enstrophy cascade and the inertial subrange are imperfect. Under weaker surface friction, the distribution is closer to the K^{-3} lines.

[4]We use stronger FFT filter in the fcd2 run, which makes the smallest eddy scale in the model 875 km instead of 750 km in the other numerical experiments discussed in this paper. We did so because of the numerical instability caused by the discontinuity of T_e across the tropopause. We find that when the larger scale baroclinic eddies near the tropopause are too weak to smooth the sharp temperature discontinuity there, the smallest scale eddies become active near the tropopause and our final states exhibit some unphysical features there, which can be eliminated by using a stronger FFT filter. By comparison we find that using stronger FFT filter only affects the equilibrium state near the tropopause and has no influence on the lower troposphere, and thus does not affect the conclusions we make in this paper.

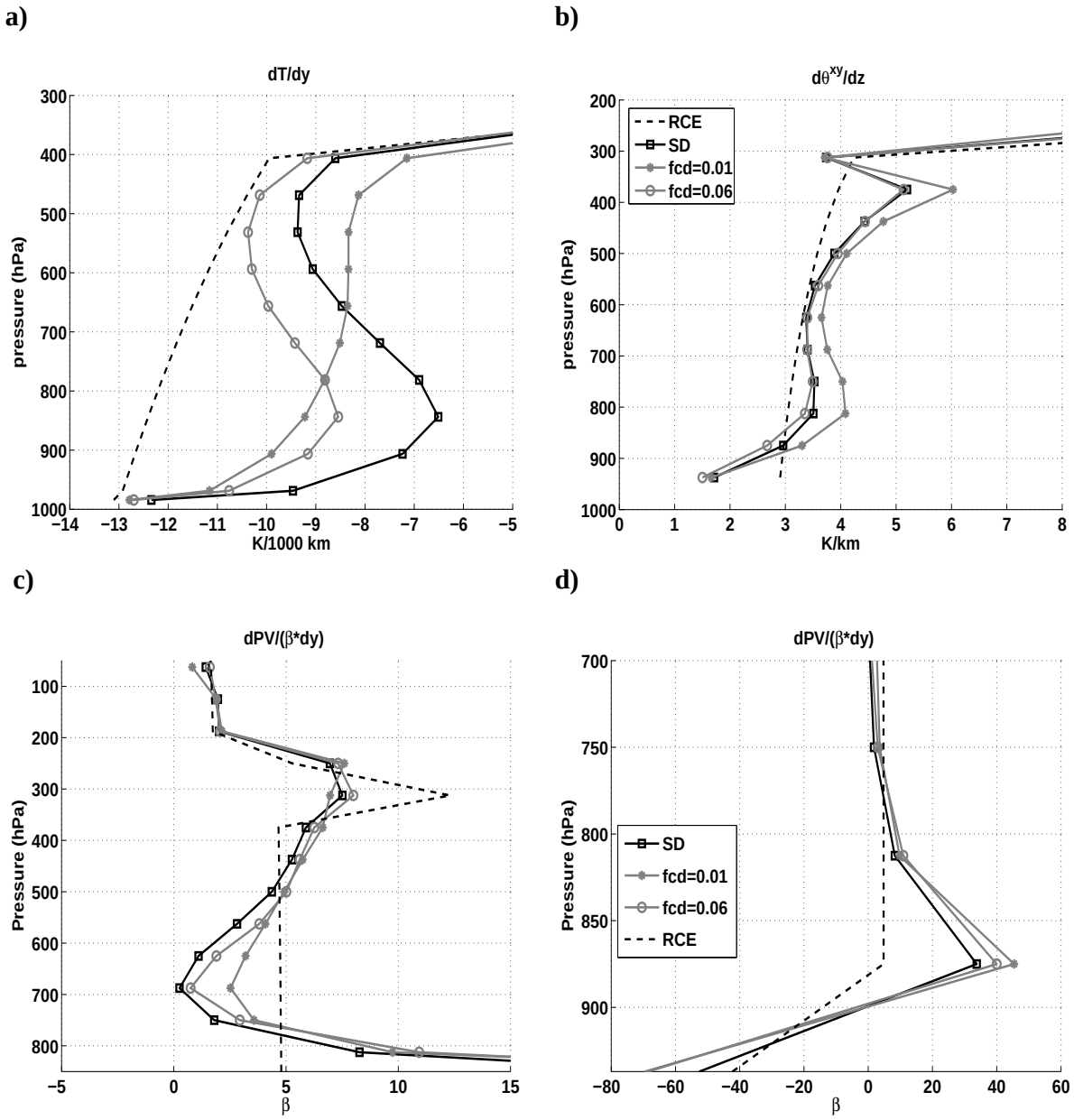

Figure 4-9: Comparison of equilibrated state a) zonal mean dT/dy at the center of the channel, b) $d\overline{\theta}^{xy}/dz$, c) zonal mean $dPV/(\beta dy)$ at the center in the free tropopause and d) in the boundary layer for standard run (open square), the $C_{df} = 0.01$ (asterisk), $0.06ms^{-1}$ (open circle) runs and RCE state (black dashed curves).

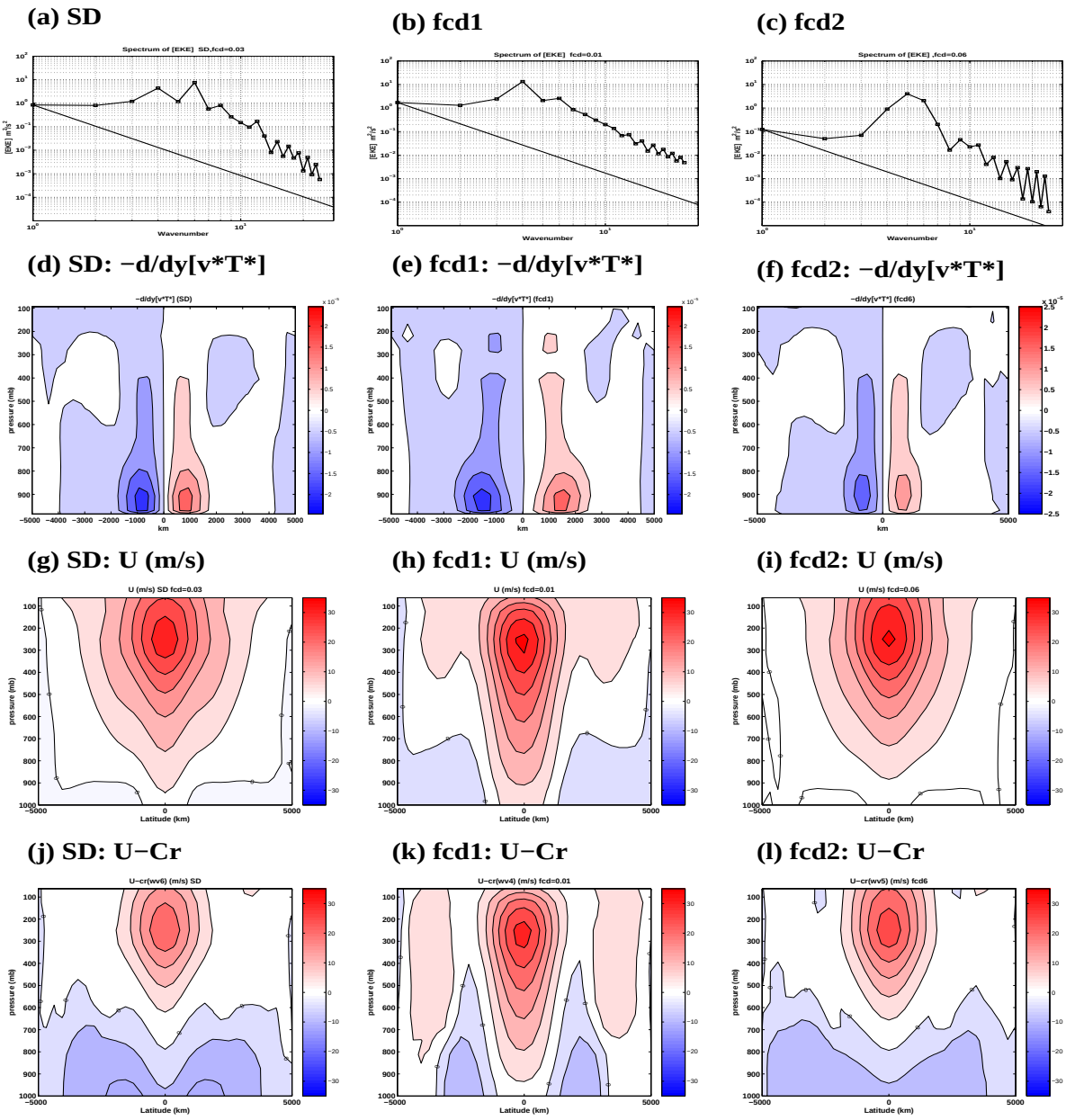

Figure 4-10: Spectral distribution of the equilibrium state eddy kinetic energy (EKE) (a), (b), (c), where the straight line denotes the k^{-3} power law and the cross sections of the equilibrium state convergence of the meridional eddy heat flux $-d/dy[v^*T^*]$ (d), (e), (f); zonal wind (g), (h), (i); and intrinsic phase speed $U - Cr$ of the dominant waves (j), (k), (l) for the standard run, $C_{df} = 0.01m/s$ run and $C_{df} = 0.06m/s$ run, respectively. Contour interval for U and $U - Cr$ is $5m/s$. Zero line is labeled.

To understand the non-monotonic response to the surface friction, the meridional distribution of the temperature differences between the equilibrium state and the initial state in the lower level ($875hpa$) and the upper level ($437.5hpa$) are plotted in Figure 4-11, from which we find baroclinic eddies reduce the temperature gradient by warming the poleward part of the flow and cooling the equatorward part of the flow. In both upper and lower levels, the magnitude of the temperature modification is larger for weaker surface friction, but the meridional distribution of the modification in the lower level is different as we vary the surface friction. When C_{df} is reduced to $0.01m/s$, the latitude of the strongest modification in the lower level moves away from the center of the channel. Thus, the temperature gradient is less reduced at the center of the channel but more modified in the flanking latitudes. In the upper levels we find that the latitude of the maximum temperature modifications are unchanged in our experiments.

4.2.5 Transient response to surface friction

To understand the variation of the lower level meridional distribution of the temperature modifications displayed in Figure 4-11, we also study the transient response of the flow to the sudden reduction of the surface friction. We did an experiment which starts from the equilibrium state of the standard run and is forced by weaker surface friction ($C_{df} = 0.01m/s$). After integrating the model for long enough times, we obtain an equilibrium state (i.e. mean field and eddy heat fluxes) almost the same as the ($C_{df} = 0.01m/s$) run in Section 4.2.4. The transient response of the lower level flow is plotted in Figure 4-12.

The domain averaged EKE as well as EPE, as shown in Figure 4-12(a), grows immediately after reducing the surface friction. Through Fourier analysis, we find the dominant wave scale switches from wavenumber 6 to wavenumber 4, which is consistent with the equilibrium run result. The meridional variation when reducing the surface friction in the lower level ($875hpa$) is also displayed in Figure 4-12, in which the direct response to the reduced surface friction is an acceleration of the lower level zonal wind. Under weaker surface friction, as shown in Figure 4-12(c), a $U - Cr > 0$ region for the dominant wave appears, with the

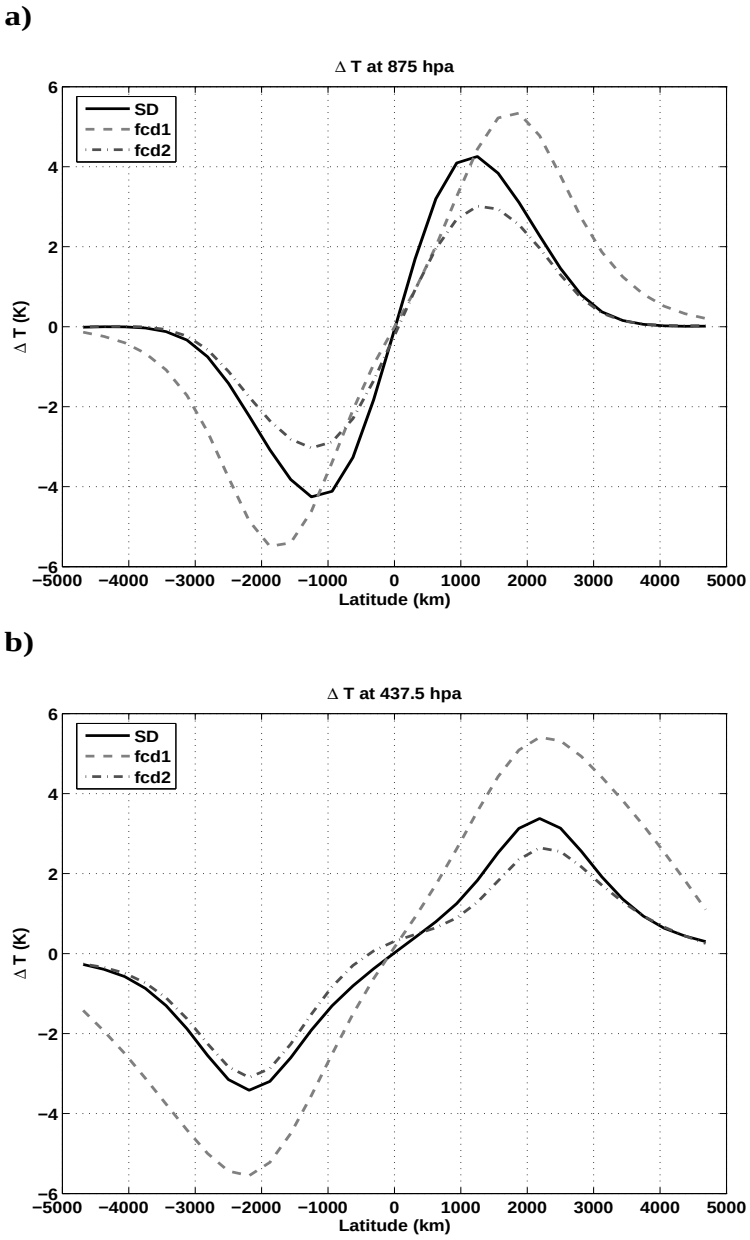

Figure 4-11: Difference of temperature between equilibrium state and RCE (initial) state for standard run (solid curves), $C_{df} = 0.01m/s$ run (dashed curves) and $C_{df} = 0.06m/s$ run (dot-dashed curves) at (a) 875 hpa and (b) 437.5 hpa.

emerging critical latitudes moving away from the center of the channel. During day 10-20, the critical latitudes reach their furthermost location, which is around $1500km$ away from the jet's center. The meridional distribution of $-\frac{\partial}{\partial y}[v^*T^*]$, which is the eddy forcing term in the thermodynamic equation (Holton, 2004), is also displayed in Figure 4-12(c), in which the locations of the maximum eddy forcing also move away from the center of the channel and reach their furthermost latitudes almost at the same time. The variation of the latitudinal distribution of the maximum eddy forcing is well correlated to the variation of critical latitudes. The latitudes where temperature is most modified compared to the RCE state, as shown in Figure 4-12(d), evolves in the same pattern as the eddy forcing, which is consistent with what we have found in Figure 4-11.

Our above transient response study implies a critical latitude - eddy forcing mechanism in our model. If we go back to our equilibrium runs in Section 4.2.4, we find that the distributions of lower level eddy forcing and critical latitudes in the equilibrium states under different surface friction, as shown in Figure 4-10, are consistent with this mechanism.

Figure 4-10(d), (e) and (f) show that the change of the meridional distribution of the temperature modifications is closely related to the meridional distribution of eddy forcing $-\frac{\partial}{\partial y}[v^*T^*]$. As we increase the surface friction, the eddy forcing becomes weaker but still keeps a similar meridional distribution. However, when the surface friction is sufficiently weak, the position of the maximum forcing in the lower levels shifts away from the center of the channel, and the eddy forcing at the center becomes weaker.

The structures of the zonal wind (Figure 4-10(g), (h), (i)) and the distributions of $U - C_r$ for the dominant wave in the equilibrium state (Figure 4-10(j)[5], (k), (l)) illustrate that even though under stronger surface friction, the lower level westerly and easterly wind bands become weaker, the distribution of $U - Cr$ has similar structure to the standard run. In both cases, the critical levels are near $800hpa$, which, as suggested by Lindzen and Barker (1985) and Simmons and Hoskins (1978), indicates that the eddies in the lower levels cannot

[5]As shown in Figure 4-10(a), wave-number 4 is the second most important component in maintaining the equilibrium state, whose distribution of $U - C_r$ is in the same pattern as wave-number 6 and the critical level in the eddy source latitudes is also near $800hpa$.

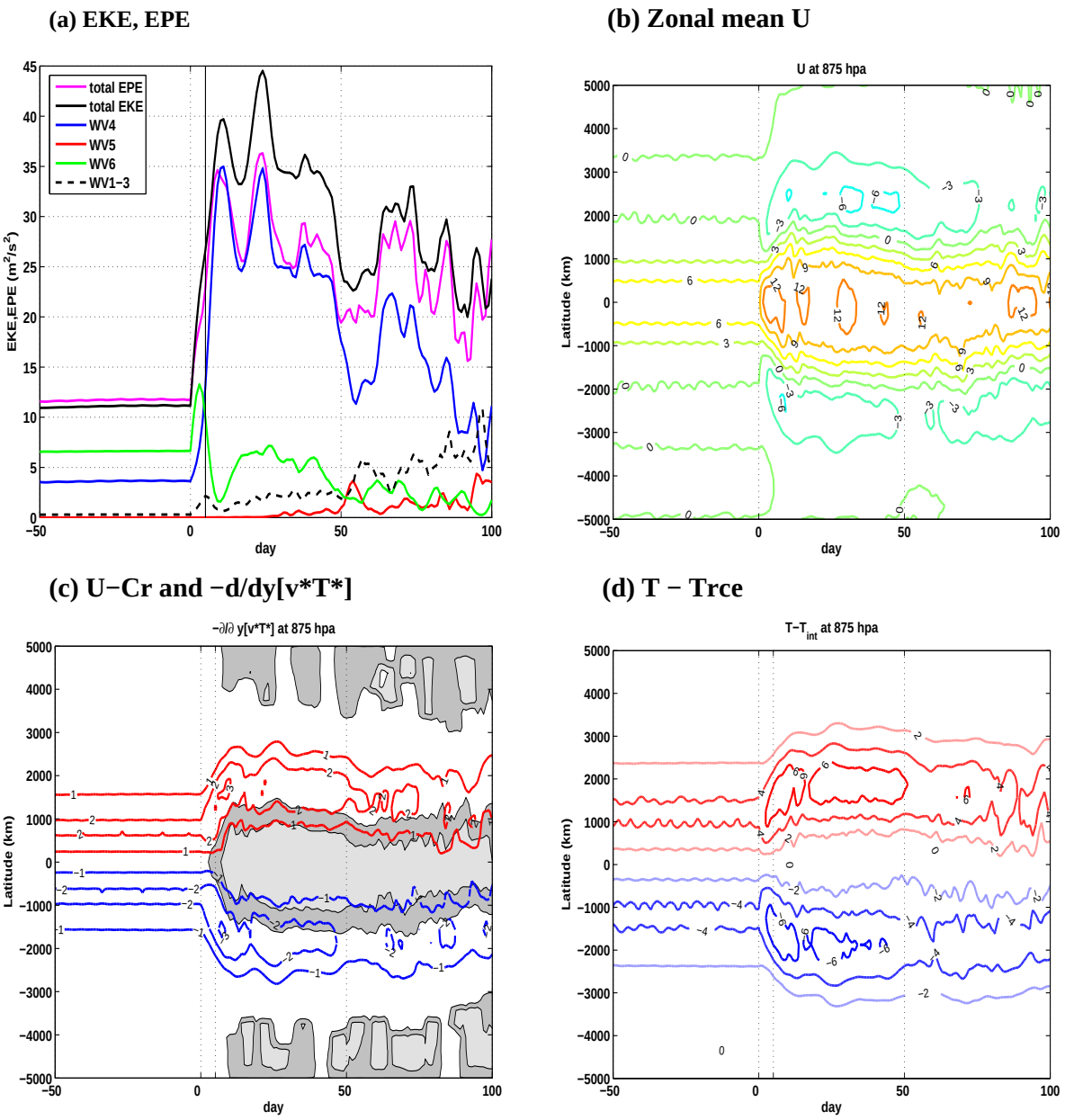

Figure 4-12: Evolution of a) total eddy kinetic energy and EKE from wavenumber 4, 5, 6 and wavenumber 1-3, and response of $875hpa$ b) zonal mean zonal wind, c) $U-Cr$ (shaded) of the dominant wave and $-\partial/\partial y[v^*T^*]$ (contour), and d) the temperature modification compared to the RCE state $T - T_{RCE}$ to the reduced surface friction. Curve interval is $3m/s$ for the zonal wind, $1.0 \times 10^{-5}K/s$ for $-\partial/\partial y[v^*T^*]$, and $2K$ for $T - T_{RCE}$. For $U - Cr$, the shaded region is the area where $U - Cr > 0$, the contours plotted are 0, 5, 10 m/s, and the thin dashed straight line shows the day when the dominant wave becomes wavenumber 4.

propagate as waves and are dissipated in their source latitude. However, when the surface friction is sufficiently weak, the jet in the lower level becomes stronger and as shown in Section 4.5, the dominant eddy scale becomes larger, with a smaller phase speed. Thus, the critical level drops to the surface. This allows the eddies in the lower levels to propagate away from the center of the channel and the location of the wave absorption in the lower levels could move away from the center.

We also want to point out that as we reduce the surface friction, as displayed in Figure 4-10(h) and Figure 4-12(b), the barotropic shear also becomes stronger. The barotropic decay term in the energy cycle also becomes stronger, which can partly compensate the reduction of frictional dissipation for the eddy energy budget. However, different from James and Gray (1986) and James (1987), the net result of reducing surface friction in our simulation is an increase of eddy energies as well as eddy heat fluxes for most of the parameter regime. The 'barotropic governor' effect, is not the dominant mechanism that helps maintain the strong temperature gradient at the center of the channel.

4.2.6 Vertical momentum dissipation

The effect of the turbulent vertical momentum transport in the boundary layer is also studied by keeping all the other parameters unchanged and varying the coefficient μ_m in Equation 2.11. Compared with the standard run, as shown in Figure 4-13, the vertical momentum dissipation in the boundary layer has little influence on the equilibrium states. The static stability is almost insensitive to the intensity of the momentum dissipation and only the lower level temperature gradient is slightly larger for the week momentum dissipation case. The influence of the momentum dissipation is weak on the PV gradient too. Vertical momentum dissipation damps the eddy heat fluxes slightly.

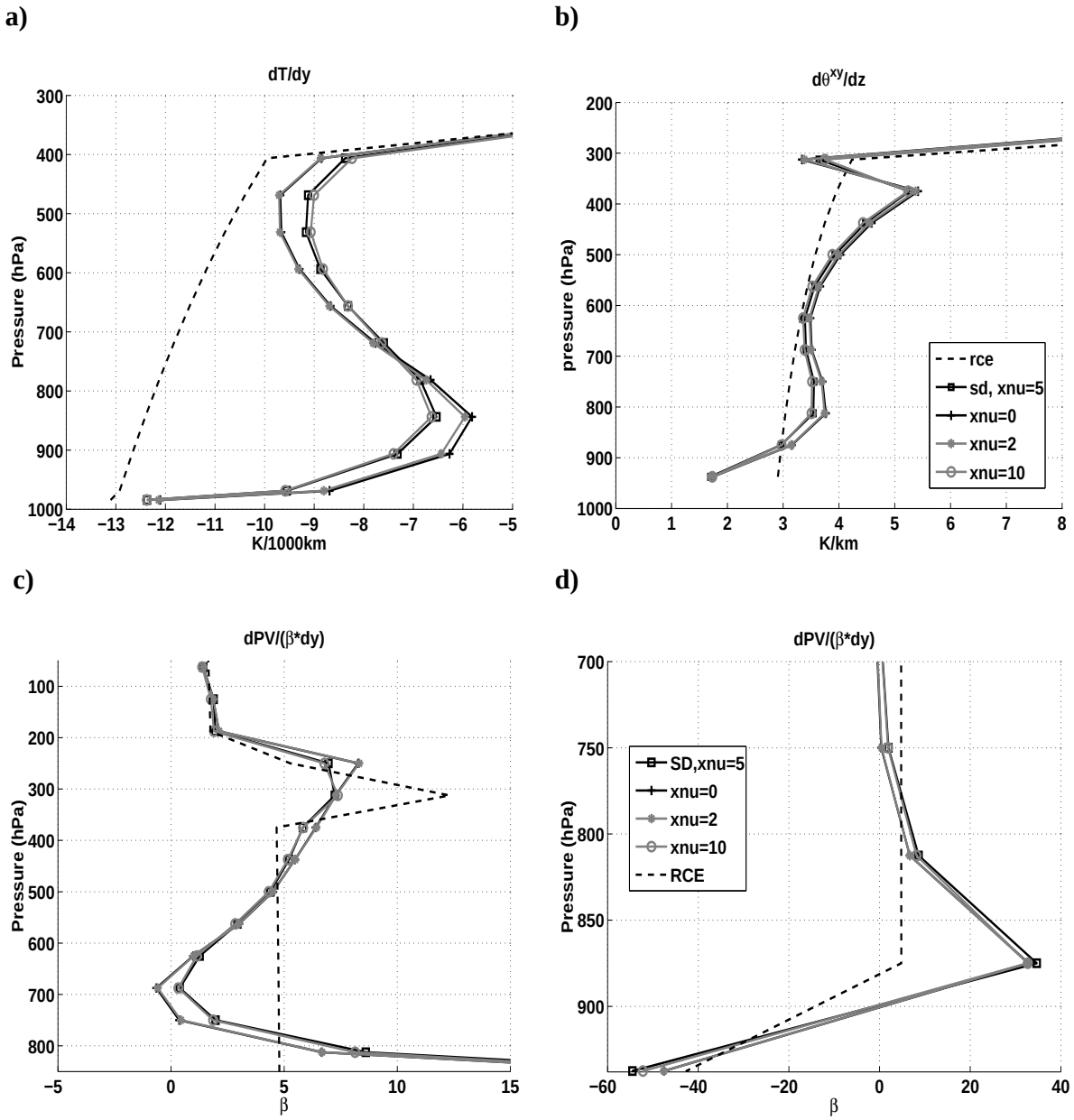

Figure 4-13: Comparision of equilibrated state zonal mean a)dT/dy at the center of the channel, b) $d\bar{\theta}^{xy}/dz$, $dPV/(\beta dy)$ at the center c) in the free tropopause and d) boundary layer for standard run ($\square$), $\mu_m = 0m^2/s$ run ($+$), $\mu_m = 2m^2/s$ run($*$), and $\mu_m = 10m^2/s$ run ($\circ$) and RCE state (black dash curves).

4.3 Dependence on the boundary layer depth

In this section, we study how the depth of boundary layer affects our results. We use four different thermal diffusion and momentum dissipation profiles to compare with the standard run : $\nu(p) = \mu(\frac{p-p_{bl}}{p_o-p_{bl}})^3 m^2/s$ for levels below p_{bl} and set $\nu(p) = 0$ for levels above it, where $p_{bl} = 1000, 850, 700, 500hpa$, respectively. ($p_{bl} = 1000hpa$ is the case where vertical thermal diffusion and momentum dissipation are not considered.)

Without boundary layer diffusion, as shown by Figure 4-14(a), (c), (e) and (g), the mean field and eddy heat flux distributions are similar to the Snu0 Run (where thermal diffusion is zero), which confirms our conclusion that boundary layer momentum dissipation has very little effect on the equilibrium state. This also indicates that the influence of the boundary layer depth is primarily associated with the vertical thermal diffusion. From Figure 4-14(g), we find that the response of the eddy heat flux is similar to that in the Snu Runs, that is deeper boundary layer diffusion results in stronger eddy heat flux. For the mean fields, the free troposphere PV gradient is also similar to the Snu Runs. The PV gradient is homogenized over a deeper layer when the boundary layer is shallower. However, the response of the mean temperature gradient and stratification is more complicated. As the boundary layer becomes shallower the temperature gradient distribution is closer to the zero boundary layer diffusion run. From Figure 4-14(c), the distribution of the static stability is sensitive to the diffusion profile. For $p_{bl} = 500, 700hpa$, the response of $d\overline{\theta}^{xy}/dz$ is also similar to the Snu Runs. Under deeper boundary layer diffusion, the lower level stabilization is more efficiently prevented. However, when the boundary layer becomes shallow, where $p_{bl} = 850hpa$, $d\overline{\theta}^{xy}/dz$ above $850hpa$ is similar to the state without boundary layer diffusion but strongly stabilized at $875hpa$.

Even though the depth of boundary layer can influence the equilibrium state, we find that with different boundary layer depths, the response of the flow to different boundary layer processes is similar to that in Section 4.2. For example, if we use the $p_{bl} = 500hpa$ profile, and do the same experiments as in Section 4.2, the equilibrium states illustrate the same tendencies to the boundary layer processes. However, as the the boundary layer becomes

shallower, our model has little sensitivity to the strength of boundary layer thermal diffusion and surface heat flux. As shown in Figure 4-14(b), (d), (f) and (h), when $p_{bl} = 850hpa$, the equilibrium state is almost insensitive to μ_s when μ_s is nonzero. However, without thermal diffusion, there are still large variations in eddy heat fluxes as well as the temperature gradient. Even with a shallow boundary layer, including these two boundary layer processes are still important in simulating the real atmosphere.

4.4 Influence of the ageostrophic wind

In Section 4.2, we neglected the frictional forcing by ageostrophic winds. This could influence our previous conclusions, especially on the role of the surface friction, since the ageostrophic winds are supposed to be largest near the surface. In this section, we will discuss how including ageostrophic winds influences our results. The ageostrophic winds are calculated according to Section 2.2.

Since surface friction is affected most by including ageostrophic winds, we have repeated the parameter study in Section 4.2.4. We varied C_{df} from 0.015 to $0.15m/s$ and found that in all these cases ageostrophic winds are comparable with the geostrophic winds only at the first model level. The response of the equilibrated state mean fields to the variation of C_{df} is shown in Figure 4-15. From Figure 4-15(a) and 4-15(b) we find, since the ageostrophic winds are always against the geostrophic winds, they reduce the shear stress by surface friction. Thus comparing with Figure 4-9, we find that the net effect of including the ageostrophic winds is similar to reducing the surface drag coefficients. The ageostrophic winds get larger with larger surface drag. This enhances the negative feedback between surface drag coefficient and surface wind. Thus, the changes of the mean fields with C_{df} are smaller. Nevertheless, the tendency of the equilibrium state to increasing surface friction is still very similar to that in Section 4.2.4, the non-monotonic response is still clearly observed in Figure 4-15(a), and the temperature in the lower levels is more efficiently modified in the flank regions of the jet for weak surface friction (Figure 4-15(b)). The PV gradient, as shown in Figure 4-15(c) and 4-15(d), is still very robust as we vary C_{df}, and due to the strong temperature gradient

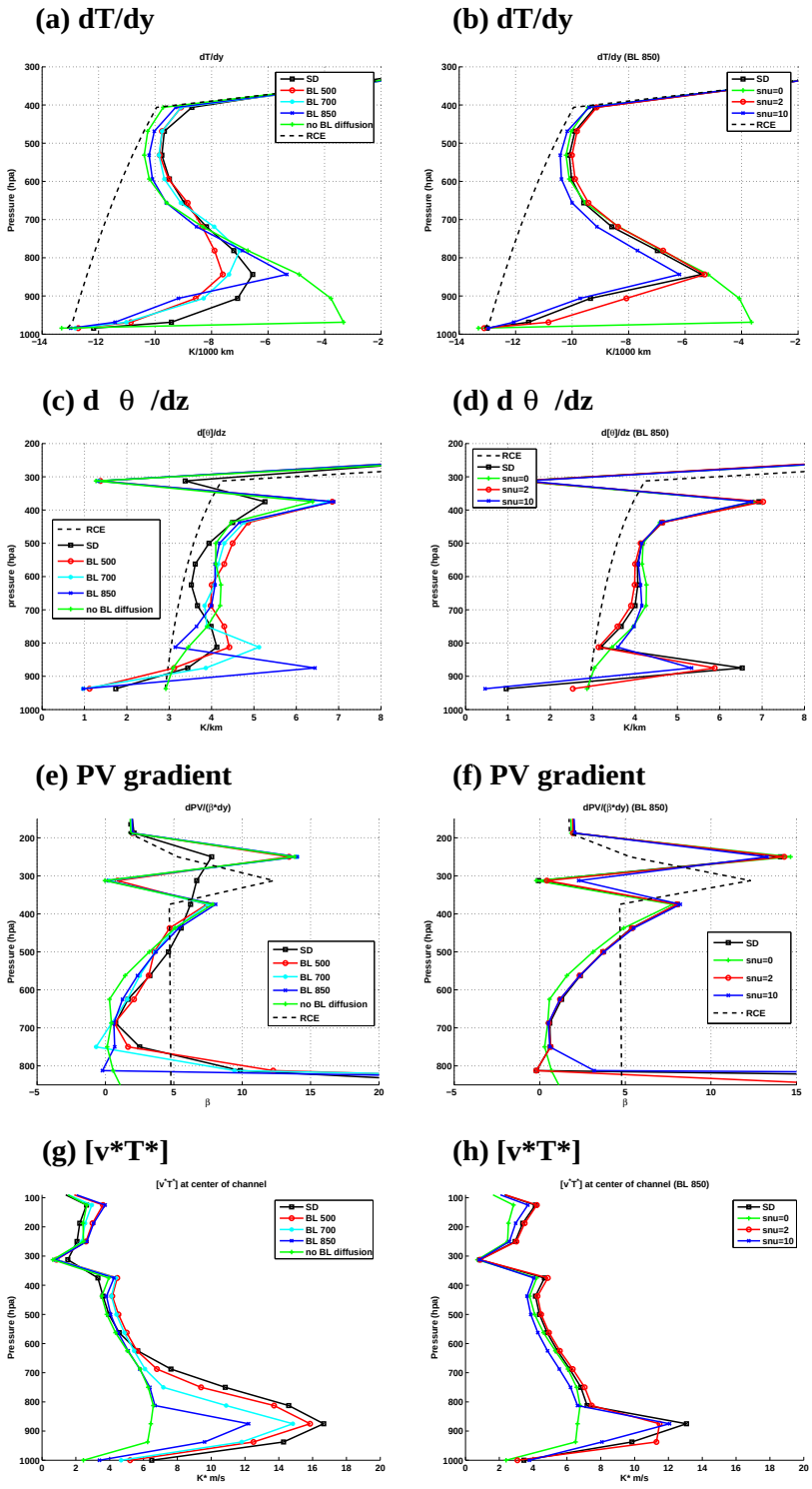

Figure 4-14: Comparison of equilibrated state zonal mean a)dT/dy at the center of the channel, c) $d\overline{\theta}^{xy}/dz$, e)$dPV/(\beta dy)$ and g) meridional eddy heat flux at the center of the channel for different p_{bl}. Figure b), d), f) and h) as for a), c), e) and h) respectively, but for different μ_s when $p_{bl} = 850hpa$.

remained in the lower levels, the PV gradient near $700hpa$ is less reduced when the surface friction is weak.

The difference of the eddy activity between simulations with ageostrophic winds and the simulations in Section 4.2.4 is also plotted in Figure 4-16. From Figure 4-16(a), we find in both cases EKE is reduced for enhanced surface friction but varies more slowly when including ageostrophic winds. The averaged eddy length scale $\bar{L}$ in both cases is plotted in Figure 4-16(b), where we define $\bar{L} = \frac{L_{channel}}{\bar{k}}$, $\bar{k} = \frac{\int kE(k)dk}{\int kdk}$, and $E(k)$ is the spectral distribution of EKE. To test whether $\bar{L}$ could be related to the Rhines scale L_β, where${L_\beta}^2 = \sqrt{EKE_{bt}}/\beta$, EKE_{bt} is the barotropic EKE, EKE_{bt} is also plotted in Figure 4-16(a). Unlike the non-monotonic response mentioned in Section 4.2.4, as EKE_{bt} decreases, the eddy length scale decreases as well. One possible reason for this difference is that EKE as well as EKE_{bt} in the geostrophic case decreases with C_{df} much faster and can reach the regime of very weak eddy activity. Thus, instead of an upscale energy cascade, the eddy behavior in this regime is more linear. As shown in the linear instability study by Card and Barcilon (1982), shorter waves are more easily damped by the surface friction, therefore the linearly most unstable mode shifts slowly to larger scales under stronger surface friction. As shown in Figure 4-16(a), the EKE_{bt} in the ageostrophic case is always larger than the geostrophic case, especially when the surface friction is strong, thus this 'linear effect' on the eddy scale cannot play a role.

We have also done experiments to test whether including the ageostrophic wind will influence the role of the momentum dissipation. For the parameter regime near the default value and with stronger momentum dissipation, we still find that the equilibrium state only varies slightly with the momentum dissipation (results are not shown here).

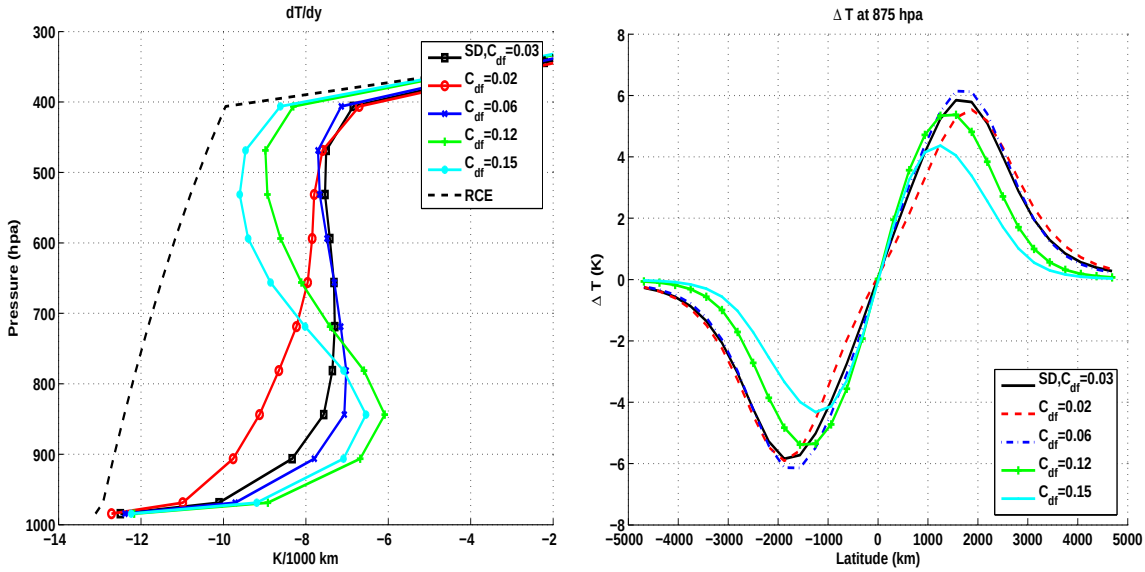

(a) dT/dy at the center

(b) $T - T_{RCE}$ at 875 hpa

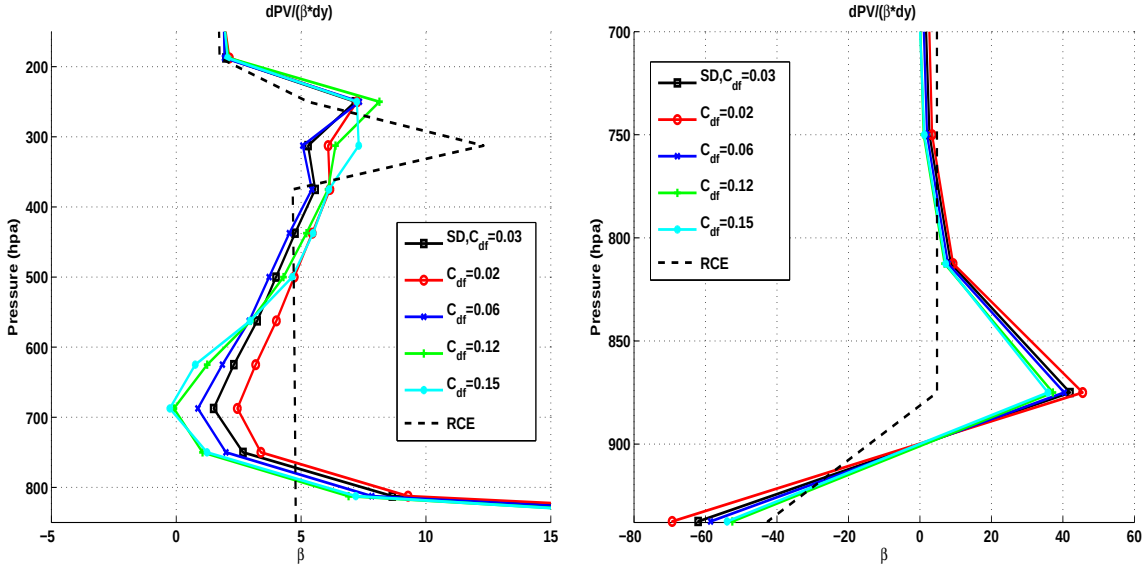

(c) PV gradient in free troposphere

(d) PV gradient in B.L.

Figure 4-15: Comparison of equilibrated state zonal mean a)dT/dy at the center of the channel, b) $T - T_{RCE}$ at 875 hpa, $dPV/(\beta dy)$ at the center c) in the free tropopause and d) boundary layer under different C_{df}, when including the ageostrophic winds.

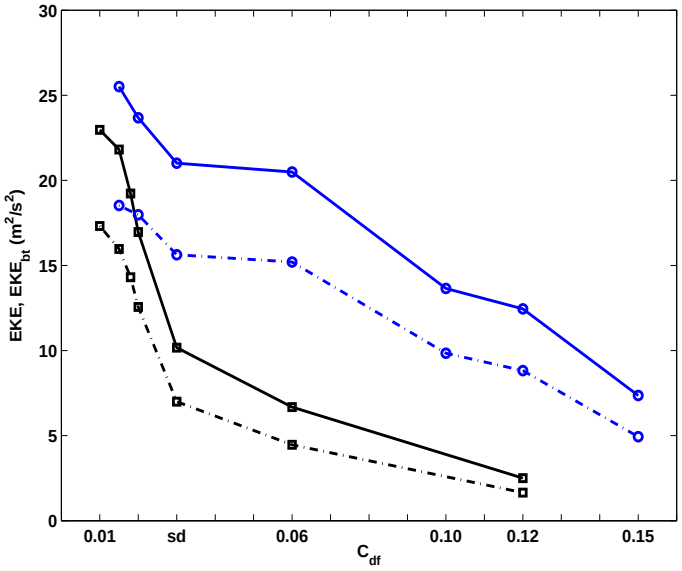

(a) EKE, barotropic EKE

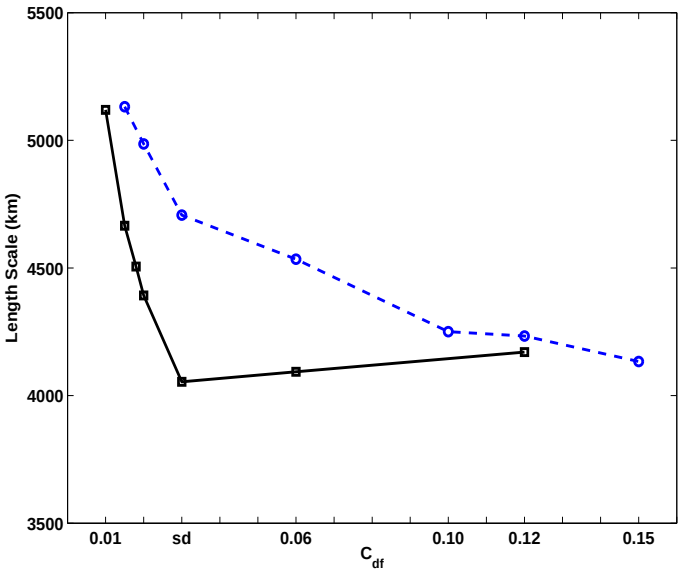

(b) Eddy length scale

Figure 4-16: Variation of the equilibrium state a) global averaged EKE (solid curves), barotropic EKE (dot-dashed curves), and b) eddy length scale as a function of surface friction when not including (□) and including (○) ageostrophic winds, where the value of C_{df} used in the standard run is labeled.

4.5 Appendix: spectral distribution of eddy heat flux and critical layer evolution

Using the same method as Randel and Held (1991), we calculate the equilibrium state zonal wavenumber - phase speed covariance spectra of $[v^*T^*]$ at $875hpa$ at the center of the channel for the standard run and $C_{df} = 0.01m/s$ run. As shown in Figure 4-17, our model has a simple spectral distribution in the equilibrium state, which is consistent with the fact that the maintenance of the equilibrium state is dominated by the wave-mean flow interaction. In the standard run, most of the lower level eddy heat flux comes from wavenumber 6 with phase speed around $8m/s$, whose magnitude is almost 10 times bigger than adjacent wavenumbers. With weaker surface friction, almost all the eddy heat flux comes from wavenumber 4 with phase speed around $4m/s$. Even though there is still a minor peak in wavenumber 6 with phase speed around $11m/s$, its contribution is much more smaller than wavenumer 4. Thus, in Section 4.2, we only plot $U - Cr$ for the dominant waves.

As displayed in Figure 4-3, our equilibrium state is not a totally steady state. Besides showing the statistical distribution of $U - Cr$ in the equilibrium state, in Figure 4-18, we also show the evolution of $U - Cr$ of the dominant waves at the center of the channel for the standard and weaker surface friction run. We find in the equilibrium state, the critical layer in the standard run varies from $750hpa$ to $850hpa$. Under weaker surface friction, the critical layer at the center of the channel disappears most of the time, and at $875hpa$, $U - Cr$ is always positive, which confirms our statistical results.

4.6 Summary and discussion

In this chapter, by studying each of the boundary layer processes, we have investigated their different roles in eddy equilibration. Our results show that vertical thermal diffusion, along with the surface heat flux, is the dominant process that prevents the homogenization of the potential vorticity in the boundary layer, which provides an explanation for why the baroclinic adjustment theory fails to work there. When including these two processes into

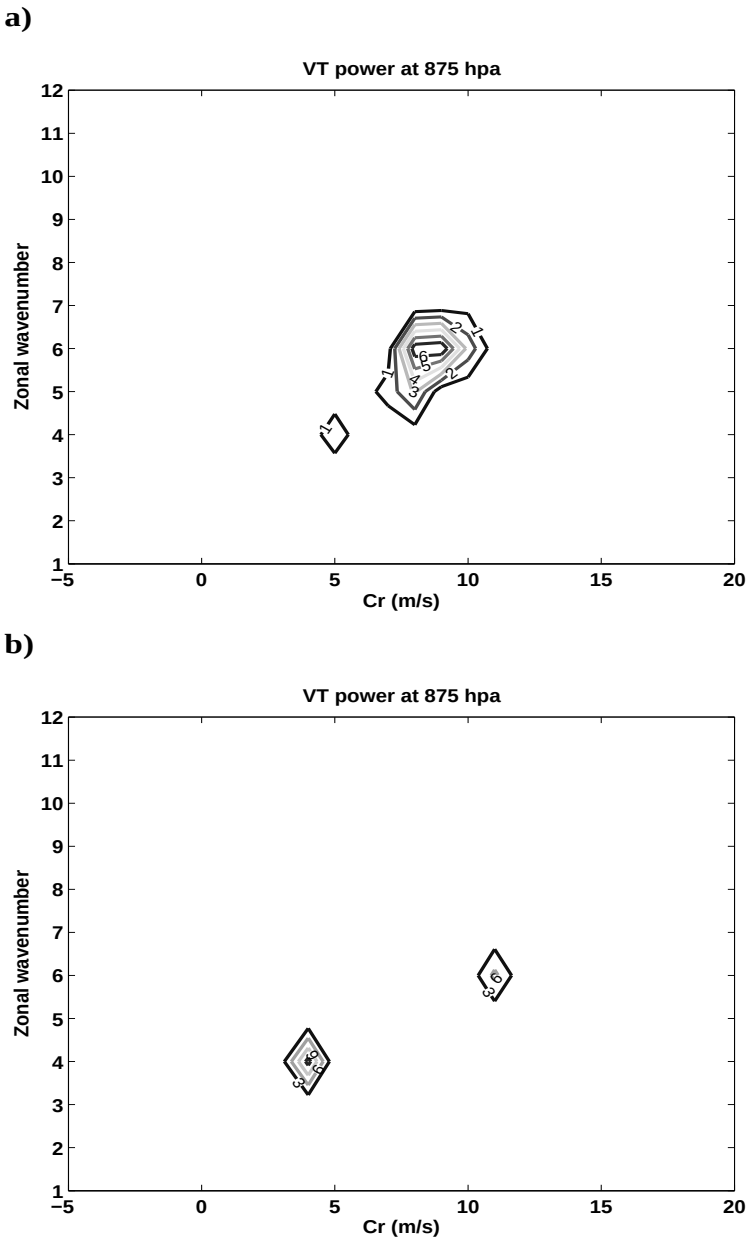

Figure 4-17: Zonal wavenumber - phase speed covariance spectra of $[v^*T^*]$ at 875hpa at the center of the channel for a) SD run and b) $C_{df} = 0.01m/s$ run. The contour interval is $1K * m/s * \Delta Cr^{-1}$ for SD run and 3 $K * m/s * \Delta Cr^{-1}$ for $C_{df} = 0.01m/s$ run (zero contour is not plotted), where the unit phase speed interval is 1.0 m/s.

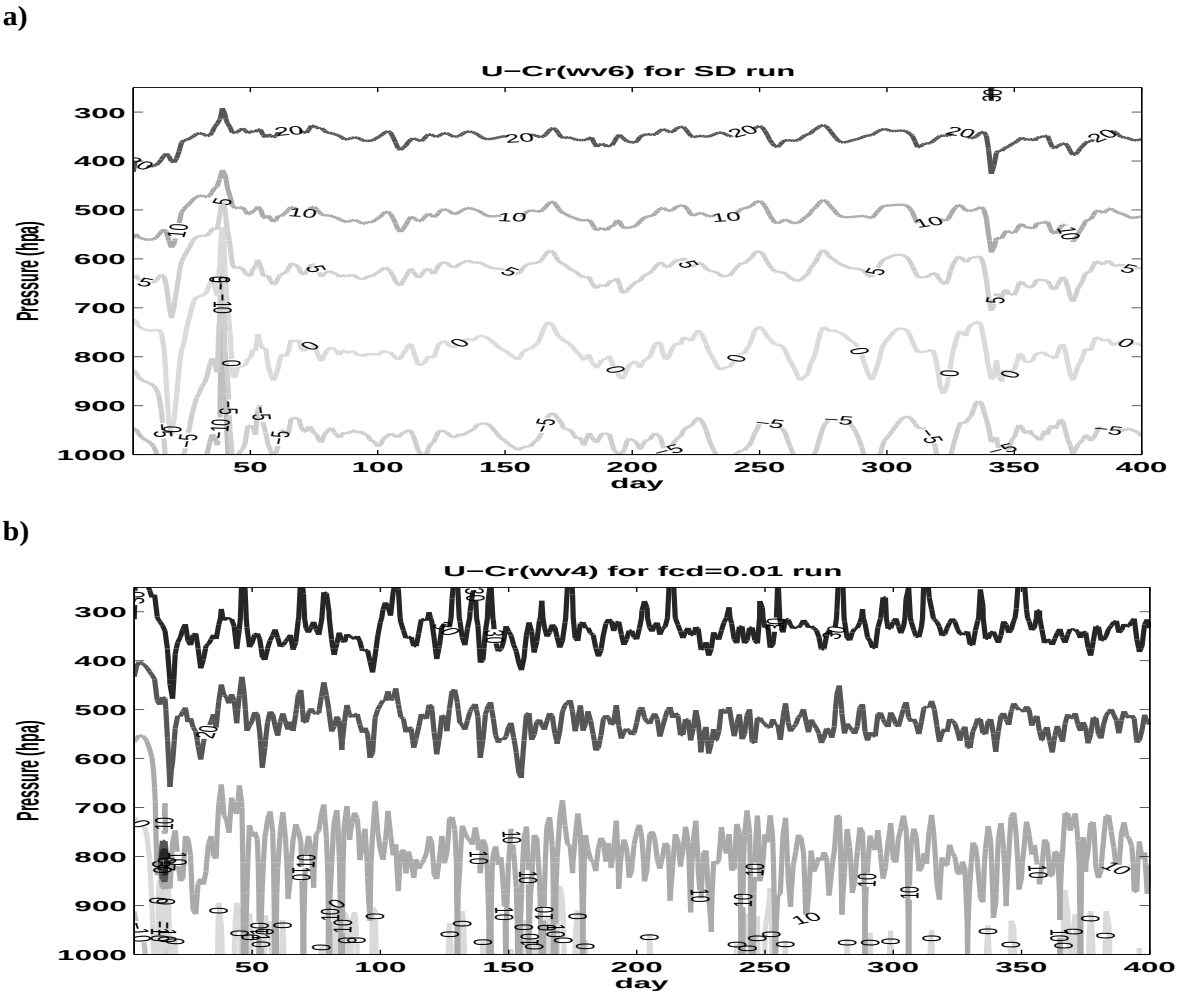

Figure 4-18: Evolution of intrinsic phase speed $(U - C_r)$ of the dominant wave at the central of the channel in the first 400 days for (a)standard run and (b)$C_{df} = 0.01m/s$ run.

the model as suggested by Swanson and Pierrehumbert (1997), we find that the surface heat flux is the dominant factor that determines the surface air temperature gradient. Vertical thermal diffusion couples the boundary layer, even the atmosphere above the boundary layer, with the surface air, so that the flow in the boundary layer can 'feel' the strong temperature gradient at the surface. Thus, even though the surface temperature mixing by the baroclinic eddies is strong, the thermal diffusion can efficiently damp the temperature changes, and the lower levels' temperature gradient cannot be greatly reduced. Therefore, by keeping the strong surface temperature gradient as well as preventing the stabilization of the boundary layer by baroclinic eddies, the vertical thermal diffusion modifies the slope of isentropes in the lower levels and suppresses the PV mixing.

The boundary layer vertical thermal diffusion as well as surface heat flux, in general, act as a damping of the modification of the mean fields by baroclinic eddies. However, it is not a damping for the eddy heat fluxes. Instead, stronger thermal diffusion in our model results in stronger eddy heat fluxes. This tendency is not inconsistent to the previous linear instability studies and the eddy life cycle study by Branscome et al. (1989). As shown in Table 4.2, the maximum EKE and poleward eddy heat flux reached in the first eddy life cycle are also reduced when including the surface heat flux. As displayed in Section 4.2.2, the immediate response of EPE and eddy heat fluxes to increased vertical thermal diffusion is still a decrease in their magnitude. However, in equilibrium, there exist two competing effects that influence the eddy behavior. The direct effect is that (consistent with the eddy life cycle study) the boundary layer thermal diffusion is always a damping term for eddy energies. On the other hand, it can also modify the mean flow and maintain the mean flow available energy which is the energy source of baroclinic eddies and can further affect the eddy activity. In equilibrium, this indirect effect on eddies dominates the direct effect, resulting in stronger eddy heat fluxes.

In our study, the equilibrated states vary only slightly with the vertical momentum diffusion, but the meridional temperature gradient displays a large sensitivity to the surface friction. The mechanism through which surface friction modifies the equilibrated states is

more complicated. First, our model shows that surface friction always acts as a damping of eddy activity. It reduces EKE as well as the magnitude of poleward eddy heat flux. In the regime of strong surface friction, this reduced eddy heat flux indicates a weaker eddy forcing and the temperature gradient is not reduced as much. On the other hand, surface friction also modifies the mean flow, and influences the eddy length scale (a phenomenon that could be suppressed in the short channel). These two effects can further influence the distribution of the critical level. In the weak surface friction regime in our model, the lower level zonal wind becomes stronger. The eddy length scale becomes larger and has a smaller phase speed (as shown in Section 4.5). Thus, the critical level in the source latitude drops below the surface and critical latitudes emerge in the lower levels. If eddies are more likely to propagate in the region of $U > Cr$, this implies that eddies in the lower levels are absorbed less near the center but more near the critical latitudes, which changes the meridional distribution of the eddy forcing. In this case, the temperature gradient in the lower levels at the center of the channel is not reduced efficiently.

Although the critical level of the dominant wave drops below the surface under weak surface friction (as suggested by Zurita and Lindzen (2001)), reducing surface friction alone does not result in efficient elimination of the boundary layer PV gradient. The strong boundary layer thermal damping still maintains the strong surface temperature gradient. Instead, the temperature gradient in the lower level is more related to the variation of the critical latitudes.

Table 4.2: Maximum eddy kinetic(EKE), available potential energy (EPE) and poleward eddy heat flux reached at the center of the channel during the first eddy life cycle. Energy expressed as domain averaged energy density. Eddy heat flux is vertical averaged.

Run	C_{dt} (m/s)	EKE (m^2/s^2)	EPE (m^2/s^2)	$[v^*T^*]$ $(K*m/s)$
SD	0.03	23	21	26.5
tcd0	0.00	35	30	31.6
tcd1	0.01	25	22	28.1
tcd2	0.06	22	19	25.3

To conclude this study, our model results have displayed that boundary layer processes play important roles in baroclinic eddy equilibration. This is especially true for the vertical thermal diffusion and the surface heat exchange, which are traditionally neglected or not well considered in the theoretical study of baroclinic eddies and in many atmospheric dynamic models, e.g. James and Gray (1986), Held and Suarez (1994) as well as many recent studies using Held and Suarez's model. The surface heat flux in the real atmosphere can act on the atmosphere with a shorter time scale than the baroclinic eddies. More important, the turbulent vertical heat transport in the boundary layer always acts to reduce the stratification, which is a process these models do not explicitly take into account. As shown in our paper it is one of the major processes that prevents PV homogenization. Without these two processes, we cannot obtain a realistic equilibrium state in the boundary layer.

In this study, we assumed fixed surface temperature, which may not be a good assumption for a land surface. When coupled with an underlying surface with interactive surface temperature, how the vertical thermal diffusion and surface heat flux influence the eddy equilibration is a topic we will investigate in a future study. In the real atmosphere, the boundary layer diffusion, besides being influenced by the turbulent kinetic energy, is influenced by the lower level static stability. In addition, the depth of the boundary layer (discussed in Section 4.3) has large variations over ocean and land. The land surface is also characterized by a strong diurnal cycle. How these factors affect our results still needs study.

Our analysis of the Lorenz energy cycle in the standard run demonstrated that during the evolution and the maintenance of the equilibrium states, boundary layer frictional dissipation is the major sink of EKE. Boundary layer thermal diffusion and the diabatic forcing all act to remove EPE, with the latter contribution being smaller. We note that in some early observational studies (Peixoto and Oort, 1992; Oort and Peixoto, 1983), the sum of these two terms (usually estimated as a residual term from the energy tendency equation) was found to be a generation term for EPE. A plausible source for EPE that is omitted in our model is the release of latent heat. This indicates the limitations of dry simulations as well as the commonly used Newtonian cooling parameterization, and suggests that a more physical

parameterization of the radiative-convective forcing might be needed.

Chapter 5

Spin-up of the atmosphere-surface coupled model

In the last chapter, using our atmospheric model, we have shown that the boundary layer vertical thermal diffusion and the surface heat exchange are the main factors that retain the strong lower level baroclinicity and PV gradient. In those experiments, the underlying surface is kept fixed during the eddy equilibration which is equivalent to assume that compared with the underlying surface temperature variation, the atmospheric adjustment is always quick. This might be a good assumption over an ocean surface but may not be a good one over land. In addition, when studying the longer time scale climate dynamics, fixed underlying surface temperature is also a considerable limitation. Thus, in this and the next chapters, we will investigate the role of the boundary layer processes in a coupled system.

In the new system, a slab surface model is coupled with the atmospheric model to provide an interactive surface temperature distribution. The governing equations of the surface temperature have been shown in Chapter 2. In this chapter, we will carry out the calibration run experiment to specify the parameters used in the surface model to simulate appropriate surface energy fluxes and the Q-flux which represents the ocean heat flux and to calibrate the surface heat budget to provide a reasonable underlying surface temperature. In Section 5.2, we will carry out spin-up runs to show how baroclinic eddies and the Q-flux influence

the equilibrium state in the coupled model.

5.1 Calibration Run

In the calibration run, we use the observed Northern Hemisphere winter time surface temperature difference, which is 43K over midlatitudes, as our calibration state surface temperature distribution, whose latitudinal variation is shown in Figure 5-1(a). With this surface temperature as the lower boundary condition, we first run the uncoupled atmospheric model to an equilibrium state, which is the same as the standard run in Chapter 4. The equilibrium state surface air temperature distribution is displayed in Figures 5-1(a) and 5-1(b). In this section, by comparing with observations and results from a model with a more sophisticated radiation scheme, we will specify the appropriate values for the parameters in Eqs.2.13 to 2.20. Then with the equilibrium state atmosphere temperature, each surface energy flux can be calculated. Based on the method used in Russell et al. (1985) and Sokolov and Stone (1998), we will estimate the 'climatological' Q-flux required in the model (as the residual of other surface energy fluxes) to maintain the calibration state surface temperature.

5.1.1 Specify radiation parameters

The net shortwave radiation into the surface is specified in our model. As shown in Campbell and Haar (1980) and Peixoto and Oort (1992), the annual mean solar radiation at the top of the atmosphere varies from around 300 to 100 Wm^{-2} across the midlatitudes. The net solar radiation at the surface has large space and seasonal variations, and it strongly depends on the cloudiness of the atmosphere (Hsiung, 1986; Hsiung et al., 1989; Darnell et al., 1992; Gupta et al., 1999; Stewart, 2005). As shown in Stewart (2005, Fig.5.3), the seasonal variation of the net solar radiation at surface was estimated under the clear sky condition from Darnell et al. (1992), in which the solar radiation varies from 250 to 0 Wm^{-2} (from 20^o to 70^o) in winter and around 350 Wm^{-2} through most of the midlatitudes in summer. In our equilibration run experiments, the net solar radiation is fixed and specified

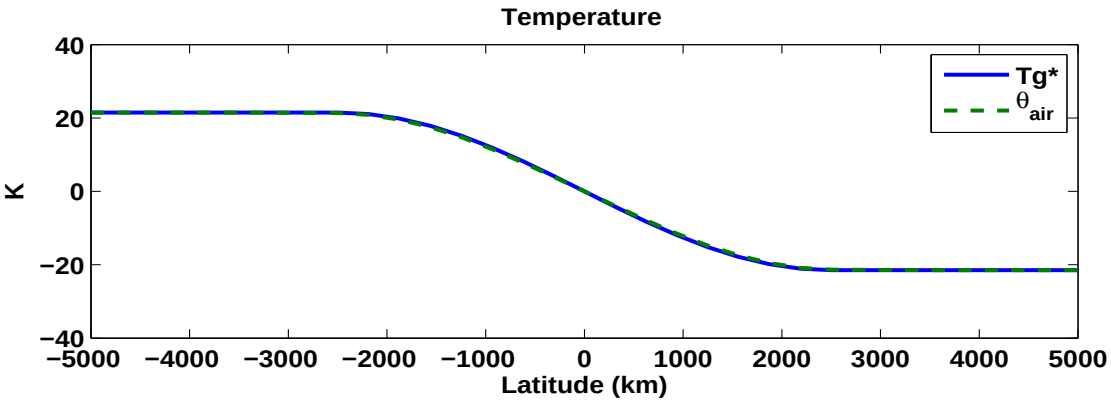

(a)

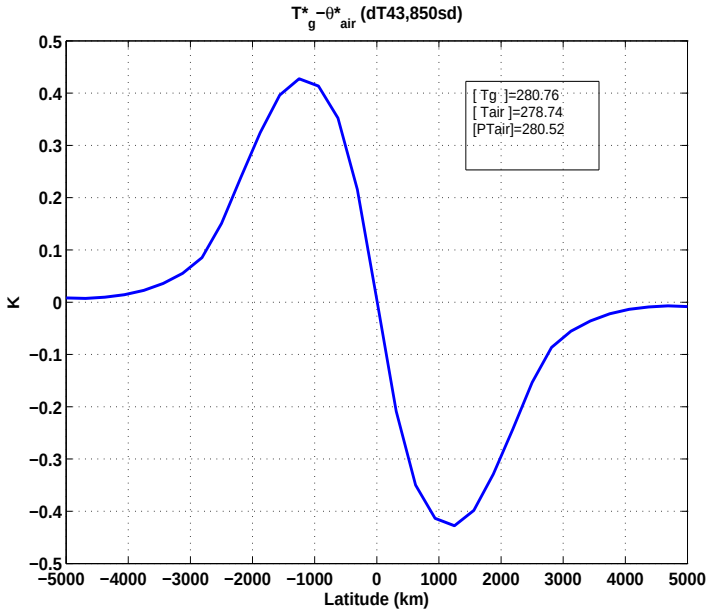

(b)

Figure 5-1: Latitudinal distribution of the calibration state (same as the standard run in Chapter 4) (a) surface temperature $T_g^\dagger$, surface air potential temperature $\theta_{air}^\dagger$, where superscript † indicates deviation from the horizontal mean, and (b) the difference between them.

close to the annual mean solar radiation into the surface. A 200 Wm^{-2} difference in the solar radiation is specified over the central half of the channel (from 300 to 100 Wm^{-2}) and there is no meridional variation of the solar radiation in both lateral regions (whose latitudinal distribution will be shown later in Figure 5-8). In fact, since we use a Q-flux to calibrate the surface heat budget in our model, the selection of the solar radiation will not affect the equilibration runs. In Chapter 6, we will further show that the latitudinal variation of the Q-flux, though it can affect the equilibrium state surface temperature gradient, will not change the response of the coupled system to the variation in the strength of different boundary layer processes. (In Chapter 8, the seasonal variation of the solar radiation will be considered.)

The downward longwave radiation into the surface is estimated from our simplified radiative transfer equation (Eq.2.20). As shown in Eq.2.17, the optical depth in our model has two components: contributions from the water vapor and from the CO_2. In our model, we set $\tau_{h_2o} = C \cdot q_{air}$, where C is a constant. The distribution of τ_{h_2o} as well as q_{air} in our calibration state is shown in Figure 5-2.

To specify the value of τ_{co_2}, we carried out a group of calculations to show its influence on the downward longwave radiation as well as the net radiative flux at the surface. We set $\tau_{co_2} = 0.001, 0.01, 0.1, 0.2, 0.5, 1.0, 1.5, 2.0, 2.5, 3.0, 3.5$, and the total optical depth, downward longwave radiation flux as well as the net radiation flux at the surface, as shown in Figures 5-3 and 5-4, are estimated by using the calibration state atmospheric temperature and surface temperature.

Compared with the situation in which CO_2 has almost no contribution to the optical depth (i.e. $\tau_{co_2} = 0.001$), we find the influence of adding τ_{co_2} on the longwave radiation is primarily in the high latitudes where the contribution from water vapor on the optical depth is very small, while in the low latitudes, its influence is negligible. Including CO_2 in the optical depth will mainly increase the downward longwave radiation and warm the surface in the high latitudes.

To further decide the appropriate value for τ_{co_2}, we compare our parameterization with a

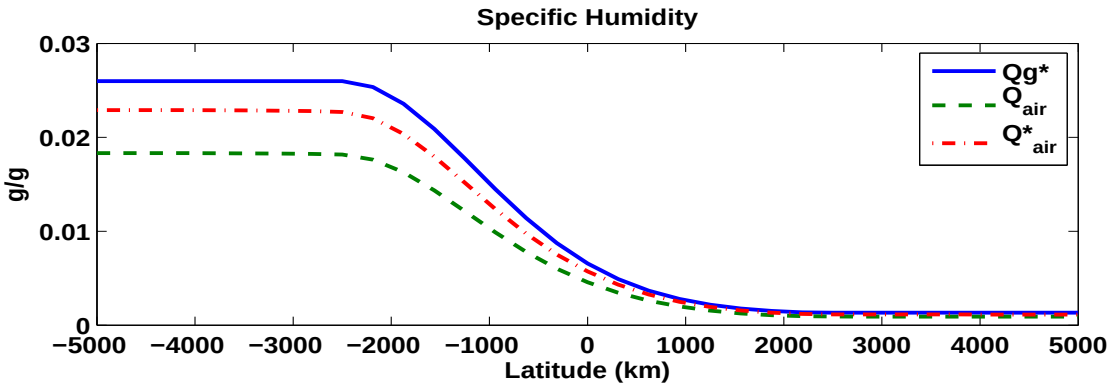

(a)

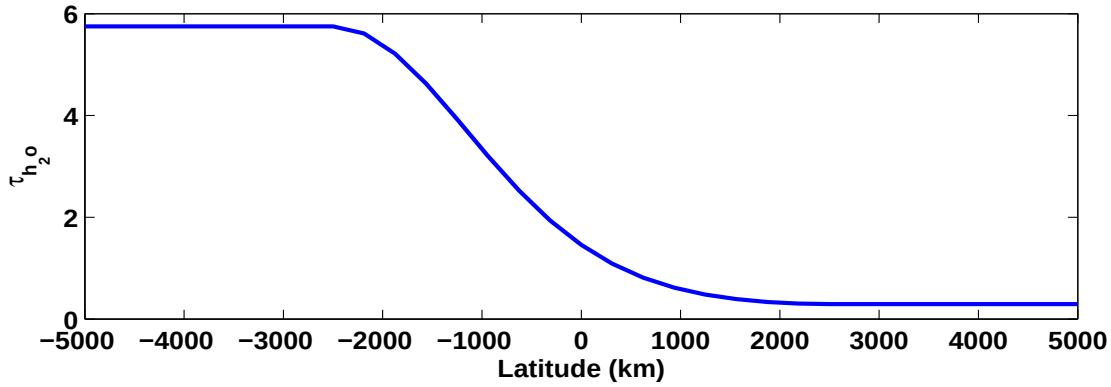

(b)

Figure 5-2: Latitudinal distribution of (a) the surface specific humidity, the surface air saturated specific humidity and specific humidity, and (b)τ_{h_2o} in the calibration state.

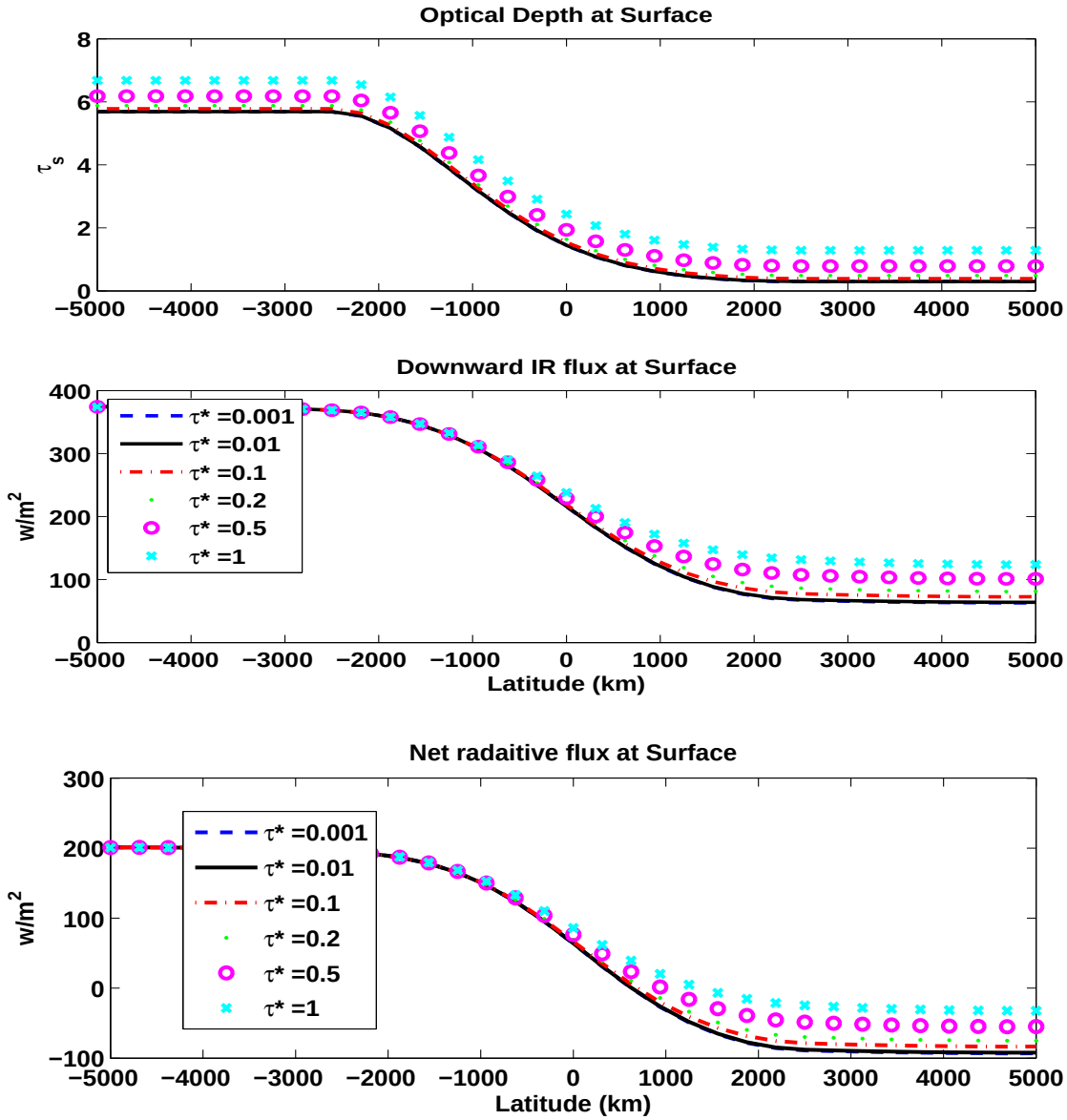

Figure 5-3: Latitudinal distribution of the total optical depth (upper), downward longwave radiative flux (middle) and the net radiative flux (lower) estimated at the surface by using the calibration state atmospheric and surface temperature when $\tau_{co_2} = 0.001, 0.01, 0.1, 0.2, 0.5,$ and 1.0 .

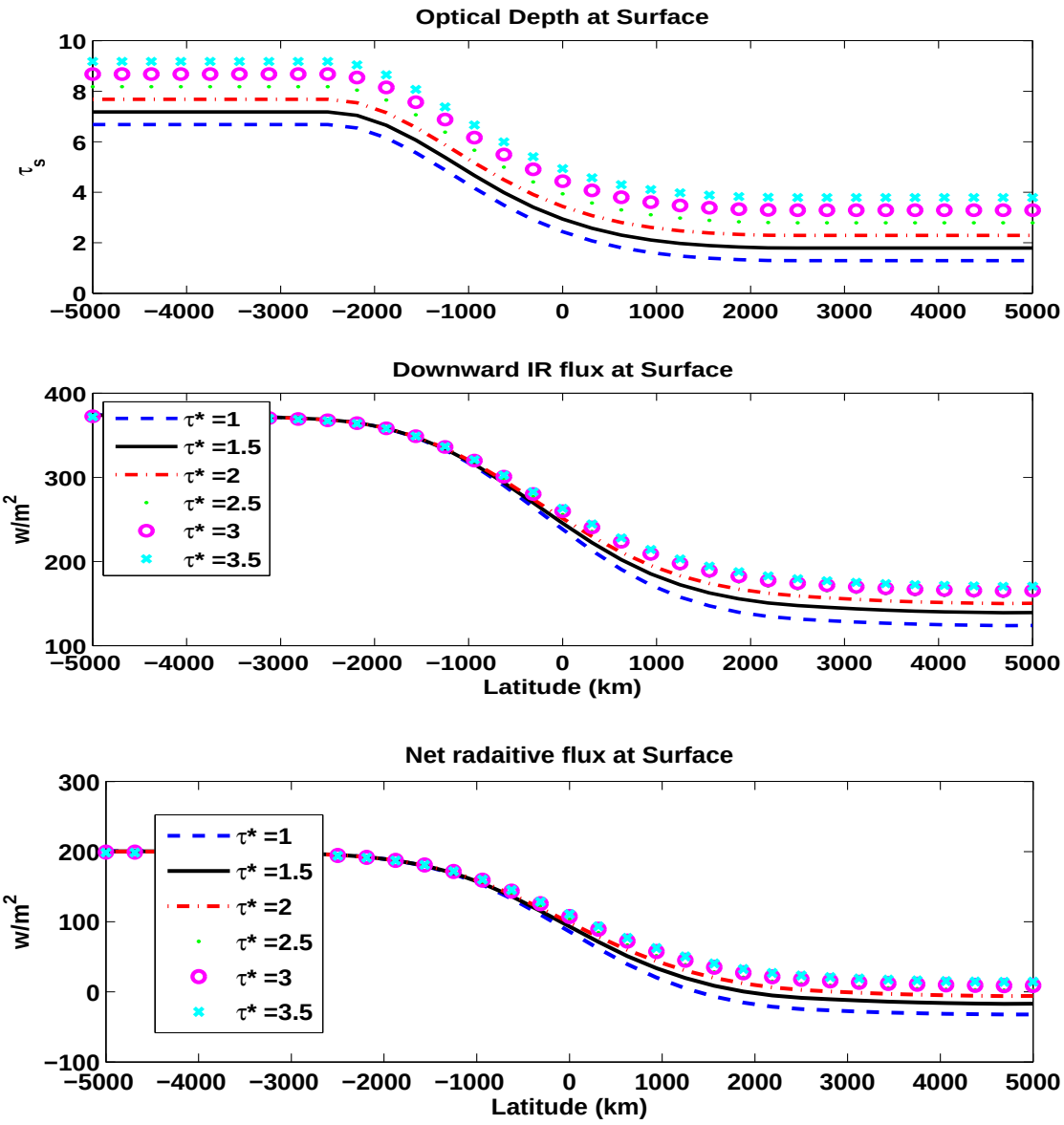

Figure 5-4: Same as Fig.5-3 but for $\tau_{co_2} = 1.0, 1.5, 2.0, 2.5, 3.0,$ and 3.5 .

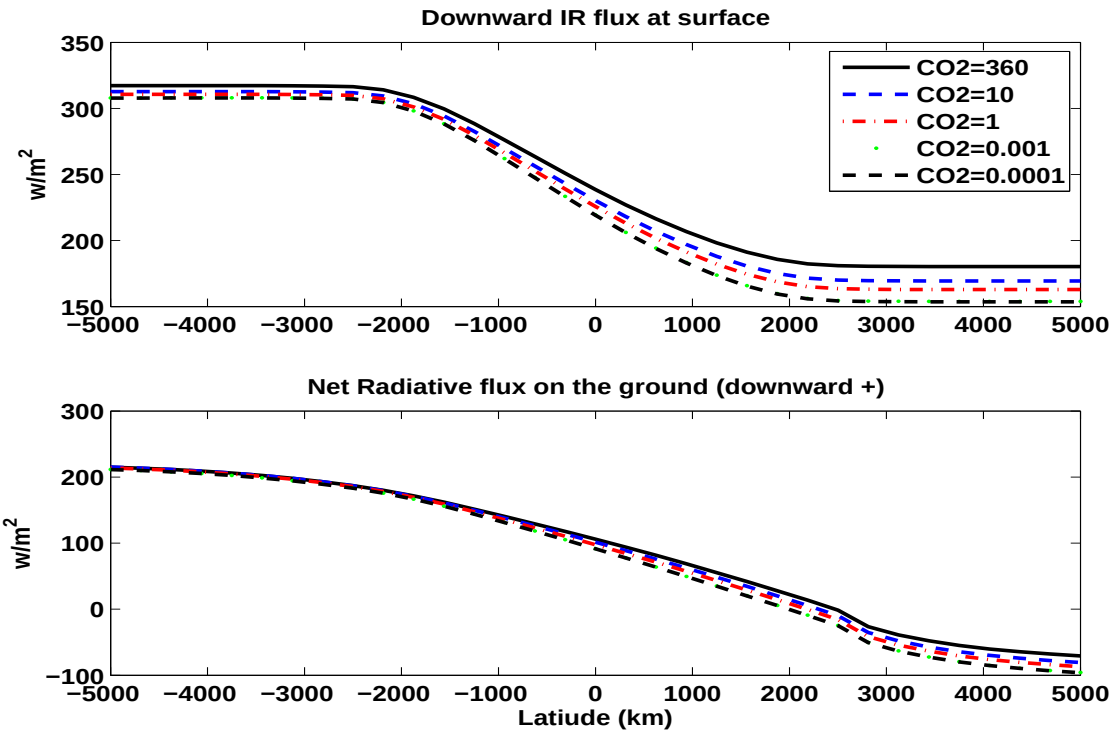

Figure 5-5: Latitudinal distribution of the downward longwave radiative flux (upper) and the net radiative flux (lower) at the surface estimated from the radiation scheme in Bony and Emanuel (2001) for different CO_2 concentration (ppm).

more complicated and physical radiation scheme in the column model in Bony and Emanuel (2001), which uses the shortwave radiation parameterization by Fouquart and Bonnel (1980) and longwave radiation parameterization of Morcrette (1991). With this model, we vary the CO_2 concentration from 360 to 0.0001 ppm. Using our calibration state temperature profile, assuming fixed relative humidity and clear sky condition, the column model output of the downward longwave radiation, net shortwave radiation, net longwave radiation, as well as the net radiation at the surface in the corresponding latitude are displayed in Figures 5-5 and 5-6.

Consistent with Figs.5-3 and 5-4, the influence of CO_2 on the longwave radiation is mainly in the high latitudes, which act to warm the surface temperature there. As expected, CO_2 has little influence on the shortwave radiation. Also, across the midlatitudes, as shown in Fig.5-6, the shortwave radiation at the surface varies roughly from 100 to 300 Wm^{-2}, which

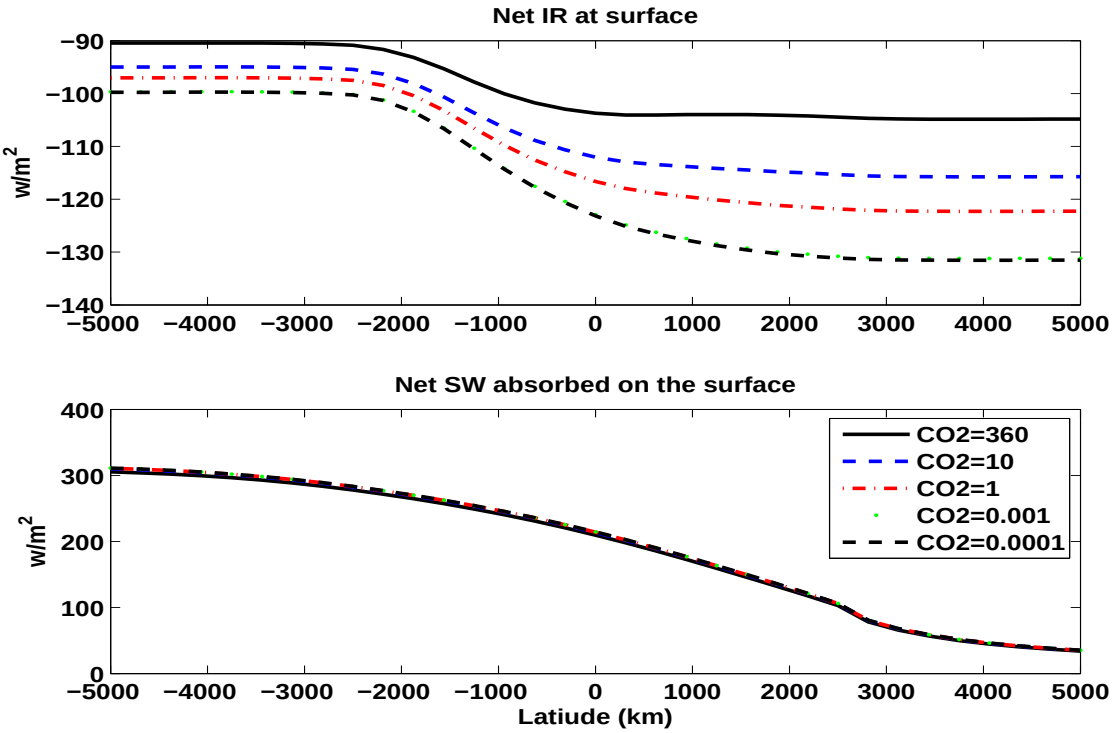

Figure 5-6: Latitudinal distribution of the net longwave radiative flux (upper) and the net shortwave radiative flux (lower) at the surface estimated from the radiation scheme in Bony and Emanuel (2001) for different CO_2 concentration (ppm).

indicates our solar radiation setting in the model is reasonable. Comparing the net radiation at the surface in Figs.5-3, 5-4 and 5-5, we find that when $\tau_{co_2} = 1$, the latitudinal distribution of the net radiation is closest to the column model prediction. This is also the default value of τ_{co_2} used in the following simulations.

5.1.2 Q-flux

Using the calibration state surface and atmosphere temperature profile, radiation and boundary layer schemes described in Chapter 2, we calculate the surface upward and downward longwave radiation (as shown in Figure 5-7), and surface latent, sensible heat fluxes (displayed in Figure 5-8). The Q-flux required to maintain the equilibrium state surface energy budget, which is also the sum of these surface heat fluxes, is also displayed. Then, in our surface model, the heating of the surface by the solar radiation is primarily balanced by the evaporation cooling and longwave cooling of the surface. The magnitude of the sensible heat flux is much smaller than other surface energy fluxes. The north-south differential heating by the solar radiation is primarily balanced by the latent heat flux and the estimated Q-flux (ocean heat flux). The magnitudes of these fluxes and their meridional variation over the the channel are also comparable with the observations (Hsiung, 1986; da Silva et al., 1994; Trenberth and Caron, 2001; Stewart, 2005; Bordoni, 2007). Compared with the annual mean ocean heat budget, i.e. Stewart (2005, Fig.5.7), our surface model can capture the basic features and well simulate the meridional variation of the surface energy fluxes. Since we use a clear sky downward solar radiation, the shortwave radiation is stronger than the observation, which is balanced by the strong longwave cooling in our model. Our surface model works well in simulating the sensible and latent heat fluxes, which we mainly focus on in this study.

Since we use a β plane channel model and the external forcing (radiative-convective heating, surface temperature gradient et al.) is confined at the center of the channel, due to the idealized geometry and topography setting in our model, it is not entirely appropriate to compare our Q-flux with the corresponding physical variable such as the observed meridional

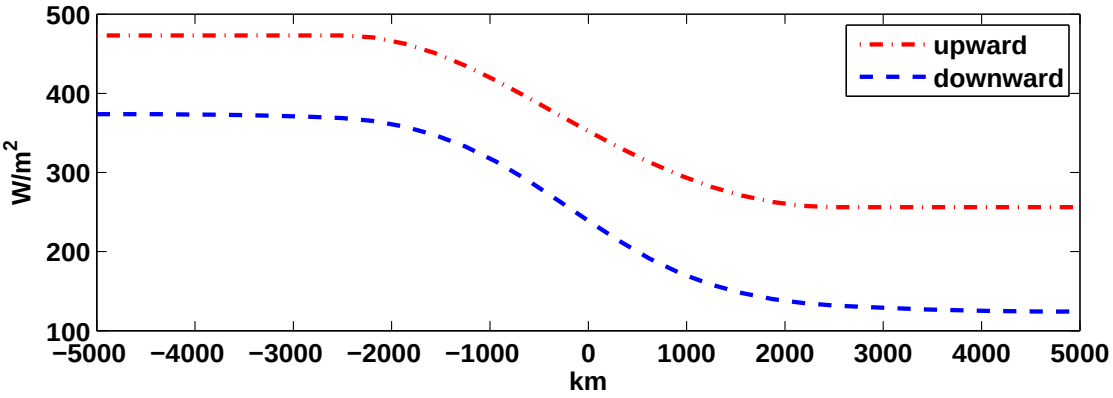

Figure 5-7: Latitudinal distribution of the surface upward longwave emission and downward Infrared flux into the surface in the calibration state.

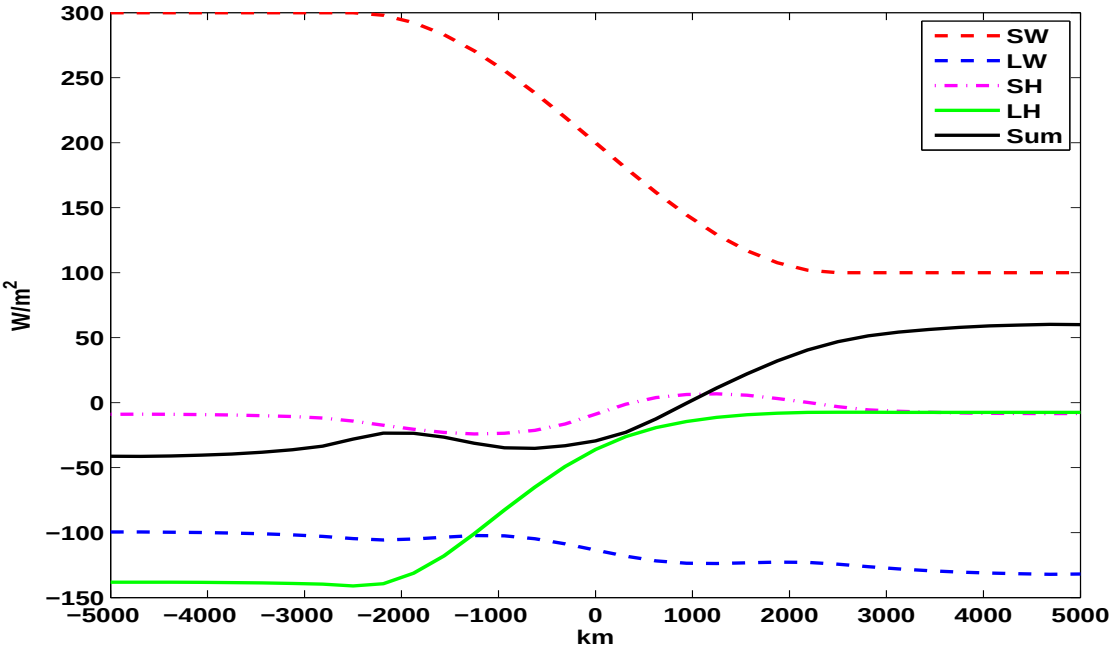

Figure 5-8: Latitudinal distribution of the net shortwave and longwave radiations, sensible and latent heat fluxes, and the Q-flux required to maintain the calibration state.

heat flux in the ocean directly. However, the observed climatological ocean heat transport divergence (Trenberth and Caron, 2001; Kållberg et al., 2005; Bordoni, 2007) implies that our calculated Q-flux is within the realistic regime. As shown in Stewart (2005, Fig.5.10B) and Bordoni (2007, Fig.5.4), in the North Pacific and in some part of the North Atlantic, the divergence of the ocean heat transport is in the similar pattern and with comparable magnitude to the Q-flux in our model.

5.2 Spin-up of the coupled model

To show the role of the baroclinic eddies and the Q-flux in maintaining the equilibrium of our coupled system, we spin up the coupled model in three steps. The latitudinal distributions of the surface temperature $T_g^\dagger$ in the equilibrium state in these steps are plotted in Figure 5-9.

1. First, without Q-flux and turning off zonal variation (without eddies), we integrated the symmetric model for 1000 days. In the equilibrium state, as shown in Fig.5-9 (which is the state averaged over the last 400 days), a steep meridional surface temperature gradient appears across the channel with the north-south temperature contrast as large as 75 K.

2. Starting from the equilibrium state of the symmetric run, we run a 3D simulation with small amplitude perturbations in zonal wavenumber 1 to 10 added at the initial moment. Due to the strong baroclinicity of the mean flow, baroclinic eddies quickly spin up in the atmosphere. After around 600 days, the coupled system reaches an equilibrium state, as shown in Fig.5-9, with the temperature gradient near the center of the channel greatly reduced.

3. Then we run the 3D simulation including the Q-flux. In the equilibrium state, the surface temperature gradient is further reduced. The temperature gradient of the underlying surface is around the observed winter time surface temperature difference 43K.

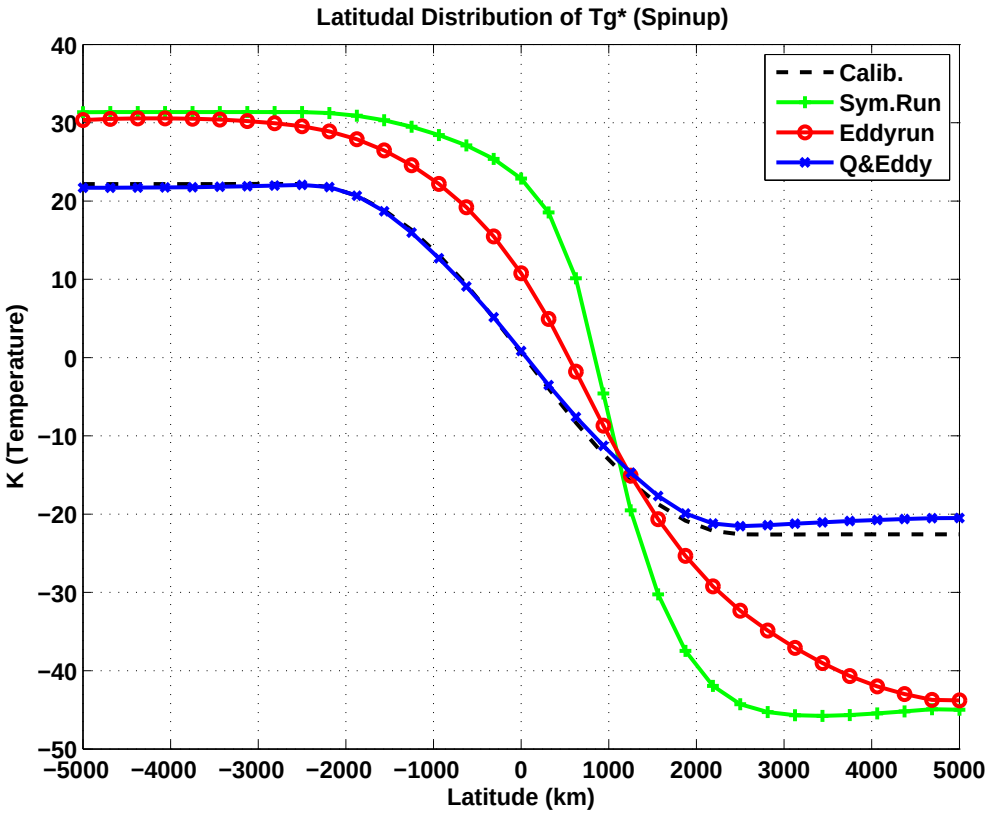

Figure 5-9: Latitudinal distribution of the underlying surface temperature in the 2D symmetric run without Q-flux, in the eddy included run without Q-flux and in the eddy included run with Q-flux compared with the calibration state temperature.

Latitudinal variations of each energy flux in the surface energy budget in the 2D and 3D runs without Q-flux and in the standard run (3D run with Q-flux) are plotted in Figures 5-10(a), 5-10(b) and 5-11, respectively. In order to clearly display the role of each energy flux in determining the surface temperature difference, only the deviation (anomaly) of each flux from its horizontal mean is plotted. (Thus, Fig.5-11 is almost the same as the calibration state surface heat budget in Fig.5-8 but only the deviation from the horizontal mean is plotted).

Compared with the standard run state surface heat budget, in the 2D run, we find that the sensible heat flux becomes almost negligible, but the latent heat flux meridional variation is steeper and enlarged. The radiative flux, more exactly, the longwave radiation, begins to act to reduce the surface temperature gradient. When turning on the eddies, as shown in Fig.5-10(b), a stronger sensible heat flux appears at the center of the channel. The latent heat flux, though becomes smoother than the 2D run, still shows stronger meridional variation than the SD run. The meridional variation of the longwave radiation also becomes smoother and acts to reduce the temperature gradient.

The different variations of the sensible and latent heat fluxes in the spin-up runs can be explained from their different dependence on the surface and air temperature as well as the eddy activity. The sensible heat flux, as indicated in Equation 2.6, is primarily determined by the air-sea temperature difference and the drag coefficient. The surface heat exchange always acts to reduce the air-sea temperature difference. As shown in Figure 5-12, if the sensible heat flux is the only dominant process that determines the surface air temperature, the surface air temperature will be forced to be equal to the underlying surface. Baroclinic eddy mixing of the surface air temperature can be another factor that determines the air-sea temperature difference. When baroclinic eddies are included, the meridional eddy heat transport will result in a cold surface air anomaly in the lower latitudes and a warm surface air anomaly in the higher latitudes. As a consequence, the lower latitude surface will lose heat into the atmosphere, while the higher latitude surface will gain heat through the sensible heat flux. Thus, baroclinic eddies, by mixing the surface air temperature gradient and

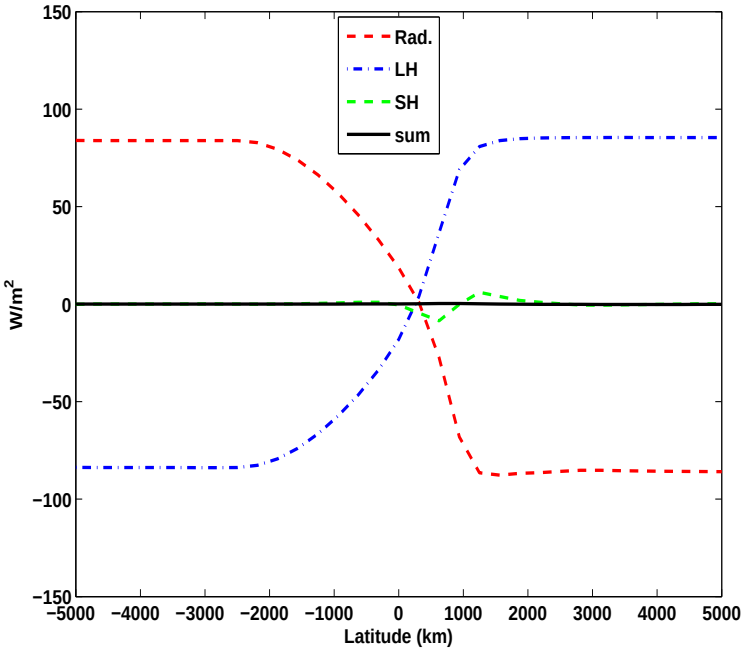

(a)

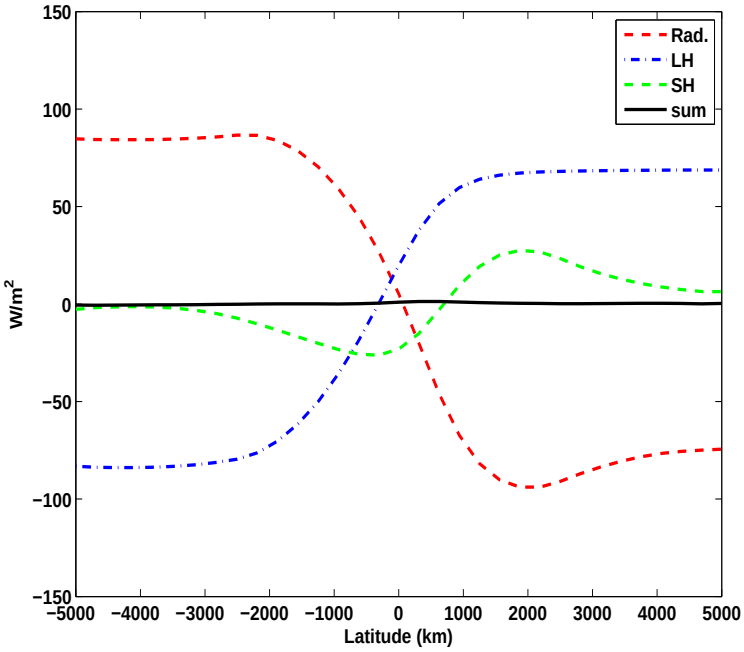

(b)

Figure 5-10: Latitudinal distribution of the equilibrium state radiative flux, latent heat flux, sensible heat flux anomalies in the underlying surface heat budget for (a) 2D run and (b) 3D run without Q-flux in the surface model.

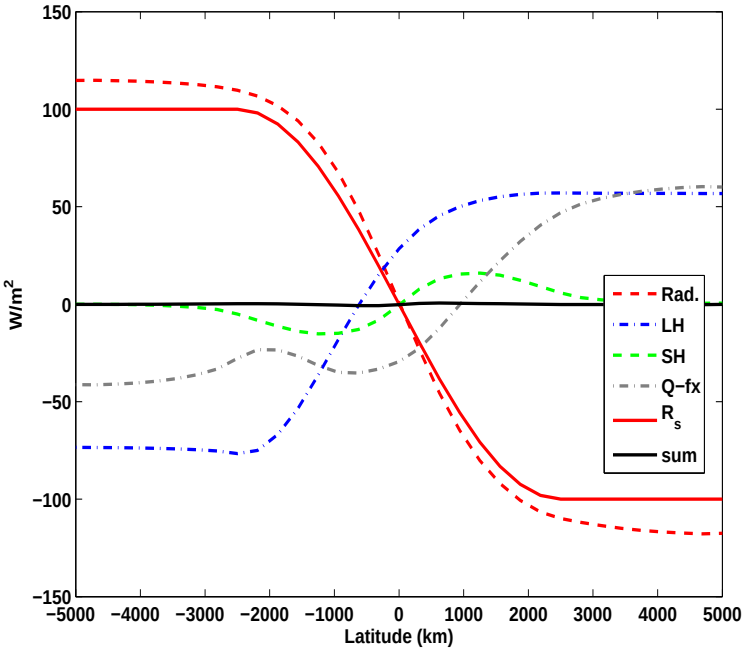

Figure 5-11: Latitudinal distribution of the equilibrium state radiative flux, latent heat flux, sensible heat flux and Q-flux anomalies in the underlying surface heat budget for SD run. The latitudinal variance of the shortwave radiation into the surface (R_s or $SW^{\dagger}$) is also plotted in the solid curve.

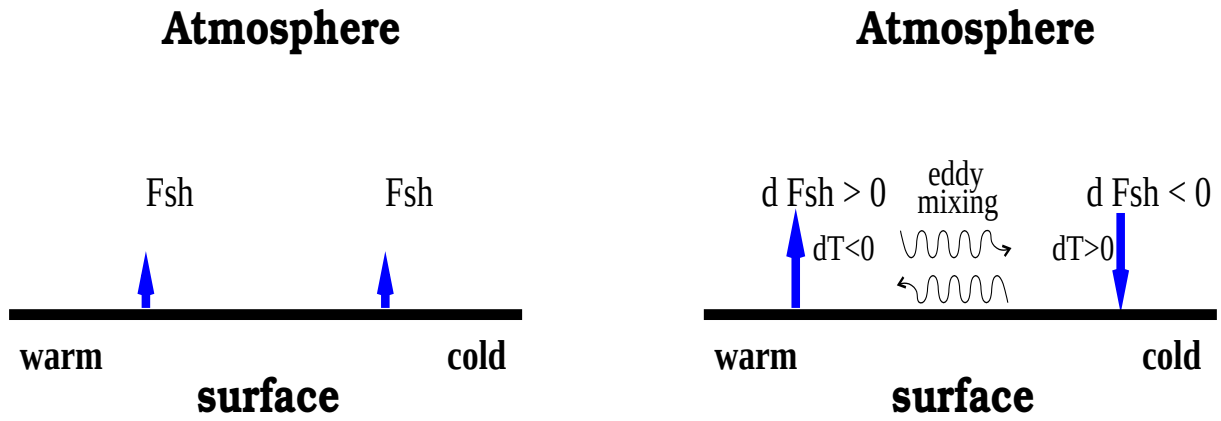

Figure 5-12: A schematic map showing how eddy mixing could influence the surface sensible heat flux.

influencing the surface heat fluxes, can result in a smaller surface temperature gradient as shown in Fig.5-9. Furthermore, we would expect that a stronger eddy mixing of the surface air temperature can result in a stronger air-sea temperature difference as well as the sensible heat flux. This is consistent with Fig.5-10(b), in which the equilibrium state mean flow has a stronger baroclinicity (stronger eddy activity) and a stronger meridional variance of the sensible heat flux is observed compared with the standard run.

The latent heat flux, from Equation 2.15, can be expanded as

$$\begin{aligned} LH &= C_{dt} L \rho_s (q_g^* - RH q_{air}^*) \\ &\approx C_{dt} L \rho_s [(1 - RH) q^*(T_g) - RH \frac{\partial q^*}{\partial T} (T_{air} - T_g)], \end{aligned} \tag{5.1}$$

where $q^*(T)$ follows the Clausius-Clapeyron relationship. With fixed relative humidity RH, near the standard pressure and temperature (i.e. 1013.25 hpa and 273 K), the water vapor in the atmosphere will increase 20% for every 3K temperature increase (Hartmann, 1994). However, the temperature difference between T_{air} and T_g is always small. From observations (Peixoto and Oort, 1992), the difference is less than 1K in most parts of the ocean over the year except in the western boundary of the Pacific and Atlantic Ocean. In our model, as shown in Fig.5-1, the air-sea temperature difference is much smaller than 1K. Thus, the contribution of the second term to the latent heat flux is much smaller than the first term

in Equation 5.1. The latitudinal distribution of the latent heat flux mainly depends on the contribution from the under-saturation of the surface air and is primarily determined by the surface temperature distribution. We find that the variations of the latent heat flux in Fig.5-10 are consistent with the variation of the surface temperature in these runs.

In our spin-up runs, we have shown that the eddy mixing of the surface air temperature can greatly influence the equilibrium state underlying surface temperature by modifying the surface sensible heat flux. As we have shown in Ch.4, the eddy activity in the lower atmosphere are substantially determined by the boundary layer processes, which would affect the surface heat fluxes as well as the underlying surface. This can further influence the atmospheric eddy activities and the mean flow. How do these boundary layer processes influence the equilibration of the coupled system? We will try to answer this question in the next chapter.

Chapter 6

The role of the boundary layer processes in the atmosphere-surface coupled model

Our study in Chapter 4 shows that the boundary layer vertical thermal diffusion and surface heat exchange are the dominant processes that prevent the boundary layer PV homogenization. These two processes couple the boundary layer, even the free troposphere, with the underlying surface and strongly damp the lower level temperature fluctuations. Thus, even though the potential temperature mixing by the baroclinic eddies in the boundary layer is strong, the strong surface temperature gradient is still retained. This result is obtained under the condition of fixed underlying surface, which is a reasonable assumption as long as the atmospheric adjustment time scale is short compared with the underlying surface temperature variation time scale. Whether this mechanism works in the real atmosphere also depends on whether the heat capacity of the underlying surface is large enough to maintain the underlying surface temperature gradient. Therefore, in this chapter we further investigate the role of the surface and the boundary layer turbulent heat fluxes with the atmosphere-surface coupled model described in Chapter 2.

Results from the spin-up runs in Section 5.2 show that in the coupled model, eddy mixing

of the surface air temperature can modify the underlying surface temperature by affecting the surface sensible heat flux. Thus, besides the boundary layer thermal damping, the frictional dissipation in the boundary layer may also affect the underlying surface indirectly by influencing the lower level eddy activity. Therefore, the role of the surface friction in determining the coupled system equilibration is also studied in this chapter.

In this chapter, similar to Ch.4, we carry out groups of sensitivity studies. The parameters used in these runs are listed in Table 6.1. Here we did not run the sensitivity test for the boundary layer vertical momentum diffusion. As indicated in Ch.4, the equilibrium state in the atmospheric model varies only slightly with the momentum diffusion and it is not a process that directly influences the surface heat budget. Thus, it is not expected to be an important process that influences the coupled system.

Table 6.1: Values of the coefficients used in the experiments that investigate the model sensitivity to different boundary layer processes in the coupled model.

Run	surface heat flux c_{dt} (ms^{-1})	B.L. thermal diffusion μ_s (m^2s^{-1})	surface friction c_{dt} (ms^{-1})	with ageostrophic winds
SD	0.03	5	0.03	no
Section6.1				no
tcd0	0.00	5	0.03	no
tcd1	0.01	5	0.03	no
tcd6	0.06	5	0.03	no
Section6.2				
snu0	0.03	0	0.03	no
snu2	0.03	2	0.03	no
snu10	0.03	10	0.03	no
Section6.3.1				
fcd1	0.03	5	0.01	no
fcd6	0.03	5	0.06	no
Section6.3.3				
SD_{ag}	0.03	5	0.03	yes
$fcd6_{ag}$	0.03	5	0.06	yes
$fcd12_{ag}$	0.03	5	0.12	yes

6.1 Surface sensible and latent heat exchange

The sensible and latent heat exchange between the surface and the atmosphere is an important component in the underlying surface energy budget. Observational studies (da Silva et al., 1994; Kållberg et al., 2005) show that in the ocean, shortwave radiation and the latent heat flux are the most important components that maintain the surface energy balance, which, as discussed in Ch.5, is also the situation in our surface model. The shortwave radiation is the primary source of the underlying surface meridional temperature gradient, while surface latent heat flux is the dominant component that acts to reduce the surface temperature gradient. The sensible heat flux, though has smaller magnitude in average, but it is a very active and important component in the storm track regions especially in the Northern Hemisphere (da Silva et al., 1994; Kållberg et al., 2005; Stewart, 2005). Over land surface, the sensible heat flux has larger magnitude, whose contribution becomes comparable with the latent heat flux especially in the midlatitudes. Our spin-up runs in Ch.5 also shows the importance of the sensible heat flux in determining the surface temperature distribution.

In this section, we carried out the sensitivity studies of the coupled system to the surface heat drag coefficient c_{dt}, which is a parameter that determines both sensible and latent heat flux strength directly. Similar to Ch.4, equilibration runs with $c_{dt} = 0$, 0.01 and 0.06 ms^{-1} are done to compare with the SD run.

6.1.1 Equilibrium state

Figure 6-1 displays the latitudinal distribution of the equilibrium state surface temperature. Compared with the SD run, stronger surface heat exchange results in smaller temperature gradient in the equilibrium state. When we turn off the surface heat exchange that is $c_{dt} = 0$ ms^{-1}, the temperature contrast across the channel reaches as large as 64 K in the equilibrium state.

The latitudinal distribution of the equilibrium state surface energy fluxes and their variations compared with the SD run (in Fig.5-11) when varying the surface heat exchange coefficients are plotted in Figures 6-2 and 6-3. Since here we mainly care about the equilib-

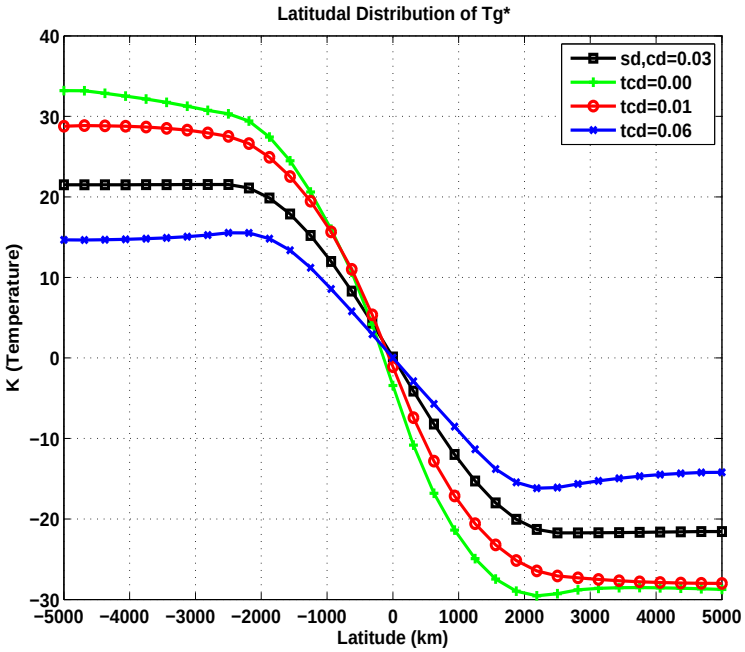

Figure 6-1: Latitudinal distribution of the underlying surface temperature when varying the surface heat exchange.

rium state temperature gradient, only the anomalies (deviations from the horizontal mean) of each flux are plotted.

In the SD run, as in Fig.5-11, the meridional difference of the solar radiation over the channel is primarily balanced by the latent heat flux and Q-flux. The sensible heat flux and the longwave radiation (which is the difference between the total radiation and the shortwave radiation in Fig.5-11) only play secondary roles. When $c_{dt} = 0\ ms^{-1}$, the latent and sensible heat fluxes are turned off. Then, as shown in the Figure 6-2, the surface heat budget anomaly is totally balanced by the variation of the longwave radiation. With enhanced temperature gradient, the surface emits more longwave radiation into the atmosphere in the lower latitude, which acts as a negative feedback to balance the exerted differential heating by the solar radiation.

When we increase the surface heat exchange coefficients, the variations of the sensible and latent heat fluxes are in different directions. As shown in Figure 6-3, increasing c_{dt} results in a stronger latitudinal variation of the latent heat flux, however, it results in weaker sensible

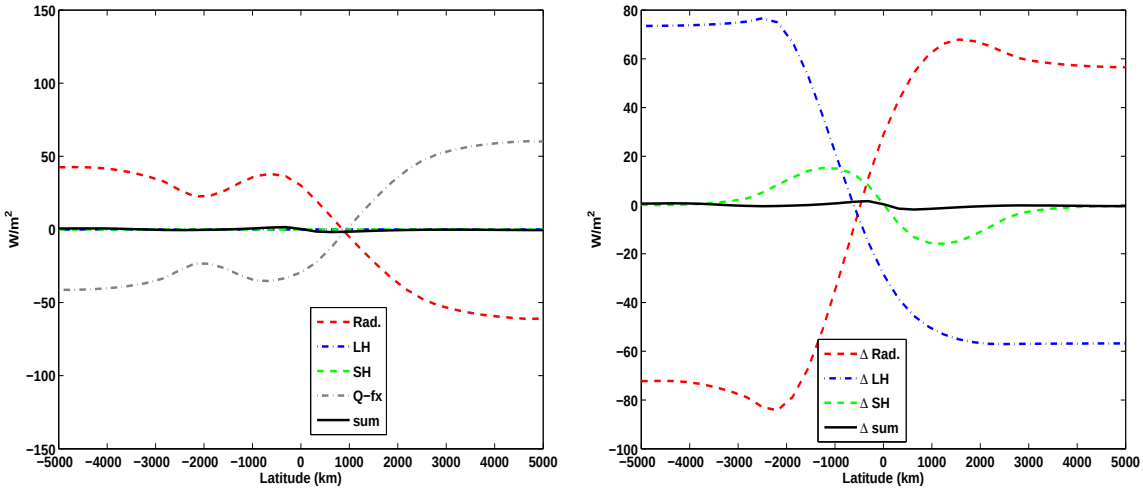

(a) (b)

Figure 6-2: Latitudinal distribution of the equilibrium state (a) radiative flux, latent heat flux, sensible heat flux, and Q-flux anomalies (deviation from the horizontal mean) in the underlying surface energy budget for $c_{dt} = 0\ ms^{-1}$ run and (b) the difference of these fluxes anomalies compared with the $c_{dt} = 0.03\ ms^{-1}$ (SD) run.

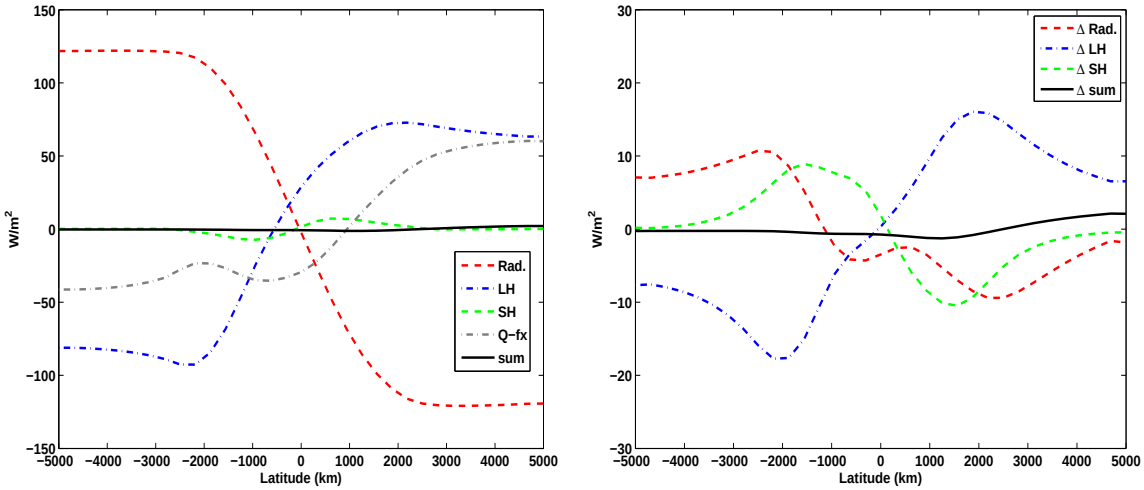

(a) (b)

Figure 6-3: Latitudinal distribution of the equilibrium state (a) radiative flux, latent heat flux, sensible heat flux, and Q-flux anomalies in the underlying surface energy budget for $c_{dt} = 0.06\ ms^{-1}$ run and (b) the difference of these fluxes anomalies compared with the $c_{dt} = 0.03\ ms^{-1}$ (SD) run.

heat flux. Such differences can be explained by the different dependence of the latent and sensible heat fluxes on the surface and atmospheric temperature. As discussed in Ch.5, the latent heat flux is mainly determined by the drag coefficient c_{dt} and the surface temperature distribution. Though the drag coefficient is doubled, the equilibrium state temperature gradient is reduced to almost two thirds of the SD run. Due to this negative feedback, the latitudinal variation of the latent heat flux in the new equilibrium state only increases around 20%. The sensible heat flux, however, is mainly determined by the drag coefficient and the air-surface temperature difference. As we will show later, in the coupled model, different from the results in the atmospheric run with fixed surface temperature, a much weaker eddy heat flux is accompanied with the weaker lower level zonal flow baroclinicity as c_{dt} increases. Moreover, the effect of the reduced eddy heat flux overcomes the direct effect of increasing c_{dt} and results in a weaker meridional variation of the sensible heat flux.

In the atmosphere, the RCE state temperature gradient distribution at the center of the channel, as displayed in Figure 6-4(a), follows the surface temperature distribution. Stronger surface heat exchange results in a weaker RCE state temperature gradient. The equilibrium state surface air temperature gradient, similar to the uncoupled atmospheric run, is closer to the RCE state as well as the underlying surface temperature gradient under stronger surface heat exchange. However, more complicated than the uncoupled atmosphere runs, the variation of c_{dt} in the coupled model, in addition to affecting the atmospheric eddy activity and the mean flow, also influences the RCE state temperature distribution as well as the subsequent radiative-convective heating exerted on the atmospheric flow. The net result of these mechanisms, as shown in Figure 6-4(a), is that at most levels of the troposphere, the influence of the radiative-convective heating is dominant. Under stronger differential heating, the atmosphere equilibrates at a state with a stronger temperature gradient. One exception is the run where the surface heat flux is turned off, in which without the surface thermal damping, the temperature gradient near the surface is greatly reduced by the mixing of baroclinic eddies. The deviation of the equilibrium state temperature gradient from their RCE states, especially in the upper troposphere, also gets larger under stronger RCE forcing.

The eddy meridional and vertical heat fluxes, as shown in Figure 6-5, indicate their relation with the zonal mean flow. Consistent with the equilibrium state temperature gradient, in the free troposphere, the eddy heat fluxes get larger as c_{dt} is reduced. In the boundary layer, when turning on the surface heat flux, accompanied with the reduced mean flow temperature gradient, eddy heat fluxes are also reduced with increasing c_{dt}. When turning off the surface heat flux, though the temperature gradient is most efficiently reduced and the stratification is most stabilized in the boundary layer, the removal of the surface heat flux also efficiently reduces the eddy energy damping. These two factors lead to a non-monotonic change in eddy heat fluxes compared with other runs with nonzero c_{dt}.

The equilibrium state stratification, as in Eq.2.3, is determined by the eddy vertical heat flux, boundary layer thermal forcing and the radiative-convective heating. Since the RCE state lapse rate is the same in these runs, the first two components are the dominant factors that determine the equilibrium state stratification. In Figure 6-4(b), consistent with the eddy heat fluxes, the flow is more stably stratified under weaker c_{dt}.

The equilibrium state PV gradient, as shown in Figures 6-4(c) and 6-4(d), displays a tendency similar to the atmospheric runs in Chapter 4. Even though in this chapter, we use a much shallower boundary layer scheme which suppresses the influence of the boundary layer processes on the free troposphere, in Fig.6-4(c), the PV gradient around the 600 to 850 hpa is still homogenized most when turning off the surface thermal damping. The tendency of the PV gradient to the varying c_{dt} is more obvious in the boundary layer, where the PV gradient is more efficiently mixed for weaker c_{dt} as shown in Fig.6-4(d).

In our sensitivity study, we include an extreme case in which the surface heat exchange is turned off. In its equilibrium state, the forcing by differential shortwave radiation is primarily balanced by the longwave radiation. The underlying surface stays in a radiative equilibrium-like state. However, with no sensible and latent heat fluxes going into the atmosphere, it would not be a good assumption to have a lapse rate including the convection and moisture effects in the RCE state. Even though losing some physical meaning, this run is still helpful in understanding the role of the surface sensible and latent heat fluxes in the coupled system.

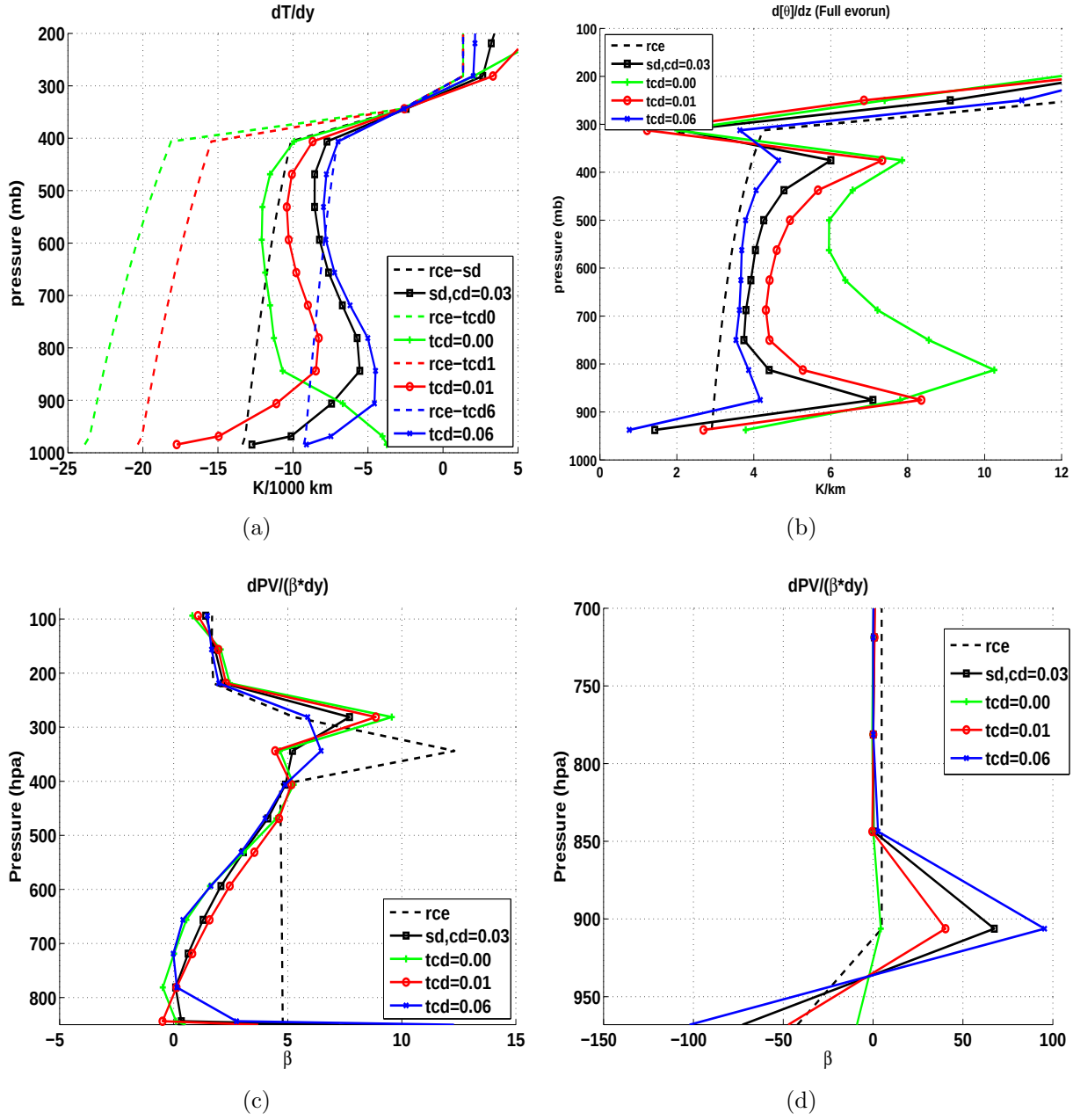

Figure 6-4: Vertical distribution of (a) the zonal mean temperature gradient at the center of the channel, (b) stratification, (c) zonal mean PV gradient at the center of the channel in the free troposphere and (d) in the boundary layer in the $c_{dt} = 0$, 0.01, 0.06 ms^{-1} runs and the SD runs.

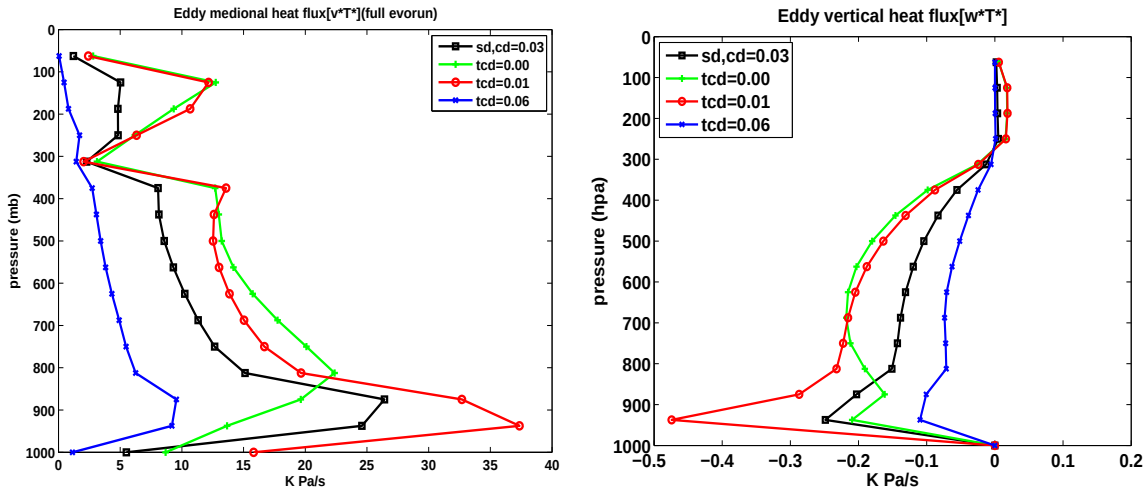

(a) (b)

Figure 6-5: Vertical distribution of the equilibrium state (a) meridional and (b) vertical eddy heat fluxes when varying the surface heat exchange.

6.1.2 Transient response to the surface sensible and latent heat exchange

To better understand the response of the coupled system to the variation in the surface heat exchange, a transient response run is also carried out. Here we start from the equilibrium state of the SD run, and suddenly increase the surface heat coefficient c_{dt} from 0.03 (SD) to 0.06 ms^{-1} at the initial moment. The transient response of the surface energy fluxes and the surface temperature are plotted in Figure 6-6. Time evolution of the poleward eddy heat flux and the meridional temperature gradient in the boundary layer is also plotted in Figure 6-7.

The immediate response to the sudden increasing of c_{dt}, as shown in Figures 6-6(a) and 6-6(b), is an increase in the sensible and latent heat fluxes. Compared with the SD run distribution in Fig.5-11, their meridional variations are doubled with c_{dt} at the initial moment. However, with the strong surface heat exchange coefficient, the enhanced sensible heat flux quickly disappears. After day1, it even becomes smaller than in the SD run. From Eq.2.6, this must be due to the greatly reduced air-surface temperature difference under

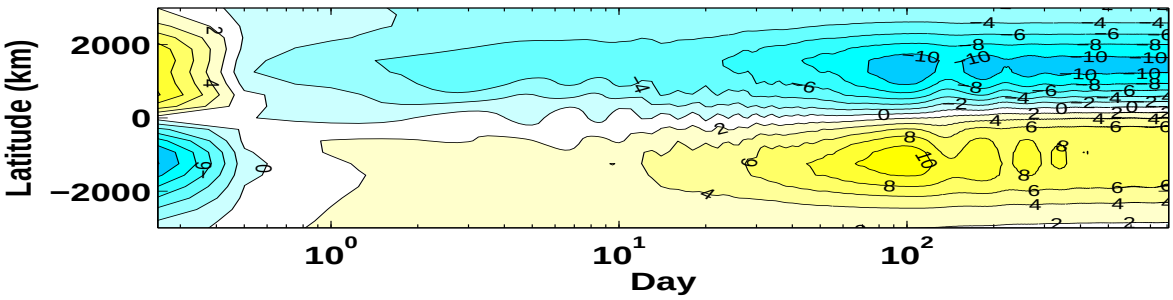

(a)

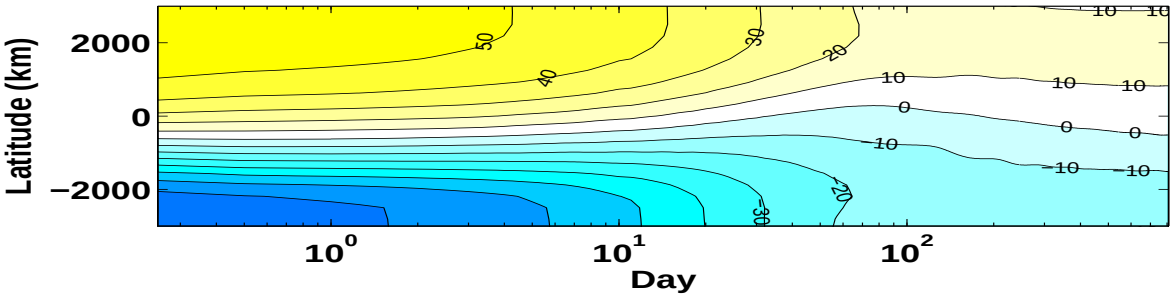

(b)

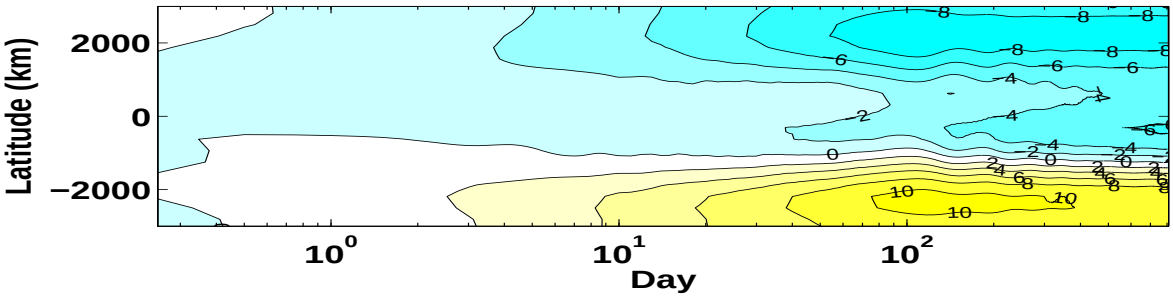

(c)

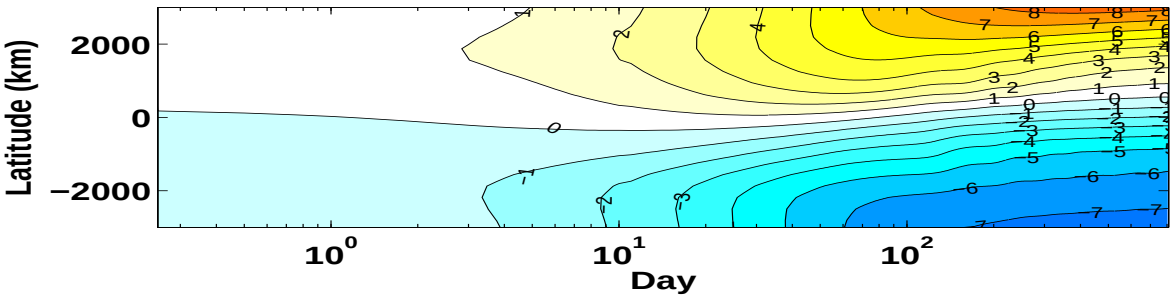

(d)

Figure 6-6: Time evolution of the (a) sensible heat flux variation $F_{sh} - \overline{F_{sh}}^{sd}$, (b) latent heat flux variation $F_{lh} - \overline{F_{lh}}^{sd}$, (c) radiative flux variation $F_{rad} - \overline{F_{rad}}^{sd}$ and (d) the surface temperature variation $T_g - \overline{T_g}^{sd}$ when suddenly increasing c_{dt} from 0.03 (SD) to 0.06 ms^{-1}, where superscript $^{-sd}$ means the equilibrium state values in the SD run. Contour interval is 2, 10, 2 Wm^{-2} in panel (a), (b), (c), respectively, and 1 K in panel (d). Note that the x-coordinate is plotted on a logarithmic scale.

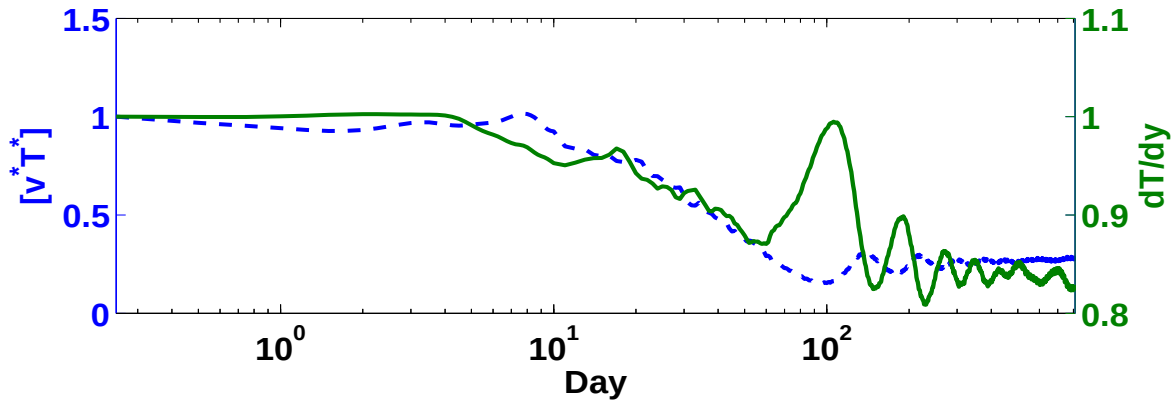

Figure 6-7: Time evolution of the boundary layer averaged poleward eddy heat flux (dashed curve) and the temperature gradient at the center of the channel averaged over the boundary layer depth (solid curve) when suddenly increasing c_{dt} from 0.03 (SD) to 0.06 ms^{-1}. Variables plotted are normalized by their standard run equilibrium state values. Note that the x-coordinate is plotted on a logarithmic scale.

the stronger surface flux. This quick adjustment time scale of the sensible heat flux is also consistent with the scale analysis in Ch.4 that the response time scale of the surface air to the surface heat flux forcing is around one day.

The later response of the latent heat flux is associated with the surface temperature variation. As shown in Figure 6-6(d), under the stronger surface latent heat flux, the surface temperature begins to change after around ten days. With the reduced surface temperature gradient, the enhanced latent heat flux starts decreasing. The longwave radiation, as the surface temperature changes, also changes to offset the anomaly latent heat flux. After hundreds of days, the surface energy budget reaches another equilibrium with reduced meridional gradient of surface temperature, sensible heat flux and radiative fluxes, but enlarged latent heat flux meridional gradient, which is consistent with Fig.6-3(b).

As shown in Fig.6-7, the immediate response of the baroclinic eddies to the increase in c_{dt} is a slight decrease in magnitude. Although the surface air is pulled closer to the underlying surface temperature, the boundary layer temperature gradient is almost unchanged during the first few days. Then with the reduced surface temperature gradient, the lower level temperature gradient is also reduced. With a few days lag, the eddy heat flux also begins to decrease. After tens of days, the eddy heat flux is reduced to less than one fourth of

its original value, while the temperature gradient displays a temporary increase. Then the eddies and the zonal flow experience negatively correlated oscillations. After a few hundreds of days, the atmospheric flow also reaches an equilibrium state with a weaker zonal flow baroclinicity and much weaker eddy activity.

As mentioned in Ch.2, to save computation time, a 5 m surface layer depth is used in the transient response experiment. This is a much shallower surface layer compared with the depth of the ocean mixed layer in midlatitudes. Even so, the transient response of the coupled model still clearly displays the different response time scales on which different processes affect the equilibration of the coupled system. The boundary layer process works on the lower atmosphere on a very quick time scale ($\sim$ 1 day). Baroclinic eddies respond to the variation in the mean flow on a time scale of a few days. The underlying surface's response time scale to the variation of the surface heat flux is dependent on the surface layer depth. In this experiment, its response time scale is hundreds of days. These processes work together to maintain the equilibrium of the coupled system.

6.2 Vertical thermal diffusion in the boundary layer

The boundary layer vertical thermal diffusion, is not a process that can directly affect the surface energy budget. As studied in Ch.4, it is a process that acts to couple the surface with the lower level atmosphere and a process that affects the eddy activities in the boundary layer. In this section, we test whether this process can further influence the coupled system by also carrying out a sensitivity study, in which the value of μ_s is varied.

The sensitivity of the surface temperature to the strength of the boundary layer vertical thermal diffusion is displayed in Figure 6-8. In the equilibrium, the underlying surface is almost insensitive to the vertical thermal diffusion. Only in the $\mu_s = 0\ m^2 s^{-1}$ run, the surface temperature shows slight variations. Thus, we would expect that the atmospheric response to the varying boundary layer vertical thermal diffusion in the coupled model is similar to the results in the uncoupled atmosphere runs in Ch.4.

The RCE state temperature gradient in the equilibrium state in these runs, as shown in

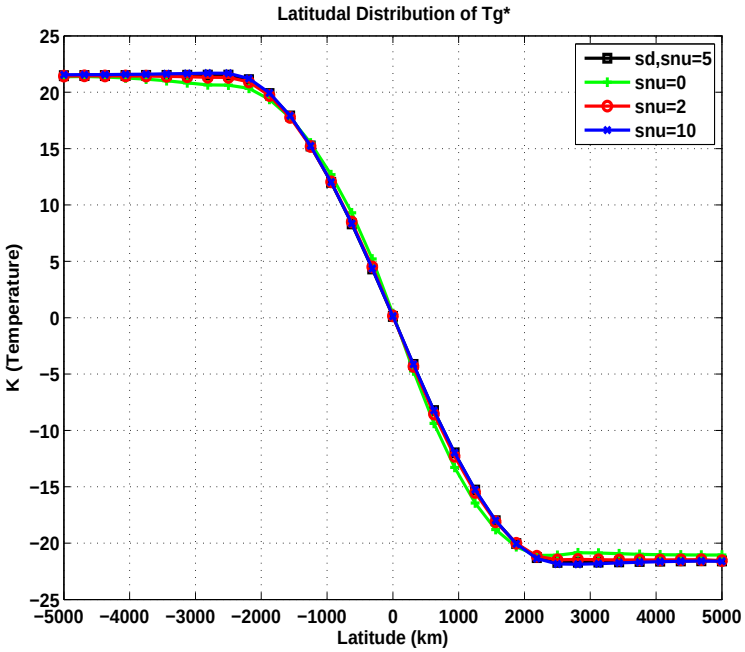

Figure 6-8: Latitudinal distribution of the underlying surface temperature in the equilibrium state in $\mu_s = 0$, 2, 10 $m^2 s^{-1}$ runs and in the SD run.

Figure 6-9(a), is consistent with the surface temperature. There are only tiny differences between the RCE state temperature gradients in these runs. Only the RCE temperature gradient in the $\mu_s = 0$ $m^2 s^{-1}$ run displays a slightly larger change. The difference of the equilibrium state temperature gradient between these runs, consistent with the results in Ch.4, primarily lies in the boundary layer. With weaker boundary layer thermal diffusion, the temperature gradient there is more efficiently reduced. The stratification, especially the stratification near the surface, is more stabilized under the weaker vertical thermal diffusion.

The response of the equilibrium state PV gradient in the boundary layer to the variation in μ_s is also similar to the uncoupled atmospheric run. The PV gradient is more efficiently homogenized when the boundary layer vertical thermal diffusion is turned off. The variation of the eddy heat fluxes in Figure 6-10 mainly lies in the boundary layer. Stronger vertical thermal diffusion results in enhanced eddy heat fluxes, which is consistent with the fact that the lower level zonal flow keeps a stronger baroclinicity under stronger vertical thermal diffusion.

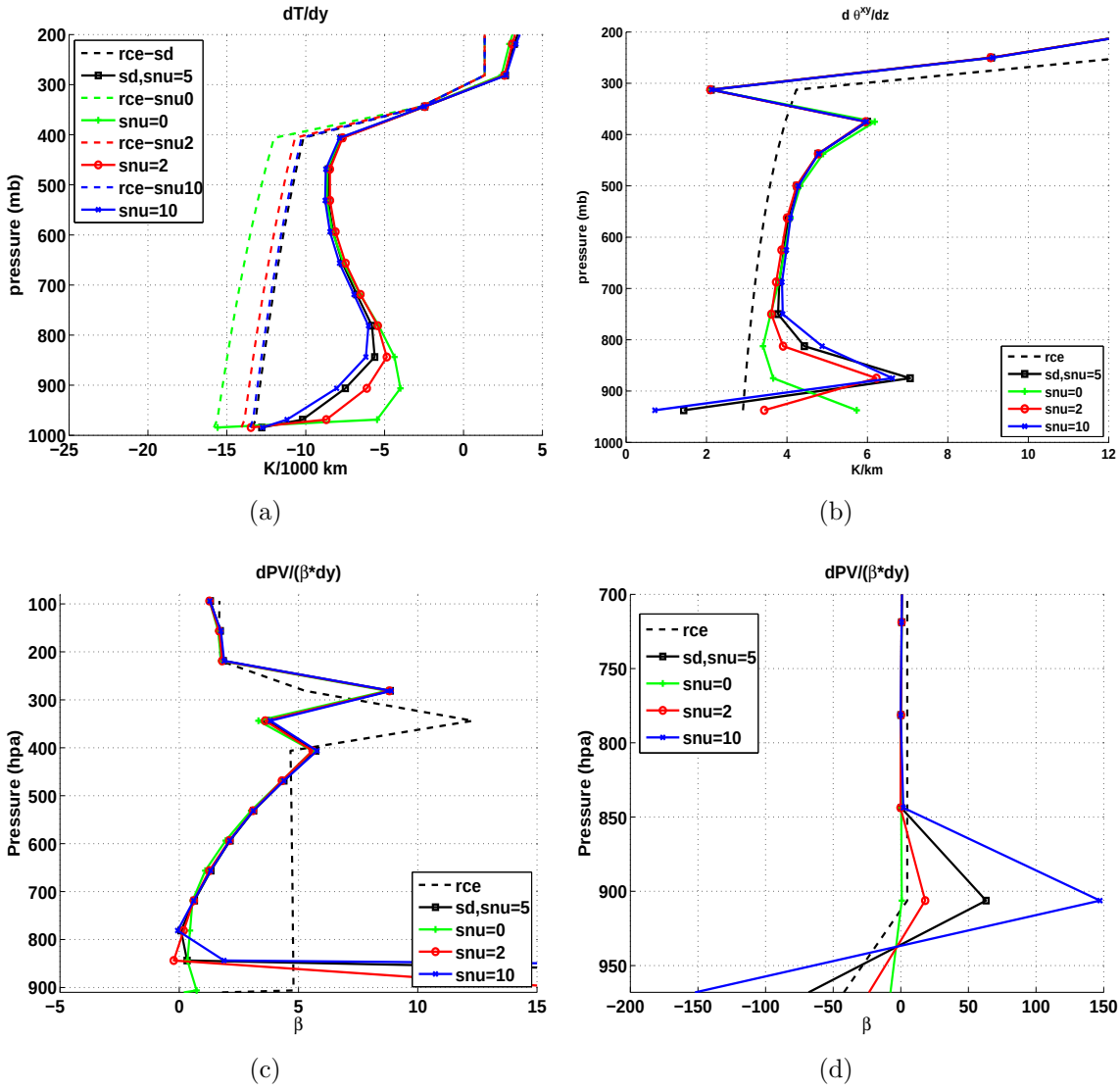

Figure 6-9: Comparison of equilibrated state (a) zonal mean temperature gradient at the center of the channel, (b)$d\overline{\theta}^{xy}/dz$, (c) zonal mean PV gradient in the free troposphere and (d) in the boundary layer for $\mu_s = 5$ (SD run), 0, 2 and 10 $m^2 s^{-1}$ runs.

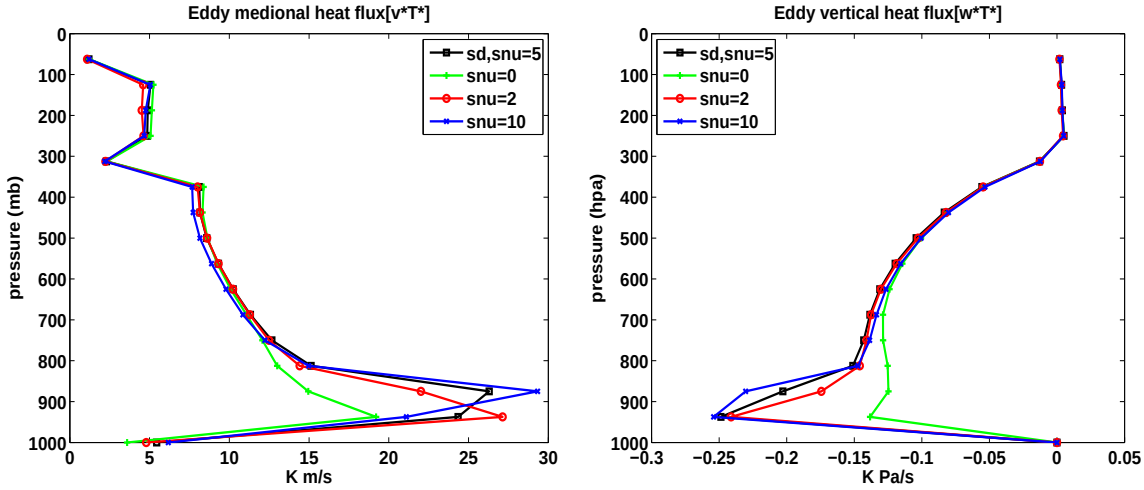

(a) (b)

Figure 6-10: Comparison of equilibrated state zonal mean (a) poleward eddy heat flux $[v^*T^*]$ and (b) vertical eddy heat flux $[\omega^*T^*]$ at the center of the channel for $\mu_s = 5$ (SD run), 0, 2 and 10 m^2s^{-1} runs.

The changes in each surface energy flux when varying μ_s is also plotted in Figures 6-11 and 6-12. The largest variation only occurs in the run where the boundary layer vertical thermal diffusion is turned off. In Figure 6-12(b), turning off the vertical thermal diffusion results in a strong reduction in the sensible heat flux, which is primarily because that without coupling with the atmosphere, the surface air temperature is more efficiently tied to the underlying surface temperature. Such reduced sensible heat flux is primarily balanced by the longwave radiation. When μ_s is nonzero, as shown in Figure 6-12, there is almost no variation in each surface energy flux.

6.3 Surface friction

As shown in Eqs.2.13 and 2.14, surface friction does not influence the surface energy budget directly. However, as discussed in Ch.4, surface friction has a large influence on the eddy activity as well as the eddy-mean flow interaction. Can it further influence the surface energy budget by modifying the eddy activity? Is the response of the coupled system to the change in the surface friction still non-monotonic? In this section, we will answer these questions

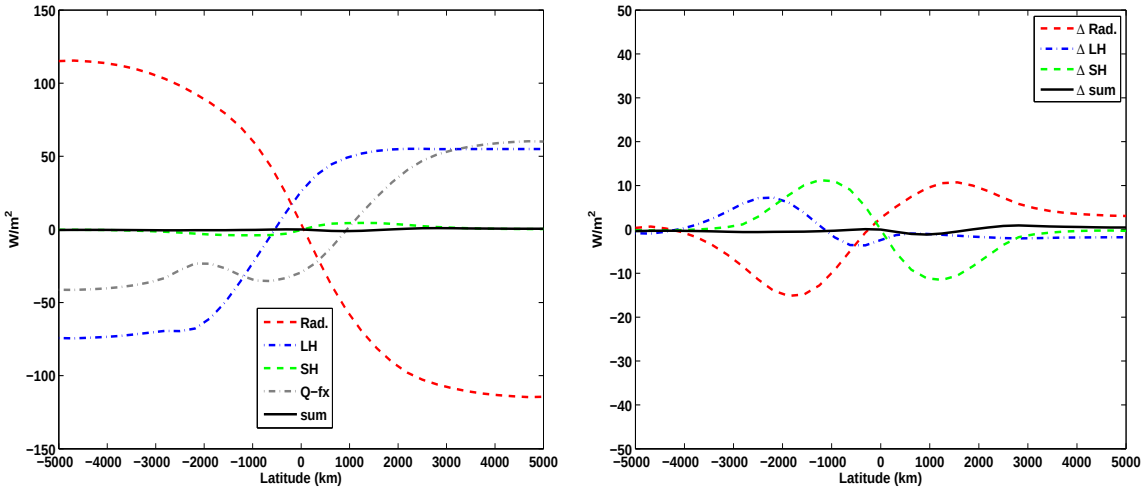

(a) (b)

Figure 6-11: Latitudinal distribution of the equilibrium state (a) radiative flux, latent heat flux, sensible heat flux, and Q-flux anomalies in the underlying surface energy budget for $\mu_s = 0\ m^2 s^{-1}$ run and (b) the difference of these flux anomalies compared with the $\mu_s = 5$ (SD) run.

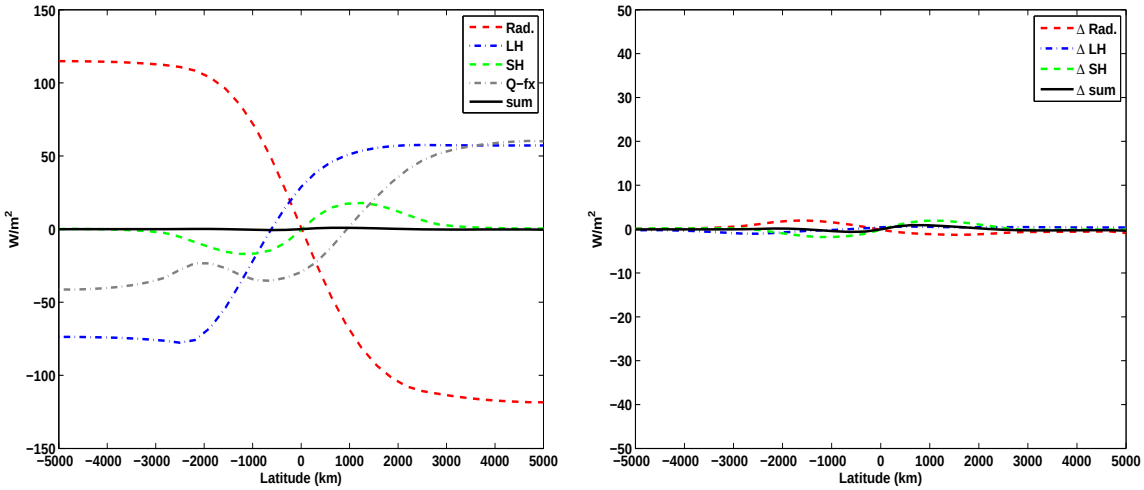

(a) (b)

Figure 6-12: Latitudinal distribution of the equilibrium state (a) radiative flux, latent heat flux, sensible heat flux, and Q-flux anomalies in the underlying surface energy budget for $\mu_s = 10\ m^2 s^{-1}$ run and (b) the variation of these fluxes anomalies compared with the $\mu_s = 5$ $m^2 s^{-1}$ (SD) run.

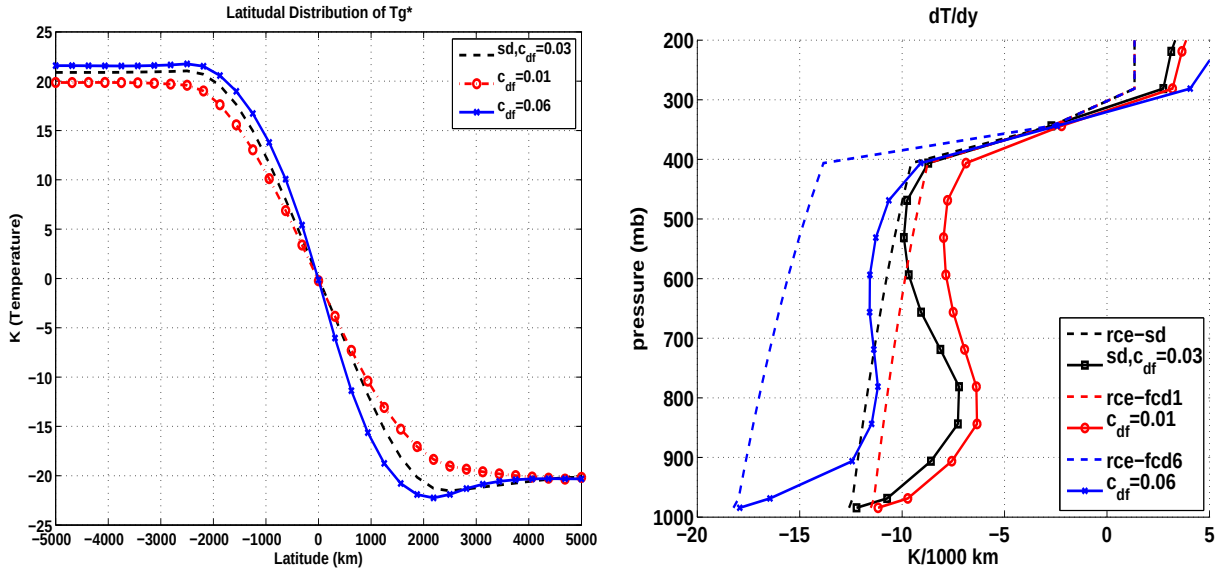

(a) (b)

Figure 6-13: (a)Latitudinal distribution of the equilibrium state underlying surface temperature and (b) the vertical distribution of the equilibrium state (solid curves) and the corresponding RCE state (dashed curves) temperature gradient at the center of the channel for $c_{df} = 0.03$ (SD run), 0.01 and $0.06 ms^{-1}$ runs.

by carrying out a sensitivity study in which the surface friction coefficient c_{df} is varied.

6.3.1 Equilibrium state

The latitudinal distribution of the equilibrium state surface temperature is displayed in Figure 6-13(a). Instead of the non-monotonic response in Chapter 4, in the coupled model, weaker surface friction results in a smaller surface temperature gradient. The equilibrium state and the corresponding RCE state temperature gradients in the atmosphere at the center of the channel with different values of c_{df} are also plotted in Figure 6-13(b). As a consequence of the reduced underlying surface temperature, the RCE state temperature gradient is also smaller under the weaker surface friction. The atmospheric temperature also equilibrates with a weaker meridional gradient.

The response of the eddy heat fluxes in Figure 6-14, however, differs from expectation. In spite of the weaker baroclinicity of the mean flow when $c_{df} = 0.01\ ms^{-1}$, the eddy heat flux

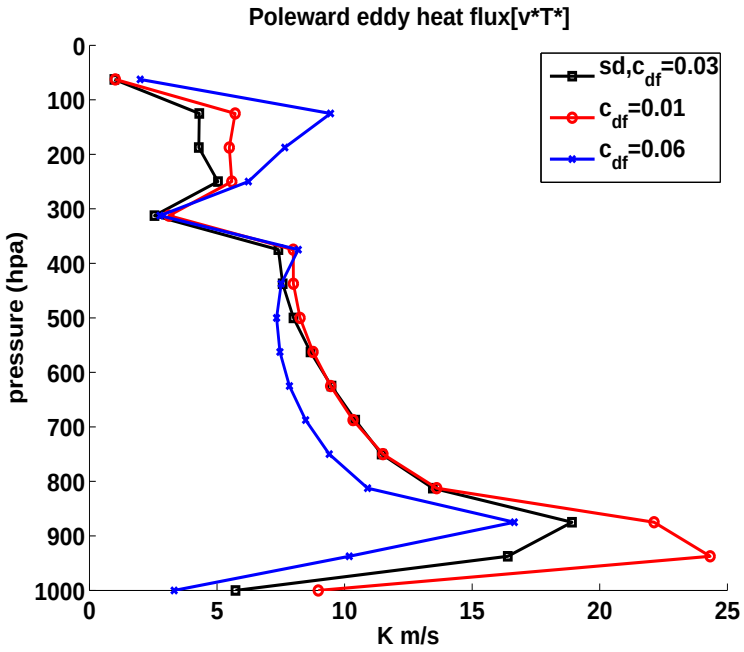

Figure 6-14: Vertical distribution of the eddy poleward heat flux when varying the surface friction.

gets stronger compared with the SD run. This indicates that under the competing effects of the weaker mean available potential energy and the weaker frictional damping on the eddy energies, the later effect becomes dominant. The meridional eddy heat flux is strongly influenced by the surface friction.

The variation of the equilibrium state PV gradient, as shown in Figures 6-15(a) and 6-15(b), is consistent with the temperature gradient. In both the boundary layer and the free troposphere, PV equilibrates with a smaller meridional gradient as the surface friction becomes weaker.

The latitudinal distribution of each surface energy flux in the equilibrium state and their variation compared with the SD run when under weaker ($c_{df} = 0.06\ ms^{-1}$) and stronger ($c_{df} = 0.01\ ms^{-1}$) surface friction are shown in Figure 6-16 and 6-17, respectively. Along with the stronger eddy heat flux and the smaller surface air temperature gradient in Figs.6-14 and 6-13(b), weaker surface friction results in a stronger surface sensible heat flux (stronger air-sea temperature difference), which acts to warm the higher latitudes and cool the lower latitudes.

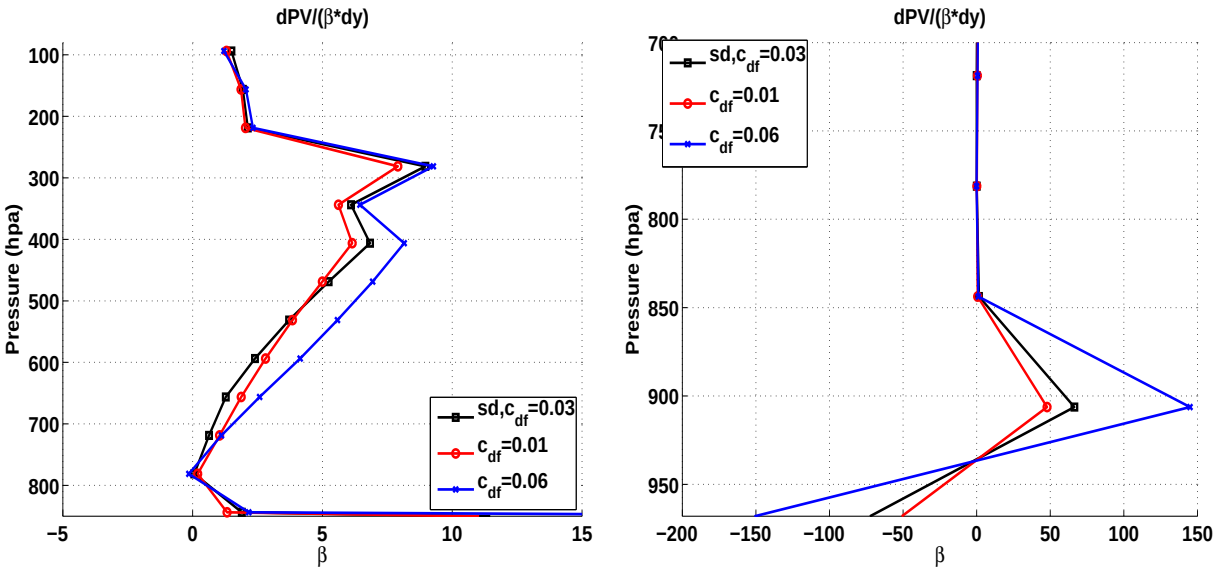

Figure 6-15: Vertical distribution of the equilibrium state meridional PV gradient at the center of the channel in the (a) free troposphere and (b) in the boundary layer for $c_{df} = 0.03$ (SD run), 0.01 and $0.06 ms^{-1}$ runs.

The latent heat flux changes are still opposite to the sensible heat flux changes, which are primarily a response to the smaller surface temperature gradient. The longwave radiation changes are similar to the sensible heat flux. In addition, different from the experiments with a varying surface heat exchange coefficient, changes in the surface energy flux are all confines within the central half of the channel where baroclinic eddies are active, which further confirms that all these variations are caused by the varying eddy activity. Under stronger surface friction, as in Fig.6-17, surface energy fluxes show similar changes but in the opposite directions.

6.3.2 Transient response

A transient response run experiment is also carried out to further investigate the mechanism through which surface friction influences the coupled system. In the experiment, we start from the equilibrium state of the SD run, and suddenly reduce the c_{df} from 0.03 to 0.01 ms^{-1}. The time evolution of each surface energy flux and the surface temperature variation

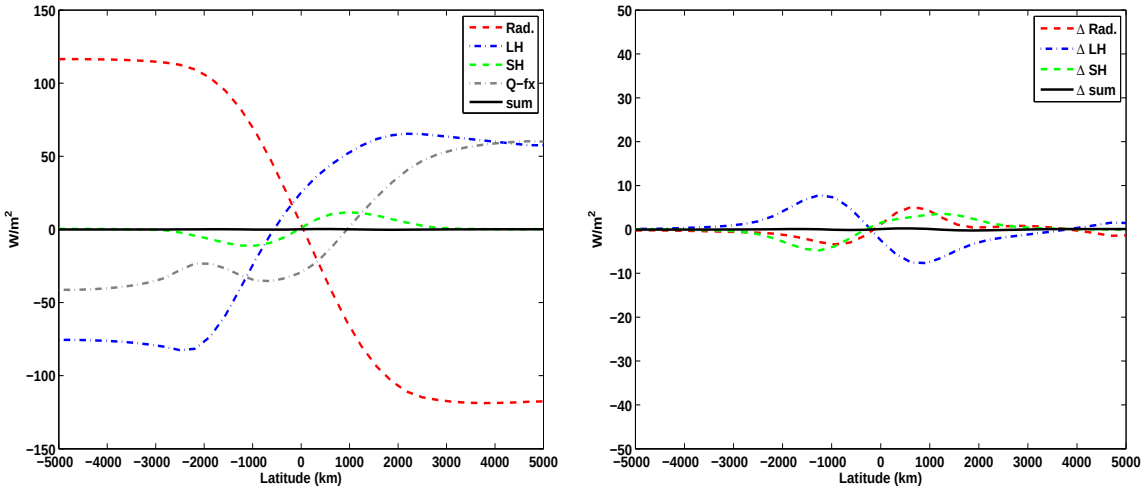

(a) (b)

Figure 6-16: Latitudinal distribution of the equilibrium state (a) radiative flux, latent heat flux, sensible heat flux, and Q-flux anomalies in the underlying surface energy budget for $c_{df} = 0.01\ ms^{-1}$ run and (b) the difference of the flux anomalies compared with the $c_{df} = 0.03\ ms^{-1}$ (SD) run.

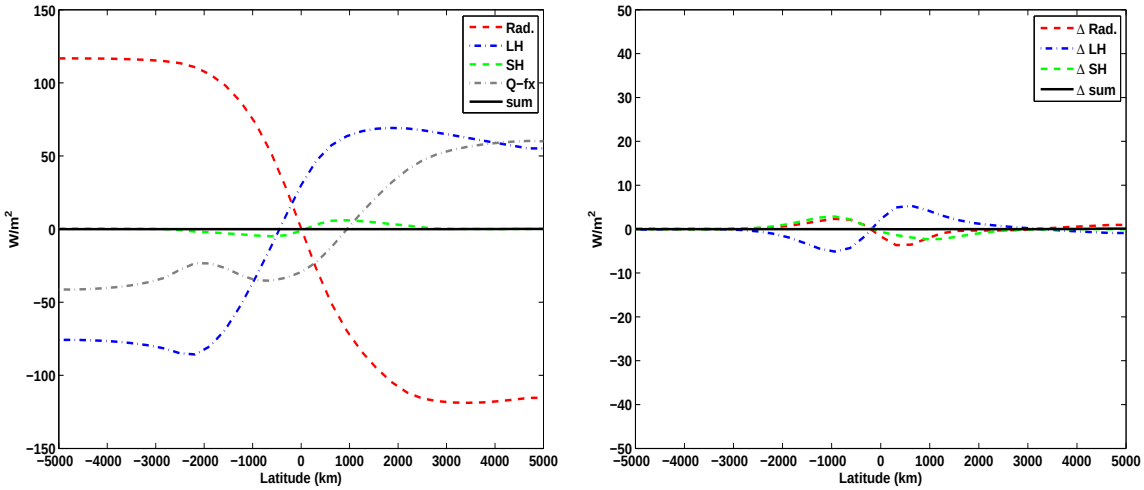

(a) (b)

Figure 6-17: Latitudinal distribution of the equilibrium state (a) radiative flux, latent heat flux, sensible heat flux, Q-flux anomalies in the underlying surface energy budget for $c_{df} = 0.06\ ms^{-1}$ run and (b) the changes of the flux anomalies compared with the $c_{df} = 0.03\ ms^{-1}$ (SD) run.

are plotted in Figure 6-18. The transient response of the poleward eddy heat flux in the boundary layer and the surface temperature gradient and the temperature gradient at 875 hpa at the center of the channel are also displayed in Figure 6-19.

The strongest immediate response to the reduced surface friction lies in the poleward eddy heat flux as well as the temperature gradient in the atmospheric boundary layer. The eddy heat flux increases to twice its original value in the first few days. The lower level temperature gradient follows the variation of the eddy heat flux, and reduced in the first few days. Then, as the eddy heat flux becomes stronger, the surface sensible heat flux is also enhanced. As a result, the surface temperature gradient at the center of the channel also begins to decrease. The meridional variation of latent heat flux is reduced with the surface temperature gradient, which acts to offset the increased sensible heat flux. After tens of days, the longwave radiation anomaly appears to reduce the surface temperature gradient, like the sensible heat flux. In this period, the surface temperature gradient is further reduced. The boundary layer temperature gradient and the eddy heat transport, vary following the underlying surface. After hundreds of days, the coupled system reaches an equilibrium state with a strongly reduced surface and atmospheric temperature gradient. The eddy heat flux, though becomes weaker in the last few hundreds days with the weaker mean flow temperature gradient, still equilibrates at a stronger state than the SD run.

We also find that as we reduce the surface friction, the transient response of the coupled system in the first few days is similar to the results in Ch.4. In Figure 6-20, the variation of the mean flow temperature at 875 hpa is also plotted. The immediate response of the mean flow is a more efficiently reduced temperature gradient. Then, as in the uncoupled atmosphere run, the latitudes where the temperature is most modified by the baroclinic eddies move away from the center of the channel, with the temperature gradient at the center not being efficiently reduced but more modified at the flank of the jet. During this period, the latitudes where the sensible heat flux and the underlying surface temperature are most modified also move away from the center of the channel. However, as the other surface energy fluxes begin to play active roles, the amount that the temperature is modified from

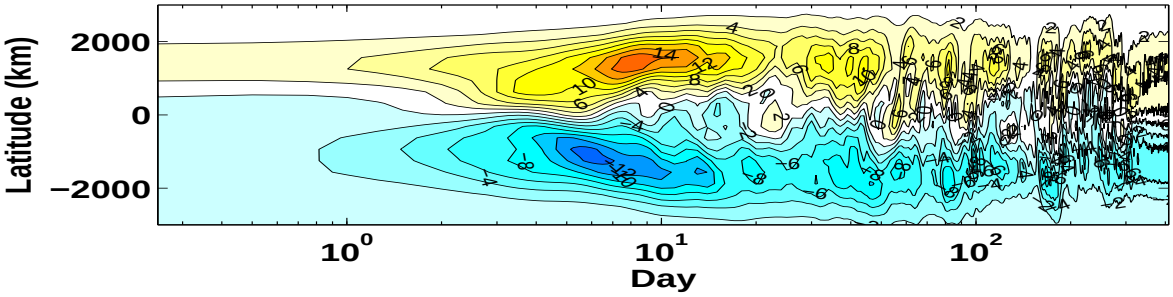

(a)

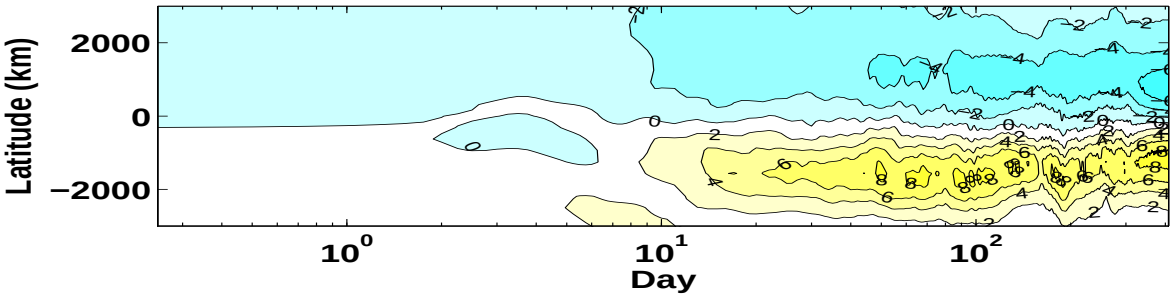

(b)

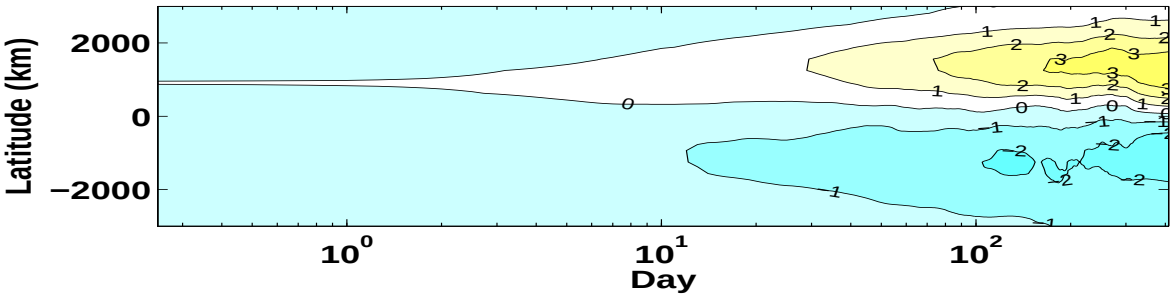

(c)

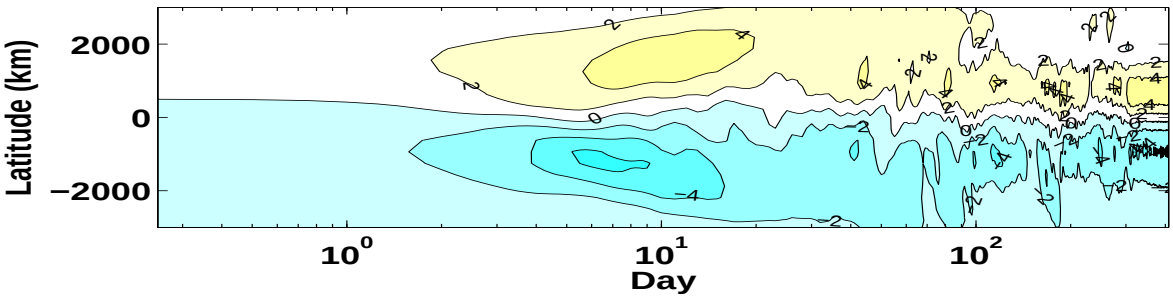

(d)

Figure 6-18: Time evolution of the (a) sensible heat flux variation $F_{sh} - \overline{F_{sh}}^{sd}$, (b) latent heat flux variation $F_{lh} - \overline{F_{lh}}^{sd}$, (c) radiative flux variation $F_{rad} - \overline{F_{rad}}^{sd}$ and (d) the surface temperature variation $T_g - \overline{T_g}^{sd}$ when suddenly increasing c_{df} from 0.03 (SD) to 0.01 ms^{-1}. Contour interval is 2, 2 and 1 Wm^{-2} in panel (a), (b), (c), respectively, and 2 K in panel (d). Note that the x-coordinate is plotted on a logarithmic scale.

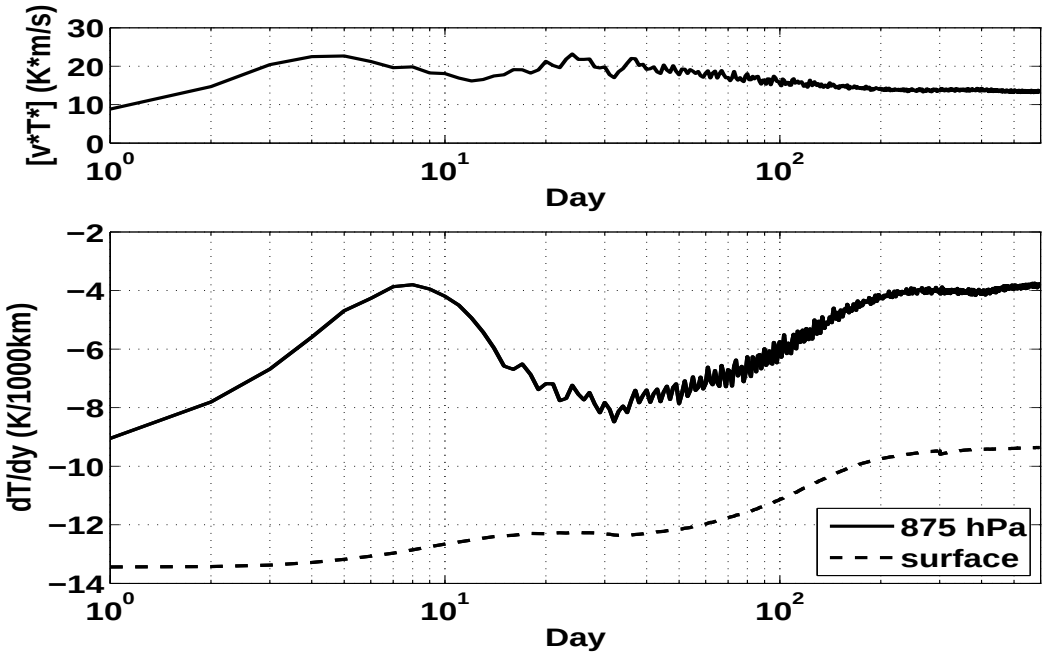

Figure 6-19: Time evolution of the poleward eddy heat flux (top), and the surface, 875 hpa temperature gradients (bottom) at the center of the channel when suddenly reducing the surface friction.

the corresponding RCE state goes back and the latitudes where the temperature is most strongly modified also move back to the center of the channel. Finally, the coupled system equilibrates with a weaker temperature gradient under the weaker surface friction.

6.3.3 Role of ageostrophic winds

In our previous experiments, the surface and the boundary layer frictional dissipation is estimated using the geostrophic winds in the model. However, in the boundary layer, especially near the surface, as shown in Chapter 4, the ageostrophic winds can be comparable with the geostrophic winds, which acts to offset the frictional dissipation by the geostrophic winds. In this section, using the method in Section 2.2 and Chapter 4, we will estimate the ageostrophic winds, and investigate how they can affect the coupled system. Here we run similar sensitivity studies on the surface friction, but consider the ageostrophic winds in Eq.2.11. The equilibrium state surface and atmospheric temperature gradient, the atmo-

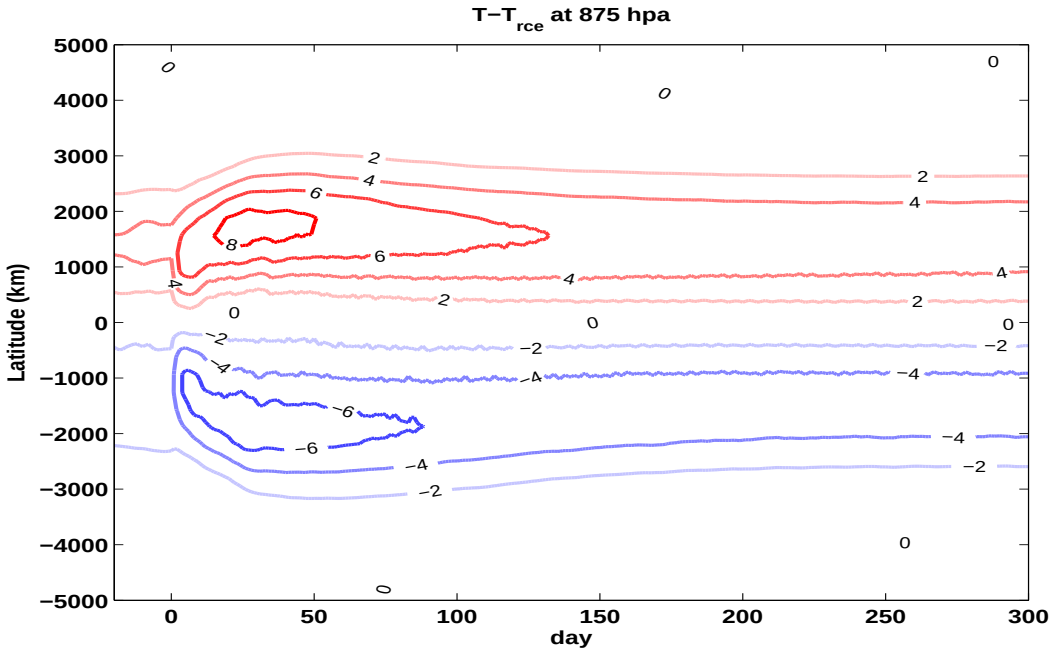

Figure 6-20: Time evolution of the temperature difference $T - T_{rce}$ at 875 hpa when suddenly reducing the surface friction. Contour interval is 2 K.

spheric stratification and the eddy heat flux are plotted in Figure 6-21.

We find that like the uncoupled atmosphere run, the net effect of including the ageostrophic winds is similar to decreasing the drag coefficient c_{df}. When including the ageostrophic winds, the coupled system equilibrates with more efficiently reduced surface and atmospheric temperature gradients and a stronger eddy heat flux. Due to the negative feedback between the surface friction coefficient and the ageostrophic winds on the frictional forcing, we find that compared with the experiments using geostrophic frictional forcing, the sensitivity of the coupled system to the value of c_{df} is greatly reduced. However, the tendency of the coupled system to increasing c_{df} is still the same. The PV gradient in the equilibrium state is much less sensitive to the surface friction as well, as shown in Figure 6-22. The tendency of the PV gradient to the surface friction is still the same.

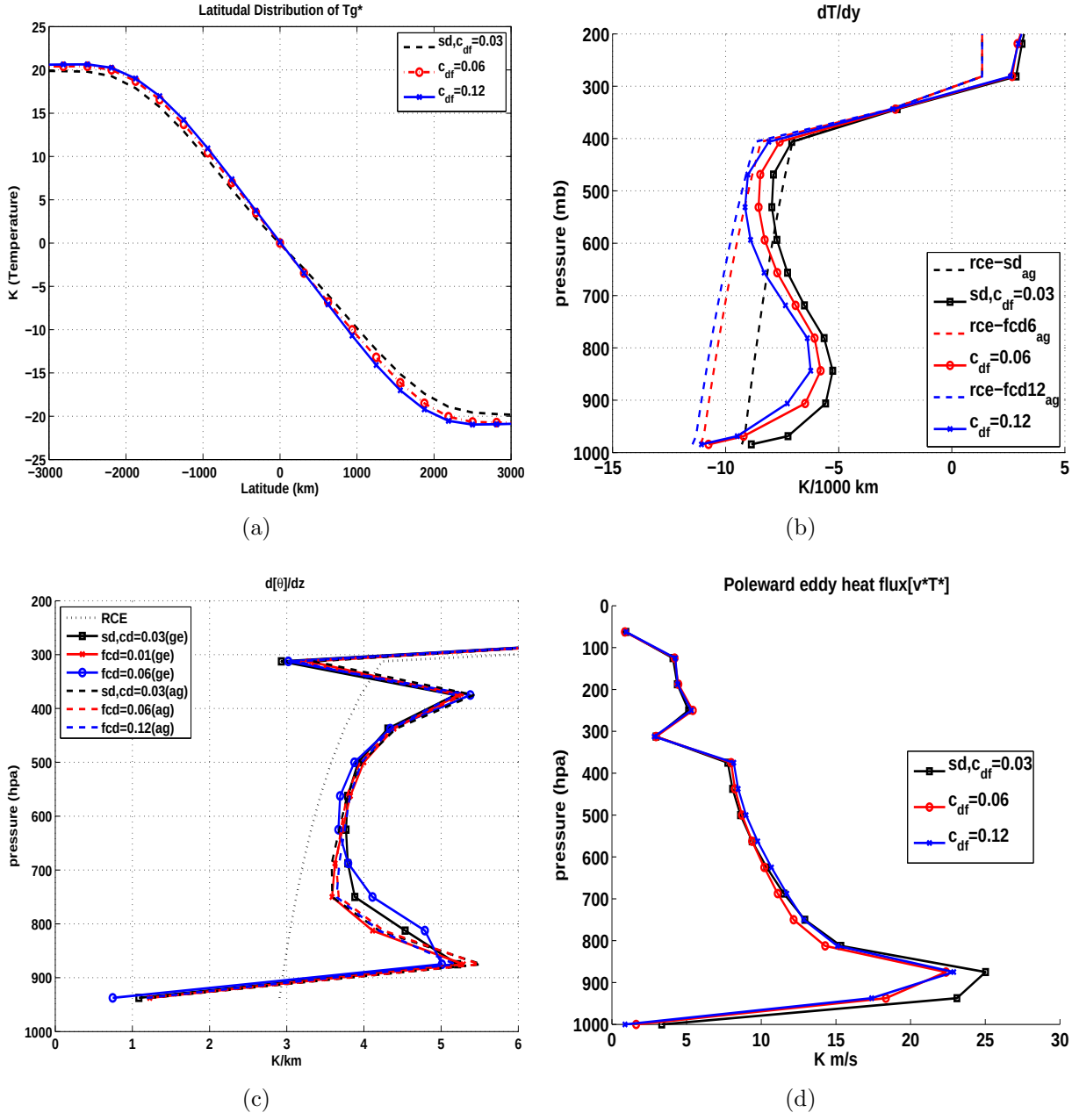

Figure 6-21: Equilibrium state (a) latitudinal distribution of the underlying surface temperature, (b) vertical distribution of the temperature gradient at the center of the channel, (c) vertical distribution of the stratification and (d) vertical distribution of the poleward eddy heat flux at the center of the channel for $c_{df} = 0.03$, 0.06 and $0.12 ms^{-1}$ runs when including the ageostrophic winds in the frictional dissipation.

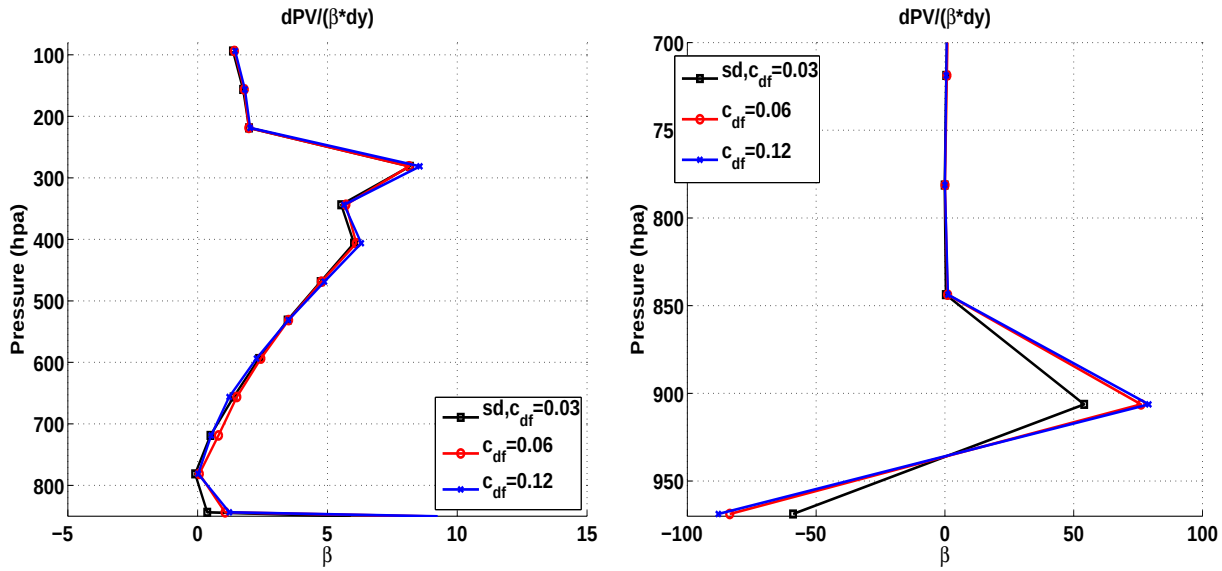

Figure 6-22: Vertical distribution of the meridional PV gradient at the center of the channel in the (a) free troposphere and (b) in the boundary layer for $c_{df} = 0.03$, 0.06 and $0.12 ms^{-1}$ runs when including the ageostrophic winds in the frictional dissipation.

6.4 Dependence on the Q-flux

In our atmosphere-slab surface coupled model, in order to obtain a realistic surface temperature gradient, a Q-flux is included in the surface energy budget as a parameter in the surface model. In this section, we will carry out another group of tests to investigate the influence of Q-flux on our results.

In this section, we still use the 43 K north-to-south temperature difference as our target surface temperature distribution but with $c_{dt} = 0.01\ ms^{-1}$ as the default value. In the equilibrium state of the uncoupled atmospheric run, as shown in Figure 6-23, the air-surface temperature difference has the same latitudinal distribution but with a larger magnitude compared with Fig.5-1(b). As the c_{dt} is reduced to one third of the SD value, the largest air-surface temperature difference is almost three times as large as in the SD run. Using the same method as in Ch.5, the latitudinal distribution of each surface energy flux and the new Q-flux are estimated. Their distributions are also plotted in Figures 6-24 and 6-25. Compared

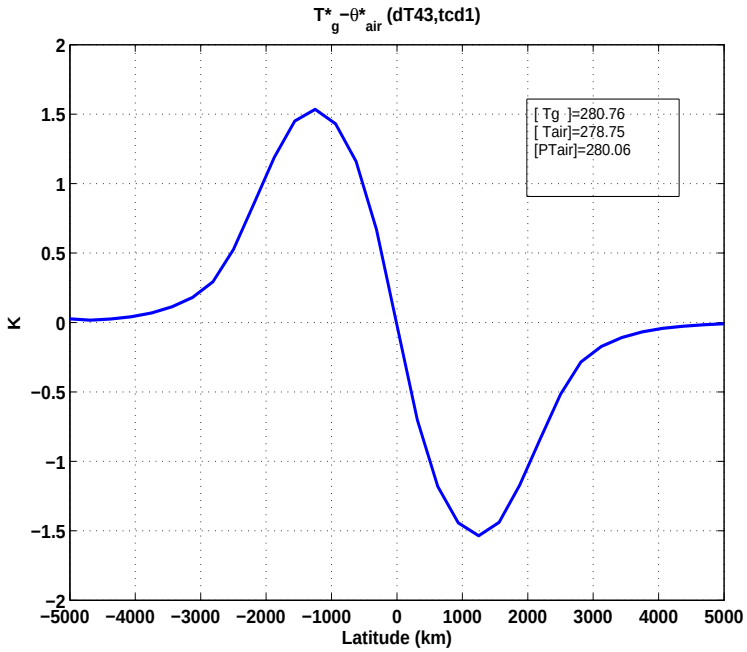

Figure 6-23: Latitudinal distribution of the difference between the surface temperature $T_g^\dagger$ and the surface air potential temperature $\theta_{air}^\dagger$ in the target state when $c_{dt} = 0.01\ ms^{-1}$, where superscript † indicates deviation from the horizontal mean.

with the SD run (Fig.5-8), the main changes in the surface energy fluxes lie in the latent heat flux. As the c_{dt} is reduced, with the same target surface temperature, the latent heat flux is also reduced to almost one third of the SD values. As the longwave radiation and the sensible heat flux are almost unchanged, to maintain the same target surface temperature, a much larger Q-flux with lager meridional variation is required. As shown in Fig.6-24, the meridional variation of the Q-flux is twice as large as in the SD run. In addition, since the evaporation cooling of the surface is greatly reduced, in the horizontal mean, a net cooling of the surface is still required to keep the same global mean surface temperature.

With the new Q-flux, we run sensitivity studies like those in Section 6.1 to check the dependence of the coupled system on the surface heat exchange coefficient. The surface temperature, atmospheric temperature gradient, stratification and the eddy heat flux in the equilibrium state under different c_{dt} are plotted in Figure 6-26.

Under the stronger Q-flux, in each run, compared with Fig.6-1, the underlying surface

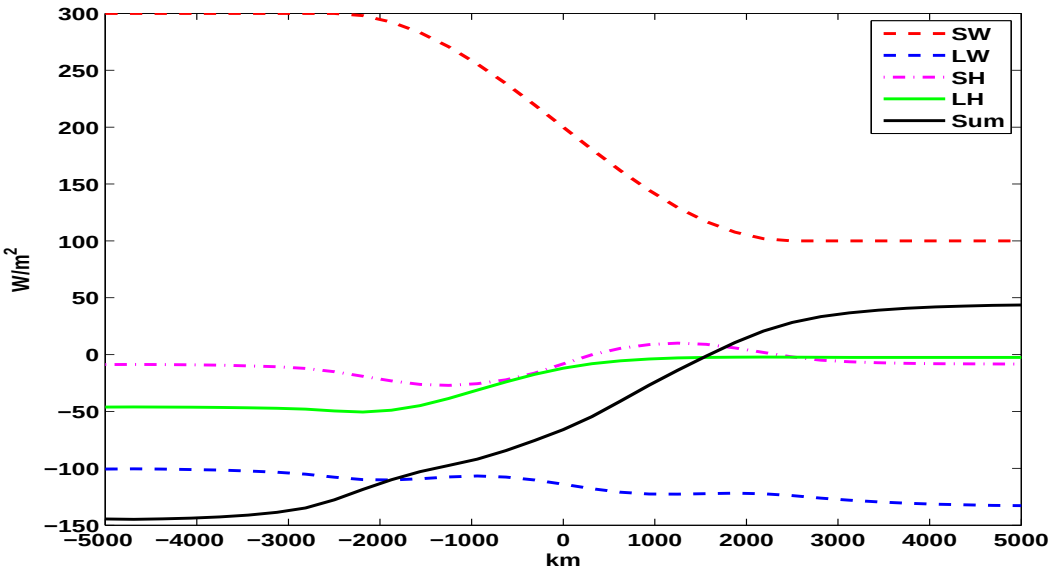

Figure 6-24: Latitudinal distribution of the net shortwave and longwave radiations, sensible and latent heat fluxes, and the required Q-flux to maintain the target state when $c_{dt} = 0.01$ ms^{-1}.

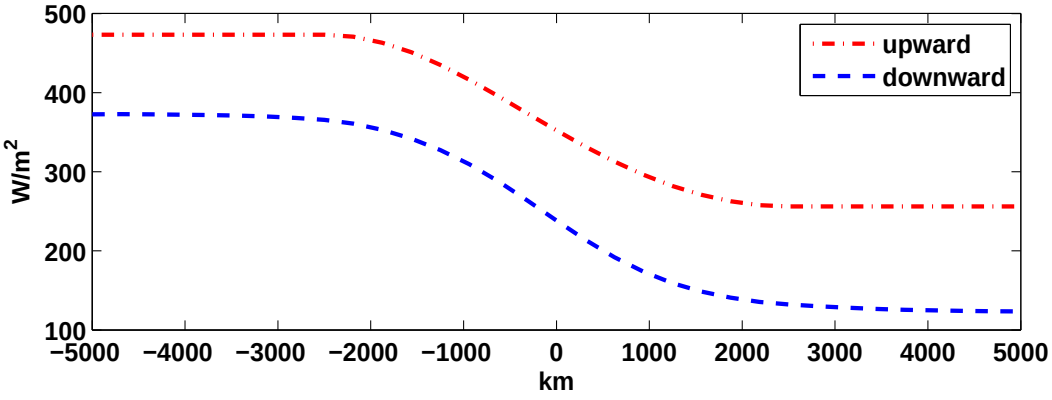

Figure 6-25: Latitudinal distribution of the surface upward longwave emission and downward Infrared flux into the surface in the target state when $c_{dt} = 0.01$ ms^{-1}.

equilibrates with a smaller temperature gradient. When $c_{dt} = 0.06\ ms^{-1}$, the north-to-south difference of the surface temperature over the channel is reduced to 20 K. However, the tendency tendency of the surface temperature to changes in c_{dt} is still the same, that is stronger c_{dt} results in a weaker surface temperature gradient.

The RCE state temperature gradient and the equilibrium state temperature under different c_{dt} are displayed in Figure 6-26(b). Similar to Section 6.1, stronger surface heat flux results in weaker RCE state temperature gradient. When turning off the surface heat flux, the lower level temperature gradient in the atmosphere is also greatly reduced. With respect to the surface heat flux, the mean flow temperature gradient is influenced by two competing factors: first, the radiative-convective heating is weaker under larger c_{dt}; on the other hand, the eddy heat flux (in Figure 6-26(d)) as well as the eddy meridional mixing of the temperature is also weaker. Thus, when $c_{dt} = 0.06\ ms^{-1}$, along with the very weak eddy activity, the temperature gradient is not efficiently reduced especially in the lower level. As a result, the response of the equilibrium state temperature gradient to variations in c_{dt} is not monotonic. In the $c_{dt} = 0.06\ ms^{-1}$ run, its lower level temperature gradient is even slightly larger than the $c_{dt} = 0.03\ ms^{-1}$ run. The variation of the stratification when increasing c_{dt} is similar to Section 6. 1, where a less stable stratification is observed under stronger surface heat exchange.

The response of the equilibrium state PV gradient under different c_{dt} is almost the same as in Section 6.1. In the free atmosphere, the variation of the PV gradient is small, while in the boundary layer, under weaker surface heat change, the PV gradient is more efficiently homogenized. A much weaker PV gradient is observed when $c_{dt} = 0\ ms^{-1}$.

As we have shown in this Section, variations in Q-flux can modify the equilibrium state of the coupled system, with stronger Q-flux equilibrating with a weaker temperature gradient. However, the response tendency of the equilibrium state to the variation in the surface heat flux and the mechanism by which the boundary layer processes affect the coupled system are still the same. These results are robust under different Q-flux.

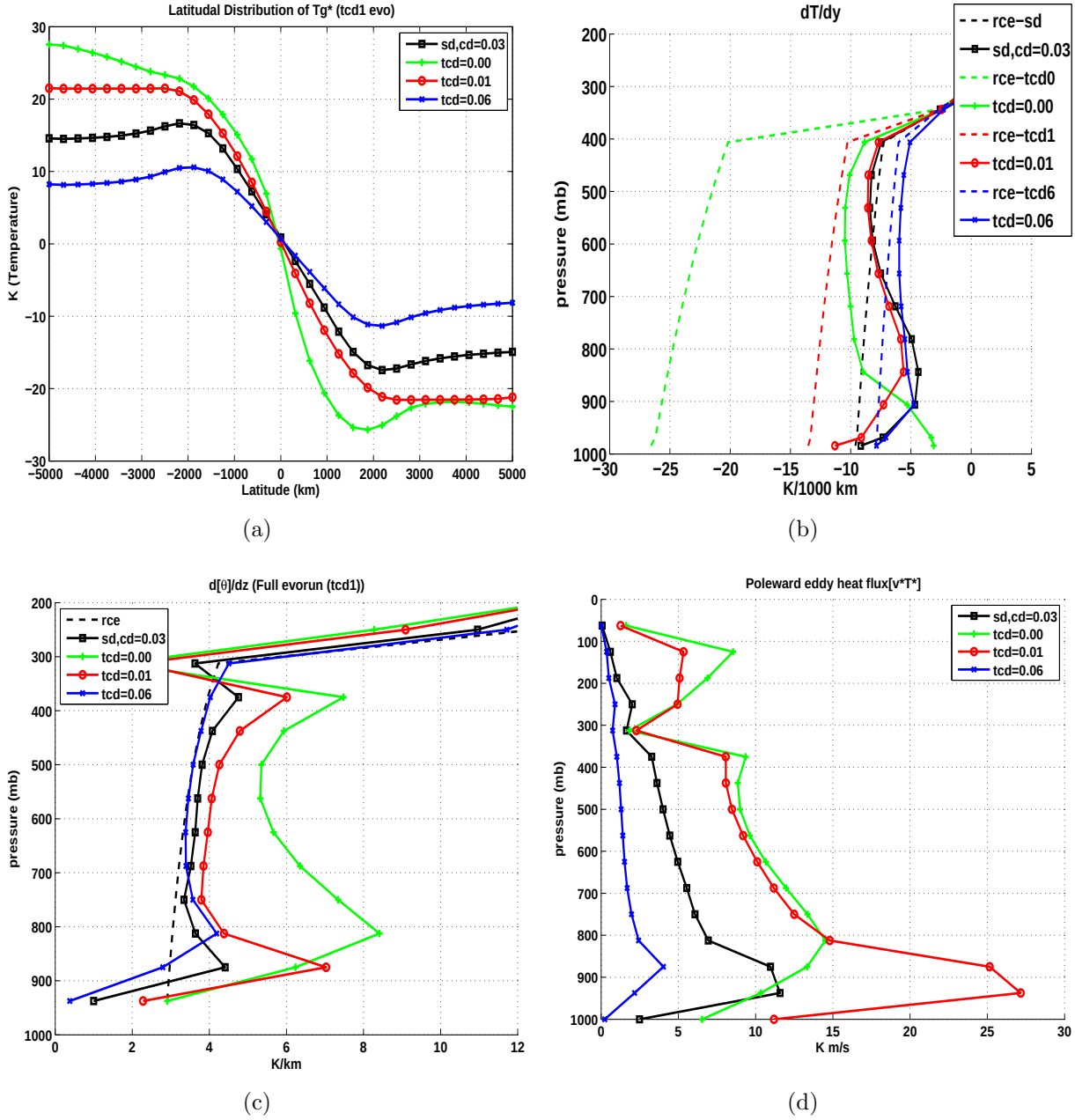

Figure 6-26: Equilibrium state (a) latitudinal distribution of the underlying surface temperature, (b) vertical distribution of the temperature gradient at the center of the channel, (c) vertical distribution of the stratification and (d) vertical distribution of the poleward eddy heat flux at the center of the channel in the $c_{dt} = 0$, 0.01, 0.06 ms^{-1} runs and the SD run with the new Q-flux.

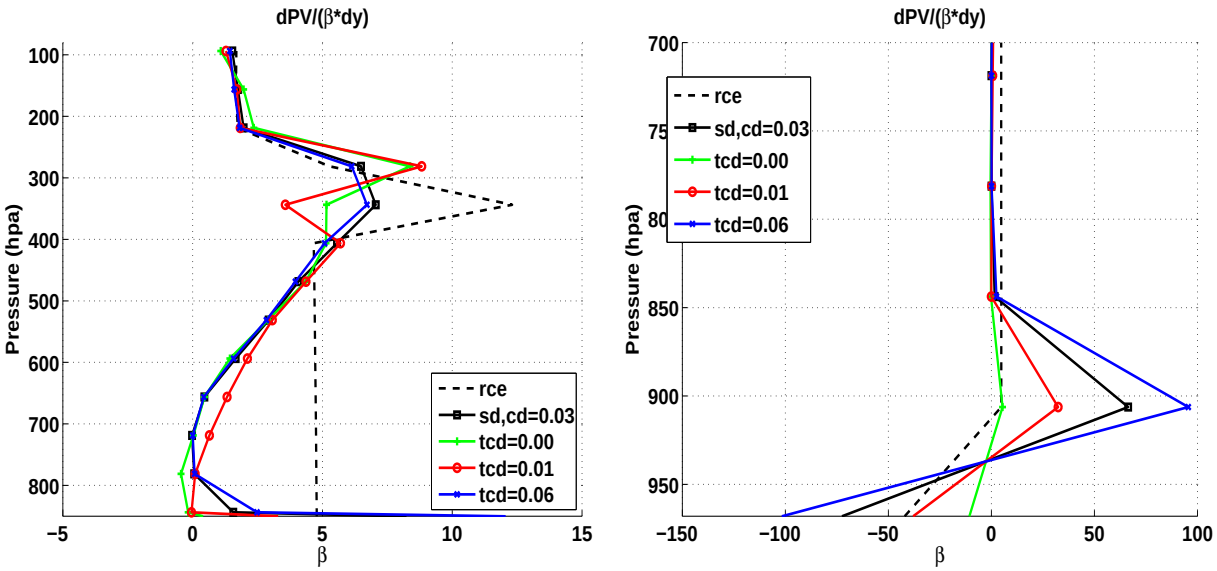

(a) (b)

Figure 6-27: Vertical distribution of the meridional PV gradient at the center of the channel in the (a) free troposphere and (b) in the boundary layer in the c_{dt} = 0, 0.01, 0.06 ms^{-1} runs and the SD run with the new Q-flux.

6.5 Summary

In this and the previous chapters, equilibration studies have been carried out to investigate the different roles of each boundary layer process in the air-surface coupled system. In addition to the mechanisms discussed in Chapter 4, in a coupled model, boundary layer processes can further influence the equilibration by affecting the surface temperature. Different boundary layer processes can affect the equilibrium state surface temperature in different ways.

The surface latent and sensible heat fluxes are the important components in the surface energy budget. Varying the surface heat coefficient can modify the surface temperature directly. Surface friction, however, can influence the equilibration of the underlying surface in the coupled system in an indirect way. As shown in the spin-up run, eddy mixing of the surface air temperature and the consequent enhanced sensible heat flux result in a weaker surface temperature gradient in the equilibrium state. As studied in Ch.4, surface friction

greatly affects the meridional eddy heat transport, especially in the boundary layer, which will further influence the underlying surface temperature in the coupled model.

In our coupled model, the modified underlying surface temperature can influence the atmospheric flow in two ways: first, it is the lower boundary condition of the atmospheric model. Through the boundary thermal processes, it can be quickly 'felt' by the lower level atmosphere; in addition, the RCE state temperature is also set to match the underlying surface, thus the radiative-convective heating exerted on the atmospheric flow is also modified. These two processes can further influence the eddy activity. Therefore, adding a slab surface means adding more complicated feedbacks to the system.

Under these competing mechanisms, our coupled model shows different responses to the different boundary layer process.

- Our model results show that reducing surface friction increases the poleward eddy heat flux in the atmosphere and results in a weaker surface temperature distribution in the equilibrium state. The transient response to the suddenly reduced surface friction indicates that the non-monotonic response in Chapter 4 to the surface friction also appears in the first few days of the transient variation, when the underlying surface has not begun to change. When the changes in the surface temperature is included, the weaker surface and RCE state temperature gradients finally result in a weaker atmospheric temperature gradient at the center of the channel.

- The response to the surface sensible and latent heat fluxes is more complicated. Under the same global averaged surface temperature, the direct effect of the surface heat flux in determining the underlying surface temperature gradient is dominant. Since the latent heat flux is the dominant component in balancing the meridional contrast of the solar radiation, different from the uncoupled atmospheric run, reducing the surface heat drag coefficient results in much stronger surface and atmospheric temperature gradients. The sensible heat flux, however, responds differently to the changes in the drag coefficient. Due to the strong eddy activity in the weak drag coefficient run, the surface sensible heat flux is increased in the equilibrium state.

- Even though different boundary layer processes influence the equilibrium state surface and atmospheric temperature differently, we find the response of the PV gradient to changes in the boundary layer processes is similar. Since we use a shallower boundary layer depth in these runs, compared with Ch.4, the influence of the boundary layer on the PV gradient around 600 to 800 hpa is weaker. However, in the boundary layer, we find that they modify the PV structure in a similar way, that is the boundary layer forcing prevents the PV homogenization there. The PV gradient is more efficiently reduced under weaker boundary layer forcing.

- The transient response of the coupled system to changes in surface friction and surface heat flux displays three different time scales affecting the equilibration of the coupled model. A quick forcing time scale of the boundary layer heat flux on the lower atmosphere ($\sim$ 1 day), a synoptic adjustment time scale of the baroclinic eddies to the zonal flow (a few days) and a much longer response time scale of the underlying surface to the surface heat flux, which depends on the depth of the underlying surface. Under a very shallow ocean mixed layer (5 m), this time scale is a few hundreds of days.

- Our study shows that the underlying surface temperature is insensitive to the vertical thermal diffusion.

In this study, to understand the effect of the surface heat flux on the atmospheric eddy equilibration, only a slab surface model is coupled with the atmospheric model to provide an interactive surface temperature distribution. The oceanic meridional heat transport is represented with a pre-calculated Q-flux. This is a good assumption as long as the variation of the ocean heat transport caused by the boundary layer processes is negligible, or the variation time scale of the ocean heat transport is much longer than the other surface energy fluxes. In midlatitudes, the meridional ocean heat transport is associated in fact with the Gyre circulations, which can be influenced by the surface wind. To improve this, investigating the role of the boundary layer processes with an atmospheric model coupled with a barotropic ocean model could be a reasonable future project. In addition, the Meridional Overturning

Circulation in the ocean is also associated with the surface heat and momentum fluxes. How the boundary layer processes influence this coupled system could be another interesting topic.

Chapter 7

Eddy equilibration under specified seasonal forcing

In many equilibration studies to investigate the relation between baroclinic eddies and the mean flow, the external forcing is always specified and kept fixed during the eddy equilibration. This is equivalent to assuming that, compared with the variation time scale of the external forcing, the atmosphere adjustment by baroclinic eddies is always relatively quick. The validity of this assumption is investigated in this chapter by studying the response of baroclinic eddies to the time varying external forcing. One example of the time varying external forcing is the seasonal cycle, especially the seasonal cycle of the external forcing in the midlatitudes of the Northern Hemisphere. Here, we investigate the baroclinic eddy equilibration under a Northern Hemisphere-like seasonal forcing and try to answer the questions as to whether the eddies can maintain a preferred equilibrium state in spite of the variation of the external forcing, and whether the theories and results we obtained in the equilibrium study still hold.

The theory we will test in the experiment is the baroclinic adjustment, which, as discussed in Chapter 1, was inspired in part by the observed robust PV gradient (isentropic slope) over the whole year in spite of the seasonal forcing (Stone, 1978). Many equilibrium studies as well as the study in Chapter 3 confirmed that, even under different strengths of

differential heating, in the equilibrium state, baroclinic eddies can always maintain a robust isentropic slope (Stone and Branscome, 1992; Solomon and Stone, 2001b; Zurita-Gotor, 2008). However, when under a time varying seasonal forcing, the validity of the baroclinic adjustment hypothesis is barely carefully investigated in the numerical study. In this study, we will test the robustness of the isentropic slope by studying the eddy behavior under specified seasonal forcing, and try to answer to what extent baroclinic adjustment can be a good approximation.

7.1 Observed seasonal cycles

Observations show that the Northern and Southern Hemispheres have different seasonality in surface temperature, atmospheric temperature and eddy activities. Primarily due to the larger portion of land surface, the Northern Hemisphere atmosphere exhibits stronger seasonal variation, while the Southern Hemisphere seasonal cycle is much weaker, and such difference in seasonality is most obvious in midlatitudes.

Figure 7-1 shows the seasonal variation of surface air temperature anomalies in midlatitudes (from 20 to 70 N) in both Northern and Southern Hemispheres, where we define temperature anomaly as the deviation from their horizontally averaged temperature over the midlatitude and the data used here are NCEP/NCAR reanalysis. In the Northern Hemisphere, the zonal averaged surface air temperature difference across midlatitudes has a clear seasonal cycle, varying from 43 K in winter to less than 20 K in summer. However, the temperature difference over the midlatitude in the Southern Hemisphere shows little seasonality. The relatively constant ocean temperature plays an important role in maintaining the atmosphere temperature gradient. The zonal averaged surface air temperature difference across 30-60 S varies only slightly over the whole year, being around 25 K. The main seasonality occurs in high latitudes (poleward of 60 S). There, as the snow/ice cover increases, the temperature decreases dramatically in the Southern Hemisphere winter.

The lapse rate ($\Gamma = -dT/dz$) in midlatitudes also shows seasonal variation in the Northern Hemisphere, especially in the lower troposphere. As shown in Figure 7-2(a), the monthly

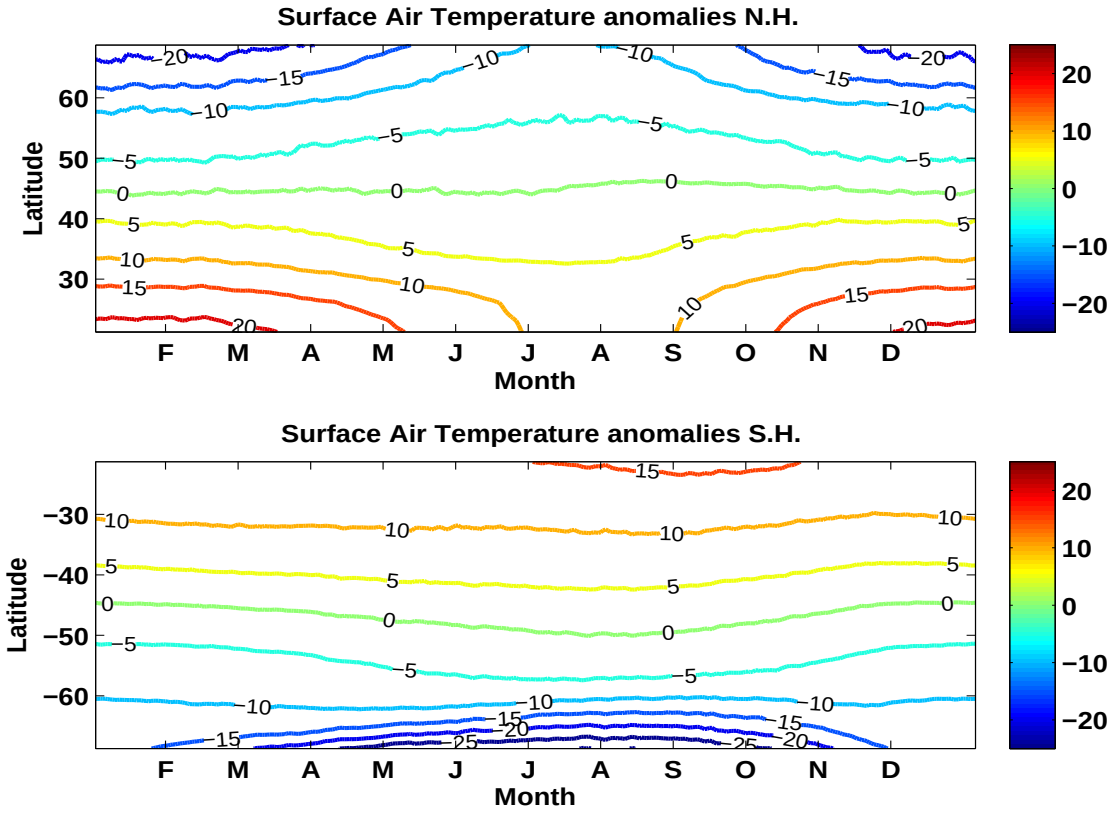

Figure 7-1: Seasonal variation of surface air temperature anomalies in midlatitudes (from 20 to 70 degree) in both Northern (upper) and Southern (lower) Hemispheres calculated from NCEP/NCAR reanalysis data.

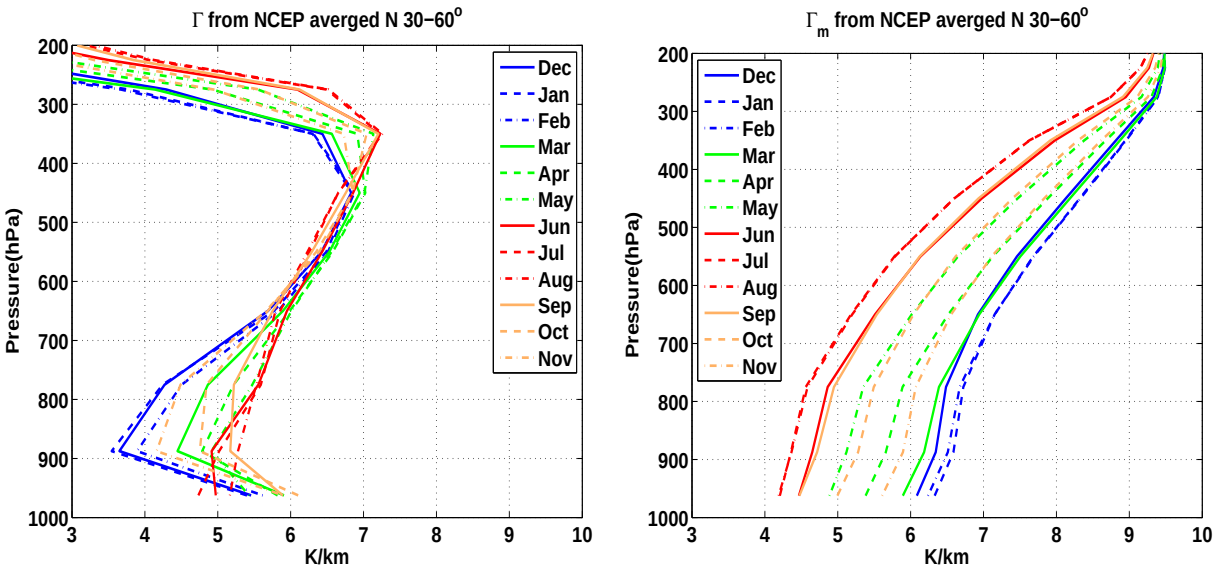

(a) (b)

Figure 7-2: Vertical distribution of the monthly mean lapse rate (a) and the lapse rate in the moist adiabatic state (b) averaged over the Northern Hemisphere midlatitudes (30-60 N) calculated from NCEP/NCAR reanalysis data.

mean lapse rate averaged over 30-60 N at 850 hpa varies from 3.6 K/km in January to 5.0 K/km in July. Consistent with Stone and Carlson (1979), its deviation from the moist adiabatic lapse rate Γ_m is characterized by a much clearer seasonal variation. Compared with the monthly mean Γ_m as shown in Figure 7-2(b), in summer, the lapse rate is close to Γ_m (4.5 K/km near 850 hpa), while in winter, the lower troposphere stratification is much more stabilized compared with Γ_m (6.7 K/km near 850 hpa).

In the Southern Hemisphere, as displayed in Figure 7-3(a), the lapse rate in midlatitudes shows weaker seasonal variation, with the lower troposphere stratification more stable than Γ_m as shown in Figure 7-3(b) all around the year and peaks around 850 hpa. In the months of January, February and March, the lower troposphere is slightly more stable than in other times of the year.

Not only the surface temperature and the zonal mean temperature field, but the eddy activity in both hemispheres also displays a different seasonal variation. As shown by Trenberth (1991), the transient eddy activity which has a characteristic life time scale of 2-8 days,

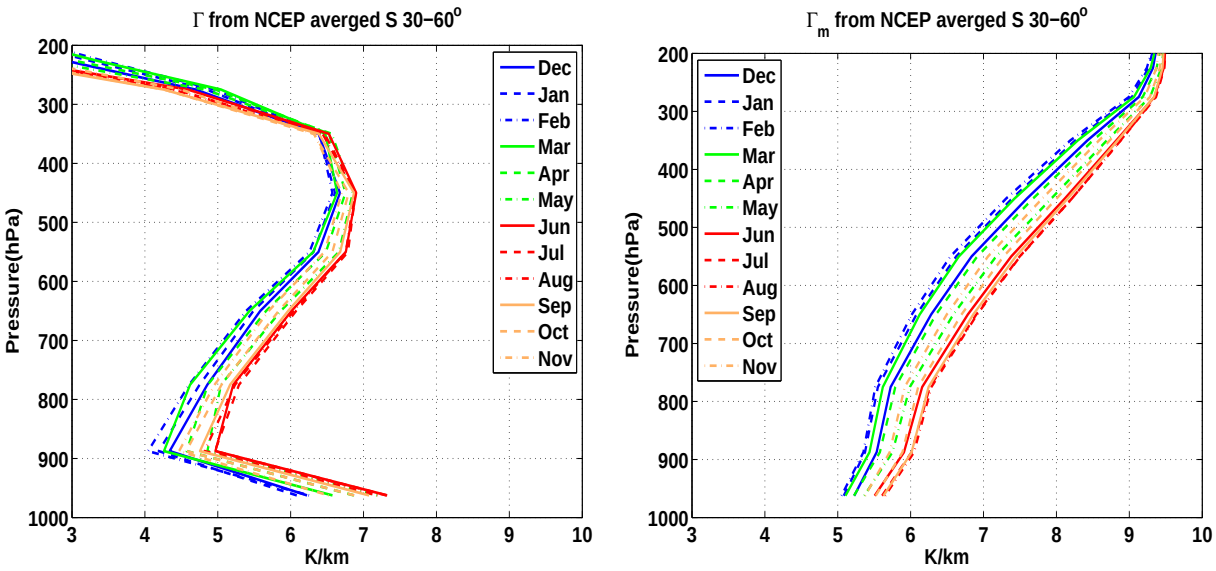

Figure 7-3: Same as Figure 7-2, but for Southern Hemisphere.

has comparable intensity all around the year in the Southern Hemisphere, which is different from the Northern Hemisphere, where eddies have the strongest heat and momentum flux in winter but with their amplitudes reduced to almost one tenth of its winter value in summer.

As shown from observations, due to the weak seasonal variation, an equilibrium study could be a relatively reasonable way to study the baroclinic eddies in the Southern Hemisphere. However, the strong seasonal behavior of the surface forcing and atmospheric response in the Northern Hemisphere makes the test of the 'quick adjustment' assumption and the seasonality of the eddy activity interesting.

7.2 Model Setup

In this chapter, we will study the eddy response to specified seasonally varying boundary condition and radiative-convective heating. More specifically, we will include these observed Northern Hemisphere-like seasonal cycles in both the underlying surface temperature T_g and the target state temperature T_e (target state potential temperature θ_e) in the Newtonian Cooling term. Instead of keeping them fixed as in the equilibrium study in Chs.3 and 4,

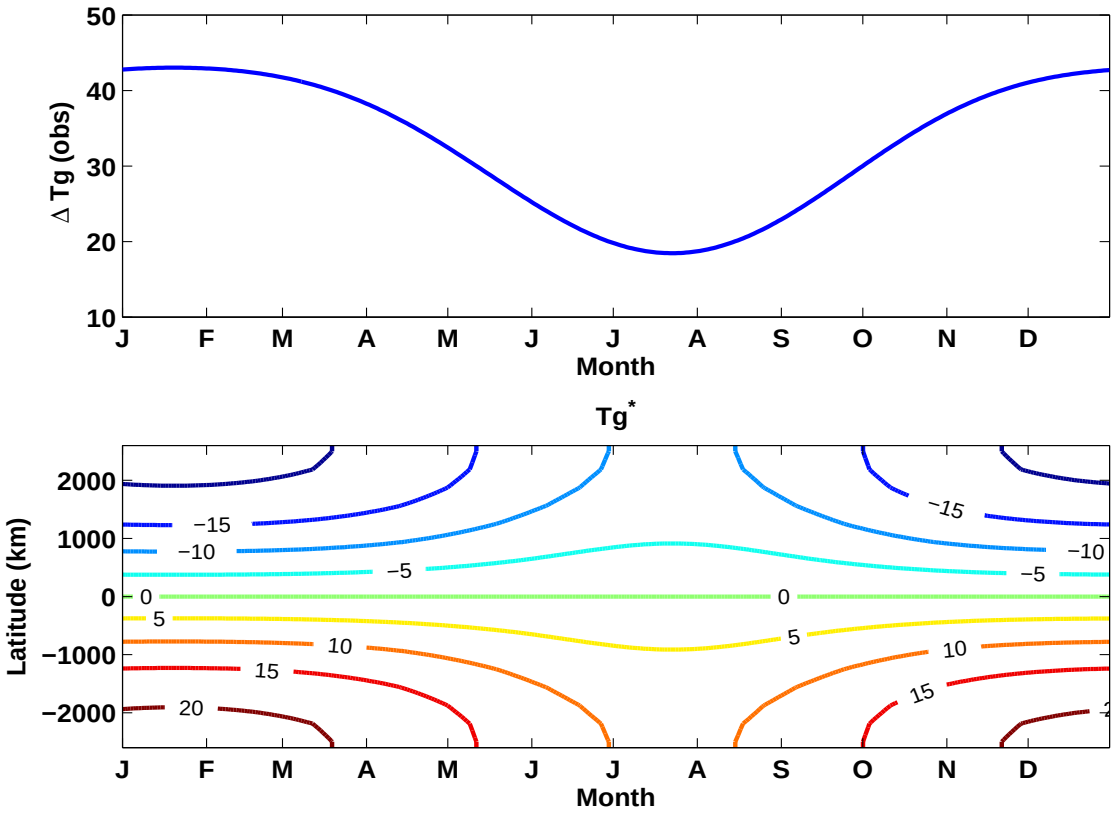

Figure 7-4: Seasonal variation of the observed 20-70 N surface air potential temperature difference (upper) and seasonal variation of the surface temperature anomalies used in the model (lower), where the plotted contour internal is 5 K.

they are specified to vary with time t_{date}. In our experiments, we let the external forcing vary with certain period T_{year}, and time variable $t_{date} = \frac{t}{T_{year}} \times 365$ day, indicates the time (phase) in a forcing period. For convenience, we still use words like summer, winter and each month to describe the state (phase) of the external forcing in a forcing period. In the standard run (SD run) experiment, which is the experiment designed to simulate the current Northern Hemisphere climate, the forcing period T_{year} is one year, 365 model days.

In our model, the surface temperature anomaly $T_g^\dagger$ over the central half of the channel, which is $1/4L \leq y \leq 3/4L$,

$$T_g^\dagger(y, t_{date}) = \Delta T_g(t_{date}) \sin\left[\frac{\pi(y - L/2)}{L/2}\right], \tag{7.1}$$

and as in the equilibrium run, there is no meridional temperature gradient in regions $0 \leq y \leq 1/4L$ and $3/4L \leq y \leq L$. As shown in Figure 7-4, in our SD run, the surface temperature difference over the central half of the channel ΔT_g is specified to vary with t_{date} as the observed 20-70 N surface air potential temperature difference. The target state potential temperature θ_e, where

$$\theta_e(y, p, t_{date}) = \theta_e^{\dagger}(y, p, t_{date}) + \overline{\theta_e}^{xy}(p, t_{date}), \tag{7.2}$$

is also specified to vary seasonally to match the underlying surface temperature. In the model, we assume that $\theta_e^{\dagger}$ has the same meridional distribution as the surface temperature anomaly $T_g^{\dagger}$ in the troposphere. Above 250 hpa, an isothermal stratosphere is included in the model. The target state temperature lapse rate also includes the seasonal cycle. As displayed in Figure 7-5, in the troposphere, we use the moist adiabatic state lapse rate Γ_m representing the RCE state lapse rate $-d\overline{T_e}^{xy}/dz$, whose seasonal variation is also taken from observations. In the stratospheres, we assume that$-d\overline{T_e}^{xy}/dz = 0$.

Although there are also interesting topics on the seasonality of the Southern Hemisphere, especially in winter, when there is a strong cross-equatorial Hadley Cell which brings a strong subtropical jet into the extratropics and another strong baroclinic zone appears in high latitudes, they are not investigated in this study.

7.3 Preliminary run: 2-D simulation

Before starting the standard run simulation, we first look at the seasonal variation of the flow in which baroclinic eddies are not present, which we call the 2D simulation. Under the QG assumption, the zonal symmetric circulation becomes simple though not very realistic. From the QG momentum equations, in 2D circulations, where $u_g = [u_g]$, $v_g = [v_g] = 0$, we have:

$$\frac{\partial [u_g]}{\partial t} = f[v_a] + [F_x]. \tag{7.3}$$

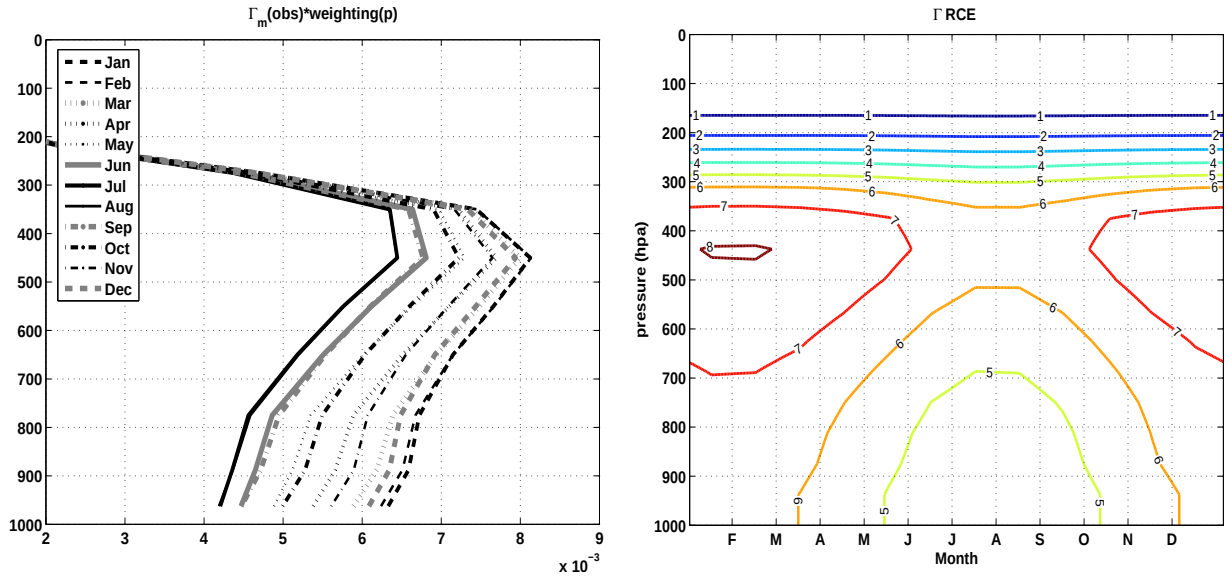

Figure 7-5: Monthly mean (left) and the seasonal variation (right) of the RCE state lapse rate used in the model.

The thermodynamic equation is also simplified to :

$$\frac{\partial[\theta^\dagger]}{\partial t} = -[\omega]\frac{\partial\overline{\theta}^{xy}}{\partial p} + \frac{\theta}{c_p T}[Q^\dagger]. \tag{7.4}$$

In equilibrium, in a stably stratified atmosphere, where $\frac{\partial\overline{\theta}^{xy}}{\partial p} < 0$,

$$-[\omega]\frac{\partial\overline{\theta}^{xy}}{\partial p} + \frac{\theta}{c_p T}[Q^\dagger] = 0, \tag{7.5}$$

then rising motion emerges where there is diabatic heating $[Q^\dagger] > 0$ and subsidence happens where there is diabatic cooling $[Q^\dagger] > 0$. In equilibrium, the meridional motion is primarily caused by the frictional dissipation:

$$f[v_a] + [F_x] = 0. \tag{7.6}$$

Above the boundary layer, where friction is much weaker, the circulation there is also weaker. In addition, the energy input by diabatic heating must be balanced by the energy dissipation

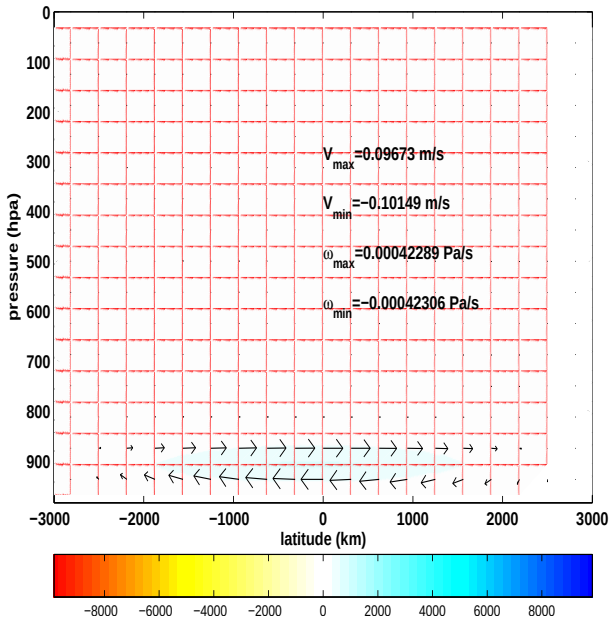

Figure 7-6: 2D equilibrium run meridional overturning circulation ($[v_a]$, $[\omega]$) and its stream function Ψ (shaded).

due to surface and boundary layer friction. The 2D equilibrium state circulation $([v_a], [\omega])$ under winter time differential heating (43K temperature difference across the channel) in our model is shown in Figure 7-6 in the form of stream function $\Phi(y, p)$, which is defined as $[v_a] = \frac{\partial \Psi}{\partial p}$ and $[\omega] = -\frac{\partial \Psi}{\partial y}$. The maximum $[v_a]$ and $[\omega]$ are also listed. As expected the 2D circulation is very weak and primarily in the boundary layer.

Under seasonal forcing, different from the equilibrium run, we may expect the differential heating $[Q^\dagger]$ to have seasonal behavior, which acts to increase the system baroclinicity in winter and to reduce the system baroclinicity in summer. This can be seen from the energy balance equation of the mean available potential energy (MPE) in the 2D flow,

$$\frac{d}{dt} MPE = G_{mpe}(Q) - C(MPE, MKE) + G_{mpe}(\sigma), \tag{7.7}$$

where MPE is defined as

$$MPE = \frac{c_p}{2} \int \sigma([T] - \overline{T}^{xy})^2 dm, \tag{7.8}$$

$$\sigma = -\frac{R\theta}{C_p T}(\frac{\partial \overline{\theta}^{xy}}{\partial p})^{-1}, \tag{7.9}$$

is the stratification parameter. In our model,

$$G_{mpe}(Q) = \int \sigma([T] - \overline{T}^{xy})([Q] - \overline{Q}^{xy})dm, \tag{7.10}$$

is the generation of MPE by differential heating Q, which has two components: radiative-convective heating Q_{rad} and boundary layer thermal forcing Q_{dif}.

$$C(MPE, MKE) = -\int \frac{R}{p}[\omega][T]dm, \tag{7.11}$$

indicates the conversion rate from MPE to MKE through the zonally symmetric meridional overturning circulation. One difference between our model and the traditional QG model is that our stratification is allowed to vary with time, thus in the balance equation of MPE, there is another generation term of MPE by changing the flow stratification,

$$G_{mpe}(\sigma) = \int (\frac{d}{dt}\sigma)\frac{c_p}{2}([T] - \overline{T}^{xy})^2 dm \tag{7.12}$$

where the tendency term $\frac{d}{dt}\sigma$ is determined by our stratification tendency equation.

Time evolution of the energy flux terms in Equation 7.7 is plotted in Figure 7-7, from which we find differential heating is the most dominant factor that determines the seasonal behavior of MPE. The two components of $G_{mpe}(Q)$ have comparable contributions and similar seasonal variations but with $G_{mpe}(Q_{dif})$ varying with an almost one month lead to $G_{mpe}(Q_{rad})$, which is primarily due to the relatively long time scale of the Newtonian cooling. $G_{mpe}(\sigma)$ also has a similar seasonal variation to $G_{mpe}(Q)$ but with a smaller contribution. When approaching the winter, less stable stratification of the target state leads to an increase in MPE, while, when approaching the summer, the very stable RCE state stratification acts to reduce MPE. The overturning circulation, although a small contribution, always acts against the differential heating. In winter, it extracts energy into MKE. In

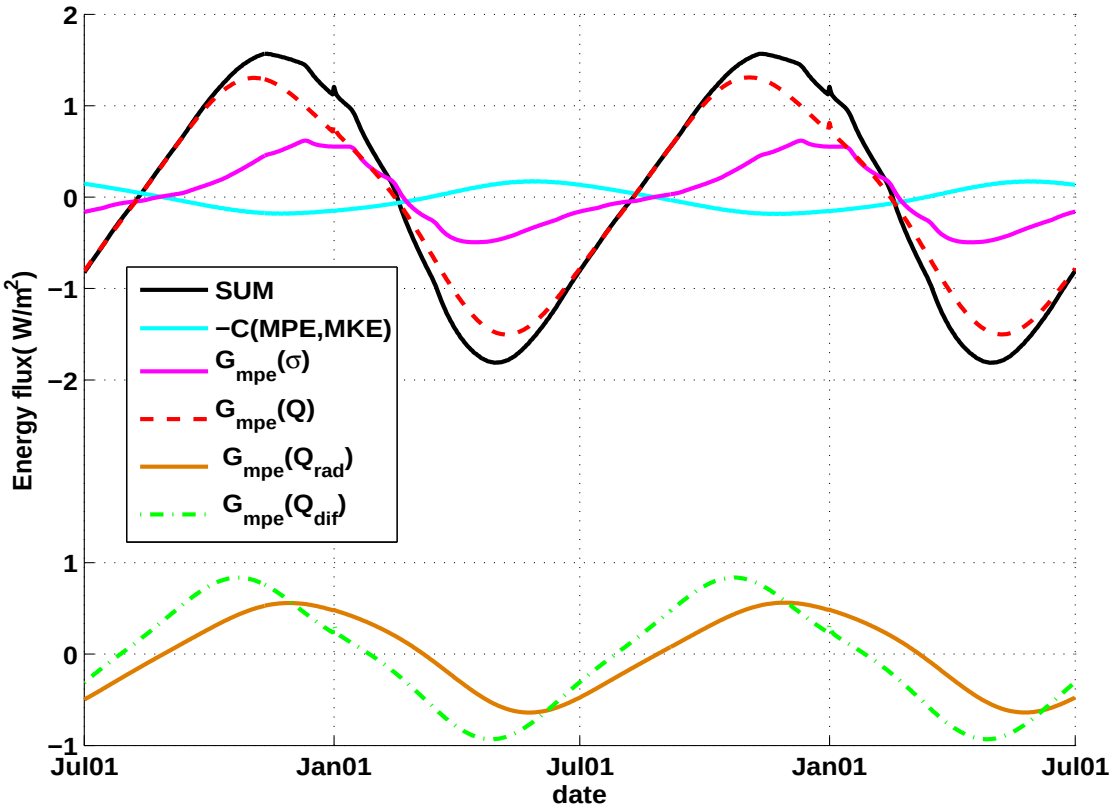

Figure 7-7: Time evolution of each term in the MPE balance equation in the 2D seasonal run. Time evolution of the two components in the MPE generation term $G_{mpe}(Q)$: Generation through radiative-convective heating $G_{mpe}(Q_{rad})$ and through boundary layer heating $G_{mpe}(Q_{dif})$ are also plotted below. Energy fluxes are plotted in W/m^2.

summer, MKE is transferred into MPE.

The time evolution of the temperature gradient at the center of the channel, as plotted in Figure 7-8(b), is consistent with the MPE seasonal cycle. Compared with the RCE state temperature gradient as plotted in Figure 7-8(a), we find that in the boundary layer, the flow can 'feel' the seasonal variation of the surface temperature and the target state temperature 'immediately', which is consistent with our analysis in Ch.4 that the boundary layer forcing on the lower troposphere flow is relatively fast so that the lower flow can respond to the boundary layer forcing in a time scale around one day. Above the boundary layer, instead of the boundary layer forcing, radiative-convective heating is the dominant diabatic heating acting on the mean flow with a time scale of 40 days specified. Thus, the upper layer flow

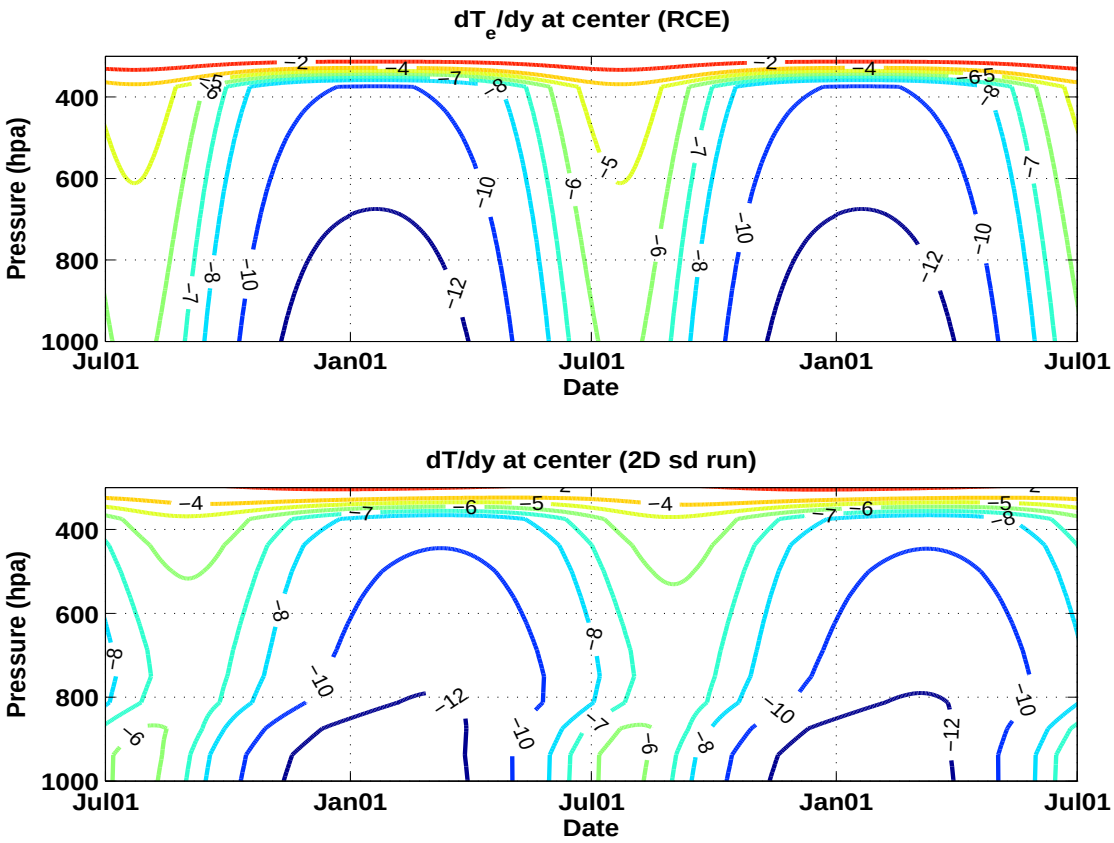

Figure 7-8: Time evolution of the meridional temperature gradient at the center of the channel in the RCE state (upper) and in the 2D simulation (lower) in two seasonal cycles.

always 'feels' the seasonal forcing slower than the lower flow.

Thus, consistent with the energy cycle, the 2D circulation also has its seasonal variability. When the differential heating acts to enhance the flow baroclinicity, similar to the equilibrium run, rising motion occurs in the warmer area and sinking motion occurs in the cooler area. A Hadley cell circulation emerges as displayed in Figure 7-9(a). As indicated from Equation 7-10, the meridional flow in the boundary layer should be still primarily balanced with the frictional dissipation, and in the upper layer, the meridional flow will act to accelerate the zonal flow $[u_g]$. Thus, as plotted in Figure 7-10, the upper layer zonal wind $[u_g]$ becomes stronger in winter and a weak westward surface wind is also observed. In summer, as the differential heating acts to reduce the flow baroclinicity, as shown in Figure 7-9(b), a reverse 2D circulation occurs. The zonal wind, also becomes weaker due to the meridional flow

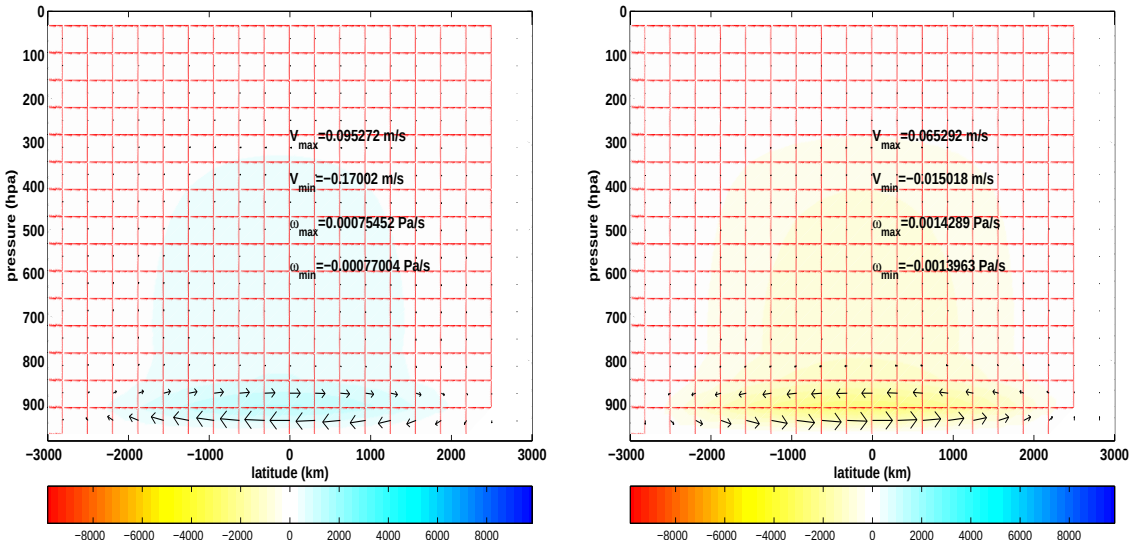

Figure 7-9: Meridional overturning circulation ($[v_a]$, $[\omega]$) and its stream function Ψ (shaded) in (a) December and (b) June in the 2D seasonal run.

deceleration in the upper layer.

Even though the 2D circulation has a weak component in the upper level, the circulation is still primarily within the boundary layer and weak compared with the other energy flux terms affecting MPE. The temperature as well as PV structures in the 2D run are mainly determined by the flow response to the external forcing. Thus, the 2D simulation can be considered as a useful tool to better understand the seasonality of the forcing exerted on the system.

7.4 3-D Standard Run

A standard run experiment (SD run) is designed to simulate the current Northern Hemisphere-like climate. In the SD run, the model is started from January 01. We set the RCE state with Jan01 forcing as the initial state and add small amplitude perturbations into the system at the initial moment. After running the model for 400 days with fixed external forcing, the flow reaches an equilibrium state. Then we turn on the seasonal variation of the external forcing. Time evolutions of the domain averaged MPE, EPE, EKE and MKE in the first

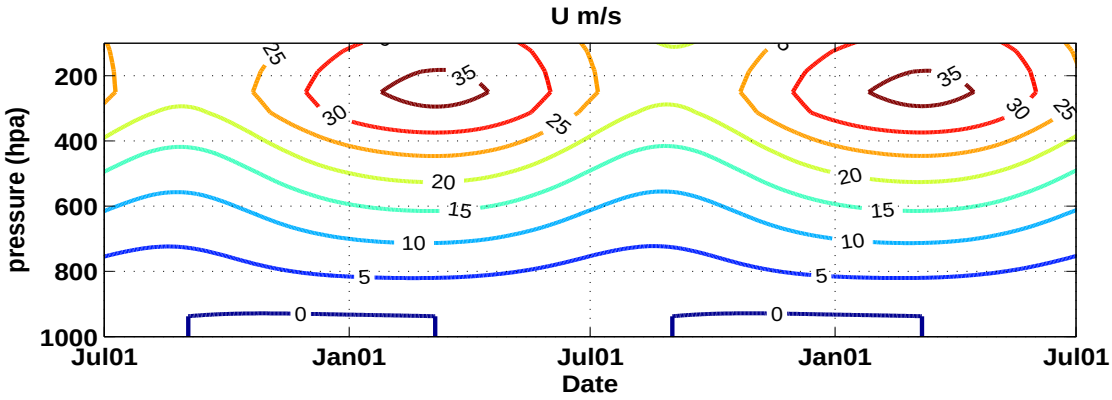

Figure 7-10: Time evolution of the zonal mean zonal wind at the center in the 2D simulation in two seasonal cycles.

three years after turning on the seasonal forcing are plotted in Figure 7-11, from which we find that after running for more than one seasonal cycle, the mean flow and the eddy activity in our model exhibit a repeated annual pattern. We integrate our model for 15 years, and as plotted in Figure 7-12, the last ten years' data are used in our following analysis.

7.4.1 Energy evolution

Annual variations of the domain averaged MPE, EPE, EKE and MKE are displayed in Figure 7-12. Thin curves in these plots show the annual behavior of energies in each of the ten years and the ten year mean annual variation of the energies are plotted with thick black curves. In Figure 7-12(a), the seasonal variation of the RCE state MPE is also plotted, which can be considered as an index for the differential heating exerted on the flow and also the source of the seasonality specified in the model. Even though the eddy activities have their own variations year by year (so does the energy in the zonal mean flow), we find their annual behaviors are very similar and have robust characteristics.

- Our model results show that there is almost no significant eddy activity from early summer to late fall, when the external forcing as well as MPE and MKE are smallest in the system.

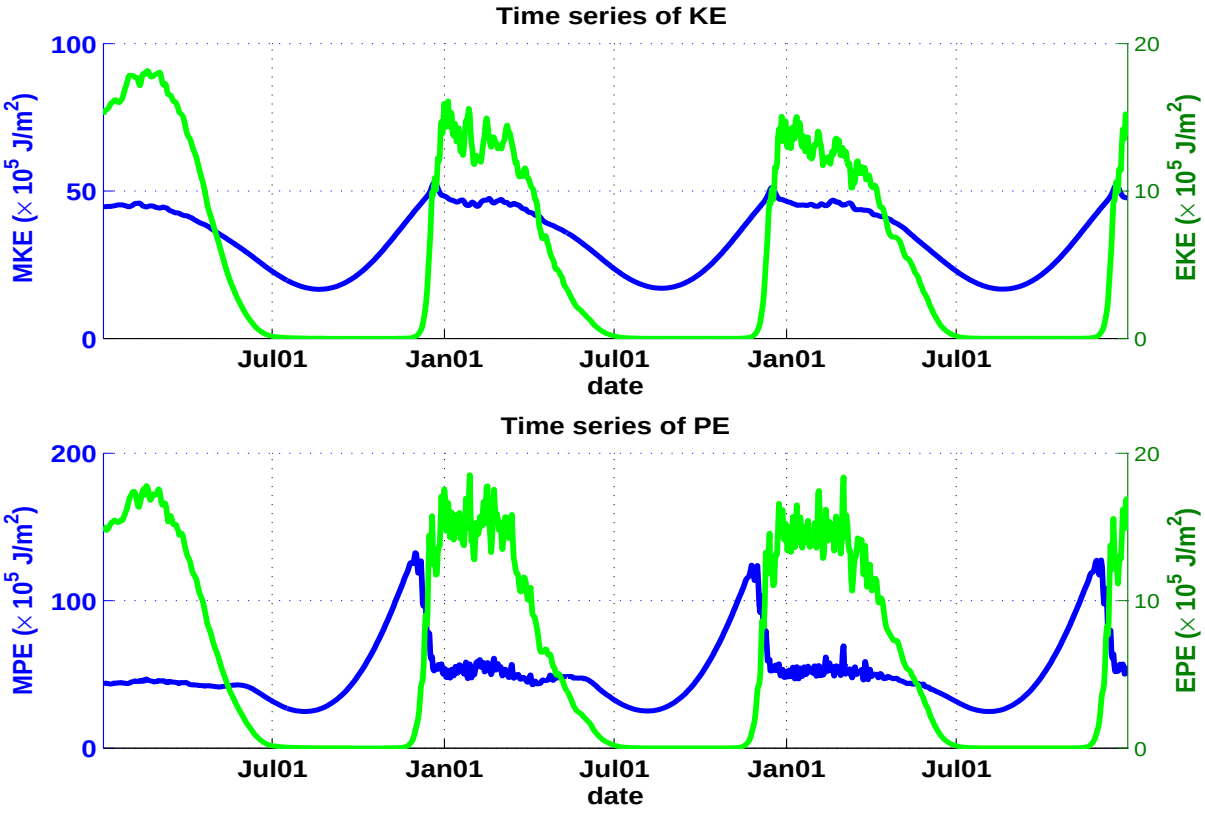

Figure 7-11: Time series of zonal mean and eddy kinetic energy (upper), and zonal mean and eddy available potential energy (lower) for the first three years after turning on the seasonal forcing in the standard run. Unit:$10^5 J/m^2$.

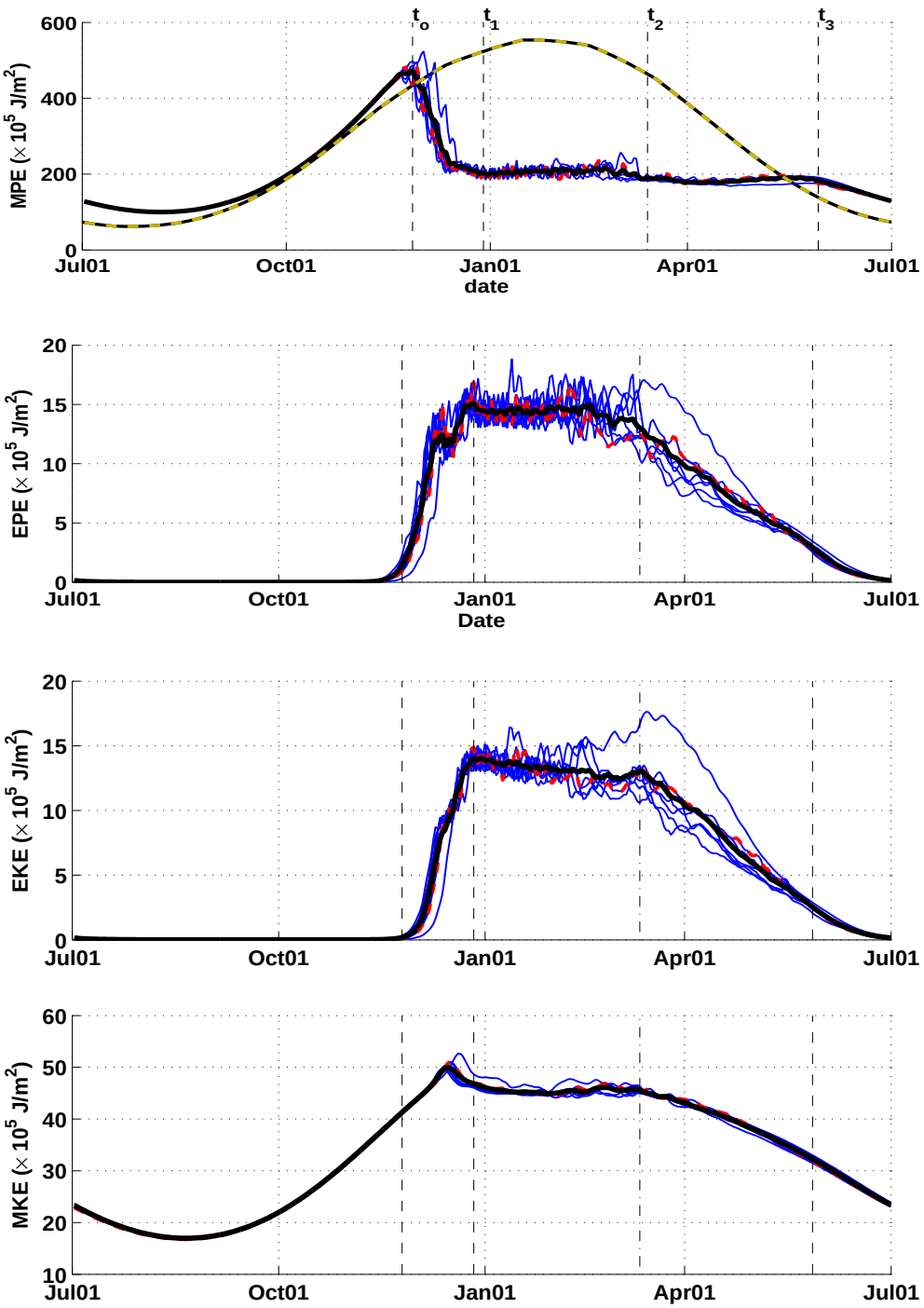

Figure 7-12: Seasonal variation of domain averaged (a) mean available potential energy, (b) eddy available potential energy, (c) eddy kinetic energy and (d) mean kinetic energy. The thin curves show the energy evolution in each of the last ten years. The dashed curve shows energy evolution in one of the ten years. The thick black curve shows the mean seasonal variations of the last ten years. In panel (a), the seasonal evolution of the RCE state MPE is plotted in grey dashed curve. Energies are plotted in unit $10^5 J/m^2$. Time t_o, t_1, t_2 and t_3 are marked with thin dashed lines.

- As the differential heating as well as MPE increase, eddies begin to spin up. Eddy energies increase almost exponentially in the late fall, while MPE starts decrease rapidly at time t_o as marked in Figure 7-12(a), even though the external forcing is still increasing in this period. Around time t_1, MPE stops decreasing, which is also the time when eddy energies reach their maximum values.

- After t_1, in spite of the variation of external forcing, MPE maintains a relatively constant value until time t_3.

- The eddy activity and MKE indicate that we can separate the time interval from t_1 to t_3 into two parts. From time t_1 to t_2, eddy energies and MKE only have mild variations with time, and the system behaves like a "quasi-equilibrium" state. Starting from time t_2, eddy energies and MKE decay quickly. At t_3, the eddy activity is reduced to small values.

- After t_3, eddies no longer play any significant role in the system and the circulation is similar to that in the 2-D simulation.

An FFT analysis is also applied to the ten-year MPE, EPE, EKE and MKE time series as shown in Figure 7-13. Compared with the frequency spectra for MPE, MKE in the 2-D run in Figure 7-14, the strongest peak still appears at the period of one year. There are also some minor peaks at period one half, one third, and one forth year, which are primarily 'harmonics'. However, different from the spectra in the 2D run, more spectral structure is observed in the higher frequency region. Most obviously, we find another peak at period around 4 days in EPE and MPE, which is the characteristic life time scale of baroclinic eddies. This is also consistent with observations that transient baroclinic eddies in midlatitudes have a period less than a week. Unlike the other energies, MKE does not show the peak in the high frequency domain. Some intraseasonal variations are also observed in all the energy spectra in the 3D run.

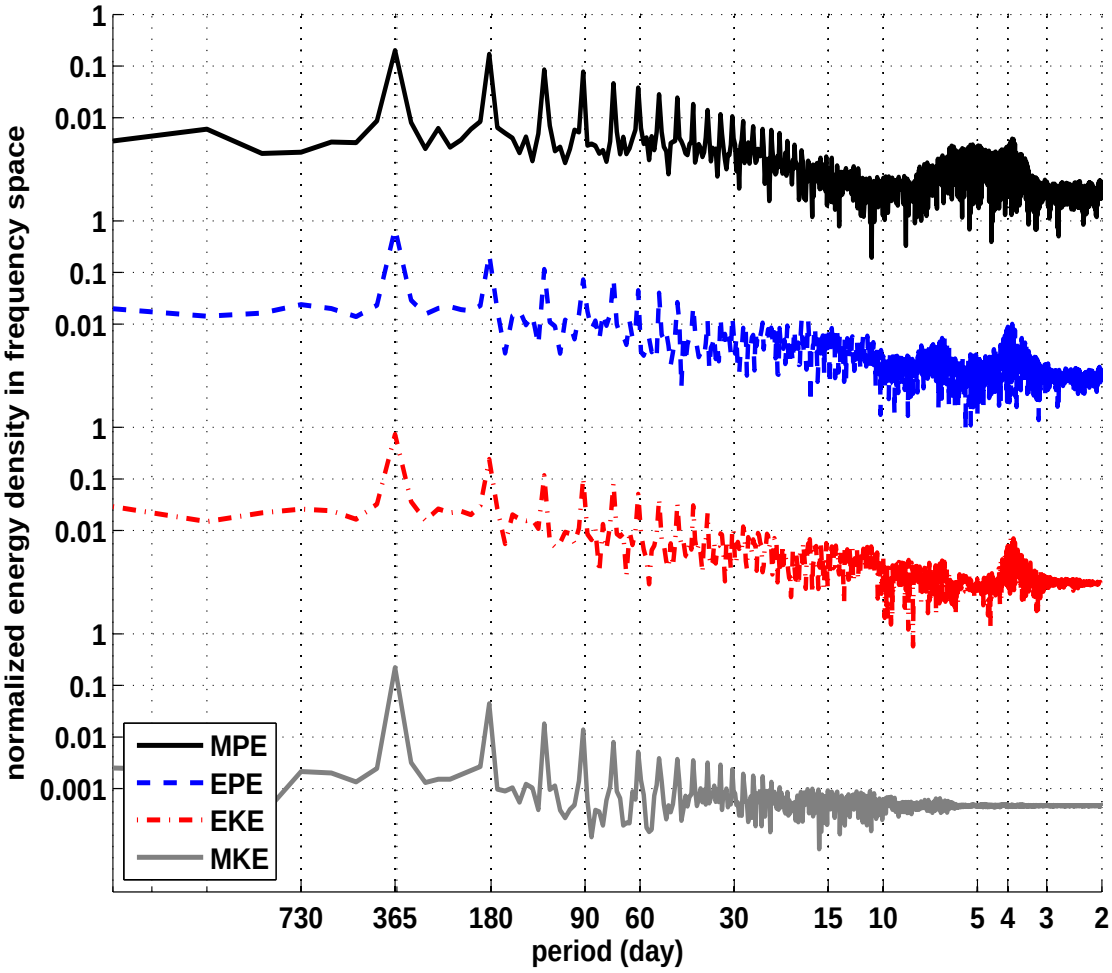

Figure 7-13: Normalized spectra of MPE, EPE, EKE and MKE density in the frequency (period) domain for SD seasonal run.

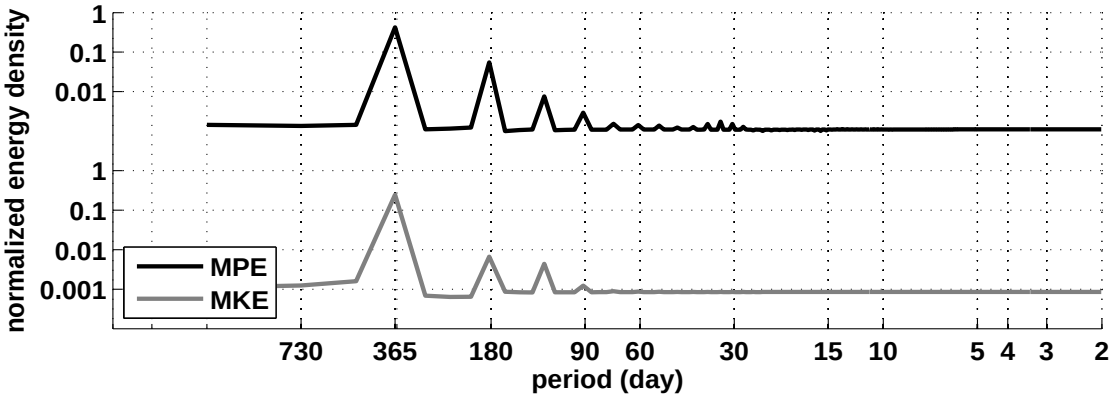

Figure 7-14: Normalized spectra of MPE and MKE density in the frequency (period) domain for the 2D seasonal run.

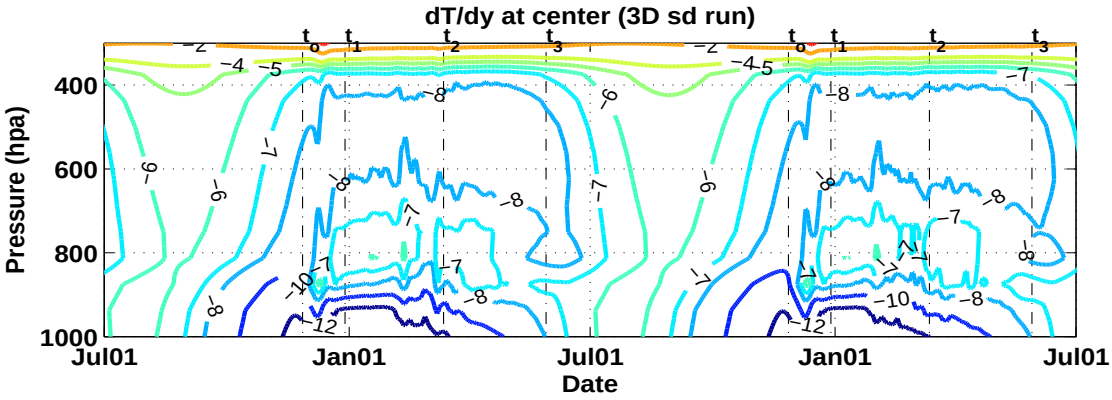

Figure 7-15: Time evolution of the meridional temperature gradient at the center of the channel in the 3D simulation in two seasonal cycles.

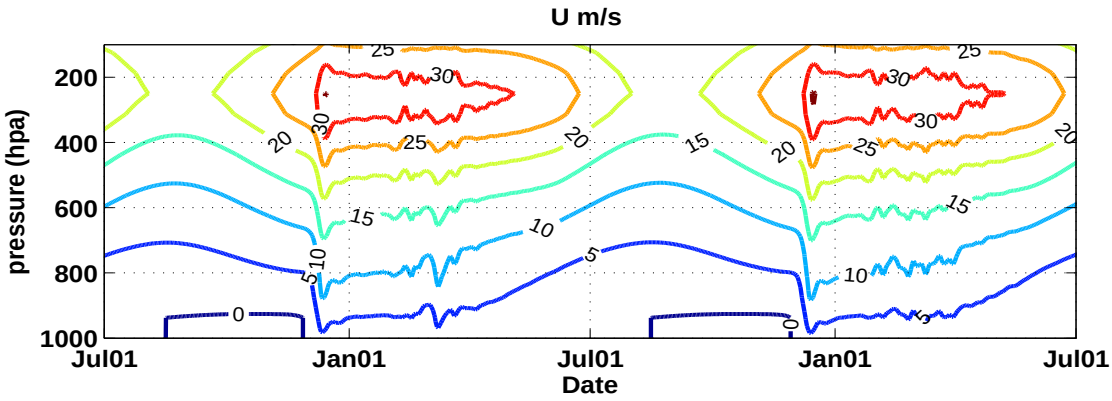

Figure 7-16: Time evolution of the zonal mean zonal wind at the center in the 3D simulation in two seasonal cycles.

7.4.2 Mean flow

Consistent with the zonal and eddy kinetic and available potential energies, the zonal mean flow also shows a clear seasonal behavior. As shown in Figure 7-15, the temperature gradient at the center of the channel, compared with the 2D symmetric run, is greatly reduced as the eddies spin up, especially near 800 hpa, which, as shown in the previous chapter, is also the location of the steering level. During the quasi-equilibrium state, the temperature gradient above the boundary layer is also maintained at a relatively constant state. After early summer, the temperature gradient again varies with time and behaves like that in the 2D run.

The zonal mean zonal wind at the center of the channel in Figure 7-16 shows a similar seasonal variation. In the eddy inactive period, zonal wind exhibits a 2D-like time variation as in Figure 7-10. As eddies begin to grow exponentially, the zonal wind through the whole troposphere experiences a strong increase and, consistent with Figure 7-12(d), does not exhibit any obvious variation until the eddy decay period, when the zonal flow through the whole troposphere experiences a barotropic decrease. In the summer, which is the inactive period, the zonal wind goes into another annual cycle.

The meridional overturning circulation in February (with active eddies and MPE in quasi-equilibrium), June (eddies inactive and MPE decreasing) and November (before eddy spin-up, MPE increasing) is also plotted in Figure 7-17. In the eddy active period, as shown in Figure 7-17(a), a strong eddy induced Ferrel Cell can be observed at the center of the channel, on each side of which, a much weaker Hadley Cell emerges. In June, as the eddy becomes inactive, the three cell circulation is almost gone. A Ferrel cell circulation similar to the 2D run in Figure 7-9(b) is still observed. In November, the circulation has the same pattern as in the 2D run in winter (Figure 7-9(a)), a shallow Hadley cell circulation within the boundary layer can be found in Figure 7-17(c).

The time evolution of the PV gradient at the center of the channel is also plotted in Figure 7-18. In spite of the strong seasonality of eddy activity, the PV gradient keeps a similar vertical distribution through the whole year. In the eddy active period, the smallest PV gradient lies around the 800 hpa, with the small PV gradient region moving lower compared with the inactive eddy period. However, even in the inactive eddy period, we still find a weak PV gradient near the top of the boundary layer. As a result, the PV structure is relatively robust around the whole year.

How can we interpret the robustness of the PV gradient? As shown in many studies, a robust PV structure is also observed in the real atmosphere (Kirk-Davidoff and Lindzen (2000), Zurita-Gotor and Lindzen (2007)) and is attributed to the baroclinic eddies. Our studies show that in the winter season when the eddy activity is strongest, a baroclinic adjustment scenario does occur, in which baroclinic eddies are able to maintain a robust

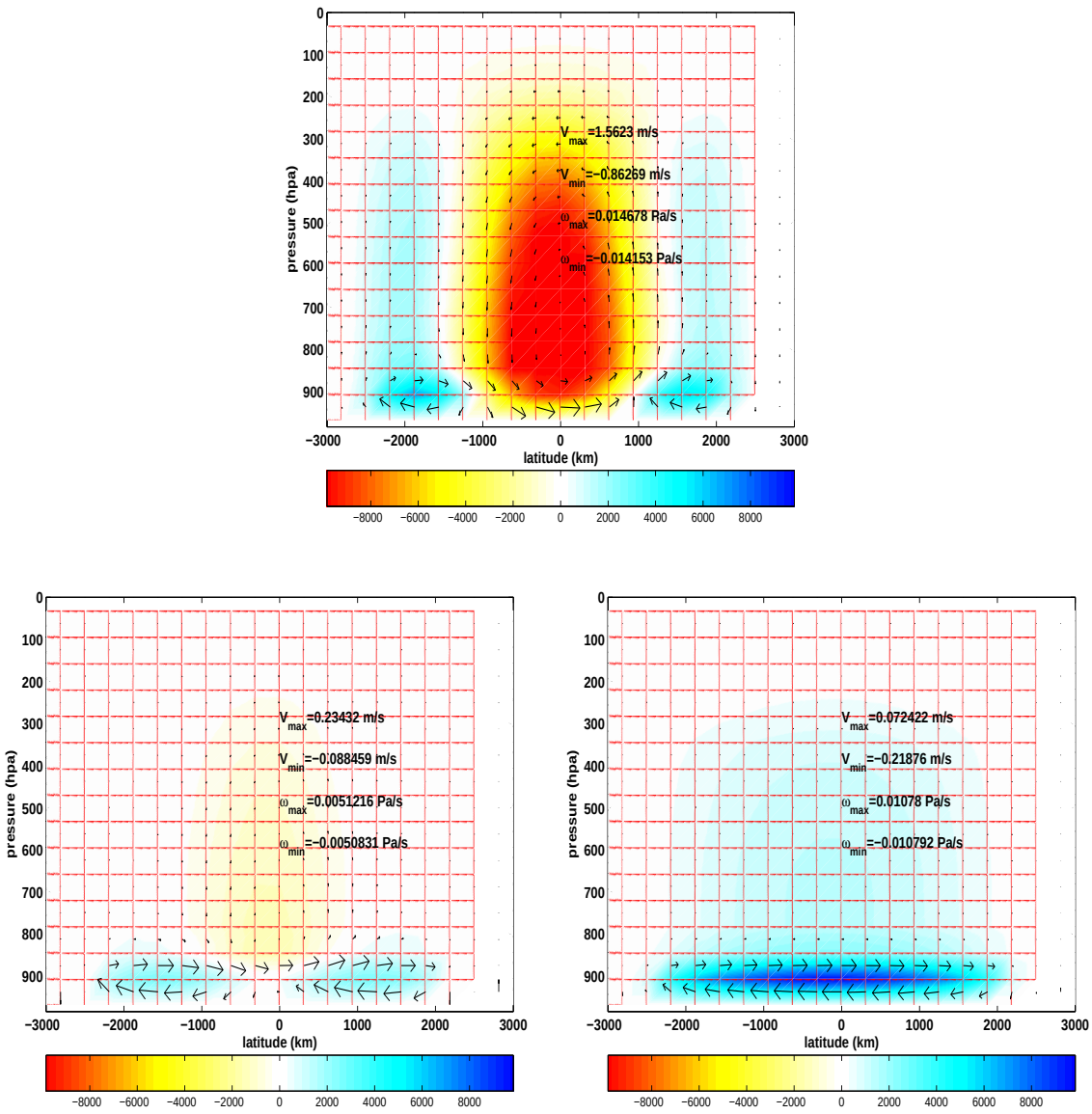

Figure 7-17: Meridional overturning circulation ($[v_a]$, $[\omega]$) and its stream function Ψ (shaded) in (a) February, (b) June and (c) November in the SD run.

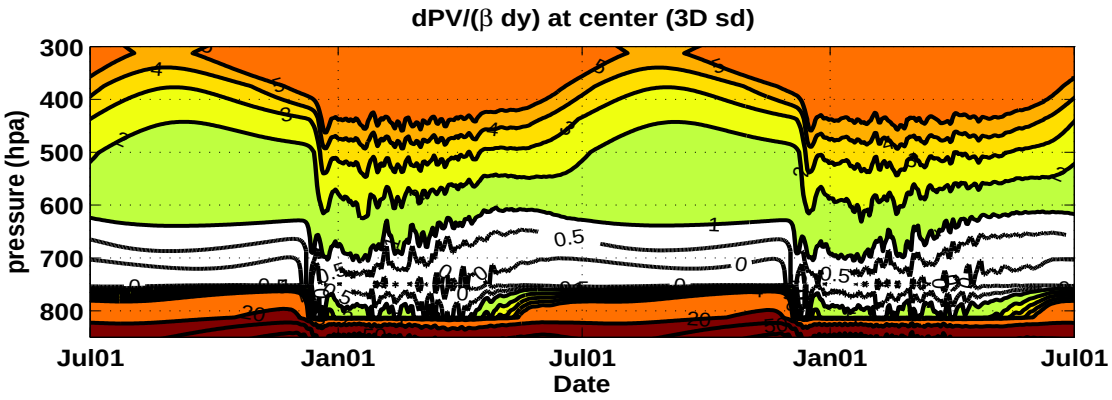

Figure 7-18: Time evolution of the meridional PV gradient at the center of the channel in the standard 3D run in two seasonal cycles. PV gradient is normalized with β. The white area indicates regions where PV gradient is weaker than β.

PV as well as thermal structure in spite of the varying external forcing acting on the flow. However, the weak PV gradient in the eddy inactive period observed in our model also indicates that baroclinic eddies are not the only candidate for the observed PV structure. In the next section, we will discuss the possible mechanisms that can maintain the PV structure observed in the real atmosphere.

7.5 PV gradient and the role of stratification

From the definition of QGPV as shown in Chapter 2, the QGPV gradient is

$$\frac{\partial q}{\partial y} = \beta - u_{yy} + \frac{\partial}{\partial p}\frac{\theta_y}{\overline{\theta}_p^{xy}}. \tag{7.13}$$

In our model and in most of the situations in midlatitudes in the real atmosphere, the second term on the right hand of Equation 7.13, which is the contribution from the meridional shear of the zonal wind, is always small. The PV gradient is mainly determined by β, which is constant in our β plane model, and the baroclinic term, which is the vertical variation of the isentropic slope. Thus, in the QG model, the PV gradient is virtually determined by the distribution of the isentropic slope. Eq.7.13 tells that if the isentropic slope becomes steeper

with height, the baroclinic term will act against β to reduce the PV gradient. Otherwise, the baroclinic term has the same sign as β, and acts to enhance the PV gradient (e.g. the strong PV gradient near the tropopause).

What can affect the isentrope slope in midlatitudes? Baroclinic eddies are often considered to play an important role in constraining the midlatitude isentropic distribution. As shown in many previous studies using two-layer idealized QG models, baroclinic eddies can reduce the lower troposphere PV gradient by strong mixing of the potential temperature. In our model, as shown in Figure 7-15, the lower level temperature gradient is also strongly reduced through eddy mixing, especially near the critical level where the eddy mixing is supposed to be strongest. However, as discussed in the previous chapter, when taking into account the boundary layer thermal forcing, the temperature near the surface cannot be efficiently eliminated, so that strong baroclinicity is maintained near the surface, which is also what we observed in the real atmosphere. Thus, if we do not consider the vertical variation of stratification, the vertical variation of the temperature gradient will act to reduce the PV gradient just above the steering level.

Different from the traditional QG model, the stratification is allowed to evolve with the flow in our model. Thus, baroclinic eddies, besides reducing the temperature gradient, can modify the PV gradient by stabilizing the lower troposphere's stratification. Gutowski (1985) in his study suggested that even without eliminating the temperature gradient, by increasing the lower flow stratification itself, baroclinic eddies can homogenize the lower level PV gradient. The role of eddy in stabilizing the lower troposphere stratification is also indicated in studies by Stone and Carlson (1979), Schneider (2004), Schneider (2006) and in the observations as shown in this chapter. The vertical distribution of the winter time lapse rate in the SD run is plotted in Figure 7-19. If we assume that $\frac{\partial p}{\partial z} = -\frac{p}{H_{scale}}$, where H_{scale} is the scale height of the atmosphere (around $8.5km$ in our model), then the isentropic slope is given by

$$\frac{\theta_y}{\overline{\theta}_p^{xy}} = \frac{-T_y}{(\frac{g}{c_p} - \Gamma)} * \frac{p}{H_{scale}}. \tag{7.14}$$

Compared with the target state lapse rate as shown in Figure 7-5(a), in our model we also

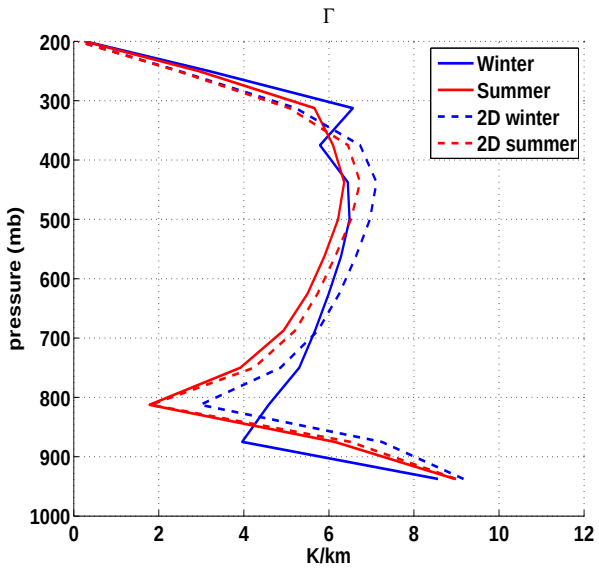

Figure 7-19: Lapse rate averaged in the winter(JFM) and summer (JAS) seasons in the 2D and 3D standard run.

find a strong stabilization of the lower level stratification by baroclinic eddies. Combined with the reduction of the temperature gradient around the steering level, the PV gradient around the steering level is efficiently homogenized.

Besides baroclinic eddies, there are physical processes in the real atmosphere which can also determine the isentrope distribution. As shown in our SD run, in the summer time when eddies are inactive and do not play any significant role, the flow under the boundary layer forcing and the radiative-convective heating also keeps a PV structure similar to winter's. Their relative role in determining the PV gradient is also studied by carrying out 2D symmetric simulations and stratification specified simulations.

Boundary layer thermal forcing

The role of the boundary layer thermal forcing in affecting the mean flow thermal structure and the eddy activity in baroclinic eddy equilibration has been studied in Ch.4. Here, we will study that without baroclinic eddies, what the effect of the boundary layer is on maintaining the PV structure. We compare two groups of 2D symmetric simulations. The first is the 2D run under standard seasonal forcing, in which the PV distribution is determined by the

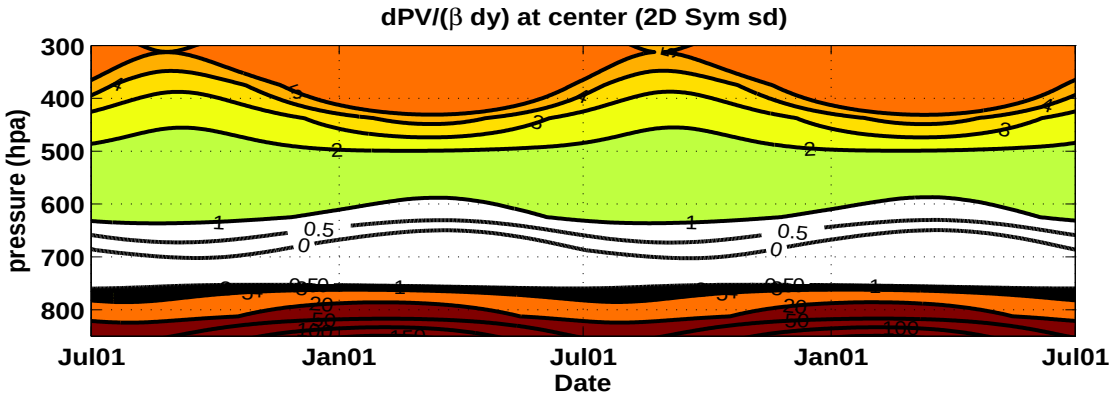

Figure 7-20: Time evolution of the meridional PV gradient at the center of the channel in two seasonal cycles in the 2D simulation under standard seasonal forcing.

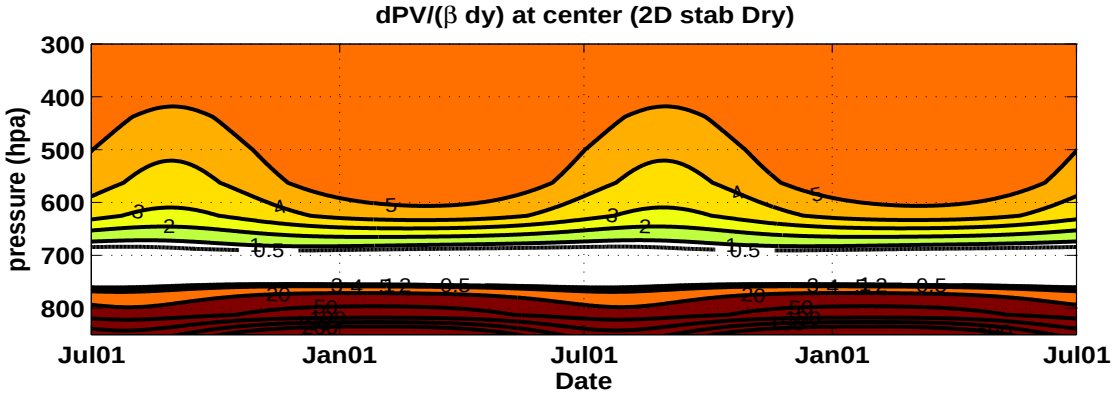

Figure 7-21: Same as Fig.7-20 but for the 2D simulation with a 8 K/km lapse rate as the target state stratification in the troposphere.

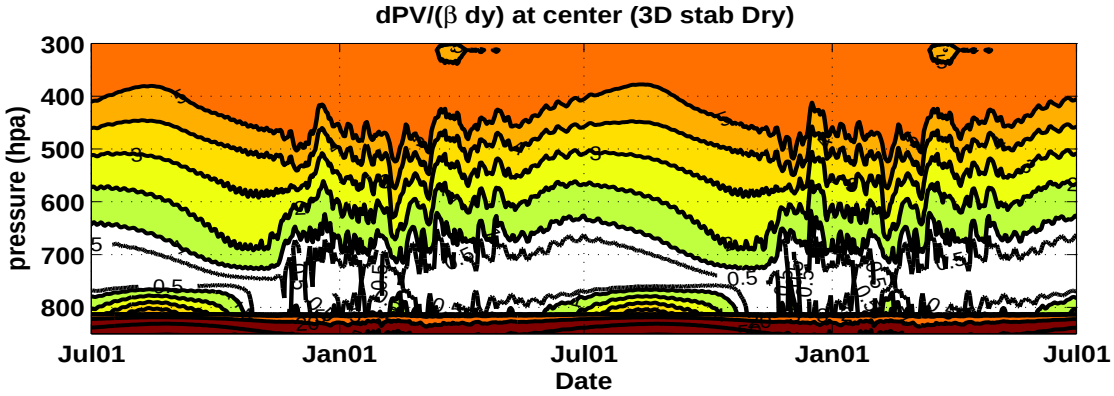

Figure 7-22: Same as Fig.7-21 but for the 3D simulation with the 8 K/km lapse rate as the target state stratification in the troposphere.

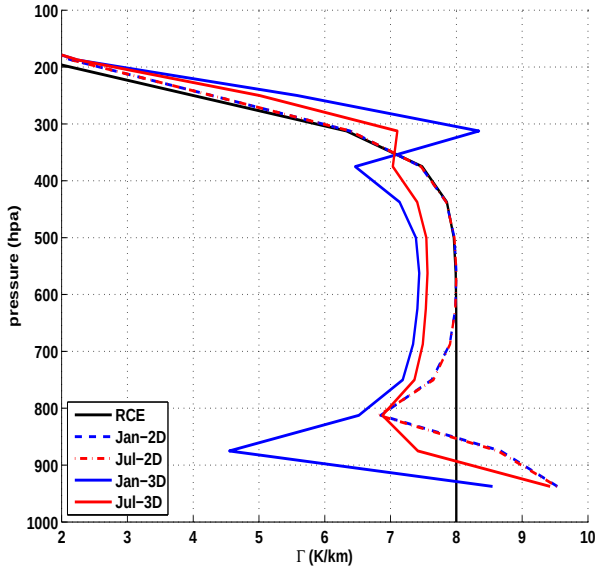

Figure 7-23: Lapse rate in the RCE state and averaged over January and July in the 2D (dashed curves) and 3D (solid curves) simulations with the 8 K/km lapse rate as the target state stratification in the troposphere.

boundary layer forcing and the radiative-convective heating. The other 2D run simulation we carried out is that instead of using the moist-adiabatic lapse rate as the RCE state stratification, we assume that the target state lapse rate is 8 K/km in the troposphere (which is closer to the dry adiabatic state) and isothermal in the stratosphere through the whole year (as shown in Figure 7-23). By comparing these two simulations, we can efficiently distinguish the influence of boundary layer from the influence of the moist-adiabatic lapse rate.

The fact that the boundary layer processes can maintain a weak lower level PV gradient by modifying the stratification there can be clearly seen in Figures 7-20, 7-21 and 7-19, 7-23. In the 2D runs, without baroclinic eddies and without the efficient reduction of temperature gradient, a weak even negative lower level PV gradient can be observed through the whole year in both runs in Figs.7-20 and 7-21. Comparing the lapse rate in Figure 7-19 with the moist adiabatic state lapse rate used in the model in Figure 7-5(a), we find that in the 2D run, in both summer and winter, the vertical stratification distribution indicates a pretty well mixed boundary layer near the surface, while at 800 hpa, which is also the top of the

boundary layer in our model, the flow is much more stable than the moist adiabatic state lapse rate, which is also the feature of a well mixed boundary layer as shown in Stull (1988). Similar trend is also found when using different target state lapse rate as shown in Figure 7-23. Since the $d\overline{T_e}^{xy}/dz$ does not vary with time, the lapse rate distribution almost the same over the whole year, which is consistent with fact that in the 2D run the stratification is determined by the boundary layer thermal forcing and the radiative-convective heating. Thus, in these two simulations, at the top of the well mixed boundary layer, the isentropic slope is greatly reduced compared with its neighboring levels, and the PV gradients there and in the levels just above the top of the boundary layer are strongly reduced as well, in spite of the strong temperature gradient in the 2D flow.

We want to point out that in the real atmosphere, except in the instantaneous lapse rate profile, in a climatological mean temperature field, we do not see such obvious temperature profile as in the well mixed boundary layer. This is primarily because that the atmospheric boundary layer itself has large spacial and time variations. For example, the boundary layer over land and ocean has different temperature profile, and the well mixed boundary layer depth over land has large diurnal cycle. However, our model shows that at the top of a well mixed boundary layer, where the stratification is very stable, weak PV gradient can be observed.

Comparison between the two 2D runs also indicates that, even though the boundary layer thermal forcing is a dominant factor responsible for the lower level weak PV gradient, the target state stratification can also affects the PV structure. As shown in Fig.7-21, a much larger PV gradient is observed almost through the whole free troposphere when the target state is weakly stratified. The role of the RCE state stratification in affecting the PV structure will also be discussed later.

In addition, a 3D run simulation with the 8 K/km lapse rate as the target state stratification is also carried out, whose PV structure is shown in Figure 7-22. Compared with the corresponding 2D run, the PV gradient is strongly reduced and the lower level PV is more homogenized over a deeper layer over the whole year. By comparing its lapse rate

distribution in Fig.7-23 with the standard run (Fig.7-19), it indicates that the eddies play an important role in modifying the thermal structure in summer as well under a less stable stratification.

Moist adiabatic state

In the moist-adiabatic state, as shown in Figure 7-2(a), in the lower levels, the stratification ($\frac{g}{c_p} - \Gamma$) is more stable as the atmosphere there is more moist and warmer. In the upper levels, the moist-adiabatic lapse rate is closer to the dry adiabatic lapse rate. Thus, in a moist-adiabatic state, the stratification also decreases with height though not as fast as that above the steering level in the SD run or at the top of the well mixed boundary layer. Thus, the vertical distribution of the moist-adiabatic lapse rate could also act to offset the planetary PV gradient β. We have done more experiments to check this effect.

Instead of having an interactive stratification, this time we specify the model stratification with the moist-adiabatic lapse rate, which is also the lapse rate in the RCE state (Figure 7-5). This simulation can be considered as a case in which the radiative-convective heating is extremely strong. By doing so, we can also eliminate the influence of the boundary layer on the stratification. Still with the Northern Hemisphere-like seasonal forcing, we run both 2D and 3D simulations. The PV gradient distributions in these two runs at the center of the channel are displayed in Figure 7-24. The temperature gradient evolutions are shown in Figure 7-25. In the 2D simulation, from Figure 7-25(a), the temperature gradient shows similar behavior as that in the 2D stratification coupled run Figure 7-8(b). However, with moist adiabatic stratification, from Figure 7-24(a) we see that β can be partly reduced which results in a weak PV gradient in the lower level even in the winter. When eddies are included, with the reduced temperature gradient especially near the 800 hpa, the PV gradient is further reduced and the PV structure is more robust.

To test to what extent in the real atmosphere, the modification of the lower level stratification by baroclinic eddies and other physical processes can contribute to the observed robust PV gradient, we carried out another group of experiments, in which we specify the

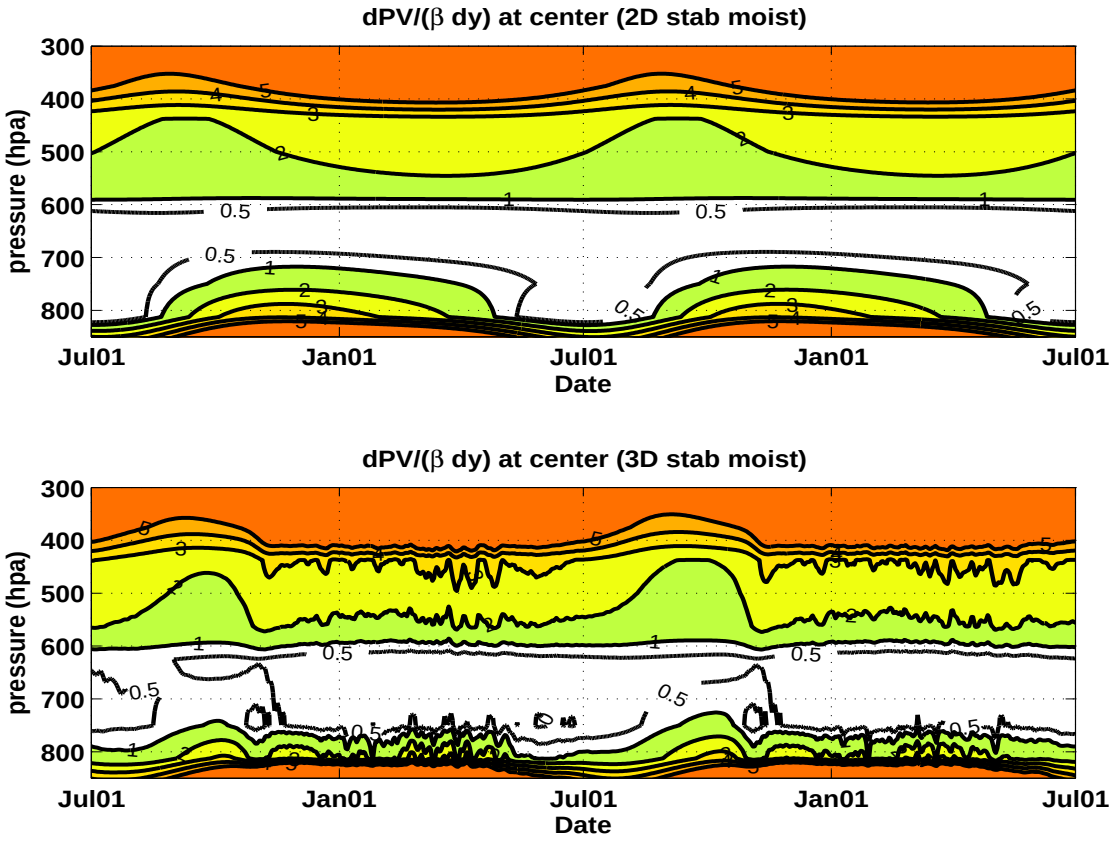

Figure 7-24: Time evolution of the meridional PV gradient at the center of the channel in the 2D simulation (upper) and in the 3D simulation (lower) in two seasonal cycles with stratification specified from the RCE state stratification $\overline{\theta}^{xy}(p,t) = \overline{\theta}_e^{xy}(p,t)$.

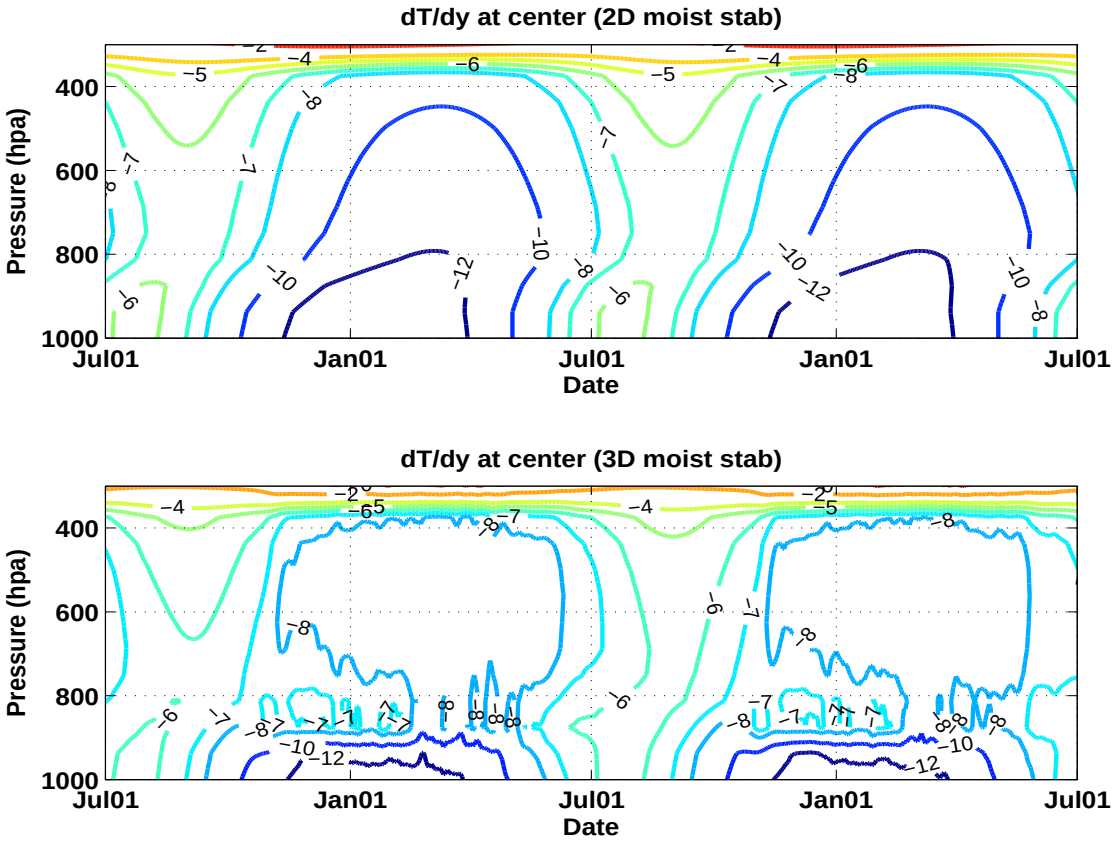

Figure 7-25: Time evolution of the meridional temperature gradient at the center of the channel in the 2D simulation (upper) and in the 3D simulation (lower) in two seasonal cycles with stratification specified from the RCE state stratification $\overline{\theta}^{xy}(p,t) = \overline{\theta}_e^{xy}(p,t)$.

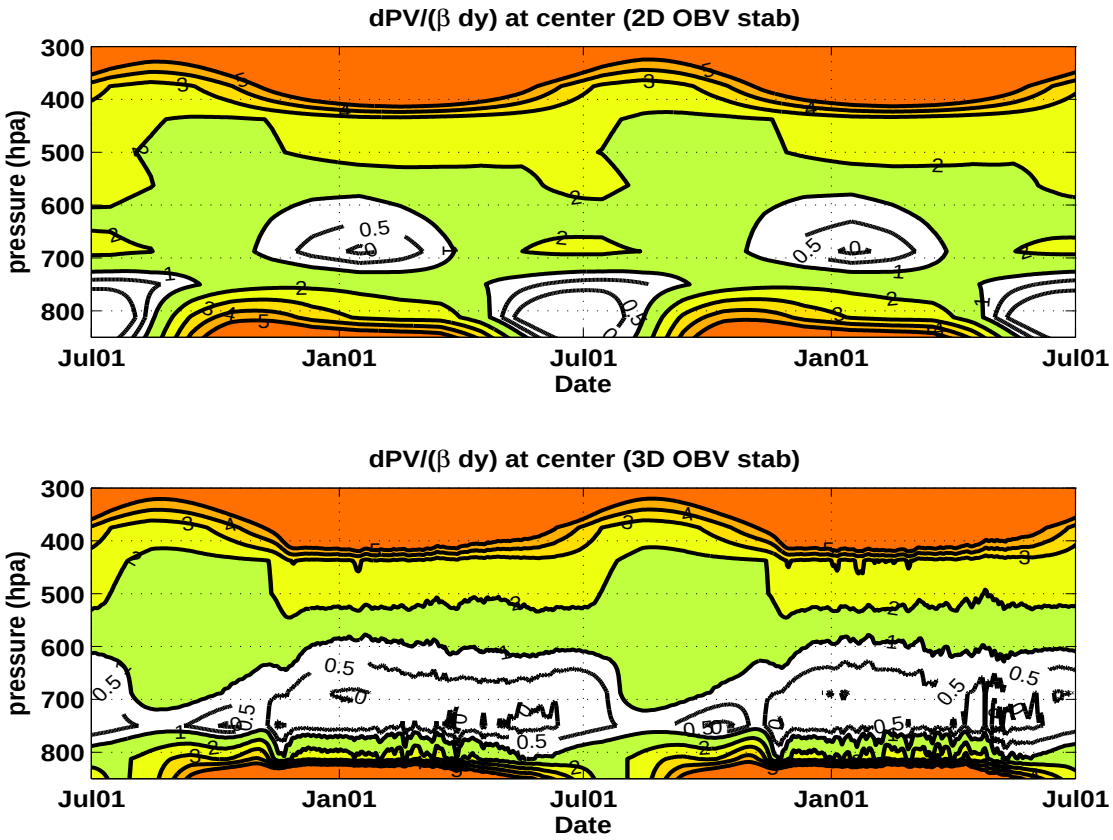

Figure 7-26: Time evolution of the meridional PV gradient at the center of the channel in 2D (upper) and in 3D simulations (lower) in two seasonal cycles with specified stratification, where stratification is specified to be the observed seasonal stratification $\overline{\theta}^{xy}(p,t) = \overline{\theta}^{xy}_{obs}(p,t)$.

stratification to be the observed lapse rate, whose distribution and time variation is shown in Figure 7-2(a). Thus, in the winter, the lower level is more stably stratified, which we assume is mainly due to the baroclinic eddies, and in summer, the stratification is close to the moist adiabatic state. We run both 2D and 3D runs.

From Figure 7-26(a) and 7-27(a), in the 2D simulation, when the temperature gradient is not efficiently reduced, in the winter, the PV gradient around 600-800 hpa can still be homogenized by increasing the stratification. In summer, the PV gradient near the 800 hpa is efficiently reduced. When including the eddies, with reduced temperature gradient, a much wider PV homogenization region can be observed all around the year.

To conclude our analysis, the stratification plays an important role in maintaining the

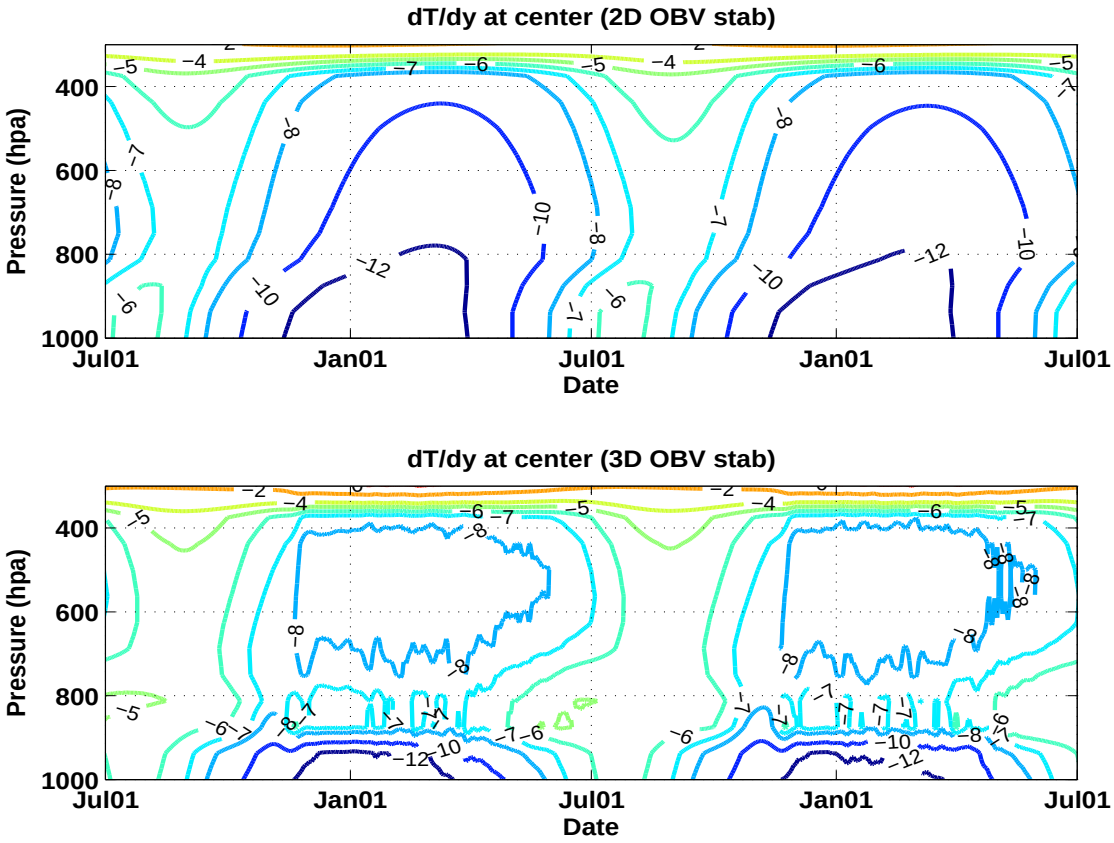

Figure 7-27: Time evolution of the meridional temperature gradient at the center of the channel in the 2D simulation (upper) and in the 3D simulation (lower) in two seasonal cycles with stratification specified with observed seasonal stratification $\overline{\theta}^{xy}(p,t) = \overline{\theta}^{xy}_{obs}(p,t)$.

robust PV structure over the whole year. Baroclinic eddies always act to keep a robust isentropic slope distribution. Near the boundary layer, especially at the top of a well mixed boundary layer, the strongly stable stratification there offsets the planetary PV gradient β and also acts to keep a weak PV gradient there. The vertical distribution of the moist-adiabatic lapse rate also helps maintain a weak PV gradient in the troposphere.

7.6 Sensitivity to the time scale of seasonal forcing

To investigate the condition under which the equilibrium assumption is valid when under time varying external forcing, in this section, we study the eddy response by artificially changing the period of the external forcing. In our SD run, the external forcing varies with t_{date} as shown in Equation 7.1, and $T_{year} = 1$ year. Now we run a group of tests by assuming $T_{year} = 5$, 2, 1/2 and 1/5 years, respectively. Still, we start the model from Jan. 01, and let the model reach an equilibrium state under winter time forcing, then we turn on the seasonal variation of the external forcing and integrate the model for 15 forcing periods. Their energy evolutions as a function of t_{date} are plotted in Figure 7-28, from which we can see the dependence of eddy activity on the varying time scale of the external forcing.

- When the external forcing period is long enough (more specifically, when the forcing periods are longer than one year), the zonal flow and eddy eddy activity show similar characteristics as the SD run: a short eddy spin-up period, a 'quasi-equilibrium' winter for MPE, a relatively longer eddy decay period and an eddy inactive summer.

- Eddies begin growing to finite amplitude earlier and the mean flow reaches the 'quasi-equilibrium' state earlier for longer forcing period runs. As we will show in the next section, this is primarily because the eddy growth rate as well as the spin-up time scale are mainly the dynamical time scale. In the longer forcing period runs, eddies have 'more' time to feel the strong baroclinicity of the background flow and have more time to grow.

- Even though eddies begin to spin up at different time, during their decaying period,

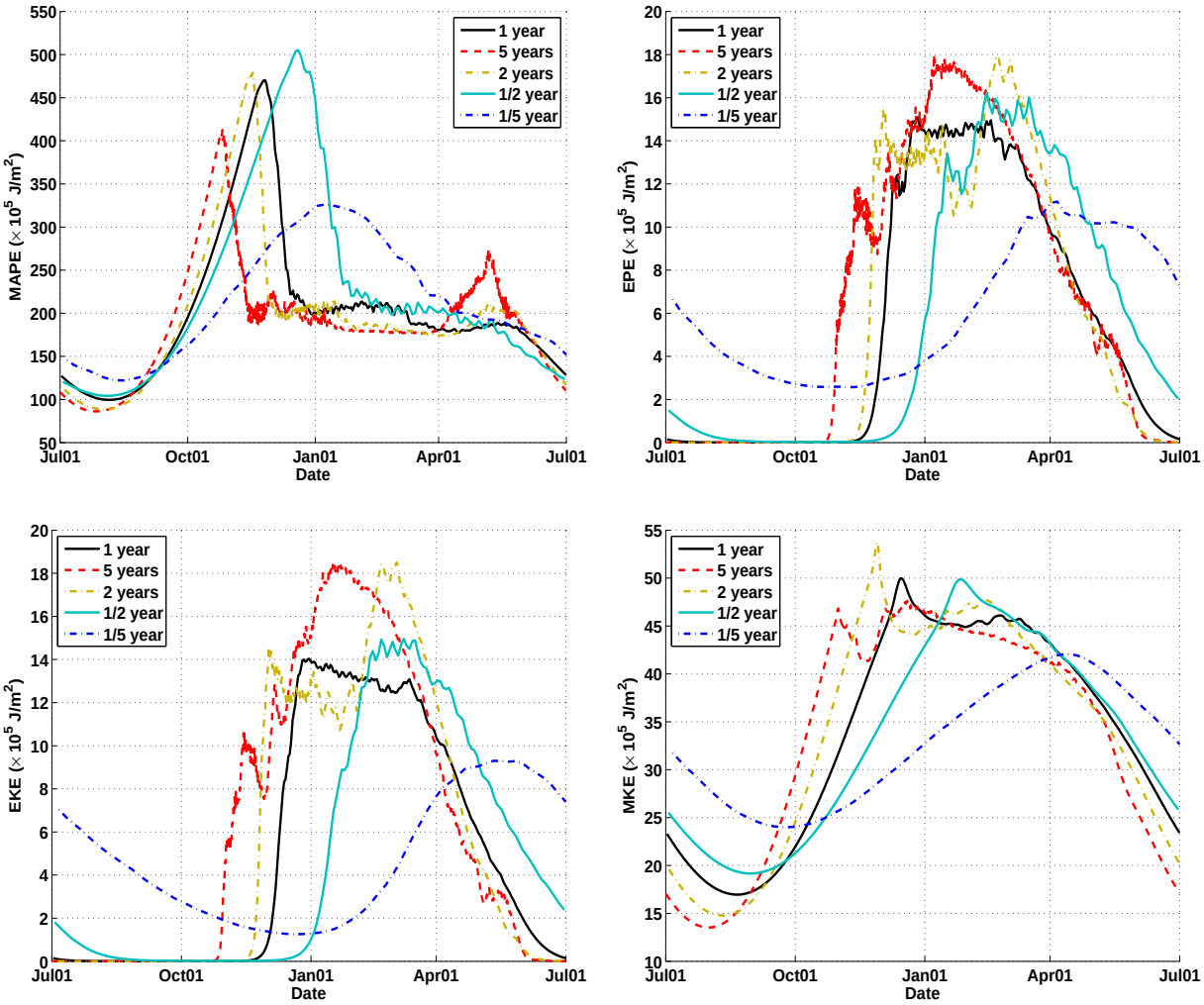

Figure 7-28: Seasonal variation of domain averaged (a) mean available potential energy, (b) eddy available potential energy, (c) eddy kinetic energy and (d) mean kinetic energy averaged over the last ten forcing cycles when we artificially increase the period of the external forcing from one year to 5 and 2 years, and artificially reduce the period to 1/2 and 1/5 year. All energy evolutions are stretched or squeezed to be plotted against their forcing date. Energies are plotted in unit $10^5 J/m^2$.

the eddy energy decaying rates relative to the forcing time scale, $dEKE/dt_{date}$ and $dEPE/dt_{date}$ seem very similar.

- When the seasonal forcing varies very slowly, $T_{year} = 5$ years, at the end of the eddy decaying state, as the eddy energies become weak, instead of keeping the 'quasi-equilibrium' state value, MPE shows a temporary increase and decays only later to smaller values.

- When the external forcing is quickly varying, especially when $T_{year} = 1/5$ year , eddy and zonal flow do not show any characteristic time scales like those in the SD run. The MPE varies almost in proportion to the external forcing, EPE and EKE as well as MKE vary with MPE but with a lag of 15 to 30 model days (75 to 150 forcing days). The maximum eddy energies are smaller than the SD run, while eddy energies still have finite amplitude activity in summer.

- An FFT analysis is also applied to the energy time series for $T_{year} = 1/5$ year run as shown in Figure 7-29, which is compared with the corresponding 2D simulation (Figure 7-30). Consistent with Figure 7-30, the system still has its largest peak at period t_{date}=365 days and minor peaks at one half and one third of the forcing period. However, different from Figure 7-13, as the eddy and zonal flow do not have any obvious characteristic time scale, all the energies have simpler spectra which mainly follow the seasonal forcing by comparison with Figure 7-30, except in the short period regime, where a peak near 4-5 model days, the characteristic life period of baroclinic eddies, is also observed except for MKE.

As we have shown in this section, the seasonality of the energies are influenced by the time scale of the external forcing. A quasi-equilibrium winter exists only under the slowly varying external forcing. When the external forcing varies quickly (e.g. 1/5 year period), we will not see any other response time scales.

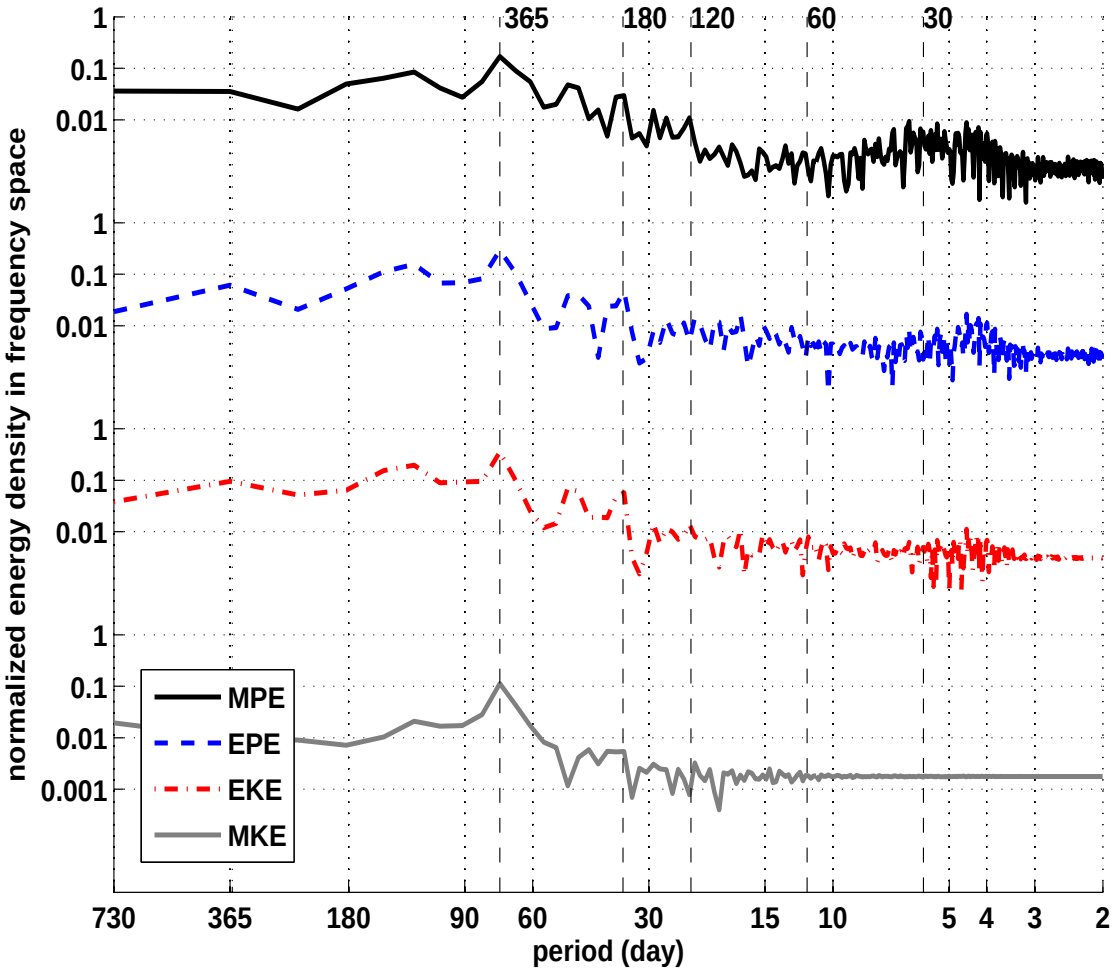

Figure 7-29: Normalized spectra of MPE, EPE, EKE and MKE density in the frequency (period) domain for the $T_{year} = 1/5$ year run. The corresponding forcing period phrased in t_{date} is also labeled at the top of the plot.

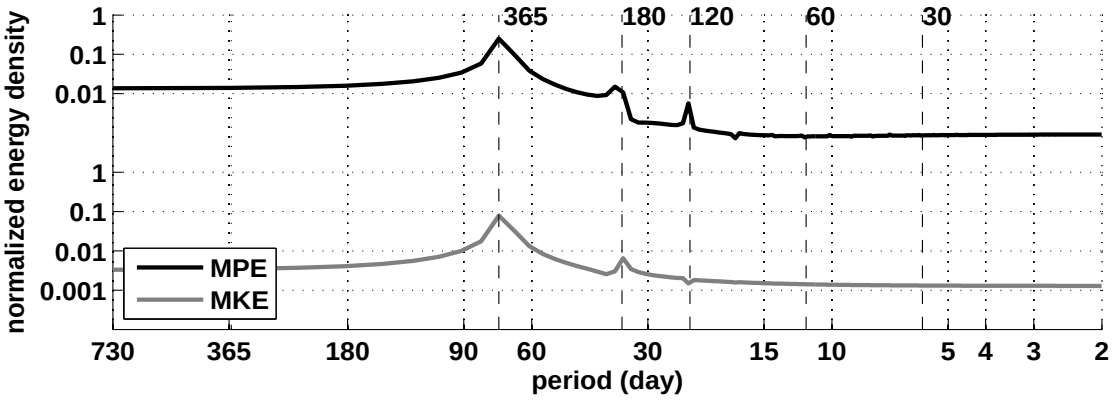

Figure 7-30: Normalized spectra of MPE and MKE density in the frequency (period) domain for the 2D $T_{year} = 1/5$ year run. The corresponding forcing time period phrased in t_{date} is also labeled at the top of the plot.

7.7 Spin-up and spin-down time scale

From Figure 7-12 and 7-28, we see that under slowly varying seasonal forcing, eddy activity exhibits two time scales: a spin-up time scale which is usually less than a month, and a spin-down time scale, which can be as long as two to three months. In this section, we are going to investigate the dominant factors that determine these time scales.

7.7.1 Spin-up time scale

Eddy growth/decay rates, defined as $\frac{1}{EKE}\frac{d}{dt}EKE$, are plotted in Figure 7-31(a) as a function of t_{date} when varying the external forcing time scales. Except for the $T_{year} = 1/5$ year run, which primarily follows the seasonal forcing, in all the other cases, eddy growth rate/decay rates show more features.

- Eddy activity experiences a fast exponentially growing period in the middle of fall or the early winter. The growth rates in this period are also plotted as a function of model day in Figure7-31(b), in which the maximum growth rate day is labeled as day0. We find that their fast growing states are all maintained for around one month and after reaching the maximum growth rate, their growth rates all drop down quickly in around ten days, which is consistent with the previous eddy life cycle studies and suggests that

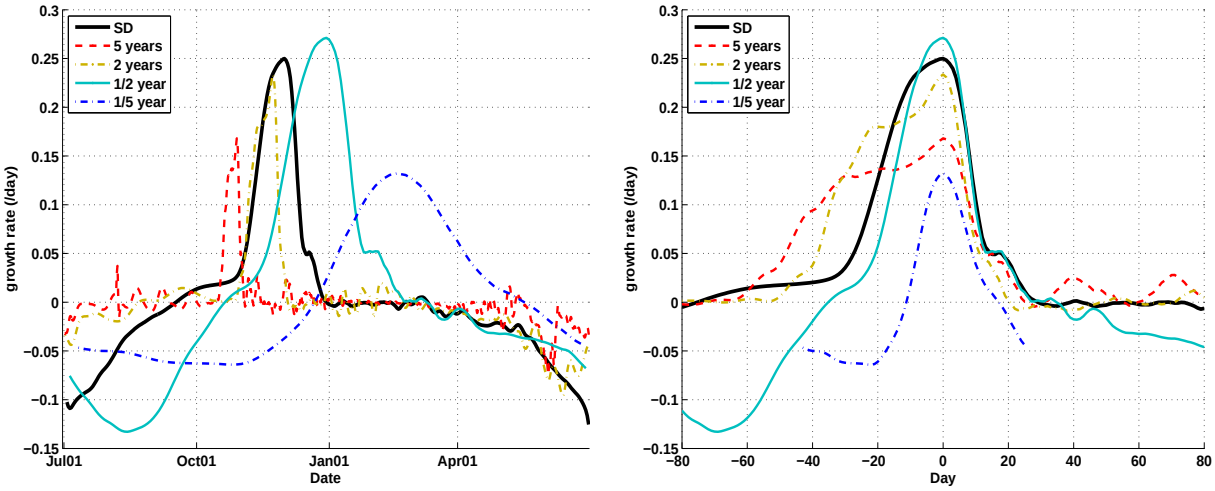

Figure 7-31: a) Seasonal variation of the eddy growth/decay rate (/day) as a function of t_{date} and b) evolution of eddy growth rate (/day) as a function of model day during eddy spin-up period, where $day = 0$ is the day that eddy growth rate is largest.

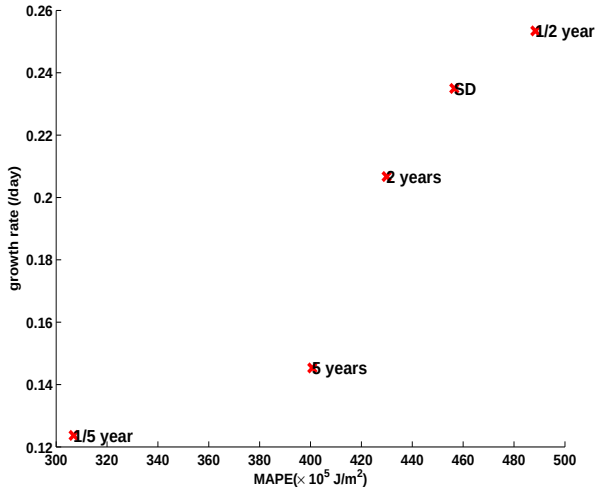

Figure 7-32: Variation of the eddy growth rate in the eddy spin-up period as a function of MPE for different T_{year}.

the increasing nonlinear interactions may act to prevent further eddy growth as their amplitudes grow.

- As the external forcing time scale increases, as shown in Figure 7-31(a), eddies begin to spin up earlier but with a lower maximum growth rate and maintain a longer period of fast growth as shown in Figure 7-31(b).

- The relation between the largest growth rate and the MPE during their fastest growing period is also plotted in Figure 7-32. Eddy growth rate is correlated with MPE in a way consistent with the linear instability theory in which the growth rate is linearly proportional to $\sqrt{MPE}$.

- In the 'quasi-equilibrium' state, the eddy growth/decay rate oscillates around the zero line until spring when eddies begin decaying. The eddies decay with a rate weaker than their growth rate but can last as long as three months.

From Figures 7-31 and 7-32 we find that when the external forcing is varying slowly, eddy behavior in their growing state shows similar characteristics as predicted in the linear instability theory. Their spin-up time scale is mainly dynamically determined.

When $T_{year} = 1/5$ year, eddies do not have an obvious spin-up or spin-down period. The eddy growth rate is largest in February, which is always the time that the external forcing is largest, and they begin decaying in the middle of spring.

7.7.2 Spin-down time scale

One characteristic during the eddy spin-down period is that, even though eddy activity decays, MPE stays at a relatively constant value through most of the period. Thus, we will start our analysis from the MPE energy budget equation.

In our modified QG model, the total balance equation of MPE is

$$\frac{d}{dt}MPE = G_{mpe}(Q) - C(MPE, EPE) - C(MPE, MKE) + G_{mpe}(\sigma), \tag{7.15}$$

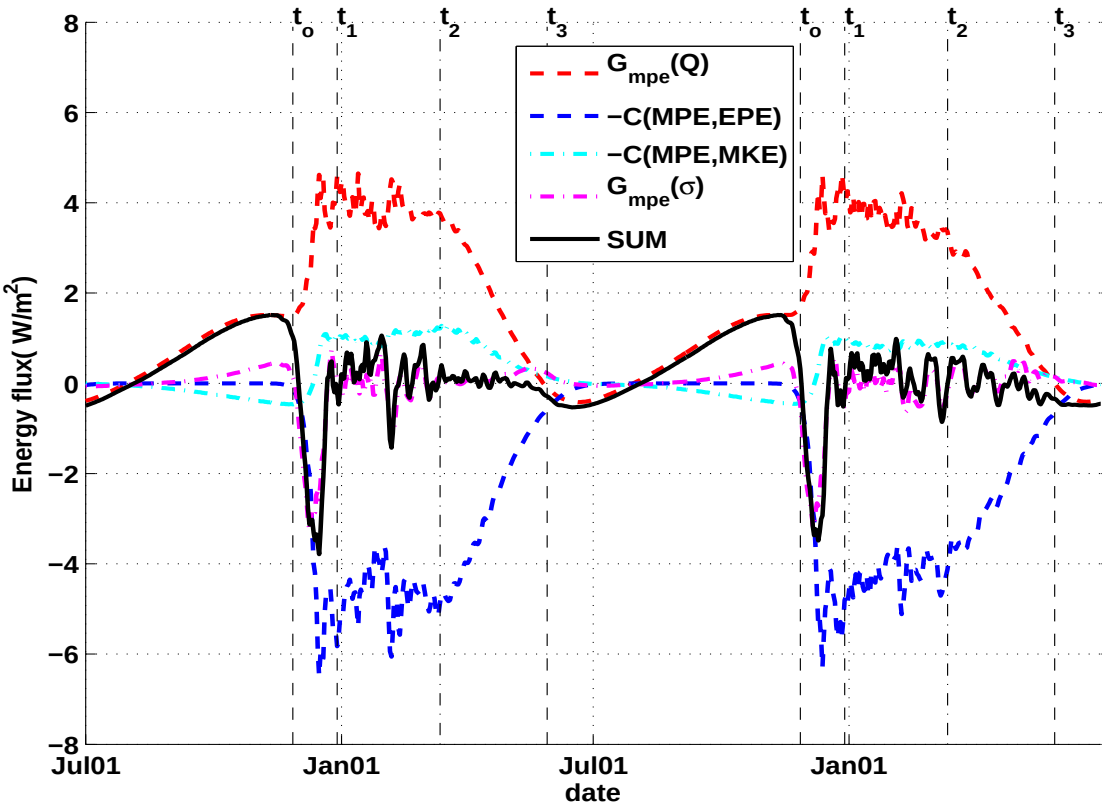

(a)

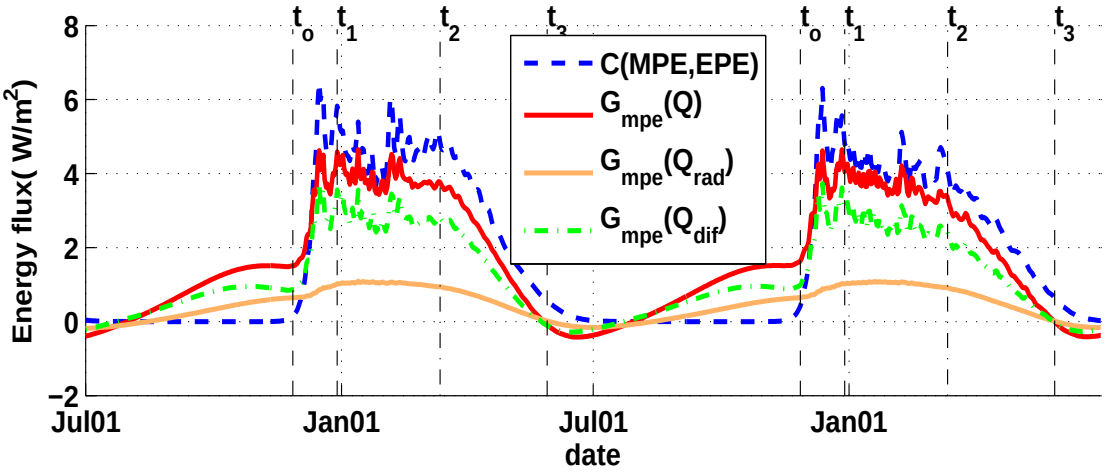

(b)

Figure 7-33: (a)Time evolution of each term in MPE balance equation in two seasonal cycles in the SD run. (b) Time evolution of $C(MPE, EPE)$, and the MPE generation term $G_{mpe}(Q)$, its two components: generation through radiative-convective heating $G_{mpe}(Q_{rad})$ and through boundary layer heating $G_{mpe}(Q_{dif})$. Energy fluxes are plotted in W/m^2. The eddy spin-up, spin-down and MPE quasi-equilibrium periods are also marked by t_o, t_1, t_2, t_3.

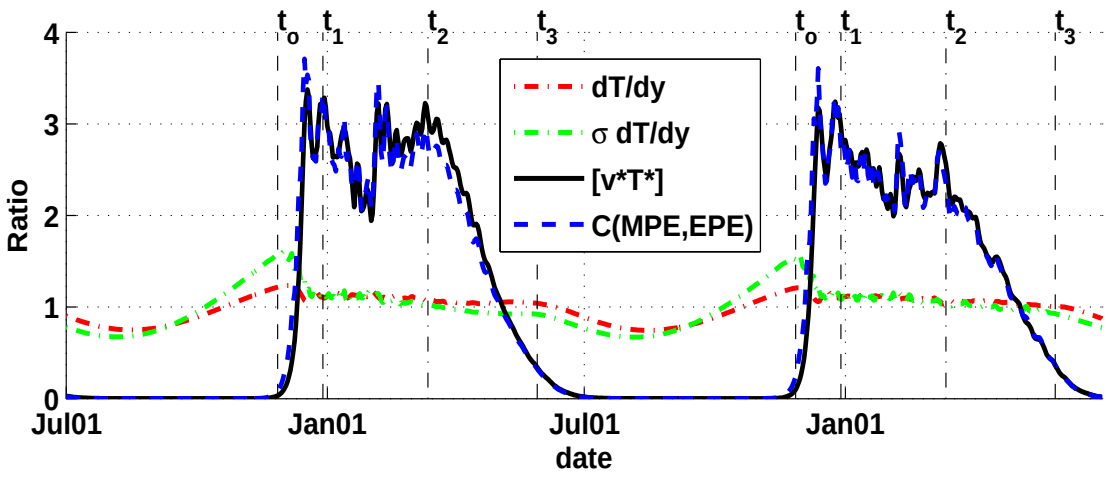

Figure 7-34: Time evolution of normalized domain averaged $\frac{\partial[T]}{\partial y}$, $\sigma\frac{\partial[T]}{\partial y}$, poleward eddy heat transport $[v^*T^*]$ compared with $C(MPE, EPE)$ in two seasonal cycles in SD run. The eddy spin-up, spin-down and MPE quasi-equilibrium periods are also marked by t_o, t_1, t_2, t_3.

where $G_{mpe}(Q)$, $C(MPE, MKE)$ and $G_{mpe}(\sigma)$ have the same definition as in Equation 7.7 (referred to Equations 7.10, 7.11, 7.12). However, different from Eq.7.7, in the 3D simulation, there is another important term in the MPE balance equation

$$C(MPE, EPE) = -c_p \int \sigma[v^*T^*]\frac{\partial[T]}{\partial y}dm, \tag{7.16}$$

which is the conversion rate from MPE to EPE through eddy poleward heat transport down the zonal mean temperature gradient.

The time evolution of these energy flux terms is plotted in Figure7-33, in which the eddy quiescent, spin-up, spin-down periods and MPE quasi-equilibrium period are also marked. From the plot we find that:

- During the eddy spin-up period, from time t_o to t_1, the eddy transport term $C(MPE, EPE)$ also increases exponentially to reduce MPE. As the lower level stratification is strongly stabilized by the baroclinic eddies, $G_{mpe}(\sigma)$ also becomes an important sink for MPE. This is the only period during the whole year that $G_{mpe}(\sigma)$ plays an important role in changing MPE. These two factors work together causing the quick decrease of MPE.

- After t_1, MPE reaches a quasi-equilibrium state, in which $G_{mpe}(Q)$ and the eddy transport term are the two dominant factors that maintain MPE. $C(MPE, MKE)$ plays a minor role in increasing the MPE given the fact that the zonal flow has a Ferrel Cell circulation in this period.

- As shown in Figure 7-33(b), these two terms are comparable and highly correlated from t_1 to t_3. A close look at the two components of $G_{mpe}(Q)$ also shows that $G_{mpe}(Q_{rad})$ and $G_{mpe}(Q_{dif})$ all act to increase the system MPE with $G_{mpe}(Q_{dif})$ having the larger contribution, which is consistent with our study in Chapter 4 that the boundary layer thermal forcing can act as a strong source of the lower level baroclinicity by dragging the air temperature near the surface close to the underlying surface temperature. Thus, in the quasi-equilibrium state, when the lower level temperature is efficiently reduced by baroclinic eddies, the strong underlying surface temperature gradient, through the strong boundary layer thermal forcing, acts as a strong source for MPE.

- Starting from t_2, the external forcing as well as $G_{mpe}(Q)$ begin to decrease. To balance it, the eddy transport term also needs to decrease. The time evolution of the different components in $C(MPE, EPE)$ is also plotted in Figure 7-34. We find that in this period, along with the robust MPE, the zonal mean temperature structure still keep unchanged. Thus, the decreasing $C(MPE, EPE)$ indicates a decay of eddy poleward heat flux and eddy energies.

- As the underling surface as well as the target state temperature gradients decrease, at time t_3, when they became smaller than the 'quasi-equilibrium' state temperature gradient as indicated from Figure 7-15 and 7-8(a), both $G_{mpe}(Q_{rad})$ and $G_{mpe}(Q_{dif})$ change sign and start acting to reduce the atmospheric temperature gradient. As shown in Figure 7-33(b), the quasi-equilibrium cannot be maintained and begins decreasing. After t_3, eddies become inactive and differential heating is the dominant factor that determines MPE evolution. Until the late summer when the target state temperature gradient begins increasing (from Figure 7-8(a)), they again act together to increase the

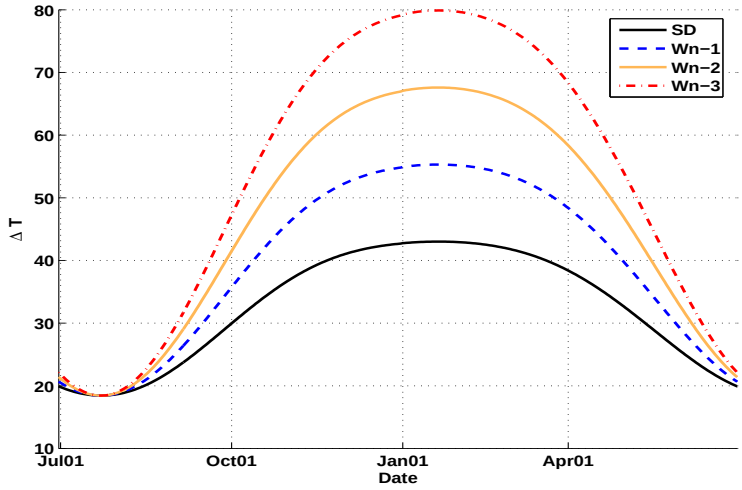

Figure 7-35: Seasonal variations of the underlying surface temperature difference across the channel used in the sensitivity study.

flow baroclinicity.

From the maintenance of MPE during the seasonal cycle we find that the decay of eddy activity is primarily the eddy response to the decreasing differential heating, which implies that the decay time scale is mainly determined by the external forcing. This is also indicated from Figures 7-28(b) and 7-28(c), where we vary the time scale of external forcing, showing that for these long forcing period runs, the eddies have similar decay behavior as a function of t_{date}.

7.8 Sensitivity to the strength of the seasonal forcing

As shown in our SD run, after eddies spin-up, in spite of the varying external forcing, MPE always stays at a relatively constant value, here we call it 'critical MPE'. We also find that for slowly varying external forcing, although we vary the forcing period, the critical MPEs are relatively the same. Then what determines the value of critical MPE? One of the candidate answers might be the strength of the external forcing, especially the forcing in the winter time. In this section we will carry out sensitivity studies to investigate the dependence of critical MPE on the strength of the seasonal forcing and to test the robustness of the critical

MPE.

As shown in Figure 7-35, besides the SD run, we carried out three sensitivity runs (wn-1, wn-2, wn-3) by artificially increasing the winter time differential heating but keeping the summer time differential heating the same. The seasonal evolutions of MPE, EPE, EKE and MKE under the different strengths of the seasonal forcing are plotted in Figure 7-36. Because of the strongest differential heating in winter, the eddies begin spinning up earliest and eddy energies reach the largest value in the wn-3 run. After a short spin-up period, MPE also decreases quickly and, roughly speaking, maintains a relatively constant value but with much stronger oscillations.

Since the MPE behavior shows stronger oscillations for the stronger external forcing in winter, to better compare the critical MPE in these runs, a histogram of MPE is also plotted in Figure 7-37. The plot shows that as the winter time external forcing increases, these runs have similar critical MPE, but 10-20 % higher than that in SD run.

An FFT analysis is also applied to the EKE and the histogram of the EKE's component in zonal wave-numbers 6, 5, 4 and 3 under different strengths of the seasonal forcing is displayed in Figure 7-38. We find that as the external forcing increases, the most active waves shift from wave-number 5 in the SD run to wavenumbers 3 and 4 in the wn-3 run. The seasonal behavior of the EKEs in wavenumbers 3, 4, 5 and 6 in the SD run and the wn-3 run is also plotted in Figure 7-39. In the SD run, as differential heating is enhanced, wavenumber 5 spins up first and reaches its maximum value around Jan01. Then EKE in wavenumber 5 decays and energy moves to wavenumber 4. As the total EKE decays in the early spring, wavenumber 6 becomes the dominant wave. In the wn-3 run, wavenumber 5 is still the dominant wave during the eddy spin-up period, after which wavenumber 4 becomes the dominant component, then wavenumber 3 finally grows to be the most active wave. In the EKE decaying period, wavenumber 3 loses its energy and wavenumber 4 becomes dominant again.

Figure 7-38 also shows that, except for the SD run, the EKE in wavenumber 5 has similar histogram distributions in these runs. Its seasonal behavior in the different runs is

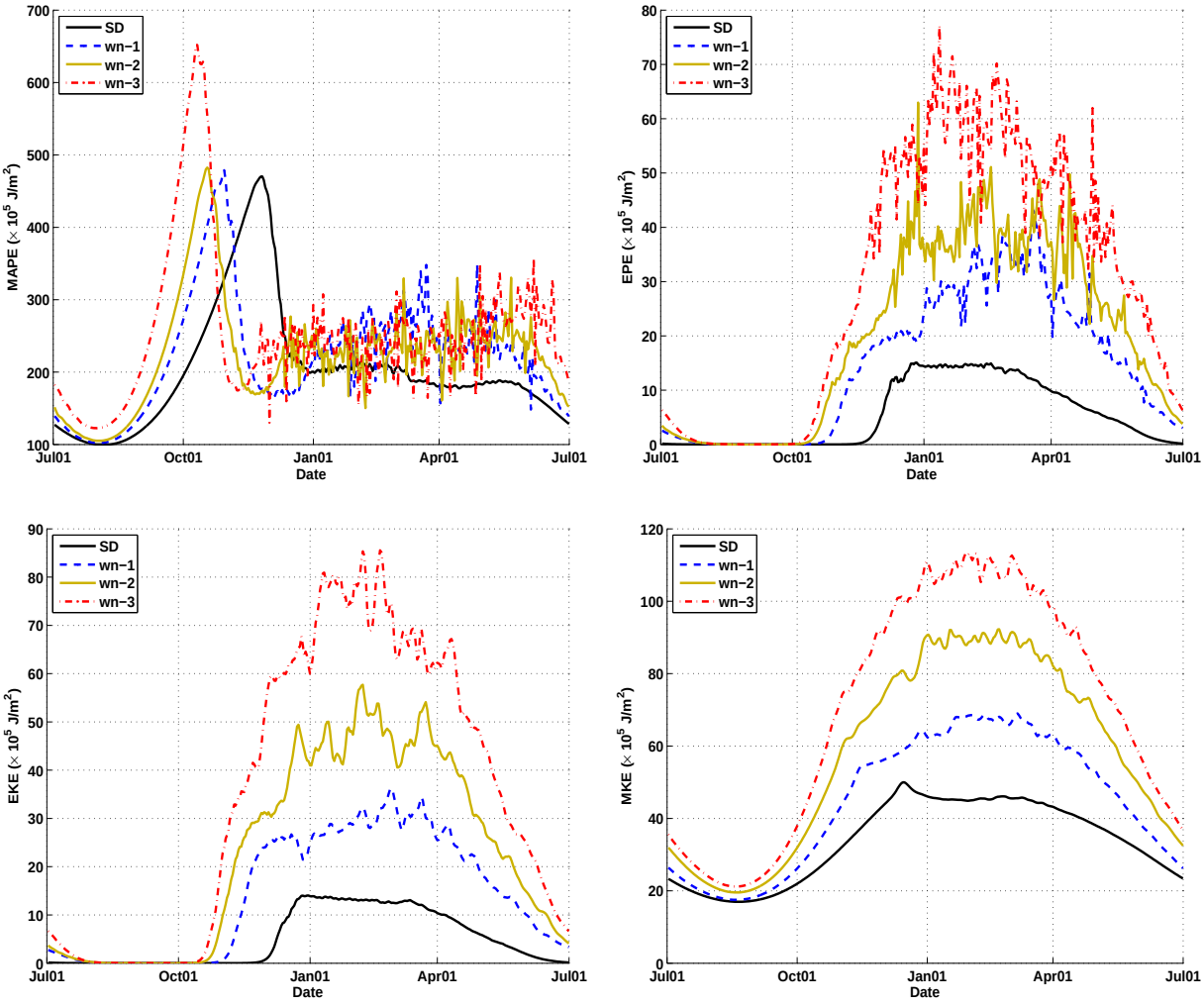

Figure 7-36: Seasonal variation of domain averaged (a) mean available potential energy, (b) eddy available potential energy, (c) eddy kinetic energy and (d) mean kinetic energy averaged over the last ten years when artificially increasing the winter time forcing. Energies are plotted in unit $10^5 J/m^2$.

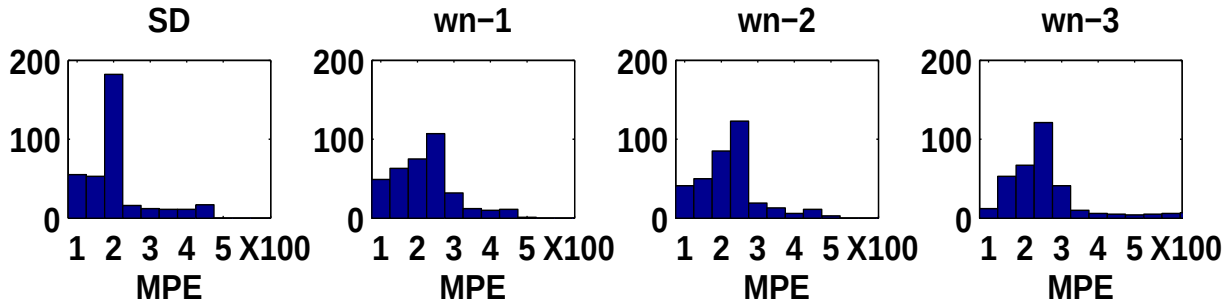

Figure 7-37: Histogram of MPE in its annual cycle. MPE is in the unit $\times 10^5 J/m^2$.

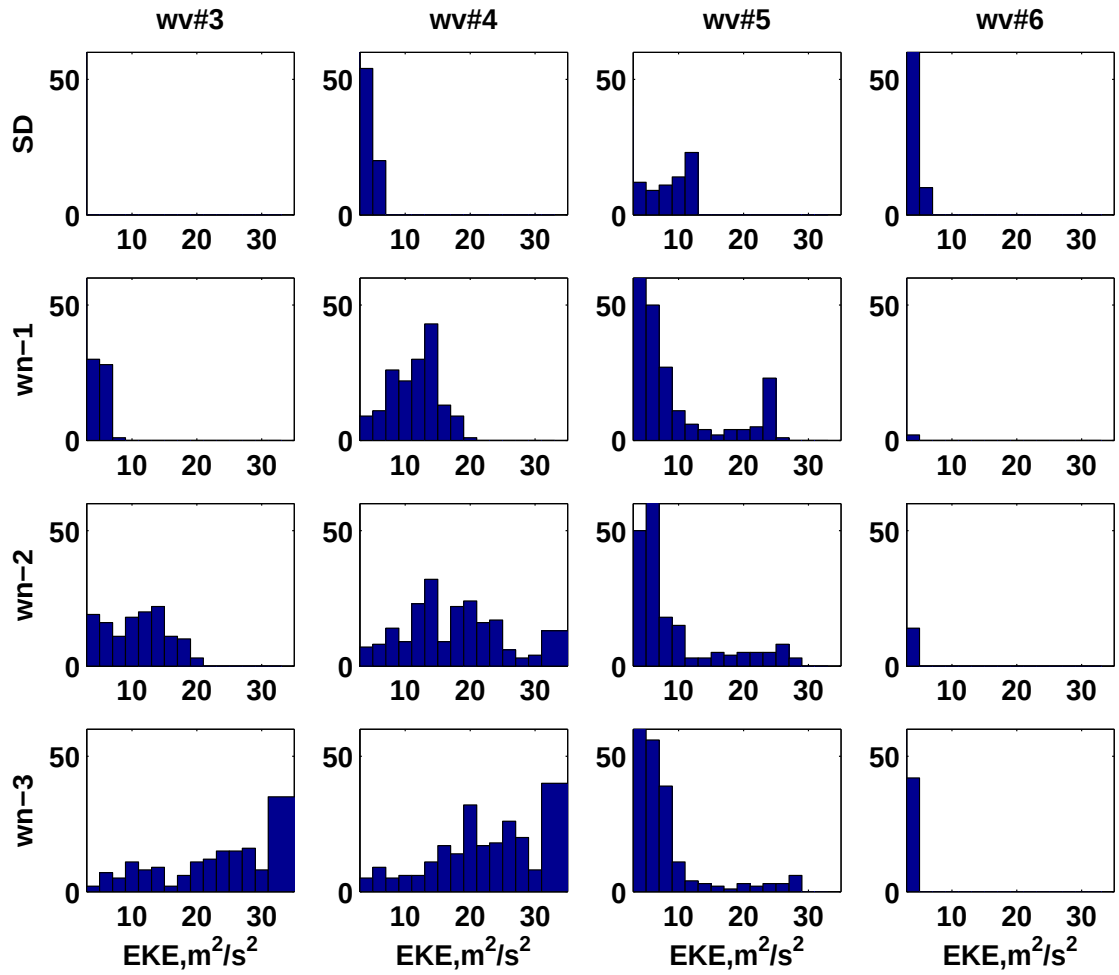

Figure 7-38: Histogram of EKE's components in wavenumbers 3, 4, 5 and 6 (from left to right respectively) for the SD, wn-1, wn-2 and wn-3 (from top to bottom) runs in their annual cycle.

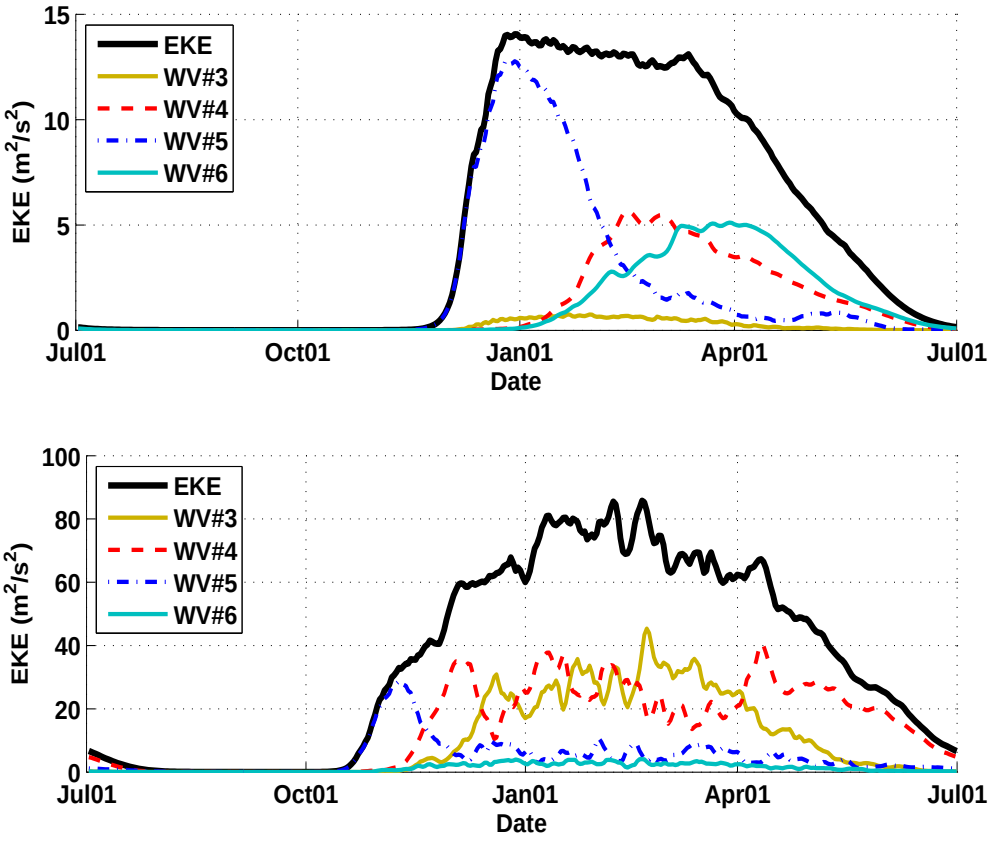

Figure 7-39: Time evolution of EKE and its components in wavenumbers 3, 4, 5 and 6 in the SD run (upper) and the wn-3 run (lower).

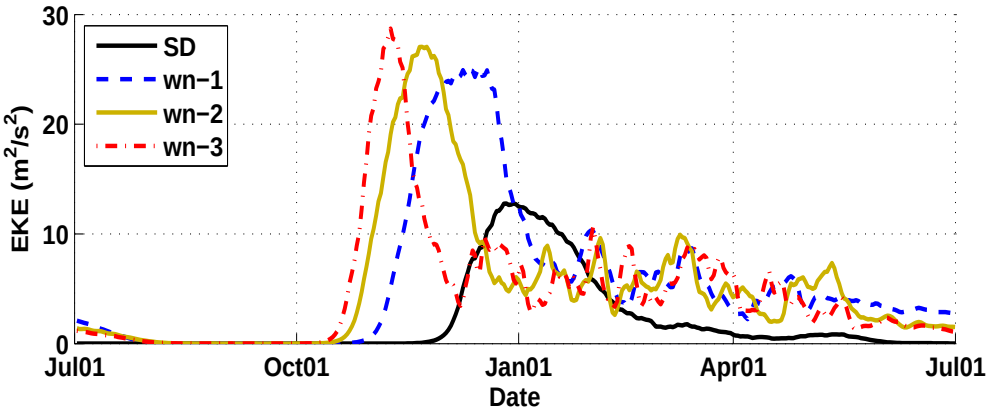

Figure 7-40: Time evolution of EKE in wavenumber 5 in the SD, wn-1, wn-2 and wn-3 runs.

also plotted in Figure 7-40. We find that wavenumber 5, after its initial dominance, has a similar seasonal behavior in runs other than the SD run. Instead of varying with the differential heating, EKE in wavenumber 5 stays around a lower constant value. Similar to Welch and Tung (1998a,b), it seems to reach a nonlinear saturated state.

Figure 7-38 also indicates that the large difference in eddy energies as we vary the strength of the external forcing primarily lies in the longer waves, especially in wavenumber 3, which becomes much more active as the external forcing gets stronger. This is a trend we do not find in wavenumber 5, which is like the nonlinear baroclinic adjustment scenario proposed by Cehelsky and Tung (1991) and Welch and Tung (1998a).

7.9 Influence of the initial condition

As shown in our SD run, under a Northern Hemisphere-like seasonal forcing, the eddy activity displays highly repeated features. In this section, we will test whether such features depend on the initial conditions. In contrast to the SD run, we will test what happens if we start the simulation from summer time with either a symmetric RCE state initial condition or an active eddy initial condition, and compare with our SD run.

The initial behavior of the zonal and eddy energies when starting from the summer time is displayed in Figure 7-41. We compare the SD run with the run which starts from the summer symmetric RCE state and with small amplitude perturbations added into the system at the initial moment. Although they have different MPE and MKE initial states, their seasonal behaviors converge to similar curves after integrating more than three months. Their eddy behavior also exhibits similarities. After integrating for one year, there is almost no difference between the two runs.

The differences between the SD run and the run starting from an eddy-active state are more obvious. When we start from a state in which eddy energies are as strong as these in the winter time, as shown in Figure 7-41, primarily due to the weak differential forcing, eddy activity decays very quickly compared to its initial state, but is not reduced to an amplitude as weak as in the SD run. Then eddies start to spin up almost one month earlier than in the

SD run, which indicates that the summer time eddy activity does influence the eddy spin-up date in the winter.

After one seasonal cycle, the differences due to the different initial conditions disappear, and they exhibit similar seasonal activity. Such repeated seasonal behavior seems to have its rationale: as in the summer that eddy activity is reduced to very small amplitude, eddy activities lose the 'memory' of last year and spin up again in the late fall. Thus, their seasonal behavior totally depends on their seasonal forcing. However, this may not be the case for the short period seasonal forcing run, especially when $T_{year} = 1/5$ year, when there are still finite amplitude eddies in the summer. Then does the eddy behavior depend on the initial condition or it is still mainly determined by the seasonal forcing? To test this, we carried out similar initial condition test runs but under the short period forcing ($T_{year} = 1/5$ year). Their eddy and zonal flow behavior is shown in Figure 7-42.

Comparisons between the SD run and the two initial condition test runs for their EPE, MPE, EKE and MKE time evolutions in the first 6 forcing years (equivalent to 438 model integrating days), are shown in Figure 7-42. Similar to Figure 7-41, the largest differences between the SD run and the other two runs are within the first forcing year. For the run starting with active eddy behavior, even though the eddy activity is also quickly reduced, it still stays at a relatively higher value and begins rising earlier than the SD run. Accompanied with this, MPE is maintained at relatively lower values in the first seasonal cycle. The MKE, which starts from a relatively higher value, also stays in a more active state in the first forcing cycle.

For the run starting from the symmetric RCE state, we find that eddies begin to grow later than the other two cases and the maximum eddy energies it reaches are also smaller in the first forcing cycle. The MPE is still kept at a higher value. Primarily due to the lower initial values, MKE is weaker in the first forcing cycle. After three forcing cycles, we find the differences between these runs almost disappears, even though there are still differences in the amplitudes in the eddy and zonal energies, these differences are smaller than the 'year-to-year' variability in the standard $T_{year} = 1/5$ year run itself. Figs.7-42 and 7-41 show that

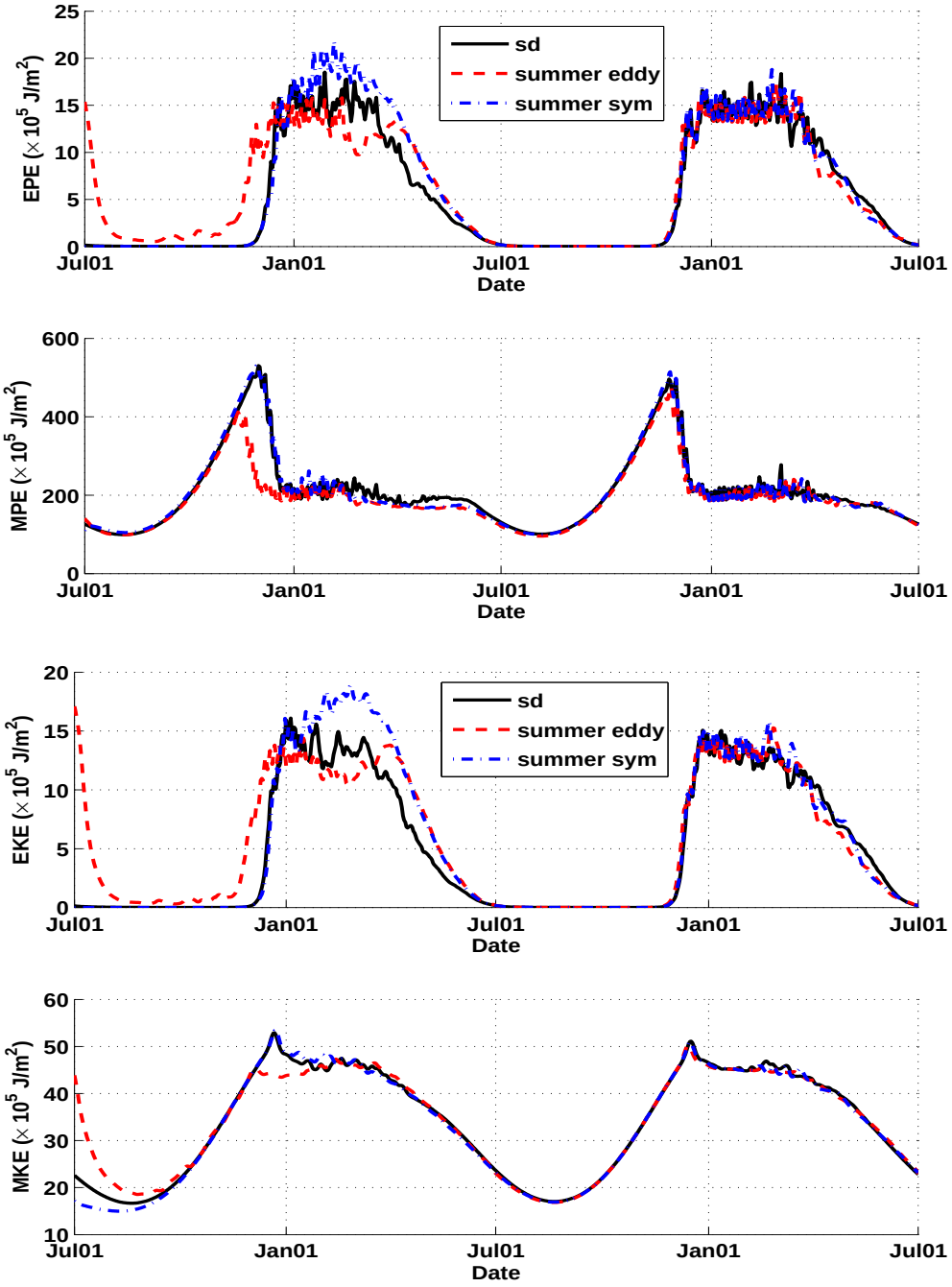

Figure 7-41: Time evolution of EPE, MPE, EKE, MKE in the first two annual cycles when starting from different initial conditions but under the same seasonal forcing in which the forcing period is one year.

the seasonal behavior in both long and short period seasonal runs are ultimately independent of the initial conditions.

7.10 Summary

In this chapter, we find that when the underlying surface temperature as well as the radiative-convective heating include a Northern Hemisphere - like seasonal variation, the response of baroclinic eddies displays some interesting features.

- Eddy activities show an obvious seasonal variation. Eddies spin up in the mid-fall with a relatively short spin-up time interval, and begin to spin down in the late spring with a three month long spin-down time interval. Our analysis shows that, the spin-up behavior is consistent with the prediction of the linear instability theory and the spin-up time scale is primarily dynamically determined. The decay of the baroclinic eddies in our SD run is primarily the eddy response to the decaying differential heating, thus, the eddy decay time scale is basically determined by the external forcing.

- After the eddy spin-up, in spite of the variation of differential heating and eddy activity, the MPE is kept at a relatively constant value, so is the isentropic slope, which is consistent with the baroclinic adjustment scenario. From the analysis of the MPE energy cycle, we find that in this MPE 'quasi-equilibrium' state, eddy energies and eddy heat flux are mainly determined by the external forcing, instead of the mean flow, since the thermal structure in this period is almost constant. This is also consistent with the scenario proposed by Stone (1978) and Lindzen and Farrell (1980).

- Although the eddy activity has strong seasonality, the mean PV gradient at the center of the channel does not vary too much during the whole year. The PV gradient has smallest PV gradient around 600-800 hpa, and large PV gradient near the surface and the tropopause. This also raises the question of how we interpret the observed robust PV structure in the real atmosphere. In our model, we find that a well mixed boundary

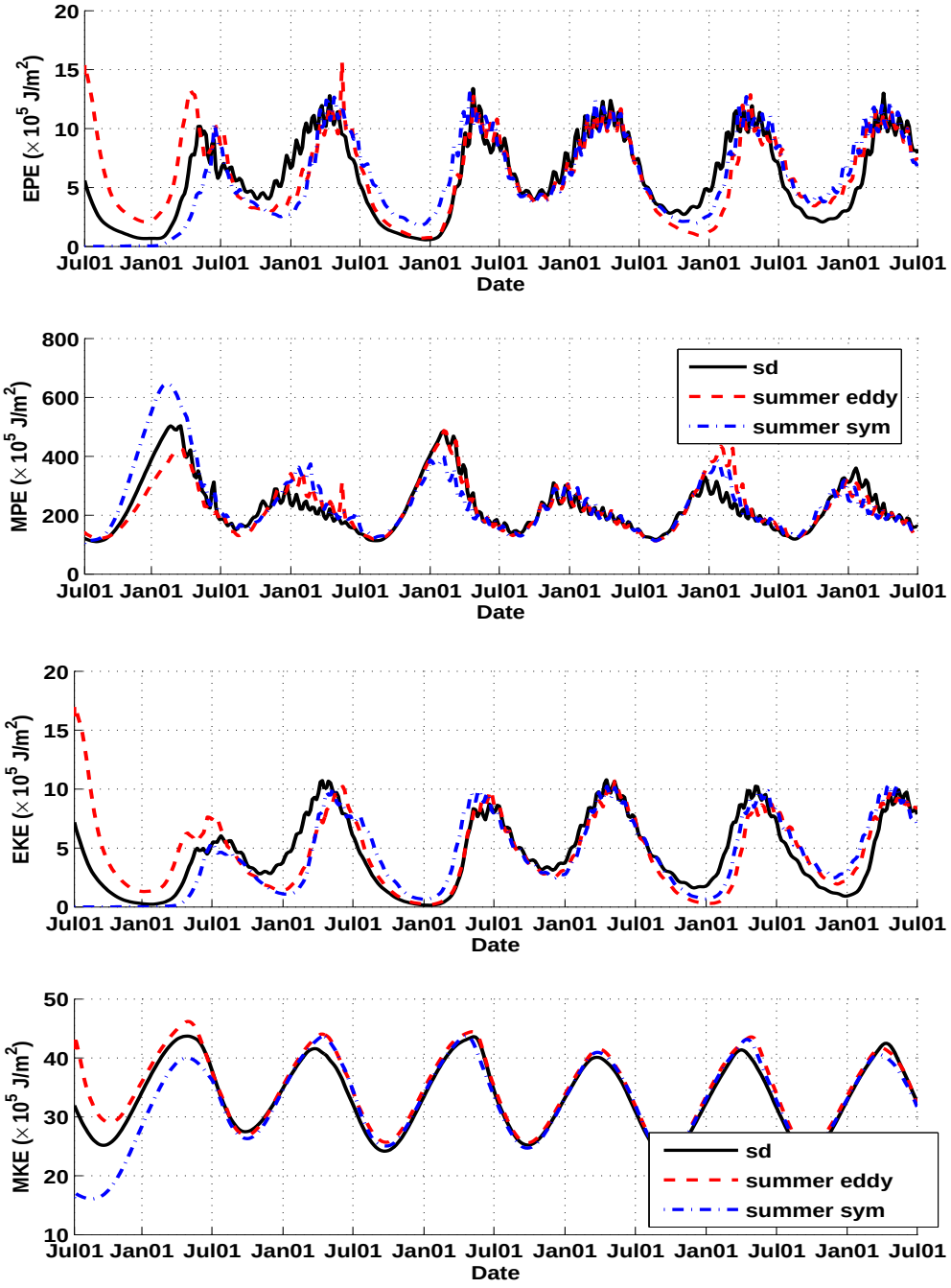

Figure 7-42: Time evolution of EPE, MPE, EKE, MKE in the first six forcing cycles when starting from different initial conditions but under the same seasonal forcing in which the forcing period is 1/5 year.

layer and the moist-adiabatic lapse rate distribution are all able to contribute to the observed PV structure. Baroclinic eddies are not the only possible candidate.

- The response of eddies to the seasonal forcing also depends on the time scale of the external forcing. All of the features we discussed above emerge only when the external forcing varies slowly. If we artificially reduce the time scale of the seasonal forcing, i.e. 5 times smaller than its realistic time scale, the zonal flow and eddy energies just vary proportionally with the fast varying external forcing. We can not find a period with robust isentropic structure.

- We also find that the equilibrium state MPE varies only slightly with the strength of the seasonal forcing. For example, when we double the winter time external forcing, the critical MPE only increases less than 20 %. A close investigate into the seasonal behavior of different waves implies that a nonlinear baroclinic adjustment (Cehelsky and Tung (1991), Welch and Tung (1998a)) seems to happen. However, further studies are still needed to investigate this nonlinear behavior.

As shown in our model results, the seasonal behavior of the eddy and the mean flow is characterized by four clearly divided time intervals. Especially after eddy spin-up, in the 'quasi-equilibrium' time interval for the mean flow, a baroclinic adjustment scenario is observed. How does this feature relate to the real atmosphere?

The seasonal variation of MPE is calculated using the NCEP/NCAR daily reanalysis data and displayed in Figure 7-43. One difficulty in comparing our model results with the observations is that MPE highly depends on the area (or the baroclinic zone) over which it is defined. As indicated in the definition of MPE in Eq.7.8, $MPE \sim \frac{c_p}{2}\sigma\langle\frac{d[T]}{dy}\rangle^2 L_{mpe}^2$, where L_{mpe} is the width of the baroclinic zone over which MPE is defined, $\langle\frac{d[T]}{dy}\rangle$ is the characteristic meridional temperature gradient in the baroclinic zone. Thus, here we estimate the MPE defined over four regions: the whole Northern Hemisphere, 90-30^o N where the eddy activity is confined, 65-25^o N where the transient eddies are most active and 70-40^o N where the stationary eddies are strongest (Peixoto and Oort, 1992).

Similar to our model results, in spite of the variation of the external forcing, the MPE defined in these area always stays at a relatively constant value in the winter. This tendency is more obvious when the MPE is calculated over the extratropical region. In Figs.7-43(b) and 7-43(d), similar to our model results, the peak of the MPE appears in the mid-fall, then the MPE also stays in a 'quasi-equilibrium' state with a smaller magnitude from the late fall to the mid-spring. However, comparison with the observation also brings out questions as to the role of the stationary eddies in midlatitude climate. In our model, we only apply a zonally symmetric external forcing, which neglects the longitudinal variation of the underlying surface (i.e.land-sea contrast) in the Northern Hemisphere, and all the eddies in our model are transient eddies. However, the stationary and transient eddies are also found highly correlated in the real atmosphere (Stone and Miller, 1980). Thus, to relate our model results to the observations, the relative roles of transient and stationary eddies in the eddy-mean flow interactions in the Northern Hemisphere need more studies.

One caveat in our model is that the eddy activity in the summer is so weak compared with observations (Peixoto and Oort, 1992). A plausible source for EPE that is omitted in our model is the release of latent heat, especially in the summer when the moisture effect is supposed to be more important. This indicates the limitations of dry simulations.

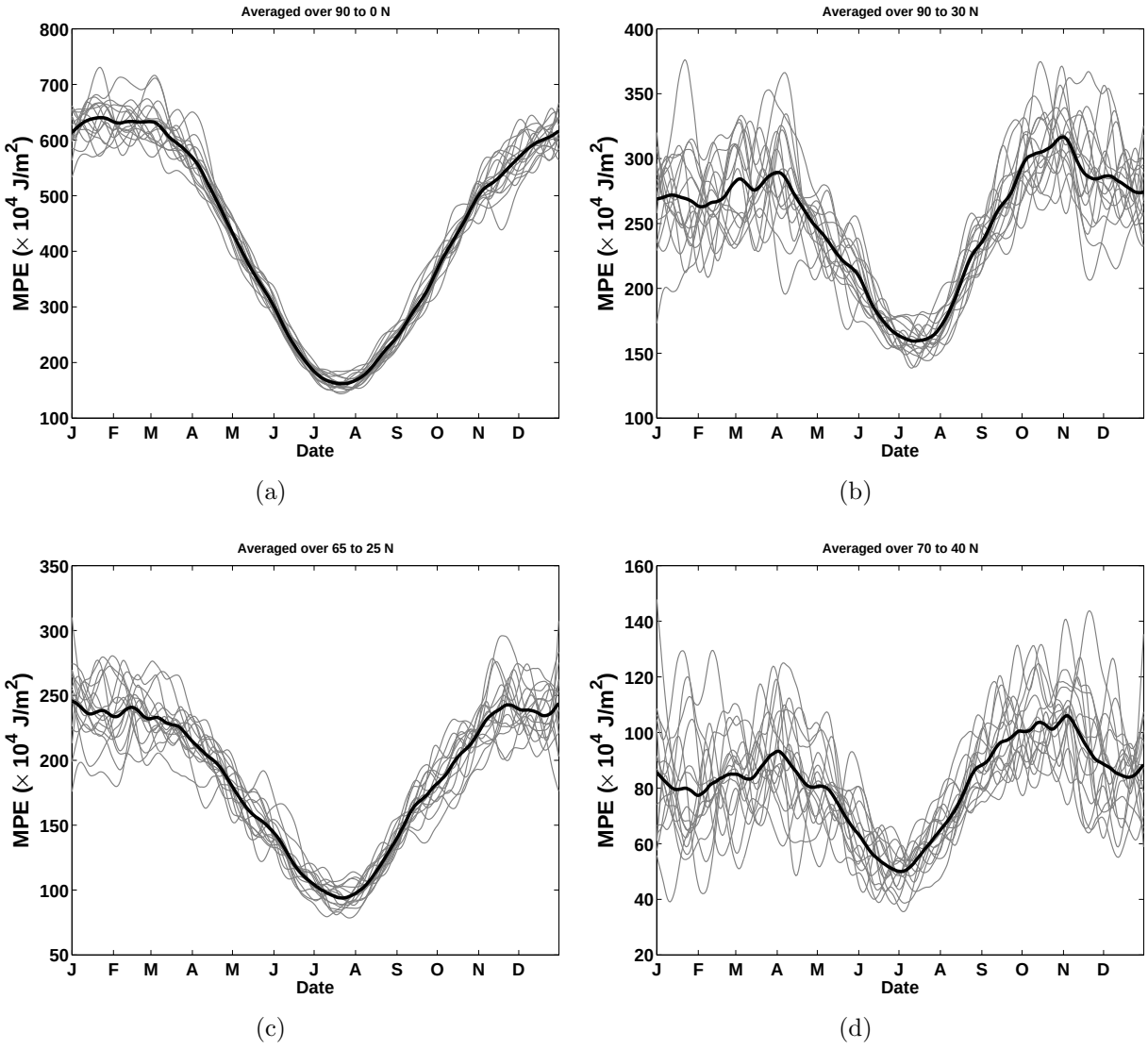

Figure 7-43: Seasonal variations of MPE averaged over the (a) Northern Hemisphere, (b) 90-30^o N, (c) 65-25^o N and (d) 70-40^o N using the NCEP/NCAR daily reanalysis data. Grey curves are the MPE seasonal behavior in each of the years between 1985-2000, black curves are the MPE averaged over these years.

Chapter 8

Seasonality in the coupled model

In the last chapter, we have investigated the eddy equilibration under specified seasonal forcing, in which the seasonal forcing is applied to the atmospheric flow from the specified seasonal variation of the surface temperature and the processes that can influence the seasonality of the underlying surface are neglected. The atmospheric flow only responds to the seasonal forcing passively. As discussed in Ch.4, this is a good approximation over a surface which has large heat capacity, but may not be an appropriate one over a surface with small heat capacity (i.e. land surface). In this chapter, the seasonality of the atmospheric and the surface flow will be further studied with the coupled model.

In Chs.5 and 6, we have investigated the eddy equilibration and the role of boundary layer processes in the equilibration with the coupled model. However, as shown in many observational and numerical studies (Meehl and Washington, 1985; Hsiung et al., 1989; Jayne and Marotzke, 2001; Kållberg et al., 2005), the seasonal behavior of the coupled system has different features from the equilibration states. First, the heat storage term becomes an important component in the surface energy budget. Second, the depth of the underlying surface can strongly affect the seasonal behavior of the atmospheric flow. Also, in the seasonal runs, the surface heat flux coefficient and the corresponding latent heat flux will greatly determines the seasonality of the underlying surface as well. In this study, we will try to answer the questions as to how the underlying surface responds to the seasonal forcing,

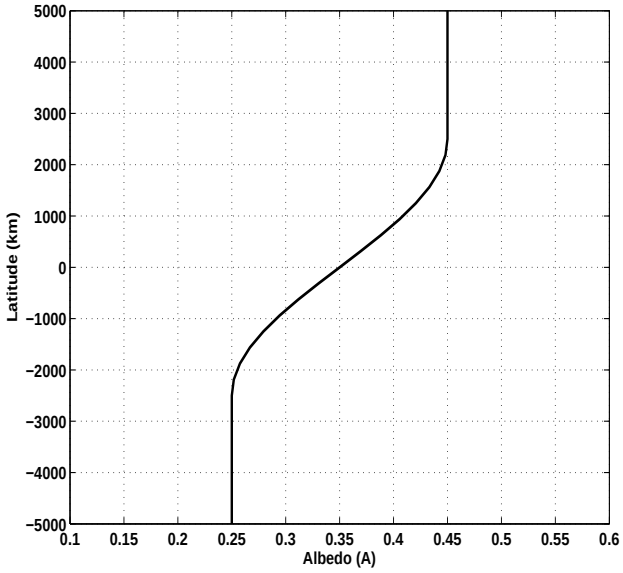

Figure 8-1: Latitudinal distribution of the albedo (A) used in the model.

and how this response depends on the surface layer depth.

8.1 Seasonal forcing

In this chapter, the seasonal forcing in the model is from the solar radiation into the surface. The incident solar radiation into the surface $F_{sw}^{\downarrow}$ is specified in the experiments. As mentioned in Ch. 2, the outgoing solar radiation is the part reflected by the surface $F_{sw}^{\uparrow} = AF_{sw}^{\downarrow}$, and the net solar radiation into the surface $SW = (1 - A)F_{sw}^{\downarrow}$. The albedo A has its meridional distribution, which, as observed by Peixoto and Oort (1992) and Campbell and Haar (1980), is set to vary from 0.25 in the low latitudes to 0.45 in the high latitudes in this model. The distribution of A is shown in Figure 8-1.

The incident solar radiation is given by

$$F_{sw}^{\downarrow} = S(d_m/d)^2 \cos Z, \tag{8.1}$$

where S is the solar constant, Z is the sun's zenith angle, d is the actual distance and d_m is the mean distance between the sun and the earth. Z is a function of latitude and time. As

shown in Peixoto and Oort (1992), from the zenith-pole-sun spherical triangle,

$$cosZ = \sin\phi \sin\upsilon + \cos\phi \cos\upsilon \cos t_h,$$

where ϕ is the latitude, υ is the solar declination, and t_h is the hour angle from the local meridian (where $t_h = 0$). Our model does not include any diurnal variation of the solar forcing. Only the daily variation of $\cos Z$ as well as $F_{sw}^{\downarrow}$ are considered. From Peixoto and Oort (1992), the daily averaged $\cos Z$,

$$\int_{sunrise}^{sunset} \cos Z dt = \frac{24}{\pi} \sin\phi \sin\sigma(t_H - \tan t_H), \tag{8.2}$$

where t_H is the hour angle at sunrise and sunset. From Eqs.8.1 and 8.2,

$$F_{sw}^{\downarrow} = \frac{24}{\pi} S(d_m/d)^2 \sin\phi \sin\upsilon(t_H - \tan t_H). \tag{8.3}$$

In our β plane model, the center of the channel is set to be 45^o N. In the central half of the channel, which is $-L/4 \leq y \leq L/4$, the corresponding latitude for y is estimated by $\phi = 45^o + \tan^{-1}(y/a)$, where a is the Earth radius. Away from the central half of the channel, solar radiation has no latitudinal variation. The seasonal and latitudinal variations of $F_{sw}^{\downarrow}$ and SW estimated from Eq.8.2 are shown in Figures 8-2(a) and 8-2(b). The meridional variation of the net solar radiation into the surface varies from 200 Wm^{-2} in the winter to less than 10 Wm^{-2} in the summer. Compared with the observations as in Peixoto and Oort (1992) and Stewart (2005), our solar radiation can well represent the solar radiation into the surface in midlatitudes.

8.2 Preliminary discussion

Before showing the numerical results, we consider the seasonal behavior of the coupled system for two extreme situations, a very deep surface layer and a very shallow surface layer. To discuss the seasonality of the coupled flow, we first decompose the surface temperature as

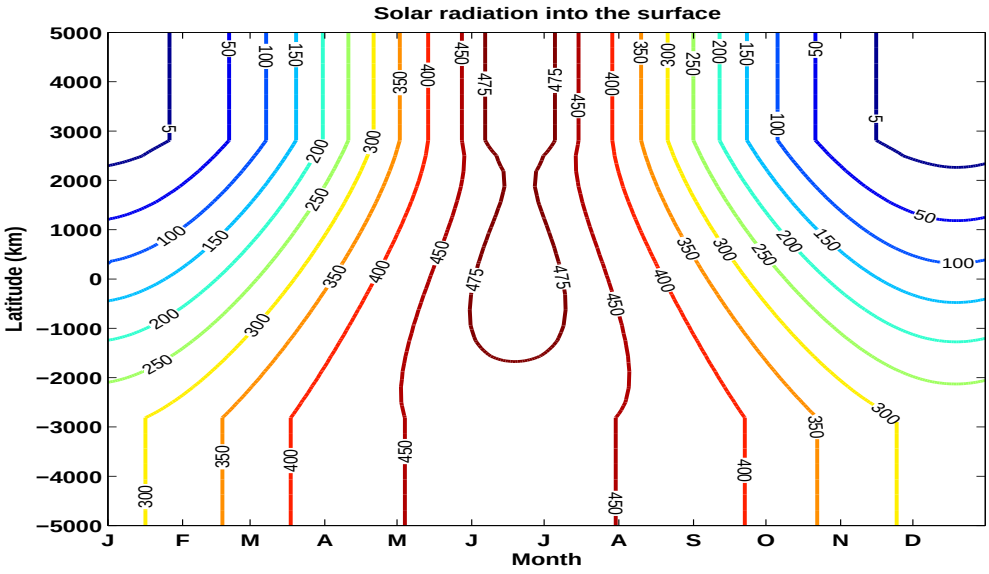

(a) $F_{sw}^{\downarrow}$

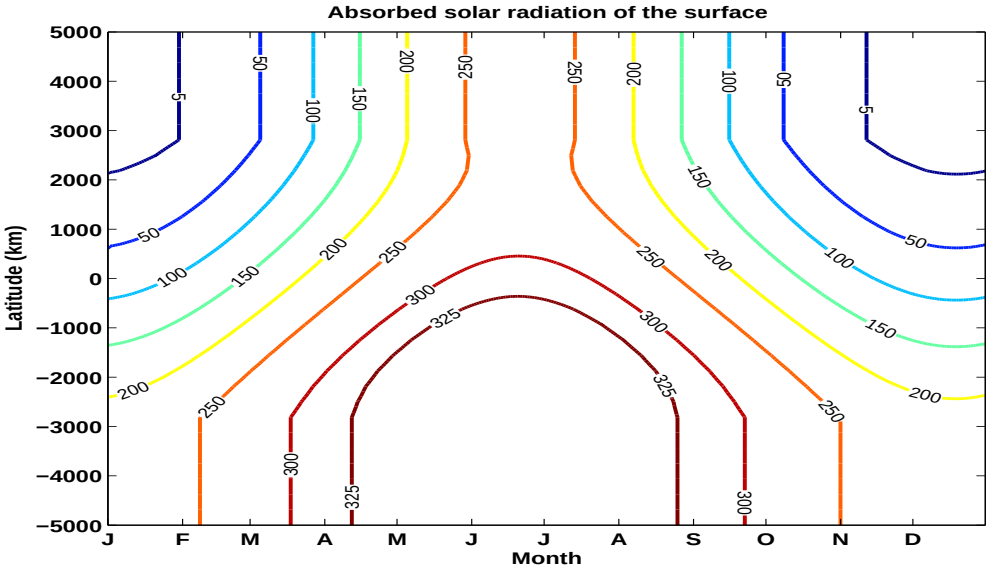

(b) $(1-A)F_{sw}^{\downarrow}$

Figure 8-2: Solar radiation into the surface $F_{sw}^{\downarrow}$(a) and the absorbed solar radiation of the surface $(1-A)F_{sw}^{\downarrow}$ (b) as a function of latitude and date. Unit: W/m^2

well as each energy flux term into the time mean and time variation terms:

$$T_g = \overline{T_g}^t + T_g{}'.$$

When our coupled model has periodic seasonal behavior and the low frequency variability (variation periods longer than the annual scale) is neglected, $\overline{T_g}^t$ represents the annual mean component and $T_g{}'$ indicates the seasonal variation. $T_g{}'$ can be further divided into two components, the horizontal average term $\overline{T_g{}'}^{xy}$ and the horizontal variation term $T_g{}'^{\dagger}$. If we decompose the solar heat flux SW in this way, as shown in Fig.8-3, we find that there is an annual mean of 175 W/m^2 meridional solar radiation difference exerted on the midlatitude surface. The solar radiation anomaly cools the surface and acts to increase the surface temperature gradient in the winter, and warms the surface as well as reduces the meridional surface temperature gradient in the summer. Then the surface energy budget in Eqs.2.13 and 2.14 can be rewritten as

$$0 = \overline{F_{rad}}^t + \overline{F_{sh}}^t + \overline{F_{lh}}^t + Q_{fx}, \tag{8.4}$$

$$\rho_g C_{pg} H_{sur} \frac{\partial T_g{}'}{\partial t} = F_{rad}{}' + F_{sh}{}' + F_{lh}{}'. \tag{8.5}$$

For the annual mean state or the equilibrium state as studied in Ch.6, the surface energy budget in Equation 8.4 is satisfied. The seasonality is predicted by Equation 8.5.

In the regime with extremely deep surface layer, that is $H_{sur} \to \infty$, due to the large effective heat capacity, the underlying surface hardly varies, that is $T_g{}' \to 0$. The seasonality from the solar radiation is mainly balanced by the heat storage term of the underlying surface, where $SW' \sim F_{rad}{}' \sim \rho_g C_{pg} H_{sur} \frac{\partial T_g{}'}{\partial t}$. Then the underlying surface temperature distribution would be close to the equilibration state under annual averaged solar radiation. In our coupled model, similar to Ch. 7, the atmospheric flow 'feels' the seasonal forcing from the underlying surface. In this case, the seasonal forcing is greatly damped by the underlying surface and the atmospheric flow would behave like the equilibration runs.

In the regime with extremely shallow surface layer, (i.e. the surface heat capacity is

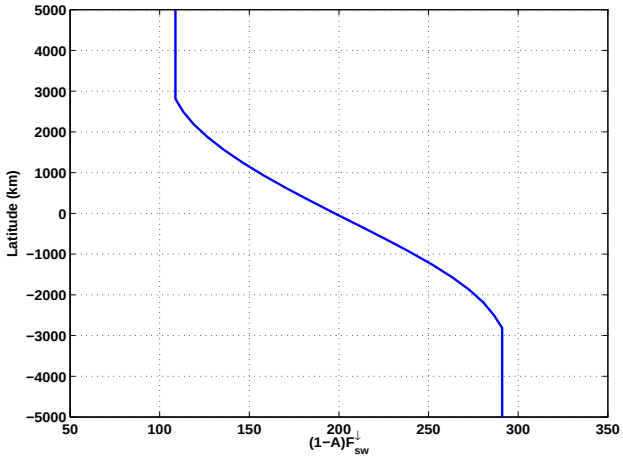

(a) $\overline{SW}^t$

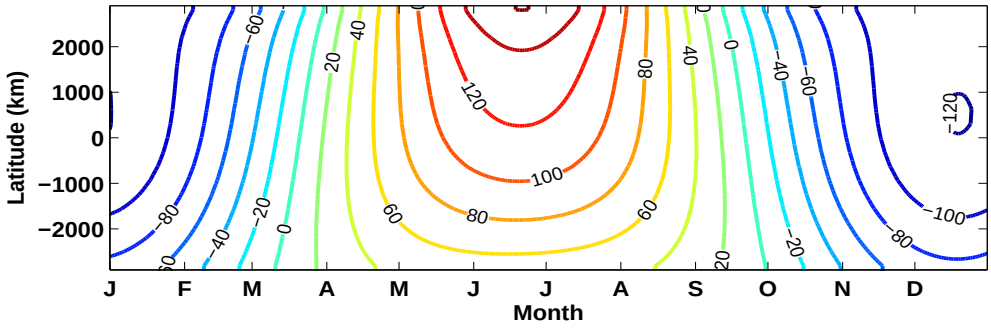

(b) SW'

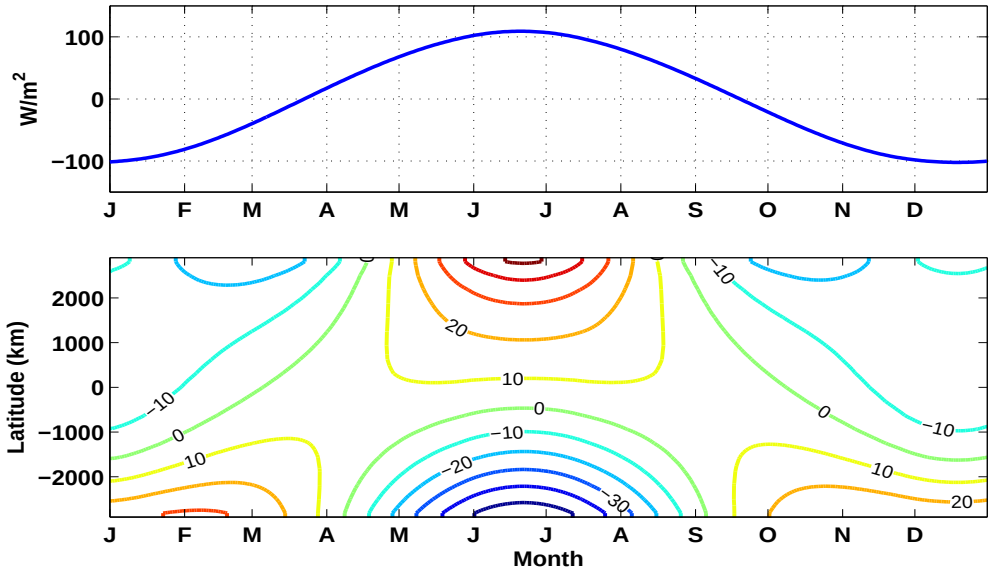

(c) $\overline{SW'}^{xy}$ and $SW'^{\dagger}$

Figure 8-3: Annual mean(a) and seasonal variation (b) of the net solar radiation SW into the surface, and (c) the two components $\overline{SW'}^{xy}$ and $SW'^{\dagger}$ of SW'. Contour interval is 20 W/m^2 in panel (b) and 10 W/m^2 in panel (c).

comparable with the atmosphere), the heat storage in the surface energy budget would be very weak and the coupled system can respond to the seasonal forcing very quickly, which would be close to the equilibrium response to the external forcing. In this case, we would expect strong seasonality of the coupled model. As shown in Ch.5 and 6, in the real ocean and also in the equilibrium runs with our coupled model, the meridional difference of the solar radiation is mainly balanced by the latent heat flux and the ocean heat transport. In this simulation, the ocean heat transport is fixed, i.e. its seasonal variation is not considered. Then when H_{sur} is extremely small, for an ocean surface, we would expect that over the channel the balance $d_y S\hat{W} \sim d_y LH$ (where $S\hat{W}$ is the the net effect of SW and Q-flux) to be hold for all seasons. As discussed in Ch.5, the latent heat flux is mainly determined by the surface temperature. From Eq.5.1,

$$\begin{aligned} d_y S\hat{W} &\sim d_y[C_{dt} L\rho_s (1-RH) q^*(T_g)] \\ &\sim C_{dt} L\rho_s (1-RH)\, d_y[q^*(T_g)], \end{aligned} \tag{8.6}$$

where $q^*(T)$ follows the Clausius-Clapeyron relationship. In this situation, given the seasonal variation of the solar radiation, the seasonal response of the underlying surface temperature, more accurately, the meridional distribution of the surface temperature, is primarily determined by the drag coefficient C_{dt}, and the total surface temperature. The stronger the drag coefficient is, the smaller the meridional variation of the surface temperature is that is required to balance the solar radiation. Since the specific humidity is more sensitive to the temperature in the warm regime, the meridional temperature contrast is also sensitive to the total surface temperature. In the warmer climate, less meridional temperature contrast is required; in the colder climate, stronger meridional surface temperature is needed to balance the meridional solar radiation contrast.

Over the land surface, however, the surface energy budget is different from the ocean surface. The sensible heat flux gets much stronger over the land surface and the latent heat flux is not as strong as that over the ocean surface. Thus the sensible heat flux has comparable contribution to the surface energy budget with the latent heat flux, and as

discussed in Ch. 5, the baroclinic eddy mixing of the surface air may have greater influence on the surface energy budget through the sensible heat flux. In addition, different from the ocean heat flux, which is primarily determined by the ocean dynamics (i.e. Meridional Overturning Circulation and Gyre circulation), the soil heat flux is primarily due to the soil heat conductivity.

In the real atmosphere, as discussed in Ch.7, the eddy activity in the Northern Hemisphere midlatitudes has strong seasonality, and the underlying surface has a complicated spatial and time distribution. Over the ocean surface, as shown in Figures 8-4(b) and 8-4(a), the ocean mixed layer has strong seasonal and meridional variations. For example, at 40-50^{o}N, as shown in Fig. 8-4(b), the ocean mixed layer depth varies from 120 m in the winter to 20 m in the summer. Over the land (i.e. Eurasia), the underlying surface has a smaller heat capacity, whose effective depth of penetration, as indicated by Peixoto and Oort (1992), is only a few meters and whose heat capacity $\rho_g C_{pg}$ can be as small as one fifth or sixth of the ocean's. Thus, the Northern Hemisphere lies between the two extreme regimes.

Facing the complicated underlying surface in the Northern Hemisphere, it is still an open question as to how the topography will influence the baroclinic eddies and the coupled system in midlatitudes. We know that due to the land-sea contrast, the baroclinic eddies in the Northern Hemisphere have a prominent stationary component compared with the Southern Hemisphere. The Northern Hemisphere has stronger seasonal variations than the Southern Hemisphere. However, observational studies suggest that it is the total eddy heat flux (sum of the transient and stationary eddy components) that is highly negatively correlated with the mean flow temperature gradient (Stone and Miller, 1980). The annual averaged eddy activity is also highly symmetric between the two hemispheres. All of these seem to suggest that the different topography in the two hemisphere, roughly speaking, mainly influence the partition of the eddy activity between its stationary and transient components. Many studies have been carried out in the literature using aquaplanet GCMs to investigate the midlatitude dynamics. In this study, for simplicity, we still use an ocean surface layer like in Ch.6 to study the seasonal variation of the coupled flow. The seasonal variation of the

surface layer depth is neglected in this study. Instead, in Section 8.4, we will test how the seasonal behavior of the coupled model depends on the depth of the surface layer, by which we hope we can have a better understanding of the flow seasonality when the surface effective heat capacity is between the two extremes discussed above.

In this chapter, the Q-flux is still the same as in Chs. 5 and 6. No seasonal variation of the Q-flux is considered. In the real ocean, as indicated in Jayne and Marotzke (2001), the seasonal variation is mainly confined to the tropics, where the majority of the variability is due to the wind-induced current fluctuations. The time varying surface wind and the Ekman transport have a large influence on the ocean heat transport there. However, in the extra-tropics, the seasonal variation of the ocean heat transport is much weaker, which indicates that the fixed Q-flux in our model is a reasonable approximation.

8.3 Standard seasonal run

As mentioned in the previous section, for simplicity, a uniform H_{sur} is assumed in the model. In this chapter, we set $H_{sur} = 75$ m as the default value, which is close to the annual averaged ocean mixed layer depth in midlatitudes. Due to the strong effective heat capacity, the standard run needs more time to equilibrate. Here we run our model for 30 years, and the annual behavior discussed in this section is the one averaged over the last ten years.

As shown in Figure 8-5, the surface temperature shows little seasonality in our standard seasonal run. The temperature gradient is slightly reduced around August, and slightly enhanced around February. Along with this, the global averaged temperature is around 3 degree warmer in the summer than the winter. Compared with the observed sea surface temperature, as shown in Figure 8-6, such seasonal variation is very similar to the observed seasonality of the surface temperature in the Southern Hemisphere, except that the surface temperature in the north end of the channel (which is corresponding to the polar region in the real atmosphere) is colder than observed SST in Fig. 8-6. In the Northern Hemisphere, due to the shallower ocean surface layer in the summer, the observed summer SST gradient is more reduced and the global averaged SST is warmer in the summer.

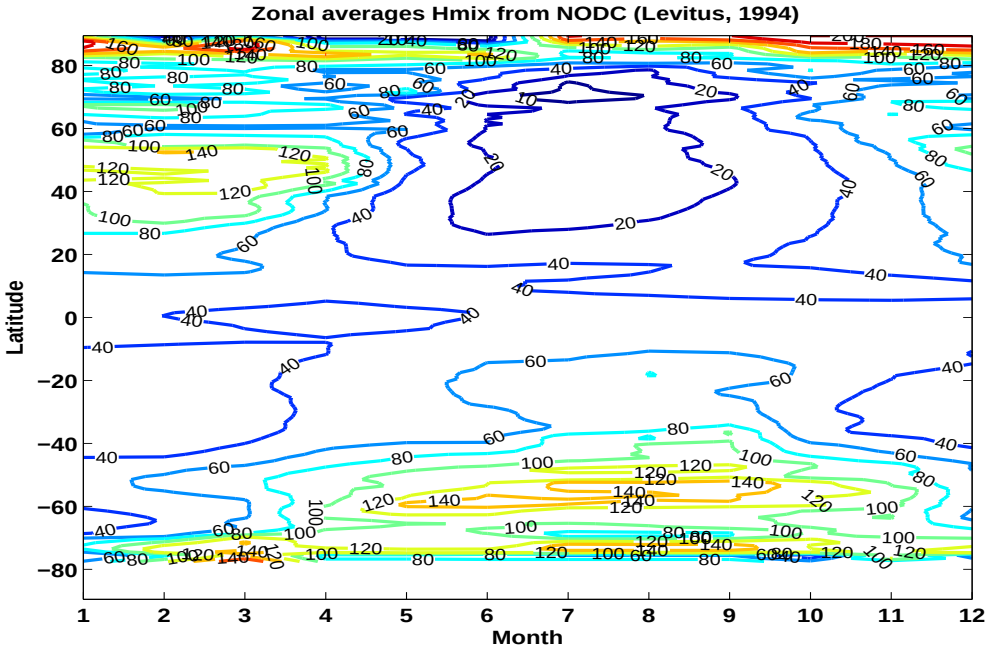

(a)

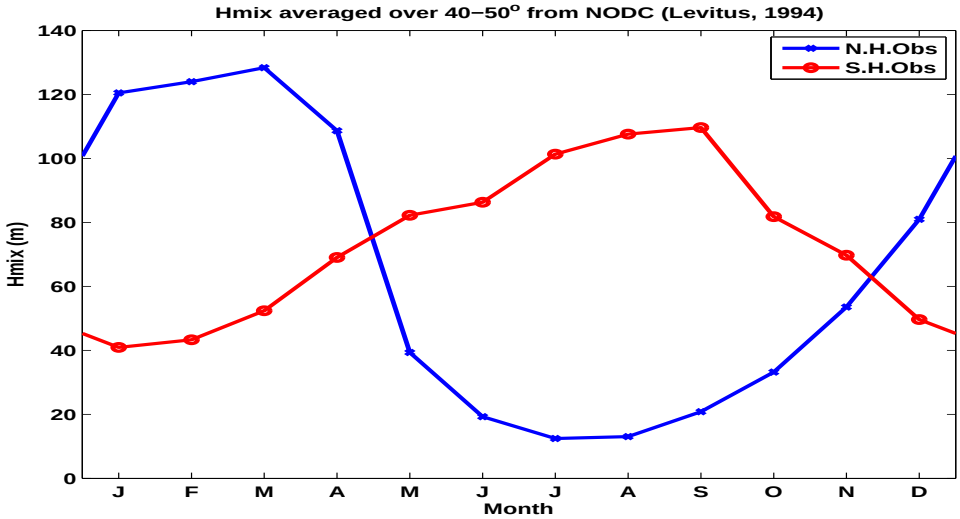

(b)

Figure 8-4: (a)Seasonal and latitudinal variations of the ocean mixed layer depth averaged zonally over the ocean area and (b) seasonal variation of the ocean mixed layer depth averaged zonally and latitudinally over the midlatitude (40-50^o) ocean area in the Northern and Southern Hemispheres using the National Oceanographic Data Center (NODC) data set (Levitus, 1994).

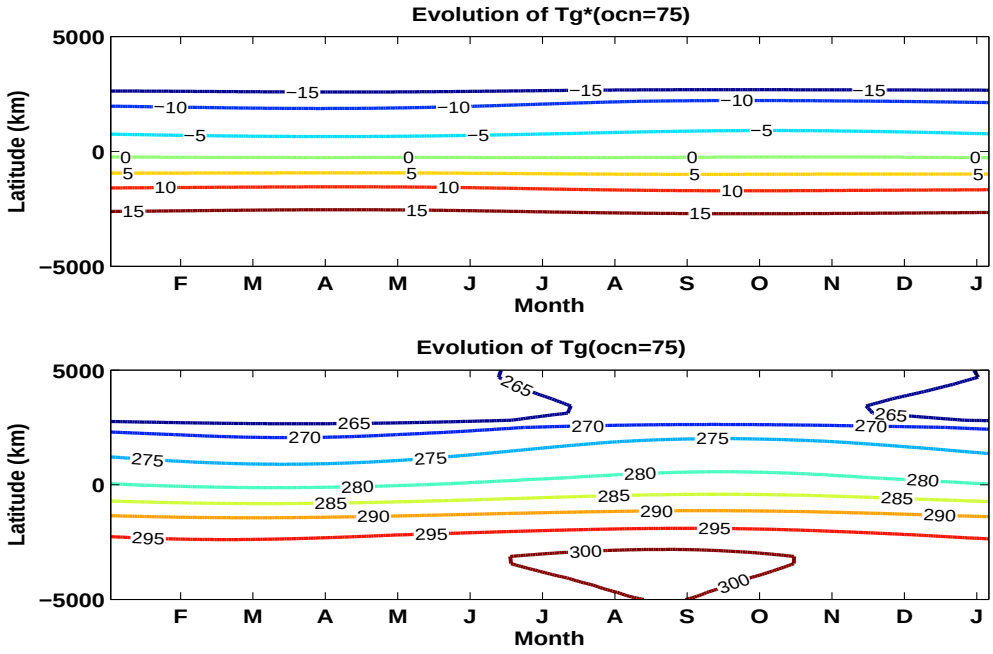

Figure 8-5: Seasonal and latitudinal variations of the (a) surface temperature anomalies $T_g^{\dagger}$(deviations from the horizontal mean) and (b) the total surface temperature T_g for H_{sur} = 75 m run.

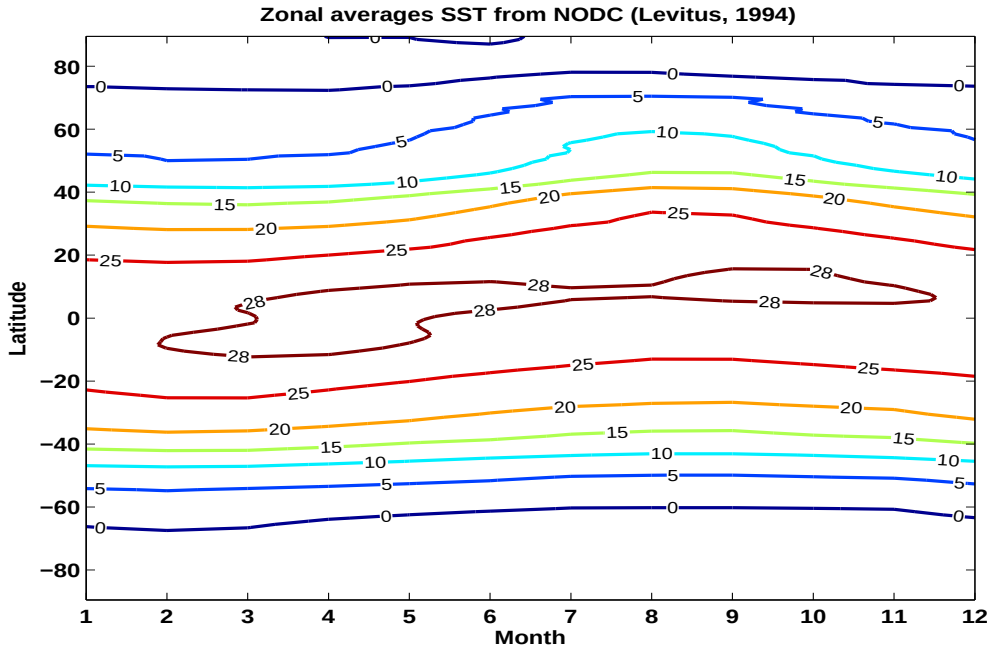

Figure 8-6: Seasonal and latitudinal variations of the ocean surface temperature (^{o}C) averaged zonally over the ocean area in the Northern and Southern Hemispheres using the National Oceanographic Data Center (NODC) data set (Levitus, 1994).

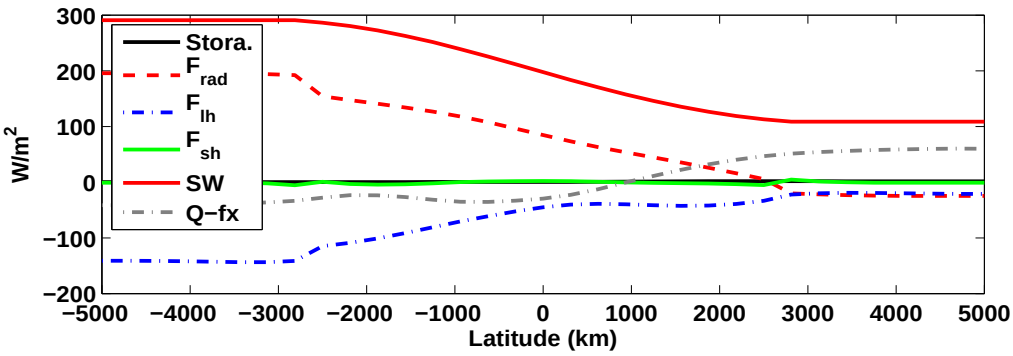

Figure 8-7: Meridional distribution of the annual mean heat storage $\rho_g C_{pg} H_{sur} \frac{\partial \overline{T_g}^t}{\partial t}$, net radiative flux $\overline{F_{rad}}^t$, latent heat flux $\overline{F_{lh}}^t$, sensible heat flux $\overline{F_{sh}}^t$ and net shortwave radiative flux $\overline{SW'}^t$ for $H_{sur} = 75$ m run.

Seasonal and latitudinal distributions of each surface energy term are plotted in Figures 8-7 to 8-11. Latitudinal distribution of each annual mean surface energy flux is plotted in Figure 8-7. Similar to the equilibrium runs in Ch.5 and the observations (Hsiung, 1986; da Silva et al., 1994; Trenberth and Caron, 2001; Stewart, 2005; Bordoni, 2007), the surface energy balance is primarily maintained by the net radiation flux and the latent heat flux. The sensible heat flux only plays a secondary role and is weaker than that in the standard equilibrium run in Ch.5, which is consistent with the fact that the temperature gradient and the eddy heat flux here is weaker than in Ch.5.

Seasonal variation of the horizontally averaged surface energy flux is shown in Figure 8-8, from which we find that, close to the situation with the extremely deep surface layer as discussed in Section 8.2, the latent and sensible heat fluxes have little seasonal variation. The heat storage term closely follows the seasonal variation of the radiation (solar radiation) flux, which acts to warm the underlying surface in the summer and cool the underlying surface in the winter.

More details of the seasonal and latitudinal variations of each surface energy term are also plotted in Figures 8-9, 8-10 and 8-11. Consistent with Fig. 8-8, among all the surface energy fluxes, the obvious seasonal variations lie in the surface radiation flux and the consequent heat storage term. The seasonal variation of the net radiative flux is primarily caused by

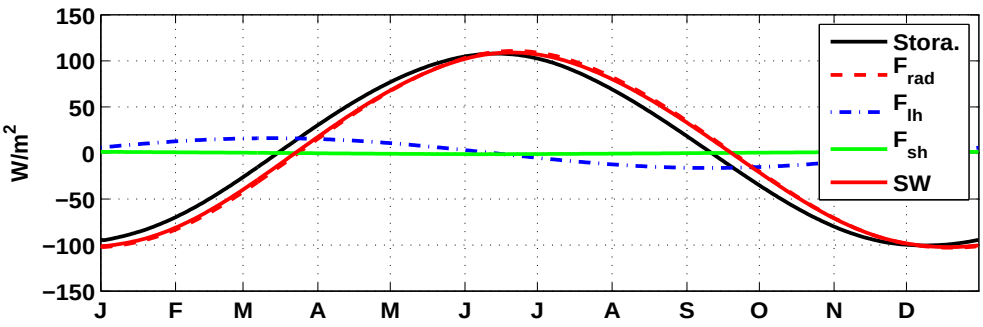

Figure 8-8: Seasonal variations of the horizontally averaged heat storage $\rho_g C_{pg} H_{sur} \frac{\partial \overline{T_g}^{xy}}{\partial t}$, net radiative flux $\overline{F_{rad}}^{xy}$, latent heat flux $\overline{F_{lh}}^{xy}$, sensible heat flux $\overline{F_{sh}}^{xy}$ and net shortwave radiative flux $\overline{SW}^{xy}$ for $H_{sur} = 75$ m run.

the solar radiative flux, and it is the dominant contribution to the heat storage term. Thus, when $H_{sur} = 75$m, $\rho_g C_{pg} H_{sur} \frac{\partial T_g'}{\partial t} \sim F_{rad}' \sim SW'$.

Although the latent heat flux is an important component in the annual mean surface energy budget, as shown in Figure 8-11(a), it has little seasonal variation. The sensible heat flux in Fig.8-11(b) has little seasonal variation as well, which is consistent with the fact that the surface temperature and the eddy activity have weak seasonal variations. From the seasonal variation of the surface energy flux, we find that with a realistic ocean mixed layer, the seasonality of the coupled system is greatly damped, which is close to the situation in the Southern Hemisphere in midlatitudes. The seasonal forcing from the solar radiation is mainly balanced by the heat storage term.

Consistent with the small seasonal variation of the surface temperature, the atmospheric flow also shows little seasonal variation. For example, the zonal mean meridional temperature gradient and the PV gradient (in Figure 8-12), and the zonal mean/eddy available potential energies (in Figure 8-13) only vary slightly through the whole year. The eddies are active in all the seasons.

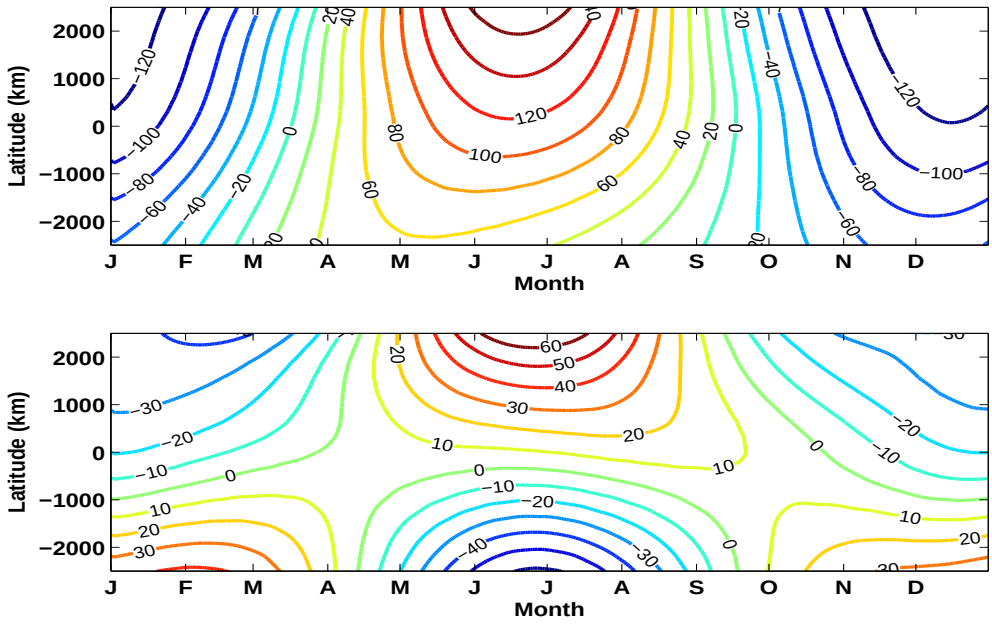

Figure 8-9: Seasonal and latitudinal variations of the surface heat storage $\rho_g C_{pg} H_{sur} \frac{\partial T'_g}{\partial t}$ (upper) and the surface heat storage anomaly $\rho_g C_{pg} H_{sur} \frac{\partial T'^{\dagger}_g}{\partial t}$ (lower) for $H_{sur} = 75$ m run. Contour interval is 20 W/m^2 in the upper panel and 10 W/m^2 in the lower panel.

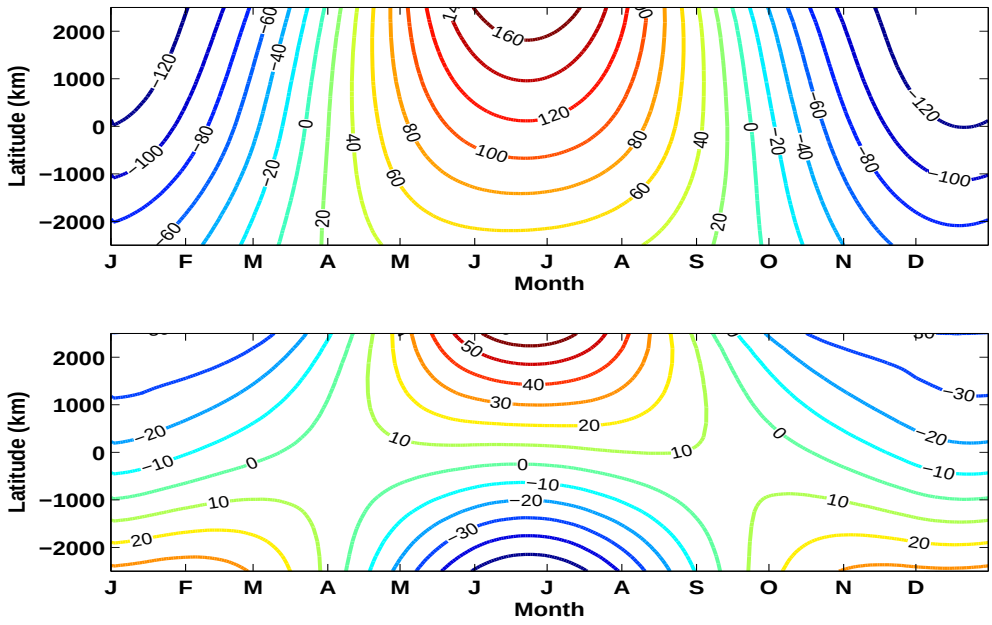

Figure 8-10: Same as in Fig.8-9 but for radiative flux F'_{rad} (upper) and the radiative flux anomaly $F'^{\dagger}_{rad}$ (lower). Contour interval is 20 W/m^2 in the upper panel and 10 W/m^2 in the lower panel.

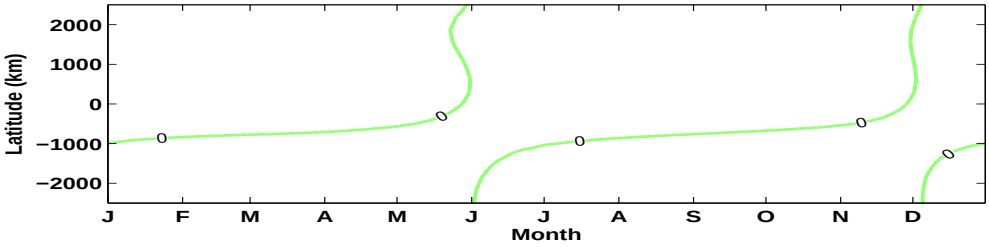

(a)

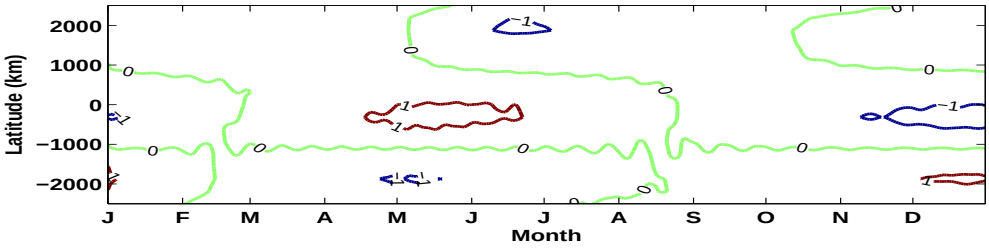

(b)

Figure 8-11: Seasonal and latitudinal variations of the (a) latent heat flux anomaly $F'^{\dagger}_{lh}$ and (b) the sensible heat flux anomaly $F'^{\dagger}_{sh}$ for $H_{sur} = 75$ m run. Contour interval is 10 W/m^2 in panel (a) and 1 W/m^2 in panel (b).

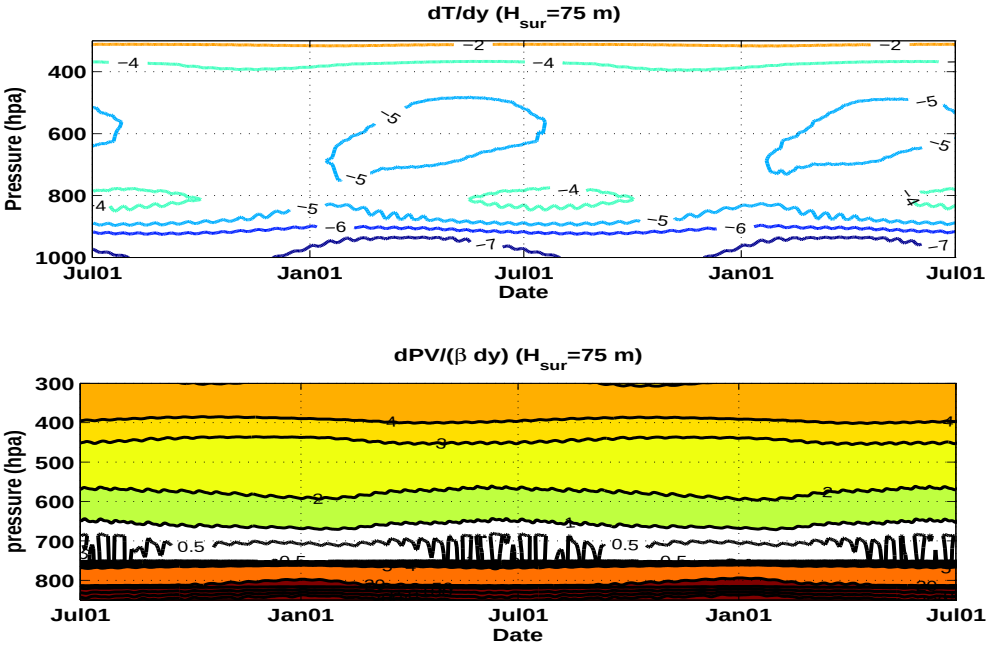

Figure 8-12: Time evolution of the zonal mean (a) meridional temperature gradient and (b) meridional PV gradient in the strongest baroclinic zone across the channel in two seasonal cycles in the $H_{sur} = 75$ m run. Contour interval is 1 $K/1000km$ in panel (a) and β in panel (b). White area in panel (b) indicates region where the PV gradient is smaller than β.

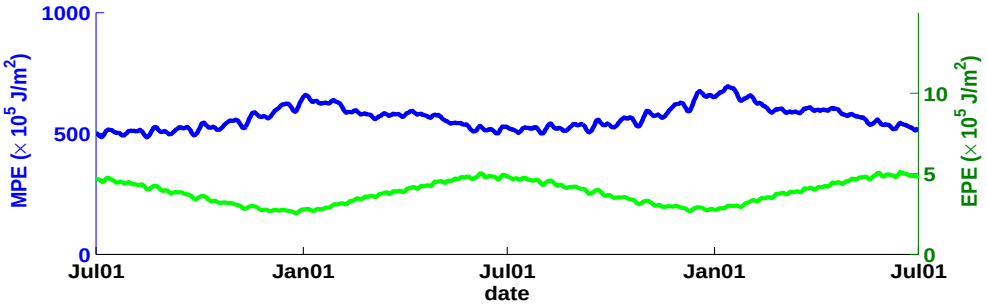

Figure 8-13: Time evolution of domain averaged MPE and EPE in two seasonal cycles in the $H_{sur} = 75$ m run.

8.4 Dependence on the H_{sur}

As shown in Section 8.3, a deep ocean mixed layer can strongly damp the seasonal forcing, and the atmosphere as well as the underlying surface have little seasonality, behaving as in the equilibrium state. In this section, we will investigate how the surface depth affects the seasonal behavior of the coupled system by repeating the standard seasonal run but with a shallower surface layer depth $H_{sur} = 20$ m and 5 m. The resulting seasonal variations of the surface temperature and energy flux are displayed in Figures 8-14 to 8-17 for $H_{sur} = 20$ m run, and in Figures 8-18 to 8-20 for $H_{sur} = 5$ m run .

When $H_{sur} = 20$ m, the surface temperature in Fig.8-14 exhibits stronger seasonal variation. The global averaged surface temperature varies from 278 K in February and March to more than 285 K in August and September. Along with this, the temperature gradient shows greater seasonal variation. The temperature difference across the channel varies from 35 K in March to 20 K in September.

The latitudinal variations of the annual mean surface energy fluxes, as displayed in Figure 8-15, do not show any obvious difference compared with the standard seasonal run in Fig.8-7. The latent heat flux is the dominant component that balances the net radiative flux, with similar magnitude to that in the $H_{sur} = 75$ m run. The seasonal variations of each horizontally averaged surface energy flux, as displayed in Figure 8-16, all show stronger seasonal variations compared with Fig.8-8. The most obvious difference lies in the latent heat flux. Consistent with the fact that the surface temperature is warmed more in the

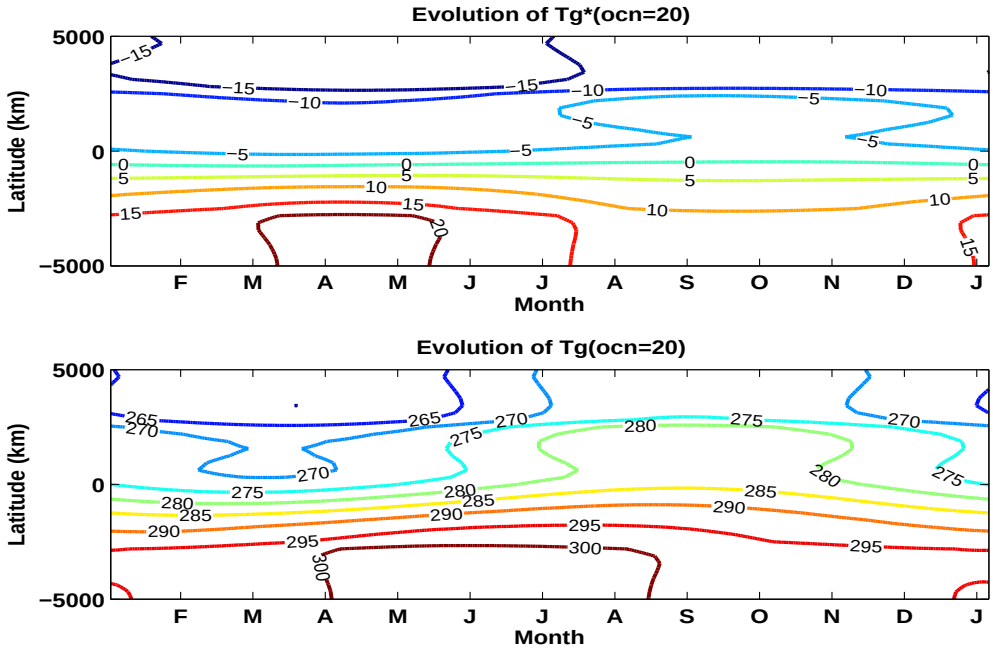

Figure 8-14: Same as Fig.8-5 but for $H_{sur} = 20$ m run.

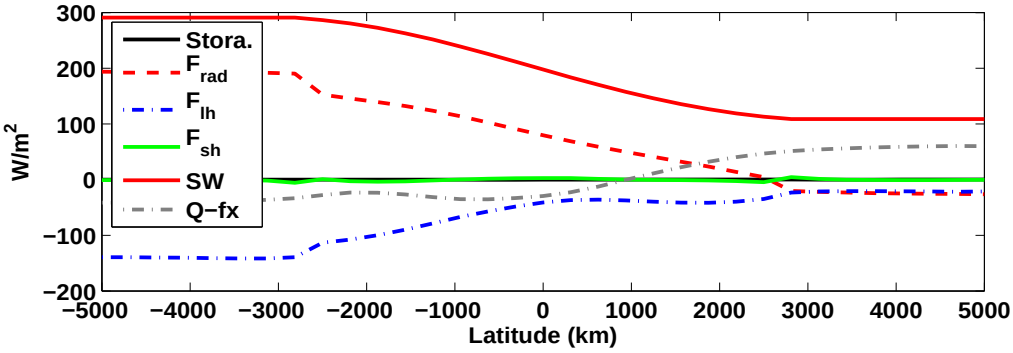

Figure 8-15: Same as Fig.8-7 but for $H_{sur} = 20$ m run.

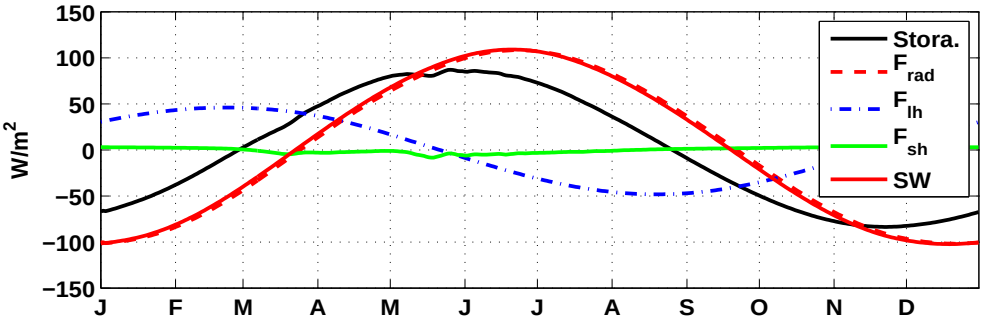

Figure 8-16: Same as Fig.8-8 but for $H_{sur} = 20$ m run.

summer and reduced more in the winter, the evaporation cooling has stronger seasonal variation as well, which acts to offset the seasonal variation of the radiative forcing with a time lag of around two months. As a result, the seasonal variation of the heat storage term is reduced compared with Fig.8-8.

The meridional and seasonal variations of each energy flux anomaly are also displayed in Figure 8-17. The radiative flux in Fig.8-17(b) is similar to the seasonal behavior in Fig.8-10. Although the latent heat flux offsets the meridional variation of the annual mean radiative flux (Fig.8-15) and the seasonal variation of the horizontally averaged radiative flux (Fig.8-16), the latent heat flux anomaly in Fig.8-17(c) shows that it acts to enhance the seasonal variation of the meridional surface temperature gradient. In the summer, due to the higher temperature and the greater sensitivity of the evaporation cooling to the temperature, the latent heat flux shows stronger meridional variation, which acts to reduce the temperature gradient. In the winter, the meridional variation of the latent heat flux is weaker, primarily due to its weaker sensitivity to the surface temperature as the temperature gets colder. The sensible hear flux still plays a minor role in the surface energy budget, as shown in Fig.8-17(d), but it also displays a clear seasonality, which has the strongest contribution in March and April, when the temperature gradient is greatest.

When $H_{sur} = 5$ m, the surface temperature in Fig.8-18 shows much stronger seasonal variation compared with Figs.8-5 and 8-14. The global averaged temperature varies from 275 K in February and March to 305 K in August and September. The meridional temperature difference across the channel varies from more than 45 K to less than 5 K.

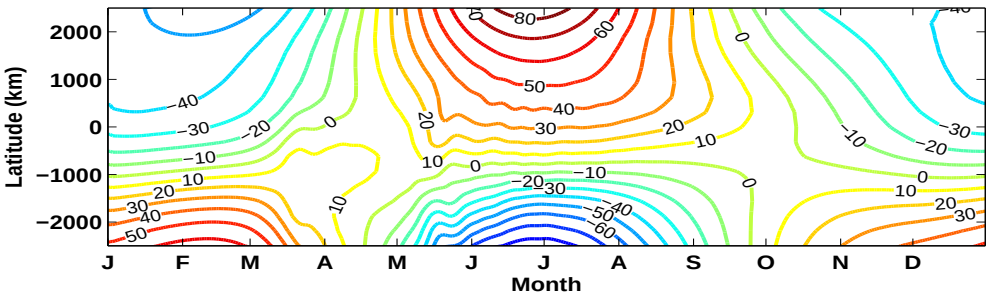

(a)

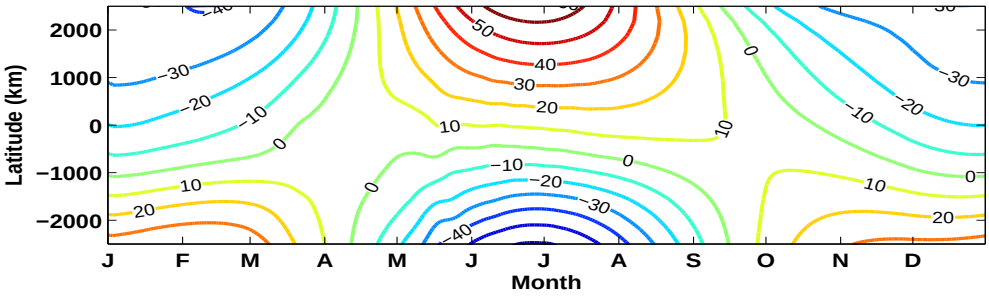

(b)

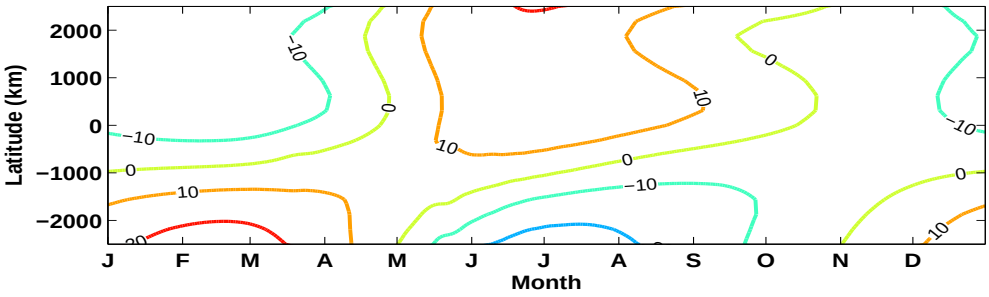

(c)

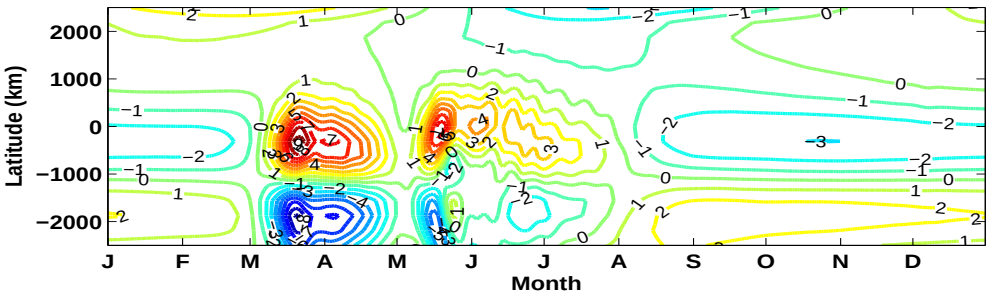

(d)

Figure 8-17: Seasonal and latitudinal variations of the (a) surface heat storage anomaly $\rho_g C_{pg} H_{sur} \frac{\partial T_g'^{\dagger}}{\partial t}$, (b) radiative flux anomaly $F_{rad}'^{\dagger}$, (c) latent heat flux anomaly $F_{lh}'^{\dagger}$ and (d) sensible heat flux anomaly $F_{sh}'^{\dagger}$ for $H_{sur} = 20$ m run. Contour interval is 10 W/m^2 in panel (a) (b) (c) and 1 W/m^2 in panel (d).

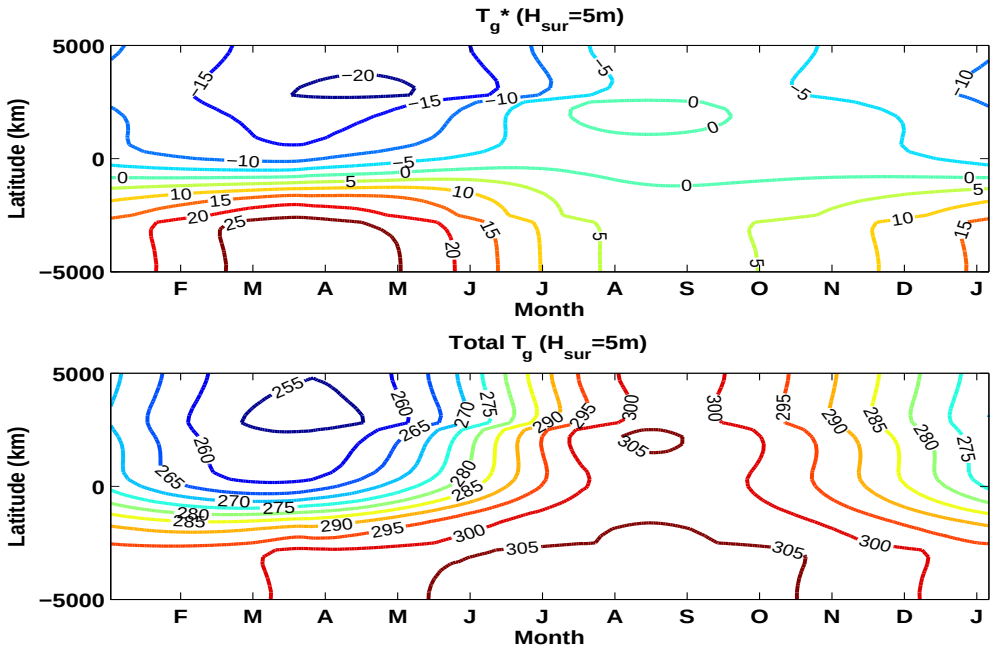

Figure 8-18: Same as Fig.8-5 but for $H_{sur} = 5$ m run.

The latitudinal distribution of the annual mean surface energy fluxes (results not shown here) still does not show any obvious variations compared with Figs.8-7 and 8-15. The seasonal behavior of surface energy fluxes, however, exhibit much stronger variations than $H_{sur} = 75$ and 20 m runs. The latent and sensible heat fluxes play more important roles in the seasonal variation of the surface energy budget. The horizontal averaged latent heat flux, as shown in Fig.8-19, acts to offset the seasonal variation of the radiative forcing more efficiently with a time lag of around one month. The lag time interval is shorter than the $H_{sur} = 20$ and 75 m runs, which indicates its dependence on the effective heat capacity of the underlying surface. The meridional variation of the latent heat flux anomaly in Fig.8-20(c) shows that it is more active in determining the seasonal cycle of the underlying surface by reducing the surface temperature gradient in the spring and helping restore the temperature gradient in the fall. The sensible heat flux, as shown in Fig.8-20(d), becomes an important component in the surface energy budget when $H_{sur} = 5$ m. Especially in March, when the baroclinic eddies in our model are strongest, the sensible heat flux becomes the dominant factor that reduces the surface temperature gradient.

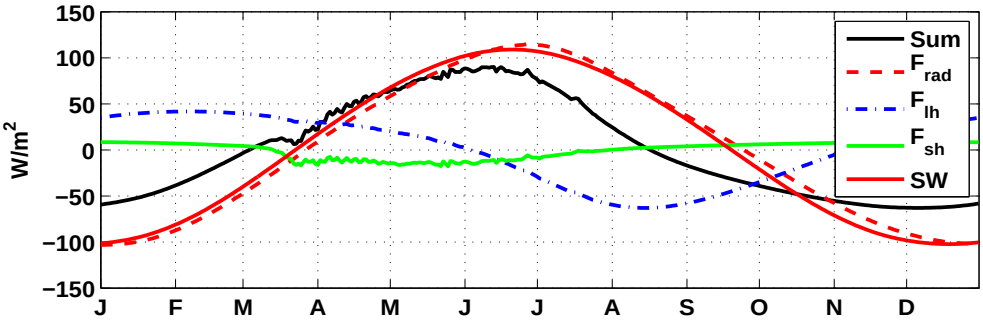

Figure 8-19: Same as Fig.8-8 but for $H_{sur} = 5$ m run.

As shown in Figures 8-21 and 8-23 (for $H_{sur} = 20$ and 5 m runs, respectively), the atmospheric flow, i.e. the zonal mean temperature gradient, is closer to the situation in the Northern Hemisphere in midlatitudes, and shows obvious seasonal variations. Along with the underlying surface, the atmospheric temperature gradient is weakest around late summer and early fall, and becomes strongest around February and March. Similar to the simulations in Ch.7, after the eddies spin up in late January, though the underlying surface temperature gradient varies, the atmospheric temperature gradient does not change a lot. The temperature gradient only begins to decrease in the late summer. The PV structure, in spite of the stronger seasonal variation of the underlying surface, also maintains a robust vertical structure through most of the seasons, with small PV gradient near the $600 - 800$ hpa. The eddy and the zonal mean available potential energies, as shown in Figures 8-22 and 8-24, though showing stronger seasonal variations with a shallower H_{sur}, like in Ch.7, they still vary with the similar seasonal pattern.

8.5 Discussion on the surface heat exchange

As discussed in Section 8.2, with a shallow surface layer, the seasonal behavior of the surface temperature will depend on the surface heat exchange as well. Though the sensitivity of the seasonal behavior to the surface heat exchange will not be investigated here, our simulations do provide insight into the effect of the surface heat exchange.

The seasonal simulations with the coupled model have shown that the latent heat flux

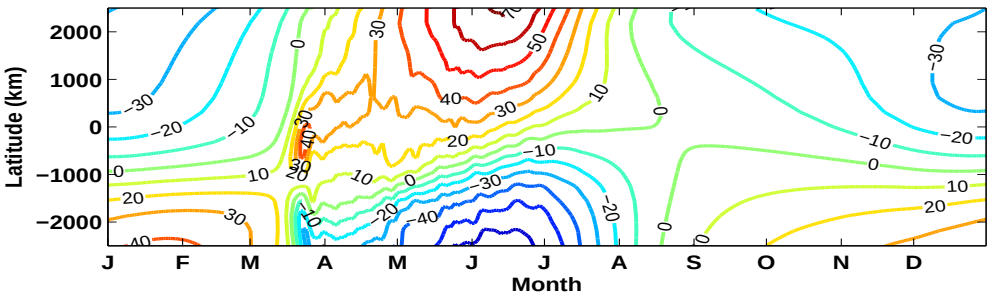

(a)

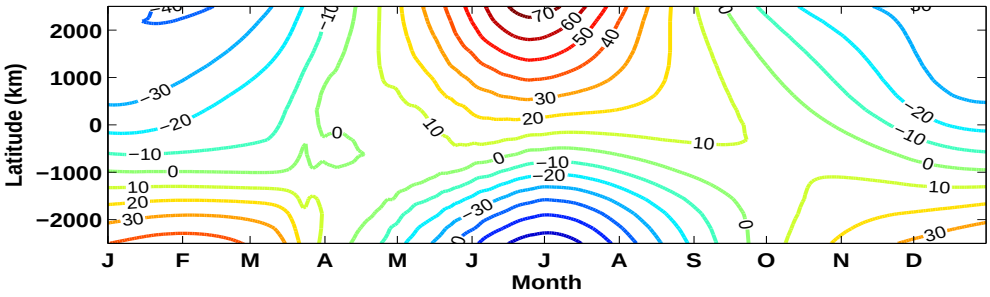

(b)

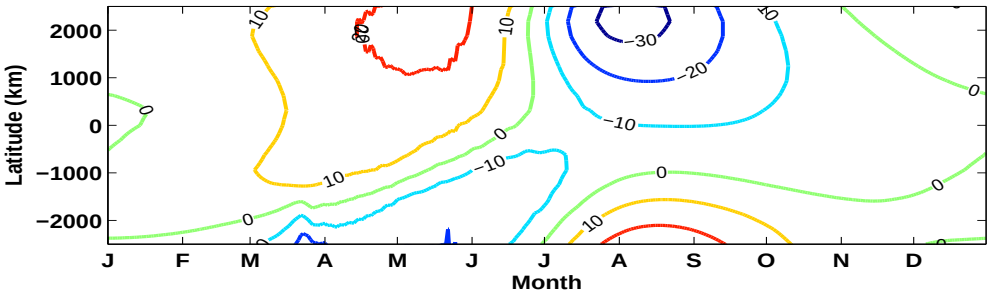

(c)

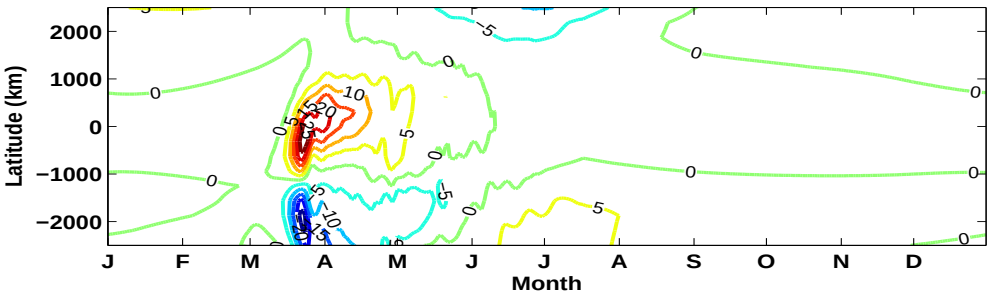

(d)

Figure 8-20: Seasonal and latitudinal variations of the (a) surface heat storage anomaly $\rho_g C_{pg} H_{sur} \frac{\partial T_g'^{\dagger}}{\partial t}$, (b) radiative flux anomaly $F_{rad}'^{\dagger}$, (c) latent heat flux anomaly $F_{lh}'^{\dagger}$ and (d) sensible heat flux anomaly $F_{sh}'^{\dagger}$ for $H_{sur} = 5$ m run. Contour interval is 10 W/m^2 in panel (a) (b) (c) and 5 W/m^2 in panel (d).

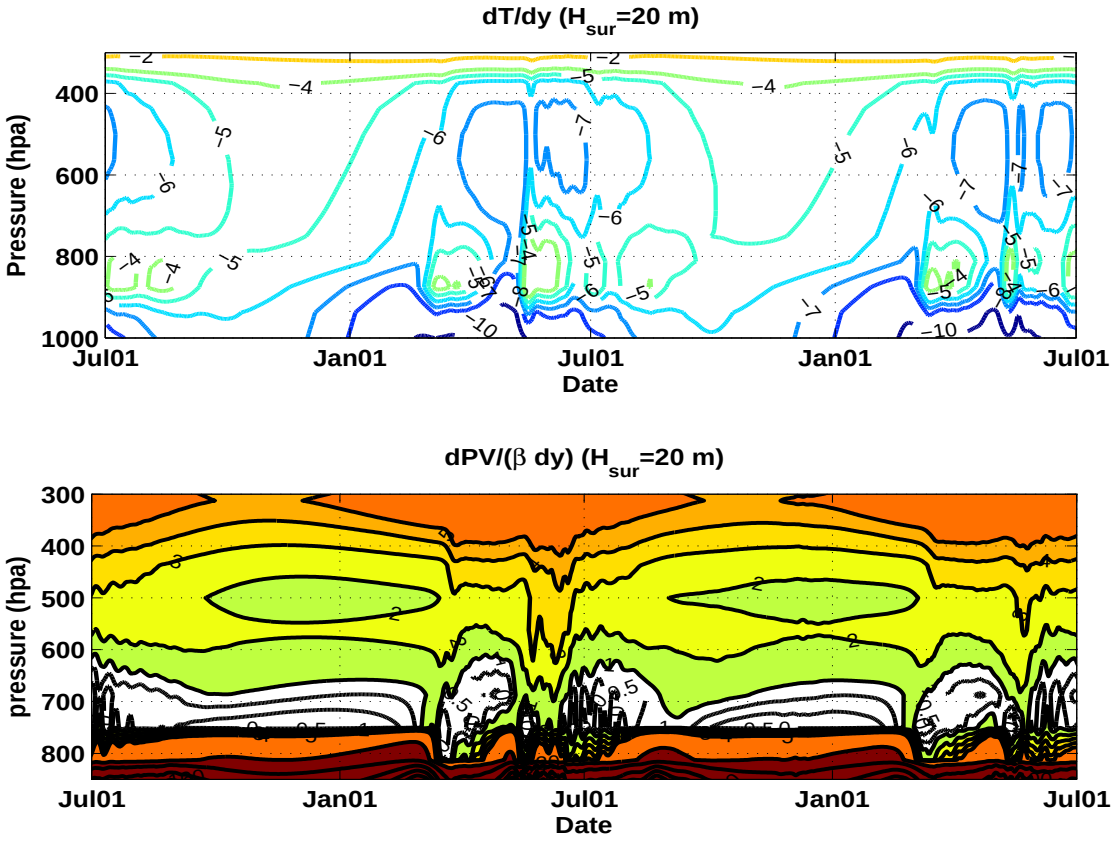

Figure 8-21: Same as Fig.8-12 but for the $H_{sur} = 20$ m run.

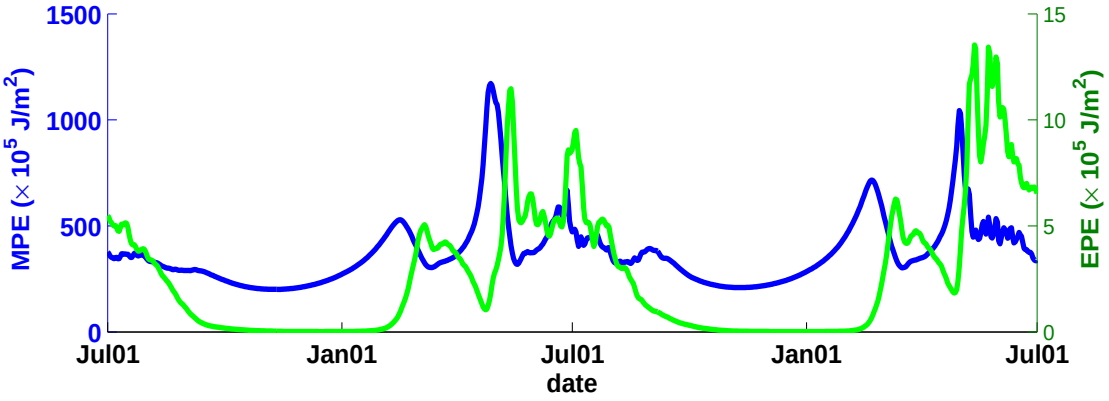

Figure 8-22: Same as Fig.8-13 but for the $H_{sur} = 20$ m run.

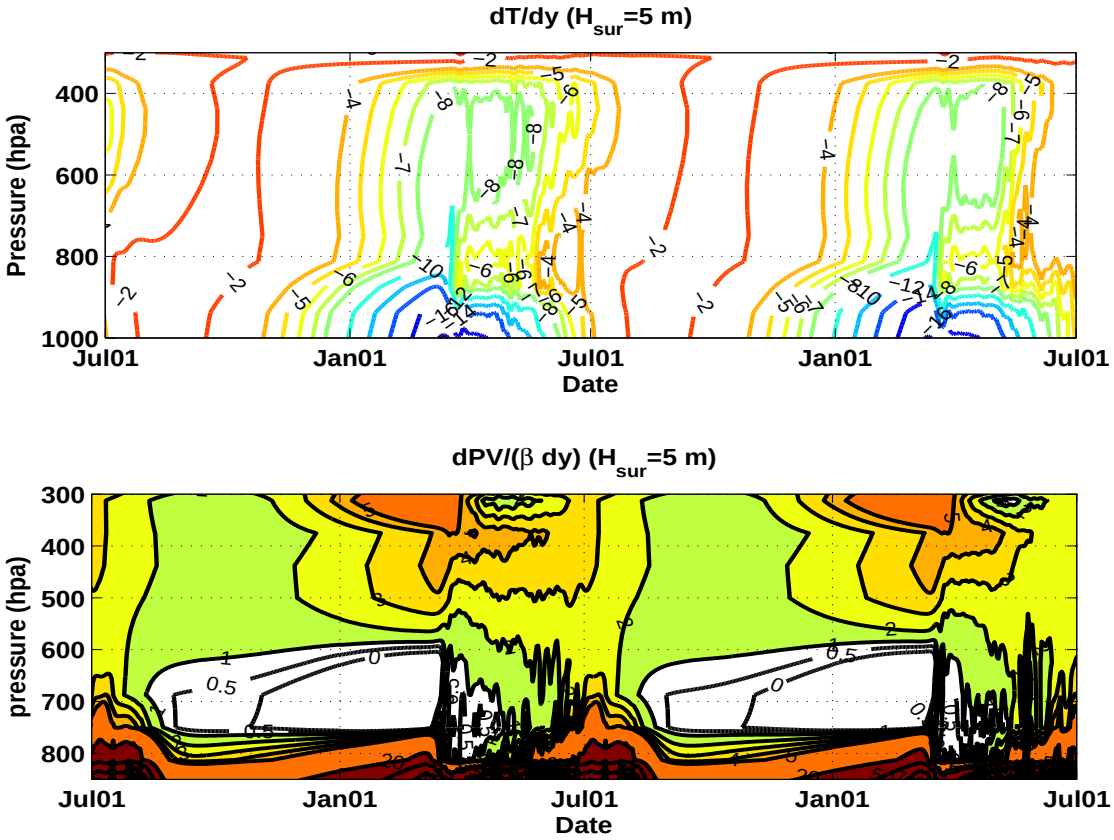

Figure 8-23: Same as Fig.8-12 but for the $H_{sur} = 5$ m run.

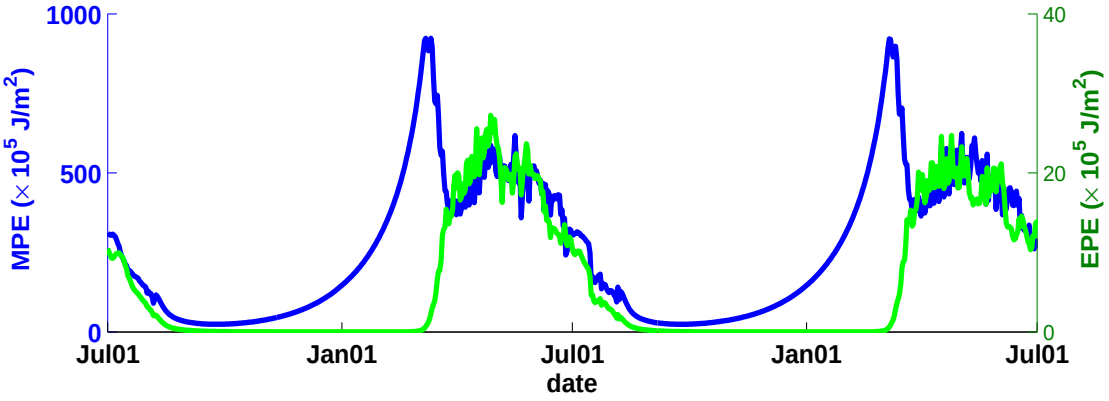

Figure 8-24: Same as Fig.8-13 but for the $H_{sur} = 5$ m run.

balances the meridional variation of the annual mean radiative flux and offsets the seasonal variation of the horizontally averaged solar radiation, but enhances the seasonal variation of the meridional temperature gradients. As shown in the equilibrium run experiments in Ch.6, under the same global averaged surface temperature, a stronger surface heat drag coefficient results in a stronger latent heat flux and weaker surface temperature gradient in the equilibrium state. In the seasonal runs, we expect this tendency still holds for the annual mean surface energy budget. For the seasonal variation of each horizontally averaged surface energy flux, we would expect the stronger the drag coefficient is, the more efficiently the latent heat flux offsets the radiative flux, which would result in weaker seasonal variation of the horizontally averaged surface temperature.

What is left uncertain is how the surface latent heat flux affects the seasonal variation of the meridional temperature gradient. In the regime with extremely shallow surface layer, as shown in Eq. 8.6 and discussed in Section 8.2, since the meridional variation of the solar radiation is mainly balanced by the latent heat flux, the meridional surface temperature gradient depends on the surface heat drag coefficient and the total temperature in each season. The drag coefficient, as discussed, influences the total temperature as well. How these two effects combined influence the seasonal variation of the temperature gradient needs further study.

8.6 Summary and discussion

In this chapter, the seasonal behavior of the atmospheric and the surface flow is studied with the air-surface coupled model. Different from the seasonal runs in Ch.7, the seasonality in our coupled model is caused by the seasonal variation of the solar radiation, which acts to warm the underlying surface and reduce the meridional surface temperature gradient in the summer, and to cool the surface temperature as well as enhance the meridional temperature gradient in the winter.

The seasonal behavior of the coupled system sensitively depends on the depth of the surface layer (effective heat capacity). With a realistic ocean mixed layer, where $H_{sur} = 75$

m, the seasonality of the coupled system is greatly damped, which is close to the situation in the Southern Hemisphere midlatitudes. The strong seasonality of the solar radiation is mainly apparent in the heat storage term, but due to the strong effective heat capacity, the surface temperature shows little seasonal variation. The atmospheric flow varies little through all the seasons as well.

With a shallower surface layer, the surface temperature and the atmospheric flow show stronger seasonality. The latent heat flux also begins to play an important role in the seasonal behavior of the underlying surface. The latent heat flux offsets the seasonal variation of the horizontally averaged surface temperature caused by the solar radiation. Its seasonal variation is out phase with the solar radiation, and the lag time depends on the surface effective heat capacity, being smaller for a shallower underlying surface. However, the latent heat flux helps to enhance the seasonal variation of the meridional temperature gradient. For example, in the spring and summer, the stronger meridional difference of the latent heat flux, along with the higher surface temperature, turns out to reduce the temperature gradient.

Though the surface and the atmospheric flow show stronger seasonality, as shown in Ch.7, a robust PV structure is still observed through the whole year. The small PV gradient in the lower troposphere can be maintained through all the year. The seasonal behavior of the atmospheric flow is similar to that in Ch.7 with the coupled model, which further confirms our previous conclusions in Ch.7.

As discussed in Section 8.2, though we test the dependence of the seasonal behavior on the effective heat capacity, our experiments still do not realistically simulate a land surface. More seasonal studies are needed with a better designed land surface model. In addition, compared with observed seasonal variation of SST meridional gradient as well as the eddy activity in midlatitudes, our slab ocean model always shows a longer lag with the solar radiation variation especially in the winter, even though we use a shallower surface layer. Further investigations are needed to understand what factors can contribute to this, e.g. the influence of the missing seasonal and spatial variations of the ocean mixed layer depth as shown in Fig.8-4(a), or the absence of the ocean dynamics in the slab ocean.

Chapter 9

Conclusions and discussions

In this thesis, we study the influence of boundary layer processes and seasonal forcing on baroclinic eddy equilibration, to understand how the baroclinic adjustment can be modified when taking into account these two factors.

Boundary layer processes

We start our study on the effect of boundary layer processes using the situation with fixed underlying surface temperature. In Chapter 4, by carrying out sensitivity studies, the role of each boundary layer process is investigated. We find that the boundary layer vertical thermal diffusion, along with the surface heat exchange, is primarily responsible for the limitation of the PV homogenization in the boundary layer. When turning off the boundary layer thermal diffusion, the PV gradient is nearly homogenized through almost the whole lower troposphere, which indicates that when the baroclinic eddies are the dominant dynamical process, a scenario predicted by baroclinic adjustment can be observed. When including the boundary layer thermal forcing as suggested by Swanson and Pierrehumbert (1997), only the PV gradient around 800 hpa, which is also the level around the critical level, can be homogenized. This is also the situation observed in the midlatitude atmosphere.

The boundary layer processes can influence the eddy activity in at least two competing ways. First, in the eddy energy budget, all the boundary layer processes act to damp the

eddy energy directly. On the other hand, the boundary layer processes also influence the mean flow, which can further influence the eddy behavior. For the boundary layer thermal damping, i.e. surface heat flux and the boundary layer vertical thermal diffusion, the indirect effect on the eddy activity becomes dominant. The boundary layer thermal damping always acts to reduce the lower layer stratification and maintain the mean flow baroclinicity. In the equilibrium state, a stronger boundary layer thermal damping results in stronger eddy heat fluxes, which is different from the result of baroclinic eddy life cycle studies (Gutowski et al., 1989) and indicates the difference between the transient and equilibrium response of the baroclinic eddies to the boundary layer forcing.

Reducing surface friction alone does not result in efficient elimination of the boundary layer PV gradient, which is different from the result of Zurita and Lindzen (2001) where only surface friction is included as the boundary layer processes in their simplified model. However, the equilibrium state thermal structure is still strongly influenced by surface friction and its response to changes in surface friction is not monotonic. Surface friction can strongly damp the eddy energies; it also reduces the zonal mean zonal wind barotropically. Surface friction, as suggested by Held (1999) and Thompson and Young (2007), also influences the length scale of the energy containing eddies and the subsequent phase speed of the energy containing eddies. As a result, varying surface friction also causes variation of the critical latitude and critical level of the dominant eddies, which is the location where eddy mixing is strongest. We find that when the surface friction is sufficiently weak, the critical level drops down below the surface and the critical latitude in the lower level moves away from the center of the jet, which causes the temperature gradient in the equilibrium state not to be efficiently reduced at the center of the jet but more efficiently reduced at the flank of the jet. In this case, the mean flow does not equilibrate at a state with homogenized PV gradient. Instead, with reduced surface friction, a stronger PV gradient as well as stronger baroclinicity are observed at the center of the channel. The mechanism of the non-monotonic response of the equilibrium state to the change in the surface friction in our study is different from the 'barotropic governor' described in James and Gray (1986) and James (1987). In our

sensitivity study, the eddy energies increase monotonically as the surface friction is reduced. The non-monotonic response is primarily due to the location change of the critical latitude as well as the eddy forcing on the mean flow.

We note that Robinson (2000, 2006) also suggested a baroclinic mechanism through which the location of the critical latitude can influence the eddy-mean flow interaction. Although his mechanism is proposed to interpret the low frequency annular-mode variation, we find that there is also similarity between his mechanism and the one we find in Ch.4. As Robinson suggested, when the baroclinic eddies are dissipated in the region where they are generated, there are negative feedback between eddy heat flux and the meridional temperature gradient. As in the experiments in Ch.4 where the surface friction is not too weak and the critical level is still around 800 hpa, the lower level temperature gradient at the central of the channel is strongly reduced. When the baroclinic eddies that are generated in lower levels propagate away and are absorbed outside the source region, Robinson suggested that the resulting EP flux convergence in the upper level can induce a secondary circulation, which acts to keep the lower level baroclinicity. Since the vertical structure is better resolved in our study than the two layer model used in Robinson (2006), we find that instead of requiring the strong upper level EP convergence, the strong lower level baroclinicity at the center of the jet is maintained just because the critical latitude in the lower level moves away from the center of the jet. Although our thesis work mainly focuses on the equilibrium state, whether the mechanism we find can have further application in interpreting the low frequency variation of the zonal flow could be another interesting topic.

The role of the boundary layer processes in the baroclinic eddy equilibration is further studied using a simple air-sea coupled model in Chapters 5 and 6. Compared with the fixed SST situation, in the coupled system, the boundary layer processes can influence the mean flow and the eddy activity in more and different ways. The surface heat flux, especially the latent heat flux acts to offset the meridional contrast of the solar radiation into the surface. In addition, as shown in the spin-up runs in Ch.5, baroclinic eddies, with strong mixing of the surface air temperature, can enhance the sensible heat exchange with the

surface, which acts to reduce the temperature gradient of the coupled system. Thus, surface thermal damping and surface friction can influence the surface energy budget indirectly by modifying the baroclinic eddy mixing near the surface. Changes in the underlying surface temperature can further affect the atmospheric flow through the boundary layer processes and the radiative-convective forcing.

The sensitivity study in Ch.6 shows that the direct effect of the surface heat exchange on the surface energy budget is dominant. Different from the tendency in Ch.4, a weaker equilibrium state temperature gradient is observed in both the underlying surface and the atmosphere under stronger surface heat exchange. Stronger surface heat exchange also results in weaker poleward eddy heat flux. One exception is the situation when turning off the surface sensible and latent heat exchange, so that the surface energy budget is maintained by the solar and longwave radiations. In this case, though the surface temperature can be 'felt' by the atmospheric flow through the radiative-convective forcing, compared with its slow response time scale (a 40 day damping time scale is set in our model), the eddy mixing becomes the dominant dynamical process and the surface air temperature is strongly reduced and not efficiently coupled with the underlying surface. In our simple air-sea coupled model, surface friction can only influence the surface energy budget indirectly; thus weaker surface friction allows strong baroclinic eddy mixing near the surface air, which results in weaker temperature gradient in the equilibrium state. In spite of the weaker zonal flow baroclinicity, the poleward eddy heat flux is still stronger under the weaker surface friction, which indicates the strong dependence of the eddy activity on the surface friction.

Although in the coupled model, each boundary layer process can influence the atmospheric flow thermal structure and the eddy behavior differently, their effect on the lower level PV homogenization is very robust. These processes all act to damp the lower level PV mixing and stronger boundary layer processes prevent the PV homogenization more strongly.

The response of the coupled system to the boundary layer forcing also indicates three clear time scales: a fast response time scale of the surface air to the boundary layer thermal damping, which is around one day; a synoptic time scale (less than 10 days) of the

atmospheric adjustment to the boundary layer forcing; and a much longer response time scale of the coupled system, which is dependent on the depth of the ocean mixed layer. In our experiment, with a shallow ocean mixed layer $H_{sur} = 5$ m, this time scale is around hundreds of days, which indicates that for the real ocean mixed layer in midlatitudes, in which $H_{sur} = 50 \sim 75$ m, this response time scale can be as long as thousands of days.

Combining our results from the atmospheric model and the air-sea thermally coupled model, we find that all the boundary layer processes tend to prevent the PV homogenization in the boundary layer, with the vertical thermal diffusion being most responsible for this. However, for the eddy heat flux and the mean flow thermal structure, the influence of different boundary layer processes and their influence in the coupled/ uncoupled models can be very different. This indicates the importance of the boundary layer processes especially the boundary layer thermal diffusion which is often neglected in the study of baroclinic eddy equilibration.

Seasonal forcing

Baroclinic eddy equilibration under seasonal forcing is studied in Chapters 7 and 8. We start our study from the situation with specified seasonal variation of the underlying surface temperature. In Ch.7, a Northern-Hemisphere like seasonal variation of the surface temperature is used to act on the atmospheric flow through the boundary layer processes and the radiative-convective heating, in which the seasonal forcing on the atmospheric stratification is also considered. Under the seasonal forcing, the eddy and the mean flow behaviors through the year can be clearly divided into four time intervals: an eddy inactive time interval during the summer; an eddy spinup time interval starting from mid-fall and lasting less than one month; a 'quasi-equilibrium' time interval for MPE from late fall to late spring; and an eddy spin-down time interval from late winter to late spring. During the 'quasi-equilibrium' time interval for MPE, in spite of the strong varying of the forcing, MPE always stays at a relatively constant value. This is consistent with the baroclinic adjustment theory, which suggests that when the baroclinic eddies are the dominant dynamical process, the mean flow

has a preferred equilibrium state. In this situation, as suggested in Stone (1978) , Stone and Miller (1980) and Lindzen and Farrell (1980), it is the eddy heat fluxes that are highly sensitive to the external forcing and act to maintain a relatively robust mean flow thermal structure. The eddy heat flux is highly correlated to the external forcing, and the eddy spin-down time scale is determined by the variation time scale of the external forcing.

The robustness of this mean flow and baroclinic eddy seasonal behavior is further investigated by 'artificially' varying the period of the external forcing. The separation into four distinct time intervals is very robust under a slowly varying seasonal like forcing. However, when the variation period of the external forcing is reduced from one year to 1/2 year, this feature becomes less obvious. When the forcing period is further reduced to 1/5 year, this feature totally disappears. A time series analysis shows that in all of these experiments, the eddy life time scale is always around 5 days, which is much shorter than the external forcing variation period $\sim$ 1/5 year. This confirms that the time scale of the baroclinic adjustment is longer than the eddy life cycle time scale. In this case, the time scale separation between the baroclinic adjustment and the external forcing is not obvious. The sensitivity of the eddy and the mean flow behavior to the strength of the external forcing is also investigated. We find that when the external forcing is strong enough, a robust mean flow available potential energy is always observed, and although the strength of the seasonal forcing changes, the equilibrium state MPE changes much less, which further indicates that a dynamic constraint exists.

Although the eddy activity has strong seasonal variation in our simulation, especially in the summer when baroclinic eddies are too weak to play any role, the zonal mean flow PV structure does not show large seasonal variation. We find that although baroclinic eddies are able to maintain a robust PV structure in spite of the time varying external forcing, it is not the only possible mechanism. The boundary layer thermal forcing and the moist convection also can help maintain the small PV gradient in the lower troposphere. We find that the moist-adiabatic state midlatitude atmosphere in our model is not far from the observed PV structure.

When comparing the seasonal behavior of the atmospheric flow in our process model with the midlatitude climate, we find that the eddy energy in the summer is much weaker than observations. A plausible source for EPE that is omitted in our model is the release of latent heat, especially in the summer when the moisture effect is more important. Stone and Salustri (1984) defined a generalized Eliassen-Palm flux by including the large-scale eddy forcing of condensation heating and showed that, in midlatitudes, including the condensation effect leads to much stronger eddy forcing, especially in summer. They further showed that, when the eddy forcing of the condensation effect is included, the strength of the residual stream-function can be three times stronger in winter and almost ten times stronger in summer. Previous studies indicate that moisture has competing effects on the midlatitude baroclinic eddies. It serves as a source of the eddy available potential energy (Emanuel et al., 1987); on the other hand, the increased moisture can increase the stratification (Frierson et al., 2006), which may weaken the eddy activity. Moist model simulations and observation studies (Oort and Peixoto, 1983) indicate that the former effect may dominate the latter one. In our simulation with the dry model, only the effect of the moisture on the horizontal averaged stratification is included, which acts to suppress the eddy activity by stabilizing the lower level flow. The radiative-convective forcing in our model through the Newtonian cooling acts to damp the eddy activity in the eddy energy cycle, which may be opposite to the net effect of the moisture on the baroclinic eddies and result in very weak eddy activity in the summer. This is also a limitation for all the dry models.

Baroclinic eddy equilibration under seasonal forcing is further studied in the coupled model, in which instead of the surface temperature, the seasonal variation of the solar radiation into the surface is considered. The seasonal behavior of the coupled system strongly depends on the effective heat capacity of the underlying surface. With a realistic ocean mixed layer where $H_{sur} = 75$ m, the seasonality of the atmospheric flow is largely damped, which is similar to the situation in the Southern Hemisphere midlatitudes. The seasonal variation of the solar radiation is primarily compensated by the heat storage term. In this situation, the mean flow and eddy activity has little seasonal variation. The seasonality gets

stronger as the surface effective heat capacity is reduced. When $H_{sur} = 20$ and 5 m, clear seasonal variations of the surface temperature and the atmospheric flow are observed. The seasonality of the solar radiation is balanced by both the heat storage term and the seasonal variation of the latent heat flux. The seasonal variations of the baroclinic eddies and the mean flow thermal structure are similar to the situation in Ch.7.

Our simulation in Ch.8 did not investigate the limit where the effective heat capacity of the underlying surface is extremely small, though this can be the situation relevant to flow over a land surface. The different surface energy budget and the different physical processes that affect the atmospheric flow over a land surface indicate that our coupled model may not be appropriate to simulate the situation over land. Future studies with a more appropriate coupled model are needed to investigate the eddy seasonal behavior over a land surface.

General conclusions

To summarize this thesis study, we go back to the questions brought out at the beginning of the thesis: to what extent can the baroclinic adjustment be applied to interpret the midlatitude climate? More specifically how can the boundary layer processes and seasonal forcing modify the baroclinic adjustment?

Our thesis work confirms that *when the baroclinic eddies are the most dominant process* (i.e. the radiative-convective heating is a slow process compared with baroclinic eddies, and the boundary layer processes especially the boundary layer vertical thermal diffusion are neglected), *when the baroclinic eddies are saturated and active enough* (i.e. in the winter time) and *under a slowly varying external forcing* (i.e. the forcing period is one year and longer), an equilibrium state suggested by baroclinic adjustment does appear and is robust in our experiments. For example, a preferred equilibrium state characterized by robust isentropic slope (as shown in Chapter 3) and well homogenized PV in the lower troposphere is observed in spite of the variation of the external forcing, and it is the eddy activity that responds sensitively to the external forcing as suggested by baroclinic adjustment. When including the boundary layer processes, the thermal structure of the mean flow in the boundary layer

as well as the eddy activity strongly depends on the boundary layer processes. In the free troposphere, the mean flow in the equilibrium state still exhibits robustness under different external forcings. This indicates that we can still expect the baroclinic adjustment to work above the boundary layer (consistent with Stone and Nemet (1996)).

On the other hand, our results also question the baroclinic adjustment in some aspects. First, in spite of the robust PV structure through all the seasons, our results indicate that baroclinic adjustment may be not the only interpretation, especially in the summer when the eddies are weak. In addition, our seasonal study suggests that the time scales of seasonal forcing and the baroclinic adjustment are just marginally separated. The time scale of baroclinic adjustment is much longer than a single eddy life cycle. Thus, when taking into account other physical processes, i.e. including the time scale of moist convection explicitly, the assumption of baroclinic adjustment could meet more challenges.

Bibliography

Barry, L., G. Craig, and J. Thuburn, 2000: A GCM investigation into the nature of baroclinic adjustment. *J. Atmos. Sci.*, **57**, 1141–1155.

Bony, S. and K. Emanuel, 2001: A parameterization of the cloudiness associated with cumulus convection; evaluation using TOGA COARE data. *J. Atmos. Sci.*, **58**, 21.

Bordoni, S., 2007: *On the role of eddies in monsoonal circulations: observations and theory*. Ph.D. thesis, University of California, Los Angeles.

Boyd, J., 1983: The continuous spectrum of linear Couette flow with the beta effect. *J. Atmos. Sci.*, **40**, 2304–2308.

Branscome, L., 1983: A parameterization of transient eddy heat flux on a beta-plane. *J. Atmos. Sci.*, **40**, 2508–2521.

Branscome, L. E., W. J. Gutowski, and D. Stewart, 1989: Effect of surface fluxes on the nonlinear development of baroclinic waves. *J. Atmos. Sci.*, **46**, 460–475.

Bretherton, F., 1966: Critical layer instability in baroclinic flows. *Quart. J. Roy. Meteor. Soc.*, **92**, 325–334.

Campbell, G. and T. Haar, 1980: *Climatology of Radiation Budget Measurements from Satellites*. Dept. of Atmospheric Science, Colorado State University.

Card, P. A. and A. Barcilon, 1982: The charney stability problem with a lower ekman layer. *J. Atmos. Sci.*, **39**, 2128–2137.

Cehelsky, P. and K. Tung, 1991: Nonlinear baroclinic adjustment. *J. Atmos. Sci.*, **48**, 1930–1947.

Charney, J., 1947: The dynamics of long waves in a baroclinic westerly current. *J. Atmos. Sci.*, **4**, 136–162.

Charney, J. and M. Stern, 1962: On the stability of internal baroclinic jets in a rotating atmosphere. *J. Atmos. Sci.*, **19**, 159–172.

Chen, G., I. Held, and W. Robinson, 2007: Sensitivity of the latitude of the surface westerlies to surface friction. *J. Atmos. Sci.*, **64**, 2899–2915.

da Silva, A., C. Young, and S. Levitus, 1994: Atlas of Surface Marine Data 1994 Volume 1: Algorithms and Procedures, NOAA Atlas NESDIS 6, US Dept. *Commerce, Washington DC, 83pp*.

Darnell, W., W. Staylor, S. Gupta, N. Ritchey, and A. Wilber, 1992: Seasonal variation of surface radiation budget derived from International Satellite Cloud Climatology Project C1 data. *J. Geophys. Res. - Atmos.*, **97**, 15741–15760.

Eady, E., 1949: Long waves and cyclone waves. *Tellus*, **1**, 33–52.

Edmon, H., B. Hoskins, and M. McIntyre, 1980: Eliassen-Palm cross sections for the troposphere. *J. Atmos. Sci.*, **37**, 2600–2616.

Emanuel, K., 1988: Observational evidence of slantwise convective adjustment. *Mon. Wea. Rev.*, **116**, 1805–1816.

Emanuel, K., M. Fantini, and A. Thorpe, 1987: Baroclinic instability in an environment of small stability to slantwise moist convection. Part I: Two-dimensional models. *J. Atmos. Sci.*, **44**, 1559–1573.

Fouquart, Y. and B. Bonnel, 1980: Computations of solar heating of the earth's atmosphere-A new parameterization. *Beiträge zur Physik der Atmosphäre*, **53**, 35–62.

Frierson, D., I. Held, and P. Zurita-Gotor, 2006: A gray-radiation aquaplanet moist GCM. Part I: Static stability and eddy scale. *J. Atmos. Sci.*, **63**, 2548–2566.

Gall, R., 1976: A comparison of linear baroclinic instability theory with the eddy statistics of a general circulation model. *J. Atmos. Sci.*, **33**, 349–373.

Green, J., 1970: Transfer properties of the large-scale eddies and the general circulation of the atmosphere. *Quart. J. Roy. Meteor. Soc.*, **96**, 157–185.

Gupta, S., N. Ritchey, A. Wilber, C. Whitlock, G. Gibson, and P. Stackhouse Jr, 1999: A climatology of surface radiation budget derived from satellite data. *J. Climate*, **12**, 2691–2710.

Gutowski, W., 1983: *Vertical Eddy Heat Fluxes and the Temperature Structure of the Mid-Latitude Troposphere*. Ph.D. thesis, Massachusetts Institude of Technology.

Gutowski, W., L. Branscome, and D. Stewart, 1992: Life cycles of moist baroclinic eddies. *J. Atmos. Sci.*, **49**, 306–319.

Gutowski, W. J., 1985: Baroclinic adjustment and the midlatitude temperature profiles. *J. Atmos. Sci.*, **42**, 1735–1745.

Gutowski, W. J., L. E. Branscome, and D. Stewart, 1989: Mean flow adjustment during life cycles of baroclinic waves. *J. Atmos. Sci.*, **46**, 1724–1737.

Hansen, J., I. Fung, A. Lacis, D. Rind, S. Lebedeff, R. Ruedy, G. Russell, and P. Stone, 1988: Global climate changes as forecast by Goddard Institute for Space Studies three-dimensional model. *J. Geophys. Res. - Atmos.*, **93**, 9341–9364.

Hansen, J., G. Russell, D. Rind, P. Stone, A. Lacis, S. Lebedeff, R. Ruedy, and L. Travis, 1983: Efficient three-dimensional global models for climate studies: Models I and II. *Mon. Wea. Rev.*, **111**, 609–662.

Hartmann, D., 1994: *Global Physical Climatology*. Academic Press, San Diego, US, 411 pp.

Held, I., 1978: The vertical scale of an unstable baroclinic wave and its importance for eddy heat flux parameterizations. *J. Atmos. Sci.*, **35**, 572–576.

— 1999: The macroturbulence of the troposphere. *Tellus B*, **51**, 59–70.

— 2007: Progress and problems in large-scale atmospheric dynamics. *The Global Circulation of the Atmosphere: Phenomena, Theory, Challenges*, T. Schneider and A. Sobel, eds., Princeton, NJ: Princeton Univ. Press, 1–21.

Held, I. and V. Larichev, 1996: A scaling theory for horizontally homogeneous, baroclinically unstable flow on a beta plane. *J. Atmos. Sci.*, **53**, 946–952.

Held, I. and E. O'Brien, 1992: Quasigeostrophic turbulence in a three-layer model: Effects of vertical structure in the mean shear. *J. Atmos. Sci.*, **49**, 1861–1870.

Held, I. and M. Suarez, 1994: A Proposal for the Intercomparison of the Dynamical Cores of Atmospheric General Circulation Models. *Bull. Amer. Meteor. Soc.*, **75**, 1825–1830.

Holton, J. R., 2004: *An Introduction to Dynamic Meteorology*. 4th edn. Elsevier, 535 pp.

Hsiung, J., 1986: Mean surface energy fluxes over the global ocean. *J. Geophys. Res. - Oceans*, **91**, 10585–10606.

Hsiung, J., R. Newell, and T. Houghtby, 1989: The annual cycle of oceanic heat storage and oceanic meridional heat transport. *Quart. J. Roy. Meteor. Soc.*, **115**, 1–28.

James, I. N., 1987: Suppression of baroclinic instability in horizontally sheared flows. *J. Atmos. Sci.*, **44**, 3710–3720.

James, I. N. and L. J. Gray, 1986: Concerning the effect of surface drag on the circulation of a baroclinic planetary atmosphere. *Quart. J. Roy. Meteor. Soc.*, **112**, 1231–1250.

Jayne, S. and J. Marotzke, 2001: The dynamics of ocean heat transport variability. *Rev. Geophys.*, **39**, 385–411.

Juckes, M., 2000: The static stability of the midlatitude troposphere: The relevance of moisture. *J. Atmos. Sci.*, **57**, 3050–3057.

Kållberg, P., P. Berrisford, and E. C. for Medium Range Weather Forecasts, 2005: *ERA-40 atlas*. ECMWF.

Kirk-Davidoff, D. and R. Lindzen, 2000: An Energy Balance Model Based on Potential Vorticity Homogenization. *J. Climate*, **13**, 431–448.

Korty, R. and T. Schneider, 2007: A climatology of the tropospheric thermal stratification using saturation potential vorticity. *J. Climate*, **20**, 5977–5991.

Lapeyre, G. and I. Held, 2003: Diffusivity, kinetic energy dissipation, and closure theories for the poleward eddy heat flux. *J. Atmos. Sci.*, **60**, 2907–2916.

Levitus, T., S.and Boyer, 1994: *World Ocean Atlas*. National Oceanographic Data Center's (NODC) Ocean Climate Laboratory (OCL).

Lindzen, R., 1988: Instability of plane parallel shear flow (toward a mechanistic picture of how it works). *Pure and Applied Geophysics*, **126**, 103–121.

Lindzen, R. and B. Farrell, 1980: The role of polar regions in global climate, and a new parameterization of global heat transport. *Mon. Wea. Rev.*, **108**, 2064–2079.

Lindzen, R., B. Farrell, and K. Tung, 1980: The concept of wave overreflection and its application to baroclinic instability. *J. Atmos. Sci.*, **37**, 44–63.

Lindzen, R. S., 1993: Baroclinic neutrality and the tropopause. *J. Atmos. Sci.*, **50**, 1148–1151.

Lindzen, R. S. and J. Barker, 1985: Instability and wave over-reflection in stably stratified shear flow. *J. Fluid Mech.*, **151**, 189–217.

Meehl, G. and W. Washington, 1985: Sea surface temperatures computed by a simple ocean mixed layer coupled to an atmospheric GCM. *J. Phys. Oceanogr.*, **15**, 92–104.

Morcrette, J., 1991: Radiation and cloud radiative properties in the European Centre for Medium Range Weather Forecasts forecasting system. *J. Geophys. Res. - Atmos.*, **96**, 9121–9132.

Nakamura, N., 1999: Baroclinic–barotropic adjustments in a meridionally wide domain. *J. Atmos. Sci.*, **56**, 2246–2260.

Oort, A. H. and J. P. Peixoto, 1983: Global angular momentum and energy balance requirements from observations. *Adv. Geophys.*, **25**, 355–490.

Pavan, V., 1996: Sensitivity of a multi-layer quasi-geostrophic β-channel to the vertical structure of the equilibrium meridional temperature gradient. *Quart. J. Roy. Meteor. Soc.*, **122**, 55–72.

Pavan, V. and I. Held, 1996: The diffusive approximation for eddy fluxes in baroclinically unstable jets. *J. Atmos. Sci.*, **53**, 1262–1272.

Pedlosky, J., 1987: *Geophysical Fluid Dynamics*. 2nd edn. Springer-Verlag, New York, 710 pp.

Peixoto, J. P. and A. H. Oort, 1992: *Physics of Climate*. Springer-Verlag New York, Inc., 520 pp.

Philips, N., 1954: Energy transformations and meridional circulations associated with simple baroclinic waves in a two-level quasi-geostrophic model. *Tellus*, **6**, 273–286.

Philips, N. A., 1956: The general circulation of the atmosphere: A numerical experiment. *Quart. J. Roy. Meteor. Soc.*, **82**, 123–164.

Randel, W. J. and I. M. Held, 1991: Phase speed spectra of transient eddy fluxes and critical layer absorption. *J. Atmos. Sci.*, **48**, 688–697.

Rhines, P., 1975: Waves and turbulence on a beta-plane. *J. Fluid Mech*, **69**, 417–443.

— 1979: Geostrophic turbulence. *Annu. Rev. Fluid Mech.*, **11**, 401–441.

Robinson, W. A., 1997: Dissipation dependence of the jet latitude. *J. Climate*, **10**, 176–182.

— 2000: A baroclinic mechanism for the eddy feedback on the zonal index. *J. Atmos. Sci.*, **57**, 415–422.

— 2006: On the self-maintenance of midlatitude jets. *J. Atmos. Sci.*, **63**, 2109–2122.

Russell, G., J. Miller, and L.-C. Tsang, 1985: Seasonal ocean heat transport computed from an atmospheric model. *Dyn. Atmos. Oceans*, **9**, 253–271.

Schneider, T., 2004: The tropopause and the thermal stratification in the extratropics of a dry atmosphere. *J. Atmos. Sci.*, **61**, 1317–1340.

— 2006: The general circulation of the atmosphere. *Annu. Rev. Earth Planet. Sci.*, **34**, 655–688.

— 2007: The thermal stratification of the extratropical troposphere. *The Global Circulation of the Atmosphere: Phenomena, Theory, Challenges*, T. Schneider and A. Sobel, eds., Princeton, NJ: Princeton Univ. Press, 47–77.

Schneider, T. and C. C. Walker, 2006: Self-organization of atmospheric macroturbulence into critical states of weak nonlinear eddyeddy interactions. *J. Atmos. Sci.*, **63**, 1569–1586.

Simmons, A. and B. Hoskins, 1980: Barotropic influences on the growth and decay of nonlinear baroclinic waves. *J. Atmos. Sci.*, **37**, 1679–1684.

Simmons, A. J. and B. J. Hoskins, 1978: The life cycles of some nonlinear baroclinic waves. *J. Atmos. Sci.*, **35**, 411–431.

Sokolov, A. and P. Stone, 1998: A flexible climate model for use in integrated assessments. *Clim. Dyn.*, **14**, 291–303.

Solomon, A. and R. Lindzen, 2000: The impact of resolution on a numerical simulation of barotropic instability. *J. Atmos. Sci.*, **57**, 3799–3816.

Solomon, A. B., 1997a: An observational study of the spatial and temporal scales of transient eddy sensible heat fluxes. *J. Climate*, **10**, 508–520.

— 1997b: *The role of large-scale eddies in the nonlinear equilibration of a multi-level model of the mid-latitude tropophere*. Ph.D. thesis, Massachusetts Institude of Technology.

Solomon, A. B. and P. H. Stone, 2001a: Equilibration in an eddy resolving model with simplified physics. *J. Atmos. Sci.*, **58**, 561–574.

— 2001b: The sensitivity of an intermediate model of the mid-latitude troposphere's equilibrium to changes in radiative forcing. *J. Atmos. Sci.*, **58**, 2395–2410.

Stewart, R., 2005: *Introduction to physical oceanography*. Texas A & M University, `http://oceanworld.tamu.edu/resources/ocng_textbook/contents.html`.

Stone, P., 1972: A simplified radiative-dynamical model for the static stability of rotating atmospheres. *J. Atmos. Sci.*, **29**, 405–418.

Stone, P. and L. Branscome, 1992: Diabatically forced, nearly inviscid eddy regimes. *J. Atmos. Sci.*, **49**, 355–367.

Stone, P. and J. Carlson, 1979: Atmospheric lapse rate regimes and their parameterization. *J. Atmos. Sci.*, **36**, 415–423.

Stone, P. and D. Miller, 1980: Empirical relations between seasonal changes in meridional temperature gradients and meridional fluxes of heat. *J. Atmos. Sci.*, **37**, 1708–1721.

Stone, P. and G. Salustri, 1984: Generalization of the quasi-geostrophic Eliassen-Palm flux to include eddy forcing of condensation heating. *J. Atmos. Sci.*, **41**, 3527–3536.

Stone, P. and M. Yao, 1990: Development of a two-dimensional zonally averaged statistical-dynamical model. Part III: The parameterization of the eddy fluxes of heat and moisture. *J. Climate*, **3**, 726–740.

Stone, P. H., 1978: Baroclinic adjustment. *J. Atmos. Sci.*, **35**, 561–571.

Stone, P. H. and B. Nemet, 1996: A comparision between theory, observations, and models. *J. Atmos. Sci.*, **53**, 1663–1674.

Stull, R., 1988: *An introduction to boundary layer meteorology*. Kluwer Academic Publishers, 666 pp.

Swanson, K. and R. T. Pierrehumbert, 1997: Lower-tropospheric heat transport in the pacific storm track. *J. Atmos. Sci.*, **53**, 1533–1543.

Thompson, A. and W. Young, 2007: Two-layer baroclinic eddy heat fluxes: zonal flows and energy balance. *J. Atmos. Sci.*, **64**, 3214–3231.

Thorncroft, C., B. Hoskins, and M. McIntyre, 1993: Two paradigms of baroclinic-wave life-cycle behaviour. *Quart. J. Roy. Meteor. Soc.*, **119**, 17–55.

Trenberth, K., 1991: Storm Tracks in the Southern Hemisphere. *J. Atmos. Sci.*, **48**, 2159–2178.

Trenberth, K. and J. Caron, 2001: Estimates of meridional atmosphere and ocean heat transports. *J. Climate*, **14**, 3433–3443.

Valdes, P. J. and B. Hoskins, 1988: Baroclinic instability of the zonally averaged flow with boundary layer damping. *J. Atmos. Sci.*, **45**, 1584–1593.

Welch, W. and K. Tung, 1998a: Nonlinear baroclinic adjustment and wavenumber selection in a simple case. *J. Atmos. Sci.*, **55**, 1285–1302.

— 1998b: On the equilibrium spectrum of transient waves in the atmosphere. *J. Atmos. Sci.*, **55**, 2833–2851.

Zhang, Y., P. Stone, and A. Solomon, 2009: The role of boundary layer processes in limiting PV homogenization. *J. Atmos. Sci.*, **66**, 1612–1632.

Zurita, P. and R. Lindzen, 2001: The equilibration of short charney waves: Implications for potential vorticity homogenization in the extratropical troposphere. *J. Atmos. Sci.*, **58**, 3443–3462.

Zurita-Gotor, P., 2007: The relation between baroclinic adjustment and turbulent diffusion in the two-layer model. *J. Atmos. Sci.*, **64**, 1284–1300.

— 2008: The sensitivity of the isentropic slope in a primitive equation dry model. *J. Atmos. Sci.*, **65**, 43–65.

Zurita-Gotor, P. and R. Lindzen, 2004: Baroclinic equilibration and the maintenance of the momentum balance. Part II: 3D results. *J. Atmos. Sci.*, **61**, 1483–1499.

— 2007: Theories of Baroclinic Adjustment and Eddy Equilibration. *The Global Circulation of the Atmosphere: Phenomena, Theory, Challenges*, T. Schneider and A. Sobel, eds., Princeton, NJ: Princeton Univ. Press, 22–46.

Zurita-Gotor, P. and G. Vallis, 2009: Equilibration of baroclinic turbulence in primitive equation and quasi-geostrophic models. *J. Atmos. Sci.*, **66**, 837–863.